NTNU

Norwegian University of
Science and Technology

Deciphering magmatic processes in the 565 Ma Umbukta gabbro, Rødingsfjellet Nappe Complex, Northern Norway

Bergliot Kulsrud Storruste

Geology
Submission date: May 2017
Supervisor: Rune Berg-Edland Larsen, IGP
Co-supervisor: Nolwenn Coint, NGU

Norwegian University of Science and Technology
Department of Geoscience and Petroleum

Abstract

The Umbukta gabbro, emplaced in Rødingsfjellet nappe complex in Nordland, have been investigated, with focus on the geochemistry, field observations and petrography. This tholeiitic gabbro has an intrusive age of 565 $\pm$ 20 Ma, uncommon for igneous rocks in the region. The primary objective of this master's thesis is to constrain the petrogenesis of the gabbro and to further investigate the relationship between the Umbukta gabbro and the synchronous Seiland igneous province, emplaced in the Kalak nappe complex, in Finnmark. Whole-rock major and trace elements compositions were obtained from XRF, ICP-AES and LA-ICP-MS analysis, and mineral chemistry was obtained from EPMA and LA-ICP-MS analysis. Fractional crystallization modelling of an evolving melt composition, was performed using whole-rock trace element concentrations and partition coefficients from literature. In addition, 10 samples were analysed for Sm-Nd isotope composition.

Igneous rocks associated with the Umbukta gabbro include olivine gabbro, olivine-free gabbro, monzodiorites, monzonites, diorites, granodiorites and felsic granitoids. Olivine gabbro represent the most mafic rock group and show compositions up to An_{66} and Fo_{71}, with MgO levels up to 21 wt%. All rocks except the felsic, show an enriched REE pattern, thought to stem from an enriched source, with a decreasing trend from La to Lu and no Eu-anomaly. Petrographic and geochemical studies, as well as field observations and trace element modelling, suggest that the range from ultramafic to intermediate compositions may be explained by fractional crystallization. A contact zone between the gabbro and the metasedimentary host rock in the north, is characterized by mingling between a peraluminous, muscovite-bearing granodioritic component and a mafic component. The granodiorite, which contains abundant metasedimentary xenoliths, is interpreted as the result of crustal anatexis in the aureole of the pluton. Mafic rocks display ε_{Nd} values from -2,5 to +5,6, and show a strong correlation between ε_{Nd} and trace element signature. Evidence for contamination is generally constrained to the margins of the pluton, which suggest that the pluton experienced crustal assimilation at the level of emplacement. These findings, combined with an excellent rate of exposure, makes Umbukta a highly appropriate locality for studying mixing and assimilation processes related to emplacement of mantle-derived magma.

Similarities between tholeiitic rocks from Umbukta and the Seiland igneous province investi-

gated in this thesis, include a wide range of ε_{Nd} values, representing both mantle and crustal isotopic signatures, and strongly enriched REE patterns relative to chondrite. These similarities is taken to indicate that similar processes may have been responsible for the formation of the tholeiitic rocks from the two regions; dominantly fractional crystallization with associated assimilation of crustal rocks. In addition, similar ε_{Nd} values ($\sim$5,5) and trace element patterns for the less contaminated samples, imply they could stem from a similar source, linking these two igneous systems to a widespread magmatic event.

Sammendrag

Umbuktgabbroen, som er innlemmet i Rødingsfjellet dekkekompleks i Nordland, er blitt undersøkt med fokus på geokjemi, feltobservasjoner og petrografi. Denne tholeiitiske gabbroen har en intrusiv alder på 565 $\pm$ 20 millioner år, en uvanlig alder for magmatiske bergarter i regionen. Hovedmålet med denne masteroppgaven er å få en økt forståelse av gabbroens petrogenese, samt å undersøke forholdet mellom Umbuktgabbroen og den synkrone Seiland magmatiske provins som er innlemmet i Kalakdekkekomplekset i Finnmark. Hoved- og sporelementkonsentrasjoner til bergartene ble bestemt gjennom XRF-, ICP-AES- og LA-ICP-MS-analyser, og mineralkjemi ble bestemt gjennom EPMA og LA-ICP-MS-analyser. Fraksjonell krystallisasjonsmodellering av en smeltsammensetning under utvikling, ble utført basert på sporelement- og hovedelement-konsentrasjoner fra bergartskjemi og partisjonskoeffisienter fra litteratur. I tillegg ble isotopsammensetningen for Sm og Nd analysert i 10 prøver.

De magmatiske bergartene som kan assosieres med Umbuktgabbroen inkluderer olivin-gabbro, olivinfri gabbro, monzodioritt, monzonitt, dioritt, granodioritt og felsiske granitoider. Olivingabbro representerer den mest mafiske gruppen av bergarter og viser sammensetninger opp til An_{66} and Fo_{71}, med MgO nivåer opp til 21 wt%. Alle bergarter, unntatt de felsiske, viser sterkt anrikede sjeldne jordarts-mønster, som er antatt å stamme fra en anriket kilde, med en nedadgående trend fra La til Lu og ingen Eu-anomali. Petrografiske og geokjemiske studier, samt feltobservasjoner og sporelementmodellering, antyder at rekkevidden fra ultramafiske til intermediære komposisjoner kan forklares med fraksjonell krystallisering. En kontaktsone mellom gabbroen og den metasedimentære vertsbergarten i nord, kjennetegnes av mingling mellom en mafisk bergart og en ”peraluminous”, muskovitt-bærende granodioritt, med rikelige metasimentære xenolitter, som kan tolkes som et resultat av partiell oppsmelting av skorpebergarter i plutonens aureol. Mafiske bergarter viser ε_{Nd} verdier fra -2,5 til +5,6, og viser en sterk korrelasjon mellom ε_{Nd} og sporelement-signatur. Bevis for kontaminering er generelt sett begrenset til plutonens ytterkanter, noe som tyder på at plutonen ble utsatt for assimilering på plutonens nivå i jordskorpen. Disse funnene, kombinert med spesielt godt eksponerte blotninger, gjør Umbukta til en svært egnet lokalitet for studier av miksing- og assimileringsprosesser relatert

til plassering av mantel-derivert magma.

Likheter mellom tholeiitiske bergarter fra Umbukta og Seiland magmatiske provins, som er undersøkt i denne oppgaven, inkluderer et bredt spekter av ε_{Nd}-verdier, som representerer både mantel- og skorpe-isotopiske signaturer og sterkt anrikede sjeldne jordarts-mønstre, i forhold til kondritt. Dette antas å indikere at lignende prosesser kan ha forårsaket dannelsen av de tholeiitiske bergartene fra de to regionene; en dominerende grad av fraksjonell krystallisering med tilhørende assimilering av skorpemateriale. I tillegg indikerer lignende ε_{Nd}-verdier ($\sim$ 5,5) og sporelementmønstre for de mindre kontaminerte prøvene at de kan stamme fra en lignende kilde, som knytter disse to magmatiske systemene til en utbredt magmatisk hendelse.

Acknowledgements

This master thesis has been carried out at the Department of Geoscience and Petroleum at the Norwegian University for science and technology (NTNU), and has been written in collaboration with the Geological Survey of Norway (NGU). All thin sections and most whole-rock analyses were prepared, conducted and financed by NGU, for which I am very grateful.

First of all, I would like to thank my supervisors, Nolwenn Coint (NGU) and Rune Berg-Edland Larsen (NTNU), for all the help you have given me. I am really grateful for the many and interesting discussions we have had, and the time you have spent on guiding me through this project, both in field and at the office. Your knowledge and enthusiasm is truly inspiring. I would also like to thank Trond Slagstad (NGU) who has helped me a lot in the lab and in the field, and who has dedicated time for long and interesting discussions, from which I have learned a lot. I have greatly appreciated this opportunity NGU has given me, to dive into the field of igneous petrology, and it has been inspiring to work at NGU, among many dedicated geologists. Furthermore, I would like to thank Stein-Martin Tilrum Fagerland, for being my field doctor and assistant in 2016, Sunniva Indrehus for helping me out with Latex-programming and my mother, Unni Storruste for proof reading.

Bergliot Kulsrud Storruste, may 2017

Abbreviations

ppm	=	Parts per million
wt%	=	Weight percent
HNC	=	Helgeland Nappe Complex
RNC	=	Rødingsfjellet Nappe Complex
fO_2	=	oxygen fugacity
REE	=	Rare earth elements
LREE	=	Light rare earth elements
HREE	=	Heavy rare earth elements
LILE	=	Large ion lithophile elements
HFSE	=	High field strength elements
MORB	=	Mid-ocean ridge basalt
XRF	=	X-ray Fluorescence
ICP-AES	=	Inductively Coupled Plasma Atomic Emission Spectroscopy
LA-ICP-MS	=	Laser Ablation Inductively Coupled Plasma Mass Spectrometry
EPMA	=	Electron Probe Micro Analyser

Amp	=	Ampibole
Act	=	Actinolite
Hbl	=	Hornblende
Cpx	=	Clinopyroxene
Opx	=	Orthopyroxene
Ol	=	Olivine
Zrn	=	Zircon
Cal	=	Calcite
Pl	=	Plagioclase
Ap	=	Apatite
Qz	=	Quartz
Ms	=	Muscovite
Bt	=	Biotite
Ep	=	Epidote
Czo	=	Clinozoisite
Ttn	=	Titanite
Rt	=	Rutile
Chl	=	Chlorite
Grt	=	Garnet
Scp	=	Scapolite
Srp	=	Serpentine

Table of Contents

Chapter 1

Introduction

A large number of ore deposits around the world are hosted by mafic intrusions, e.g the Skaergård intrusion in east Greenland, and the Bushveld complex in South Africa. Among other factors, this is related to the fact that mafic magmas are intrinsically enriched in metals such as Ni, Co, Cr, V, Cu, Pt and U, by comparison with more evolved magmas (Robb, 2005). Thus, the understanding of igneous processes responsible for the formation of such mafic intrusions is vital in exploration for future resources. Igneous petrology involves study of processes related to genesis and evolution of igneous rocks. Studies of magmatic differentiation processes by Harker (1909) and Bowen (1928) have laid the foundations for modern petrology, and many of the processes described by these authors are still applicable today. It was early demonstrated that there are significant interaction between mantle derived magma and continental crust, and that magma mixing is an important differentiation process leading to compositional diversification of magmas (Harker, 1909; Bowen, 1928). However, as petrology involves study of processes occurring deep within the earth, it is largely based on indirect evidence, such as geochemical and geophysical data. Thus, it is a continuously developing field, and this study may contribute to enhance the understanding of these subsurface processes.

The current study involves investigation of the Umbukta gabbro, an intrusive rock unit which is located 30 km south-east of Mo i Rana in Nordland. It belongs to the Rødingsfjellet nappe complex which is interpreted as a part of the Uppermost Allochton of the Scandinavian Caledonides. This tholeiitic gabbro has a roughly rectangular shape, stretching approximately 15 km east-west and 4 km north-south. Very little work has been done on this gabbro, until recently, when U/Pb-zircon dating led to some interesting results; the Umbukta gabbro exhibits

an intrusive age of 565 $\pm$ 20 Ma, which is uncommon for intrusive rocks in the Scandinavian Caledonides. However, it has been shown that the Umbukta gabbro has a similar geochemical signature and age as the Seiland Igneous Province, situated in western Finnmark (Høyen, 2016).

1.1 Aim of thesis

The primary objective of the current study is to understand the petrogenesis of the Umbukta gabbro which is not well constrained. Based on geochemical, mineralogical and isotopic analyses as well as field observations, this thesis will seek to answer what processes was dominating in the formation of the Umbukta gabbro and the associated igneous rocks. Secondly, the relationship between the Umbukta gabbro and the Seiland igneous province will be investigated.

Detailed studies of mineral trace element chemistry was the intended scope of the thesis, as this may provide information on magmatic differentiation processes, but early thin section studies revealed that few primary igneous minerals were preserved. Thus, analysis of whole-rock major- and trace- element compositions by X-Ray Fluorescence (XRF) and Laser Ablation Inductively Coupled Plasma Mass Spectrometry (LA-ICP-MS) became the main data foundation for this study, as incipient alteration causes little change in the overall composition of a basaltic rock (Gill, 2010). Fractional crystallization is considered a major differentiation process responsible for the diversity of igneous rocks (Rollinson, 1993; Best, 2003), and thus modelling of fractional crystallization have been performed, for a semi-quantitative estimation of the amount of fractional crystallization. Model parameters have been determined based on a combination of textural and mineralogical information from thin section studies, trends from whole-rock major and trace element plots, as well as published partition coefficients.

Assimilation, another important cause of magmatic differentiation, involves incorporation of crustal material in an ascending magma. The result is contaminated magma, which may have a significantly altered composition. The effects of contamination is commonly unravelled through isotopic and trace element investigations. A complex contact zone between the Umbukta gabbro and the host rock, with implications for assimilation, became the focus of the second field season. In addition, isotopic ratios of samarium (Sm) and neodynium (Nd) was acquired from mafic rocks from this area as well as from other parts of the gabbro. As isotopic Sm-Nd ratios ratios remain unchanged during later fractionation events, they can be applied for investigation

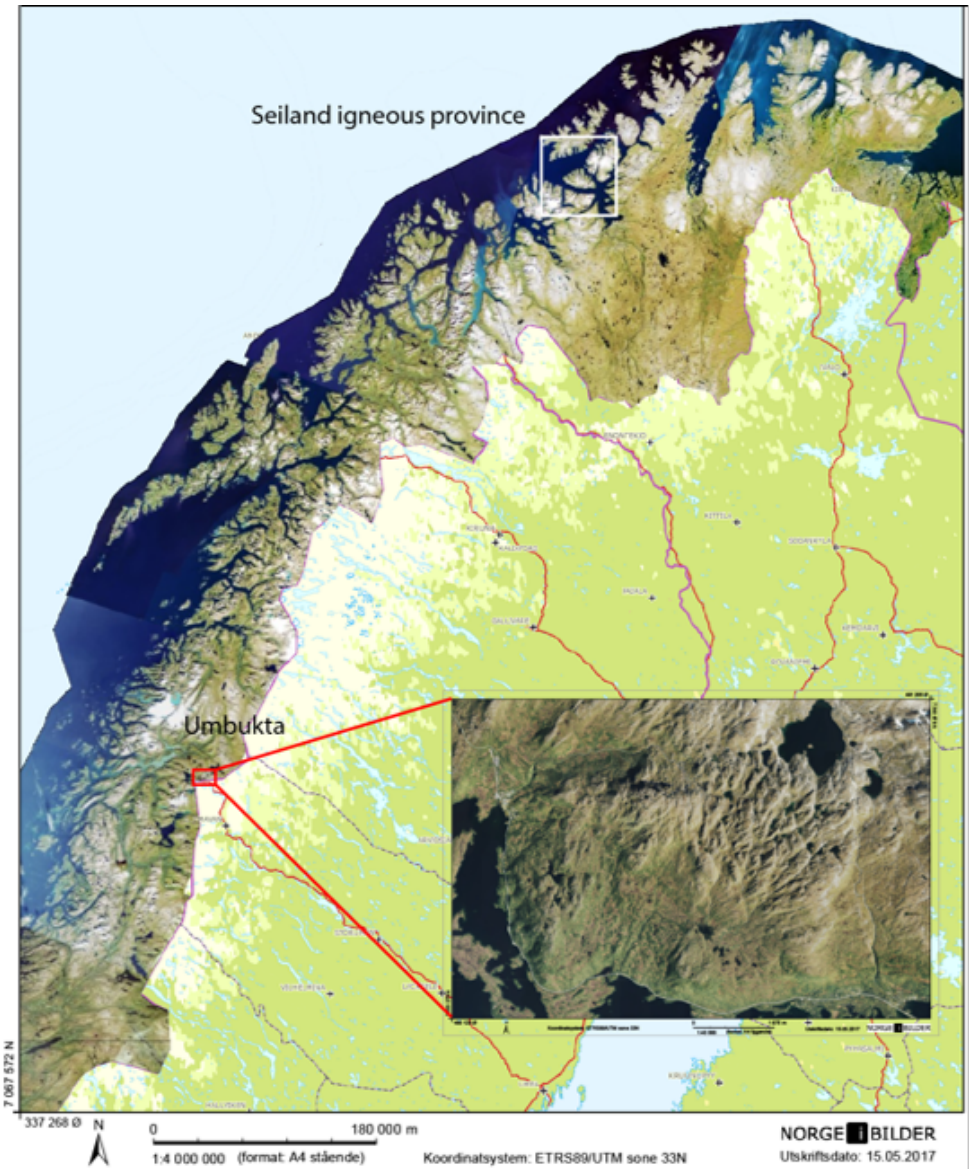

Figure 1.1: Map of Northern Norway where the location of the study area is marked by a red rectangle. The location for Seiland is indicated by a white square. The map is acquired from www.norgeibilder.no

of the source region and the effect of crustal contamination, especially in combination with trace element compositions.

This thesis also represents a continuation of the work done by Høyen (2016). The analysed Sm-Nd isotopes have given the upportunity to compare the source and the processes responsible for the formation of the Umbukta gabbro and the mafic rocks of the Seiland igneous province.

Chapter 2

Background

2.1 Regional geology

2.1.1 A tectonic overview of Laurentia and Baltica

The ancient continent of Baltica comprise the basement for most of today's northern Europe, including Norway (Cocks and Torsvik, 2005). In the Neoproterozoic, Baltica was located at the northwestern margin of Rodinia, whereas Laurentia comprised the center of this supercontinent. After the break-up of Rodinia from about 800 Ma, the early protobaltica remained attached to Laurentia until 570-550 Ma during the Ediacaran times (Cocks and Torsvik, 2005). By the time Laurentia and Baltica began to seperate at about 600 Ma, they were located at latitudes of 30 degrees south (Torsvik et al., 1996). The separation of these two continents resulted in the opening of the Iapetus ocean through asymmetrical rifting accompanied by intracontinental tholeiitic magmatism (Torsvik et al., 1996). For over 100 Myr these two continents drifted and rotated independently until the late Ordovician where Baltica collided with Avalonia at about 443 Ma (Cocks and Torsvik, 2005) Subsequent collision with Laurentia resulted in the formation of a new supercontinent - Laurussia (Torsvik and Cocks, 2005). This collision, that culminated in the Silurian, included the closure of the Iapetus ocean with subduction of Baltic crust under Laurentia with subsequent crustal thickening (Torsvik et al., 1996). In the Carboniferous, Laurussia merged with Gondwana and intervening continents to form Pangea, a second supercontinent, that existed until the late Permian (Torsvik and Cocks, 2004). After the break-up of Pangea, Baltica formed the northwestern part of Eurasia where it has persisted until today (Torsvik and

Cocks, 2005).

2.1.2 Continental break up and Ediacaran magmatism

Evidence for rift-related magmatism that culminated in the Ediacaran, have been detected along both the western margin of Baltica and the eastern margin of Laurentia (Gee et al., 2008). Tholeiitic and alkaline rocks with an age between 615 and 560 Ma, which are located along these margins, have generally been attributed to the break-up of Rodinia and the opening of the Iapetus ocean in the late Neoproterozoic (Kirsch and Svenningsen, 2015). The emplacement of the Long Range Dykes in North-East Canada, with an age of 615 Ma, represent the early stages of rifting along the Laurentian margin (Kamo et al., 1989; Kamo and Gower, 1994). A survey from southeastern Canada propose that the earliest phase involved intrusion of tholeiitic dyke swarms at 615 and 590 Ma (Higgins and van Breemen, 1998). Such mafic dyke swarms can be regarded as evidence for extensional environments (Kamo and Gower, 1994). A later, more widespread event that occurred between 575 and 565 Ma, involved emplacement of basalts, alkaline intrusions, carbonatites and kimberlites (Kamo et al., 1989; Kumarapeli, 1993; Higgins and van Breemen, 1998). The Sept Iles layered mafic intrusion, which is considered to be the third largest layered intrusion in the world, was emplaced during this event (Namur et al., 2010; Higgins and van Breemen, 1998).

Along the western margin of Baltica, Neoproterozoic dyke swarms are found in basement rocks as well as in Caledonian nappes of the Middle Allochton and Upper Allochton (Kirsch and Svenningsen, 2015). The mafic rocks related to this widespread extensional event exhibit alkaline to tholeiitic compositions (Kirsch and Svenningsen, 2015). The Egersund dykes, which represents the earliest stages of rifting along the Baltican margin, were emplaced in proterozoic basement rocks with an intrusive age of 616 Ma (Bingen et al., 1998). The Sarek dyke swarm of 608 Ma (Svenningsen, 2001) and the Kebnekaise intrusive complex of 578 Ma (Kirsch and Svenningsen, 2015) are both contained in the Seve nappe of the Upper Allochton in northern Sweden. The former is believed to mark the onset of sea floor spreading in the Iapetus ocean along the Baltoscandian margin (Svenningsen, 2001). In Central Sweden, the Ottfjället dykes of 665 Ma are contained in the Särv nappe of the Middle Allochton (Claesson and Roddick, 1983). The Kalak Nappe Complex of northern Norway, which also belong to the Middle Allochton, hosts the 582 Ma old Corrovarre dolerite dykes (Roberts, 1990) as well as the Seiland

Igneous Province (SIP). The SIP records a short period of magmatism between 560-570 Ma (Roberts et al., 2006), which is synchronous with the most extensive magmatic event in the neoproterozoic along the Laurentian margin (Higgins and van Breemen, 1998). Mafic rocks of neoproterozoic age are not common in the Uppermost Allochton (UmA), but the Umbukta gabbro, located in the Rødingsfjellet Nappe Complex in the UmA have been dated to 565 Ma (Høyen, 2016).

2.1.3 The Caledonian Orogeny - a tectonic overview

The Caledonian orogeny denotes a sequence of orogenic events occurring in the early Paleozoic, related to the closure of the Iapetus ocean. The orogeny can be traced along the eastern and western side of the Atlantic Ocean from the Arctic region to the British Isles (Corfu et al., 2014b). The formation of the orogen resulted from collision of the continental margins of Baltica, Laurentia and Avalonia, the continents bounding the Iapetus Ocean, in the Ordovician and Silurian (McKerrow et al., 2000). The Appalachian orogen, located at the eastern margin of North America, can be regarded as an extension of the Caledonides as these two orogens have experienced some of the same major tectonic events related to the closure of the Iapetus ocean (Van Staal et al., 1998). A major component of sinistral shear related to this continental collision is recorded in both the Appalachian and Caledonian orogen (Roberts, 2003).

An early Cambrian tectonic event known as the Finnmarkian, was introduced in 1978 (Sturt et al., 1978). The peak of this event was estimated to 500-505 Ma and was believed to have resulted from the collision of the eastern Baltic margin with a magmatic arc (Roberts, 2003). However, the concept of a Finnmarkian phase have been questioned and recent studies suggest that the structures interpreted to have been formed during the Finnmarkian orogen were in fact much older (Kirkland et al., 2006), (Corfu et al., 2007).

The initial stages of Iapetus contraction have been attributed to the Taconian orogeny, a Late Cambrian to Mid-Late Ordovician event involving eclogite formation and westward obduction an island arc onto Laurentia (Van Staal et al., 2009). Taconic-style deformation is characteristic for the Appalachian orogen at the eastern margin of North America (Yoshinobu et al., 2002). Northwest-vergent folds and thrusts observed in the most far-travelled segments in the Scandinavian Caledonides are believed to originate from the Taconian orogeny (Yoshinobu et al., 2002; Roberts, 2003). However, some of these structures are overprinted by SE-vergent struc-

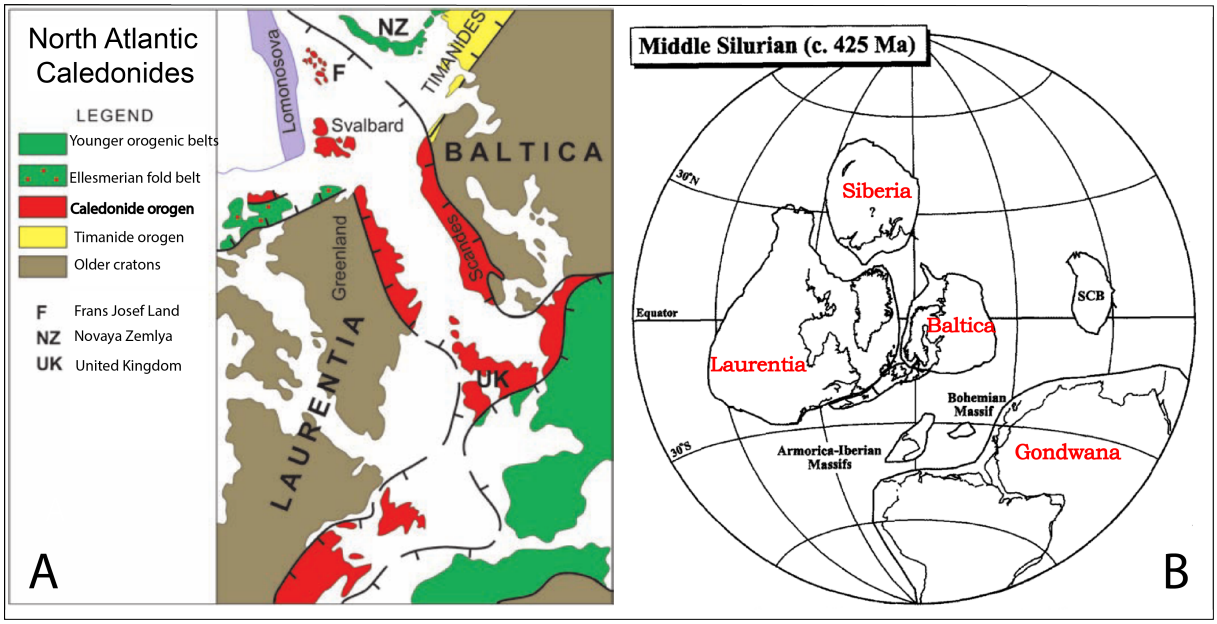

Figure 2.1: A. Overview of the North Atlantic Caledonides (in red) from Gee et al. (2008). B. Mid-Silurian reconstruction where the position of Laurentia and Baltica is well constrained. Modified after Torsvik et al. (1996).

tures from the Scandian event, regarded as the main orogenic event that gave rise to the Scandinavian Caledonides (Gee, 1975). The Scandian event can be seen as a product of oblique collision between Laurentia and Baltica which led to deep subduction of Baltican crust and simultaneous nappe stacking (Roberts, 2003). The presence of microdiamonds and coesite in the Western Gneiss Region is consistent with crustal depths of up to 125 km (Gee et al., 2008). This collisional event lasted throughout the Silurian and ended in the Early to Mid Devonian (Corfu et al., 2014b). A subsequent period of orogenic collapse which lasted into the late Devonian, led to W to NW directed extension along detachments (Gee et al., 2008).

2.1.4 The Scandinavian Caledonides

The Scandinavian Caledonides can be followed for over 1800 km from the Barents Sea region via western parts of Sweden and Finland to the Stavanger district of southwestern Norway (Roberts and Gee, 1985). The orogen is characterized by a variety of flat-lying thrust sheets of variable origin and lithologies that have been translated east- to southeastward for up to several hundreds of kilometers (Roberts and Gee, 1985; Corfu et al., 2014a). The Scandinavian Caledonides are generally considered to be divided into four units; the Lower, Middle, Upper and Uppermost Allochtons, which overlie autochtonous to parautochtonous basement (Roberts and

Gee, 1985). This subdivision has been the tectonostratigraphic framework for the interpretation of the orogen for the last 30 years. The Lower and Middle Allochton in Norway are composed of Neoproterozoic to Ordovician sedimentary and crystalline rocks deformed under subamphibolite facies (Yoshinobu et al., 2002; Stephens et al., 1985). The Upper Allochton contains low to high grade metasedimentary and igneous sequences, including island-arc complexes and ophiolites formed in the Ordovician to Lower Silurian (Stephens et al., 1985; Gee et al., 2014). Migmatitic gneisses deformed under amphibolite facies and marble-schist sequences dominates the Uppermost Allochton. In addition, the allochton comprise a large number of syn-orogenic plutons, with a dominantly granitoid composition (Stephens et al., 1985). The Lower- and Middle Allochtons are believed to be derived from Baltoscandian margin, whereas the Upper Allochton represents the Iapetus ocean and the Uppermost Allochton has affinities to the Laurentian margin (Stephens et al., 1985; Roberts et al., 2007).

Recently, this division has been criticised for being too rigid and simplistic. As pointed out by (Corfu et al., 2014a) a problem with this subdivision is that the different allochtons often imply a specific paleogeographic origin, while each allochton may in fact be composed of units derived from a variety of different sources. One example is from the Kalak nappe, interpreted to be positioned in the Middle Allochton derived from the Baltic margin. A recent study by Høyen (2016) suggested a common source for the mafic intrusions in the Seiland igneous Province in the Kalak Nappe Complex and the synchronous Umbukta gabbro in the Rødingsfjellet Nappe Complex in the Uppermost Allochton, linking these two distinct nappe complexes together. Kirkland et al. (2005, 2007) argued that evidence for Neoproterozoic tectono-thermal activity in the Kalak nappe is atypical for both Baltic passive margin and Iapetus-derived units and suggested that the Kalak nappe is more likely to have developed outside of Baltica instead of at the Baltican margin, which was the previous conception (Ramsay et al., 1985).

2.1.5 The Uppermost Allochton

The Umbukta gabbro is located in the Uppermost Allochton, which is considered to be the structurally highest and the most far-travelled segment of the Scandinavian Caledonides (Fig. 2.2). It was translated from the Laurentian margin onto the Baltican craton during the Scandian event (Roberts, 2003; Stephens et al., 1985). The time of deposition of the more continuous metasedimentary successions within the Uppermost Allochton correspond to Riphean to Early

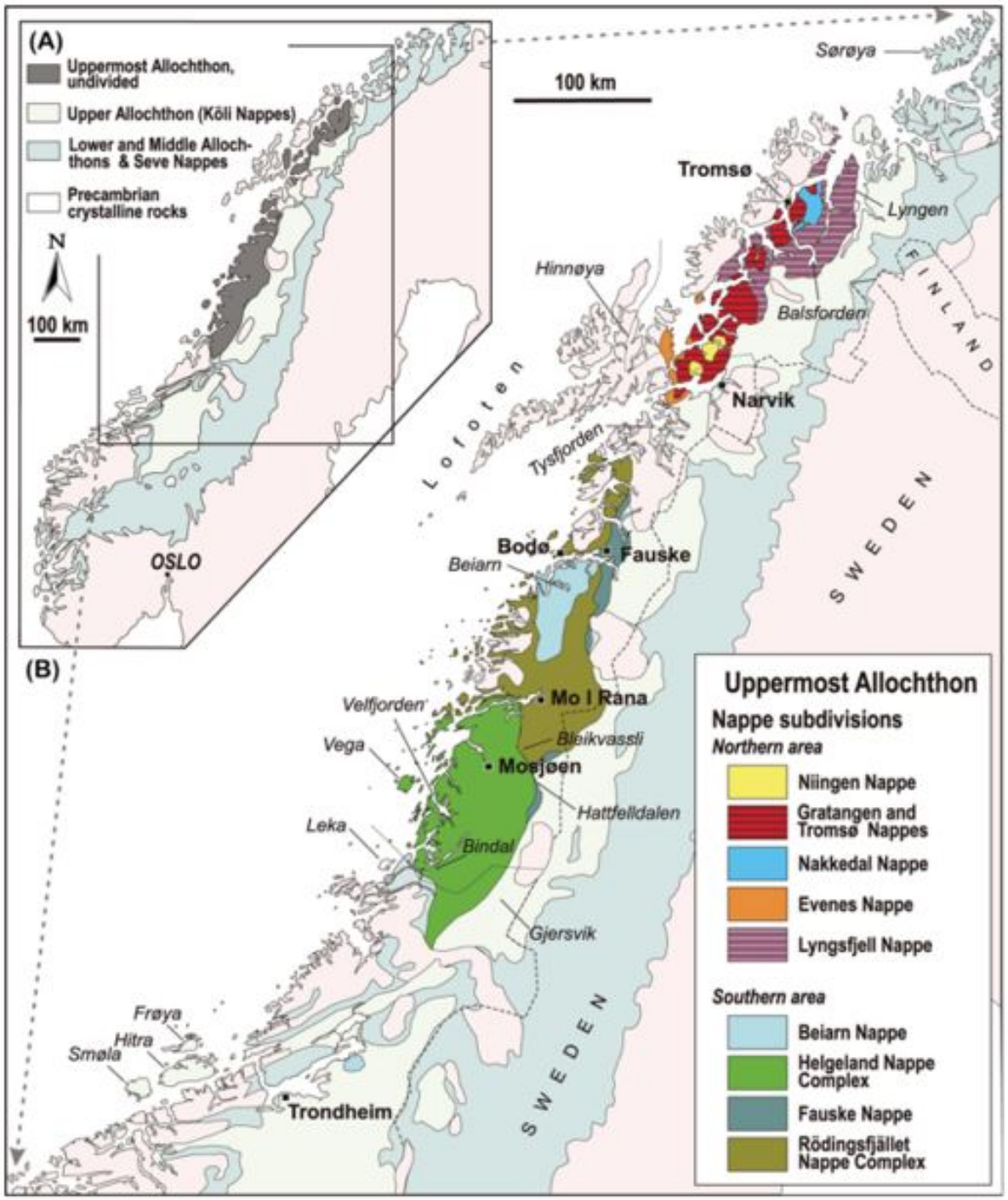

Figure 2.2: A) Overview of the Scandinavian Caledonides B) A map of the nappe subdivisions in the Uppermost Allochton of the Scandinavian Caledonides, from Roberts et al. (2007). The Umbukta gabbro is emplaced in the Rødingsfjellet nappe complex, and is located close to Mo i Rana.

Silurian (Roberts et al., 2007). The Uppermost Allochton is dominated by two major nappe complexes, situated in the county of Nordland: The Helgeland Nappe Complex (HNC) and the underlying Rødingsfjellet Nappe Complex (RNC) (Roberts and Gee, 1985). Slivers of crystalline basement occur notably in these two tectonic mega-units as locally migmatized gneisses

(Roberts et al., 2007). The other exposed section of the Uppermost Allochton is situated in the county of Troms and is composed of both named and unnamed nappe units, and the temporal and spatial relationship between these units is poorly known (Roberts et al., 2007; Augland et al., 2013).

The Rødingsfjellet Nappe Complex (RNC), which covers most of the Rana area, is composed of six nappe units which are in large part characterized by medium- to high-grade metamorphic rocks dominated by marbles (Melezhik et al., 2015). One of the middle nappe units, known as Ravnålia nappe, can be further subdivided into three units; the lowermost Kjerringfjellet group, the Dunderland formation and the Ørtfjellet group. The Kjerringfjellet group is composed of paragneisses intruded by granitic plutons post-dating the orogenesis (Melezhik et al., 2015) in addition to Neoproterozoic mafic intrusions, such as the Umbukta gabbro. The marbles and mica schist of the Dunderland formation make out the principal host rocks of the abundant iron formations in the Mo i Rana area (Melezhik et al., 2015). The more intensely studied Helgeland Nappe Complex (HNC) is composed of five nappe units which can be divided in two groups. One of the groups include the Lower, Upper and Horta nappes which are composed of marbles, calc-silicates and migmatitic gneiss, whereas the other group comprising the Middle and Sauren-Torghatten nappes, consist of marbles, metaconglomerates, calc-silicate and pelitic schist in addition to fragments of Iapetan oceanic crust (McArthur et al., 2014). The HNC is dominated by voluminous synorogenic granitic intrusions, where the largest is known as the Bindal Batholith. It represents a wide spectrum of igneous rocks ranging from gabbro to leucogranite (Nordgulen et al., 1993). Emplacement of the oldest plutons are probably synchronous to a migmatization event at about 477-468 Ma, which is also corresponding in time with the Taconian orogeny (Yoshinobu et al., 2002).

2.2 Previous work

Even though previous work on the Uppermost Allochton have to a large extent been focusing on the HNC, the RNC have been mapped in 1:50 000 scale (Marker et al., 2012). Studies of the Umbukta gabbro and the surrounding rocks are mainly restricted to a few master theses, which have involved detailed mapping as well as geochemical and geochronological studies (Sneltvedt, 1981; Høyen, 2016). The work of Sneltvedt (1981) involved mapping of the Kalvatn

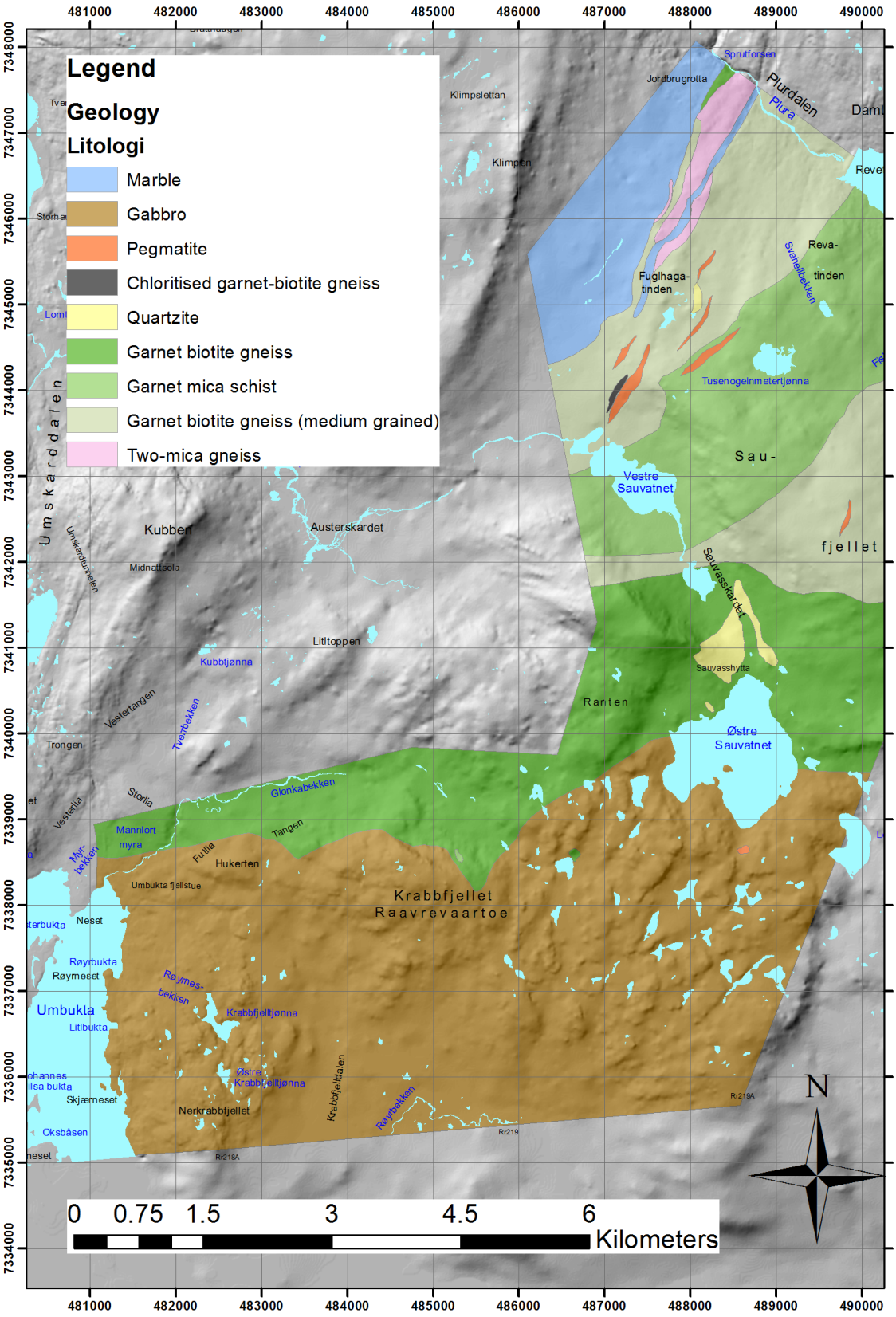

Figure 2.3: Field map of the study area by Høyen (2016). The Umbukta gabbro is marked with brown colour and the hostrock is marked with dark green.

area in Rana, resulting in an interpretation of the tectonostratigraphy and reconstruction of the deformational and metamorphic history of the different nappe units. The Umbukta gabbro was described as a metagabbro complex and interpreted to have been intruding quartzofeldspathic gneisses of supracrustal origin (Sneltvedt, 1981). Repetetive intrusions of mafic magma alongside fractionation were believed to have been the dominant processes forming the gabbro complex. Magmatic breccia was interpreted to have been a late-stage phenomena, formed as the result of simultaneous intrusion of mafic and monzonitic to monzodioritic melts accompanied by movements in the partly solidified magma. The origin of the monzonitic to monzodioritic melts is not known (Sneltvedt, 1981).

The recent project of Høyen (2016) focused on the Kjerringfjellet group in the RNC which is intruded by the Umbukta gabbro. Geochronological studies provided a U-Pb zircon age of 565+/- 20 Ma for the gabbro and a depositional age of less than 1000 Ma for the host rock, which is described as a garnet biotite gneiss (Høyen, 2016). She argues that the deformation of the host rock occurred prior to intrusion, and that a granitoid, observed at the contact between the gabbro and the host rock, is likely to stem from partial melting of the host rock during emplacement of the gabbro. The whole rock geochemistry of the mafic rocks indicates a tholeiitic intrusion formed in an intracontinental rift or back-arc setting (Høyen, 2016). Based on geochronology and geochemical characteristics, she further suggests a possible genetic relation between the Umbukta gabbro and the Seiland Igneous Province, implying that these intrusions which are traditionally placed in the Uppermost and Middle Allochton, should in fact be part of the same allochton (Høyen, 2016). However, she emphasizes the need for further research to confirm or reject this theory.

A study by Claesson (1980) reported the presence of granitic dykes, up to a few metres in thickness, cutting migmatitic metasediments of the RNC and in part the Umbukta gabbro complex. A Rb-Sr isochron provided an age of 447+/-7 Ma for the granitic dykes (Claesson, 1980).

Chapter 3

Theory

3.1 Classification and distribution of elements

Elements can be classified according to their abundance in a rock and separated into major, minor and trace elements. Major elements are present in concentrations greater than 1.0 wt% and they control to a large extent the mineralogy (Rollinson, 1993; Best, 2003; Winter, 2010). They are usually presented as oxide and some examples are SiO_2, Al_2O_3, FeO, MgO, CaO, Na_2O_3 and K_2O. Minor elements are present in concentrations between 0.1 wt% and 1.0 wt% and they mostly substitute for major elements. However, if they reach a sufficiently high concentration, they may form separate mineral phases (Winter, 2010). Trace elements constitute less than 0.1 wt% of a rock and their concentrations are given in ppm. Due to their low concentrations trace elements substitute for major elements and occupy the preferred sites in the minerals (Rollinson, 1993). Trace elements are incorporated in different phases with great selectivity and are highly sensitive towards igneous differentiation processes. As a result, trace elements are particularly suited for reconstructing the evolution and the origin of igneous rocks (Winter, 2010; Rollinson, 1993). Goldschmidt (1937) formulated three simple rules for predicting the behaviour of trace elements based solely on the element's valence and radius:

1. Ions with equal radius and valence state should behave the same and thus enter into a solid solution in amounts proportional to their concentration.

2. For ions with equal valence but different radius, the smaller ion is preferably incorporated into the solid rather than into the liquid.

3. For ions with equal radius but different valence, the ion with the higher charge is preferably incorporated into the solid rather than into the liquid.

3.1.1 Partition coefficient

Every trace element will be distributed between a mineral and a melt according to the element's affinity for each phase. This distribution can be expressed by a an equilibrium constant, Kd, known as the partition coefficient (McIntire, 1963):

$$Kd_i = \frac{C_i^{mineral}}{C_i^{melt}} \tag{3.1}$$

Kd_i is the partition coefficient for trace element *i*. $C_i^{mineral}$ represents the concentration of element *i* in the mineral, whereas C_i^{melt} represents the concentration of element *i* in the melt (Rollinson, 1993). Partition coefficients can be determined either experimentally or from natural systems where both minerals and a glassy matrix have been preserved. In case of the latter, minerals need to be physically separated from the matrix and the composition precisely measured for both parts (Thompson and Malpas, 2000). Compatible elements are defined as elements that show a preference for the mineral. Thus, Kd > 1 for compatible elements, whereas the Kd < 1 for incompatible elements, which show a preference for the melt. Whether an element is regarded as compatible or incompatible depends particularly on the composition of the melt, but is also dependent on the minerals involved and the temperature and fO_2 of the melt (Rollinson, 1993; Green and Pearson, 1986). Several studies have shown that Kd-values for the rare earth elements (REE), and presumably other elements, systematically increase with increasing silica content (Green and Pearson, 1986; Brophy et al., 2011). Equation 3.2 shows how the bulk partition coefficient, D_i can be calculated if the percentage of each crystallizing mineral phase is known and if a Kd for all elements in every crystallizing mineral phase is known. X_j is the weight fraction of mineral j and Kd_i^j is the partition coefficient of element *i* in mineral j (Rollinson, 1993).

$$D_i = \sum X_j \times Kd_i^j \tag{3.2}$$

3.1.2 Substitution of trace elements in minerals

Incompatible trace elements can be subdivided into two groups based on their ratio of valence to ionic radius. Large ions with small charge are known as large ion lithophile elements (LILE) and include K, Rb, Cs, Ba, Sr , $Pb^{2+}$and Eu^{2+} (Winter, 2010). LILE are considered to be mobile during alteration, especially if a fluid phase is involved, which should be accounted for when dealing with trace element analysis of altered samples (Rollinson, 1993; Winter, 2010). Sr is incompatible in most minerals except for plagioclase in which it substitutes for Ca, while Rb, and Ba in particular, substitute for K in mica and K-feldspar (Severs et al., 2009; Best, 2003). The high field strength elements (HFSE) are characterized by high charge and a small ionic radii which include the REE (explained below), Th, U, Pb^{4+}, Zr, Hf, Ti, Nb, Ta, Y and Sc (Rollinson, 1993; Winter, 2010). During metamorphism and alteration the HFSE remain relatively immobile (Winter, 2010). Ti-rich phases such as ilmenite and Ti-magnetite provide high partition coefficients and readily incorporate Nb, Ta and Ti (Green and Pearson, 1987; Best, 2003). The abundance of zircon strongly controls the concentration of Zr and Hf and zircon is known to concentrate Th and U (Bea, 1996).

The Rare Earth Elements (REE) is a coherent group of trace elements that are widely used to study igneous petrogenesis (Best, 2003). The REE comprise elements with atom number 57-71 and is commonly subdivided into three groups: The light REE (LREE), the middle REE (MREE) and the heavy REE (HREE). The series include the following elements: La, Ca, Pr, Nd, Pm, Sm, Eu, Gd, Tb, Dy, Ho, Er, Tm, Yb and Lu. All elements form stable 3+ ions and their ionic radii decrease with increasing atomic number, causing them to behave as a continuous series. However, two elements of this group which may exist in other oxidation states, are Ce^{4+} and Eu^{2+}. The decreasing ionic radii make the HREE more compatible than the LREE, which lead to rare earth elements being fractionated relative to each other. One of the advantages of using REE is the fact that they are considered some of the least soluble elements, which makes them stable during alteration and weathering, in most cases. In that way the REE signature in an altered rock may still represent the original igneous signature (Rollinson, 1993). Accessory minerals such as zircon, apatite and titanite have a strong influence on the REE pattern as these provide high partition coefficient for the REE (Hollings and Wyman, 2005). Apatite, an early crystallizing and long lasting phase, is particularly known to accommodate the LREE (Hoskin et al., 2000; Chu et al., 2009). Titanite and amphibole have commonly high partition coefficient

for the MREE (Best, 2003; Brophy et al., 2011), whereas zircon, equal to garnet, accommodate the HREE (Bea, 1996). Of the rock forming minerals, garnet is one of the richest in the HREE and typically have very low LREE concentrations (Bea, 1996). Clinopyroxene is also a typical host for the REE and accommodates these elements by substitution of Ca (Dobosi and Jenner, 1999). As a divalent cation, Eu^{2+} is strongly partitioned into plagioclase, where it substitutes for Ca^{2+} (Winter, 2010). This substitution will only occur under conditions of low oxygen fugacity (f_{O2}). Thus, a Eu-anomaly in a REE-plot reflect crystallization under reducing conditions, in which a negative anomaly reflect plagioclase fractionation, whereas a positive anomaly reflect plagioclase accumulation (Hollings and Wyman, 2005; Winter, 2010). The ratio Eu/Eu^* is a measure of the europium anomaly and the calculation is shown in equation 3.3 from Rollinson (1993).

$$\frac{Eu}{Eu^*} = \frac{Eu_N}{\sqrt{Sm_N \times Gd_N}} \tag{3.3}$$

Subscript *N* represent normalized values, which is used to eliminate variation in abundance between even and odd atomic numbers in addition to identify fractionation of the REE group relative to chondritic values (Rollinson, 1993). There are a number of normalization values but the most widely cited are the primitive mantle and chondritic values from Sun and McDonough (1989) (Hollings and Wyman, 2005).

Another significant group of trace elements are the transition metals, with atom number 21-30. The elements of this group include two major elements, Fe and Mn in addition to the trace elements Sc, Ti, V, Cr, Co, Ni, Cu and Zn. In contrast to the REE, there is not a coherent geochemical behaviour within this group. While Ti is incompatible with a valence state of 4+, the divalent Mn, Co, Ni, Cu and Zn are compatible and so are the trivalent V and Cr (Rollinson, 1993). The transition metals are commonly associated with primary igneous minerals. Sc, for instance, shows a strong affinity towards clinopyroxene in mafic to intermediate magmas, while Co and Ni are strongly associated with olivine (Hollings and Wyman, 2005; Foley et al., 2013). It has also been shown that the Cr content of clinopyroxene is correlated with the Mg# (Davì et al., 2009). Primary magmas, which is defined as an unmodifed magma after leaving its mantle source, are recognized on the basis of high concentrations of Cr (>1000ppm), Ni (>400) and high Mg# (>0.66) (Best, 2003; Winter, 2010).

3.1.3 Classification diagrams

Major element data are commonly used for classification of rocks. For igneous rocks, the most useful classification scheme available is the the total alkali- versus silica diagram (TAS-diagram) developed by Cox (1979) which became the recommended classification by the IUGS (Le Bas et al., 1986). The diagram consist of 15 fields of different rock names and was constructed on the basis of 24 000 analysis of fresh volcanic rocks (Rollinson, 1993). The TAS-diagram was developed for volcanic rocks and display only extrusive rock names. However, an adaption to intrusive igneous rocks was made by Middlemost (1994) which will be used in this thesis (see Fig. 3.1).

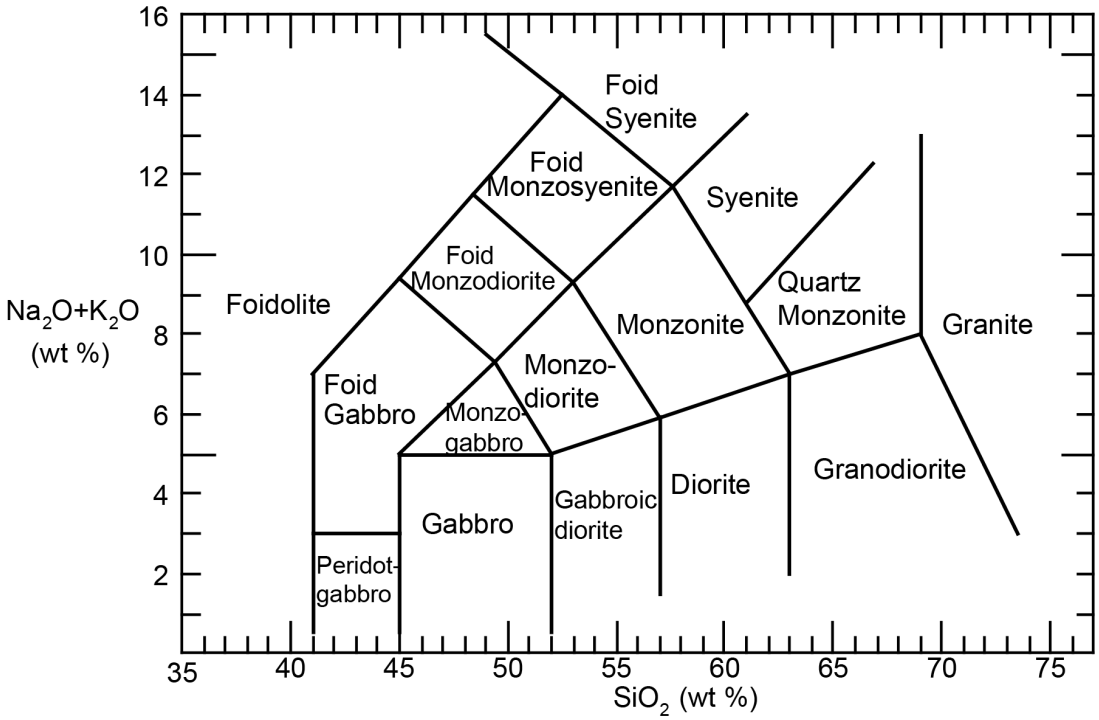

Figure 3.1: Chemical classification and nomenclature diagram after Middlemost (1994).

The igneous AFM diagram is widely used to distinguish between tholeiitic and calc-alkaline trends in the subalkaline magma series. A series of cogenetic rocks may be classified according to their concentration of alkalis (A = Na_2O_3 + K_2O), total iron (F = FeO + Fe_2O_3 = FeO*) and magnesium (M = MgO) (Rollinson, 1993). A dividing line between the tholeiitic and the subalkaline trend within the AFM diagram was presented by Irvine and Baragar (1971) seen in figure 3.2. The parent magmas plot closer to the MgO corner whereas the more evolved samples plot closer to the alkali corner (Winter, 2010). It is accepted that a crystallizing tholeiitic magma will generate a distinct iron-enrichment, known as the *Fenner trend* which is characteristic of

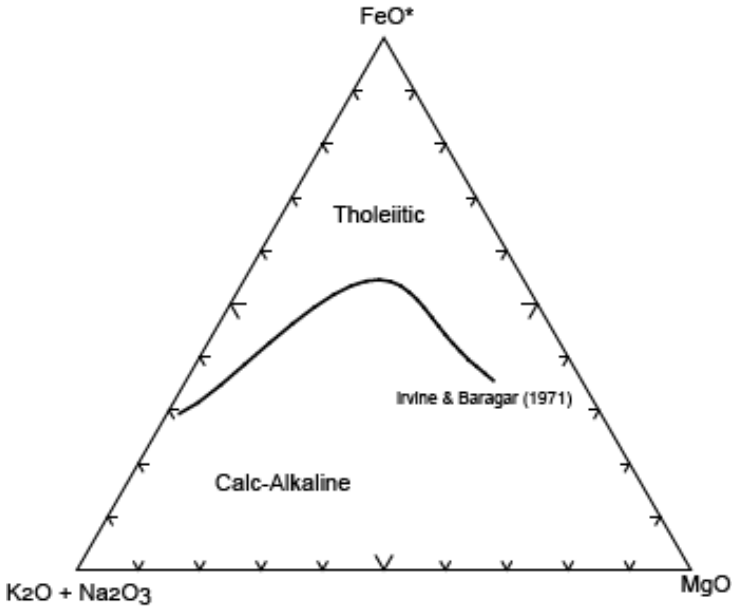

Figure 3.2: Igneous AFM diagram, where the tholeiitic and subalkaline field is seperated by a division line by Irvine and Baragar (1971)

large, closed intrusive systems, such as the layered mafic Skaergård intrusion (Wilson, 1993; Jang et al., 2001). In contrast, if the system is subjected to progressive oxidation as it evolves, the samples will plot in the calc-alkaline field (Wilson, 1993).

3.2 Differentiation processes explained by geochemistry

One of the primary goals of igneous petrology is to determine and evaluate the processes responsible for chemical differentiation of magmas (Wilson, 1993). A useful device for describing differentiation processes is the (major element) variation diagram in which a series of cogenetic rocks is plotted in a bivariate or ternary plot. To be able to identify trends in a variation diagram, a sufficiently high number of samples which represent various stages in the evolution of the magma is required (Rollinson, 1993). One of the most common bivariate variation diagrams is the Harker diagram, in which various major element oxides are plotted against silica, a common differentiation index that generally increases with progressive differentiation (Wilson, 1993). However, the change in silica content does not necessarily change significantly for all rock suites, thus other differentiation indices may be more applicable. For mafic endmembers, for instance, the MgO content or Mg# are more appropriate (see equation 3.4) and this factor will decrease with ongoing magmatic evolution (Winter, 2010; Rollinson, 1993).

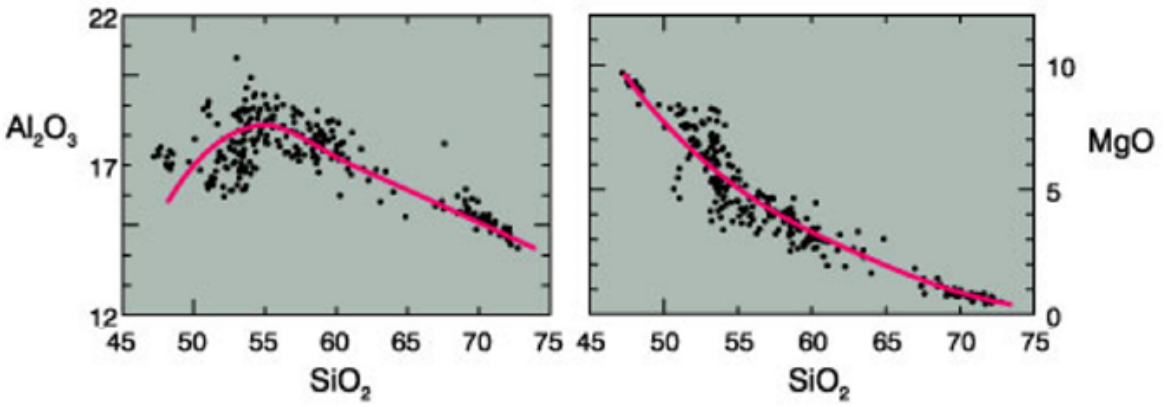

Figure 3.3: Harker diagrams from Crater Lake, from Winter (2010). The continuous trends reflect that these rocks are genetically related. Note the peaked Al_2O_3 curve, which indicate fractionation of an Al-rich phase after the system had reached a silica content of 55%.

$$Mg\# = \left(\frac{Mg^{2+}}{Mg^{2+} + Fe^{2+}}\right) = \left(\frac{\frac{MgO}{40}}{\frac{MgO}{40} + \frac{FeO}{72}}\right) \tag{3.4}$$

The molecular weight of MgO is 40 and the molecular weight of FeO is 72. Other useful differentiation indices are the incompatible trace elements Th and Zr, which concentrate in late melts rather than in early crystallizing phases. Thus, they serve as applicable differentiation indices of more chemically evolved rock suites (Winter, 2010). Zr is also an abundant phase in many rock-forming minerals, from early precipitates such as ortho- and clinopyroxene to late phases such as ilmenite, titanite and K-feldspar (Bea et al., 2006).

3.2.1 Fractional crystallization

Most natural magmas are formed from the melted source rock by either equilibrium melting or by partial melting. Basaltic melts, which are derived from the mantle, will be highly enriched in incompatible elements if only small quantities of melt is produced by partial melting (Robb, 2005). Fractional crystallization, or Rayleigh fractionation, is considered a major process responsible for the diversity of igneous rocks (Rollinson, 1993; Best, 2003). In an ideal case, all crystals are removed after precipitation, due density contrasts between the crystals and the melt, thus the crystals can no longer react with the residual melt. The composition of the melt is continuously varying and represent the new bulk composition (Winter, 2010; Best, 2003). Equation 3.5 describes the trace element concentration in the residual melt, C_L, which can be calculated from the bulk partition coefficient, D_i, the weight fraction of melt remaining, F, and

the original composition of the fractionating melt, C_0.

$$\frac{C_L}{C_0} = F^{D_i - 1} \tag{3.5}$$

As crystallization proceeds, F increases, and the abundance of the incompatible elements will increase exponentially in the melt, whereas compatible elements will be enriched in the crystallizing phases (Robb, 2005)(Fig. 3.4). Magmatic rocks formed from accumulation of crystals from a cooling magma are known as cumulates and mafic cumulates are generally composed of the early crystalling phases olivine, pyroxene and sometimes plagioclase. It is believed that only aphanitic rocks and glass, which have not experienced any crystal fractionation or accumulation, may represent the true liquid melt composition (Rollinson, 1993). A curved trend is expected for fractionation of changing minerals from a changing magma (Best, 2003; Wilson, 1993). It is also known that trends produced by fractional crystallization are identical to trends produced by partial melting (Rollinson, 1993). A modelled and expected trend for fractional crystallization can be seen in figure 3.4.

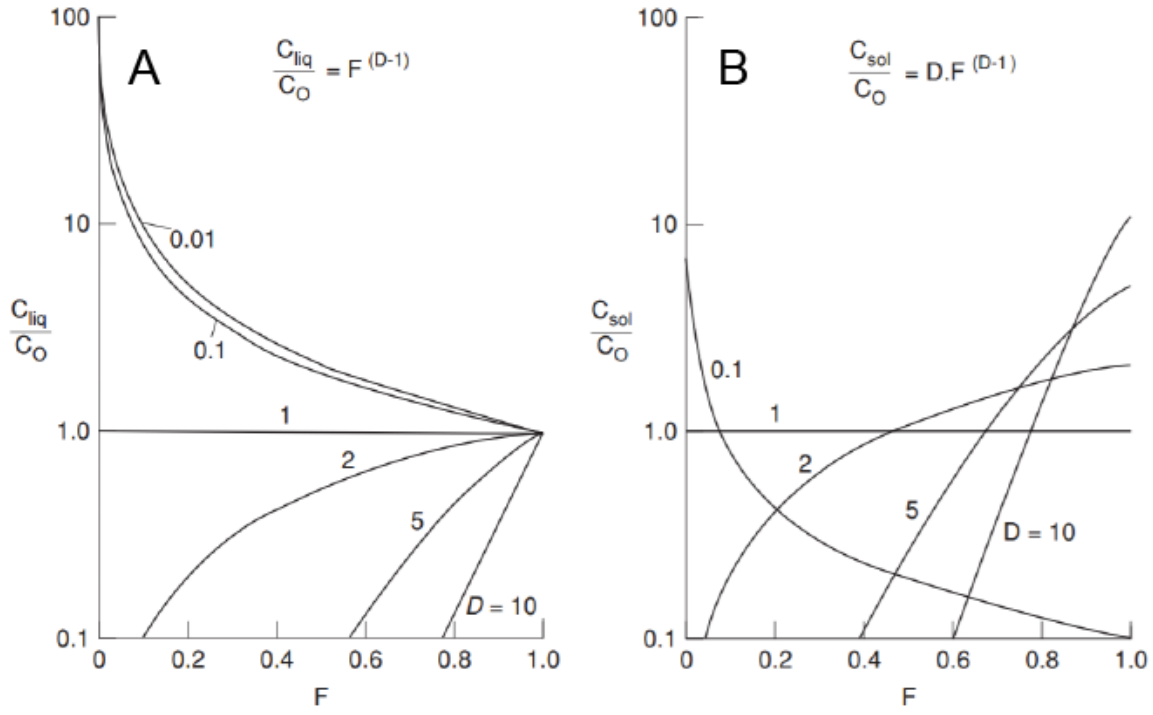

Figure 3.4: Trace element distribution during fractional crystallization in A) the residual melt and B) the solid crystallizing phases, from (Robb, 2005). The various lines represent different bulk distribution coefficients, D.

3.2.2 Magma mixing

The composition of a magma may also be modified on route to the crystallization cite, by mixing or assimilation. The term mixing refers to the process where two magmas blend and form a new hybrid magma of intermediate composition (Best, 2003). The extent to which magmas will mix depends on difference in rheological properties and the relative proportions of the different magmas (Sparks and Marshall, 1986). If the property contrasts are large, the mixing process will be incomplete, resulting in a mingled magma, composed of two identifiable units. Typical features indicative of mingling and mixing is the occurrence of net-veined complexes, consisting of mafic, felsic and hybrid rocks with quenched mafic pillows surrounded by felsic material (Kokfelt et al., 2015; Wilcox, 1999). In a variation diagram, rocks produced from mixing are expected to plot on a straight line between the two end-members from which it was formed (Best, 2003). This is illustrated in figure 3.5.

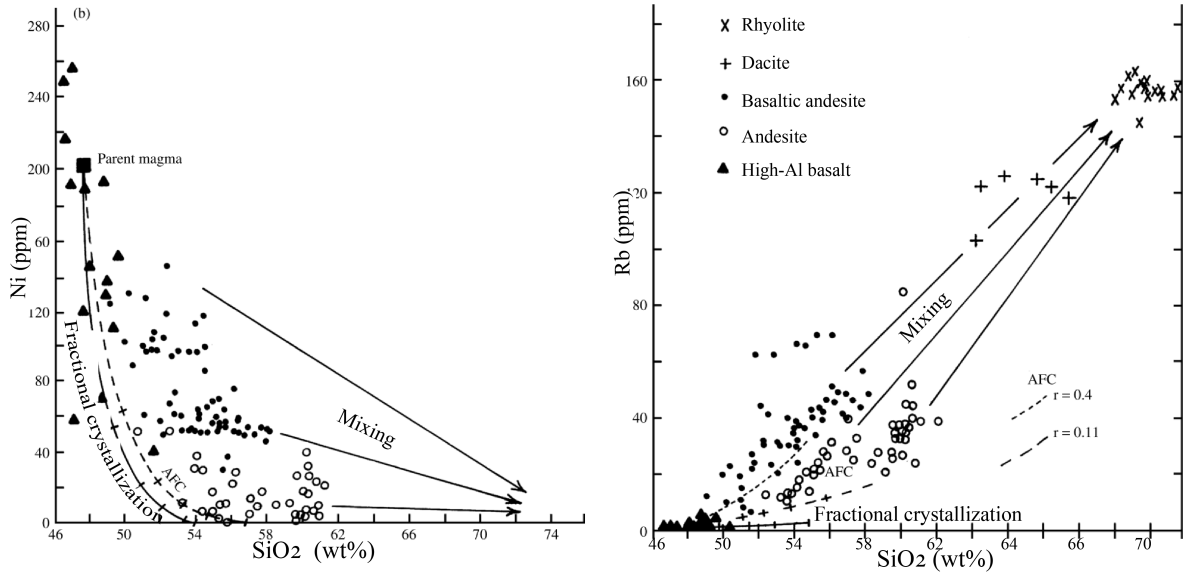

Figure 3.5: Chemical trends produced by mixing and fractional crystallization, from Best (2003). Mixing tend to produce linear trends, whereas trends which can be explained by fractional crystallization, tend to be more curved.

Mixing may also be detected by studying chemical zonation in igneous minerals. This is drawn from the fact that the concentration of trace elements, which are compatible in certain minerals, are expected to decrease from core to rim in an evolving magma (Barnes et al., 2016). However, if a reverse or oscillatory chemical zoning is detected, this will be indicative of influx and mixing with a more primitive magma, and several pulses of magma replenishment may be identified (Davì et al., 2009; Namur et al., 2010; Barnes et al., 2016).

3.2.3 Assimilation

Assimilation involves physical incorporation and chemical dissolution of country rock in a magma resulting in a contaminated magma with a composition between the initial magma and the country rock (Best, 2003). The constituents may be incorporated by melting of country rock or by stoping, the process in which fragments of brittle country rocks are engulfed by magma (Best, 2003). Large scale assimilation may occur under the condition that enough heat is available to bring the temperature of the country rock close to the melting point (Bowen, 1928; Winter, 2010). This heat may be provided by latent heat, which is released during crystallization of the magma (DePaolo, 1981). However, if there are no turbulent flows, the crystallizing magma which supply the required heat, may form a barrier at the cooler margins of the pluton, which will inhibit further assimilation (Winter, 2010). The process is similar to mixing in the way that a hybrid magma is produced. As the composition of the hybrid magma will be a mix of the magma and the host rock, the effect will be more easily detected if the two endmembers are compositionally distinct, such as continental crust assimilated by mantle-derived magma (Winter, 2010).

Studies of isotopic ratios is probably one of the better ways to depict the chemical effects of assimilation (Winter, 2010). The isotopic ratio characteristic of the source region from which a magma is extracted, will remain unchanged during later fractionation events. This can be explained by the small mass difference between any radiogenic pair of isotopes used in geochemistry (Rollinson, 1993). Thus, certain sources may be recognized based on their characteristic isotopic ratio and mixing may be recognized between magmas of isotopically distinct sources (Rollinson, 1993).

3.2.4 The Sm/Nd isotopic system

Samarium (Sm) and neodymium (Nd) is an element pair commonly used to unravel the effects of assimilation. As both elements are LREE with atom number 60 (Nd) and 62 (Sm) their chemical properties are very similar; they are relatively immobile, incompatible elements and tend to fractionate into melts (Winter, 2010). Thus, they will behave mostly the same during magmatic differentiation processes. However, as Nd has a slightly larger ionic radius, it is slightly more incompatible relative to Sm. The consequence is that the Sm/Nd ratio will always

be lower in partial melts than in the mantle from which the melt is derived (DePaolo, 1988). There are numerous isotopes of both Sm and Nd but the most interesting for geochemistry is the radioactive ^{147}Sm isotope which decays by the α-process to the radiogenic ^{143}Nd (DePaolo, 1988). The half-life of ^{147}Sm is 106 Gy, almost 23 times the age of earth. These two isotopes are normally plotted as a ratio with the nonradiogenic ^{144}Nd.

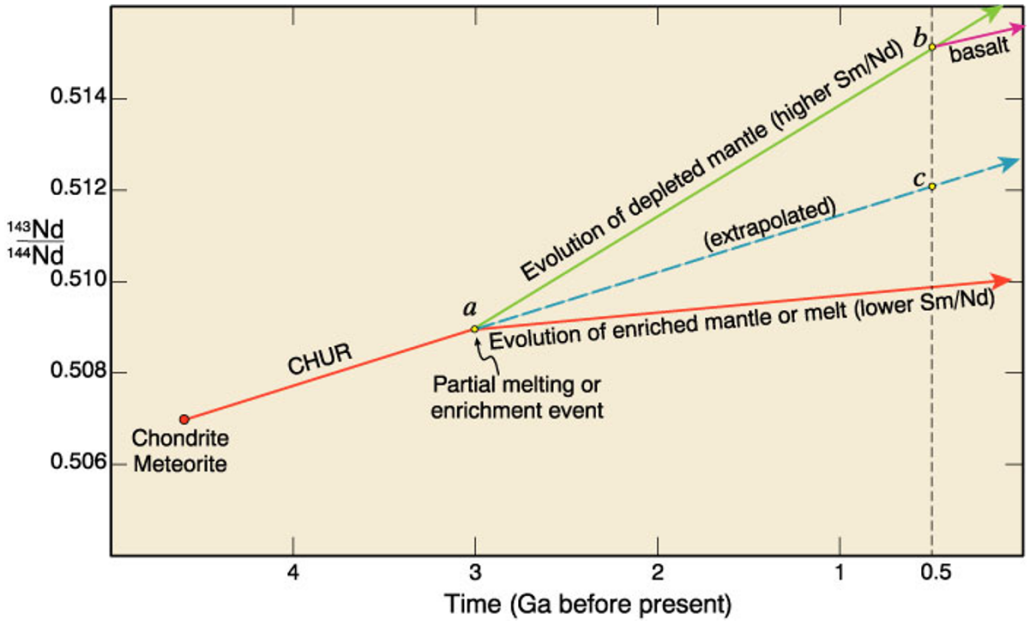

Figure 3.6: The evolution of the Sm/Nd trend from Winter (2010)

However, as variations in the ^{143}Nd/^{144}Nd ratio is very small in nature it is common to use the ε_{Nd} notation for expressing the degree of Nd enrichment in a rock, relative to the bulk earth.

$$\varepsilon_{Nd}(t) = \left[\frac{(\frac{^{143}Nd}{^{144}Nd})_{Sample(t)}}{(\frac{^{143}Nd}{^{144}Nd})_{CHUR(t)}} - 1 \right] 10^4 \tag{3.6}$$

CHUR, (chondrite uniform reservoir) which is an estimate of the average chondrite composition, is thought to represent the composition of bulk earth before the earth was segregated into mantle and core (Winter, 2010). The ε_{Nd} notation indicates the deviation in the ^{143}Nd/^{144}Nd of the sample compared to the CHUR at time *t* (DePaolo, 1988). In the early history of earth, the ^{143}Nd/^{144}Nd ratio in the mantle increased steadily, but by the time the crust and mantle was segregated at 3 Gya, the fractionation of Sm and Nd led to a steeper positive slope for the mantle (higher Sm/Nd ratio) and a more shallow positive slope for the crust (see Fig. 3.6) (Winter, 2010). Because the ε_{Nd} of the Bulk earth is zero, mantle derived rocks will have a positive

ε_{Nd} value while most continental crustal rocks have a negative ε_{Nd} value (DePaolo, 1988). A mantle-derived rock which have experienced assimilation of continental crustal material should display a ε_{Nd} value that is either less positive or negative.

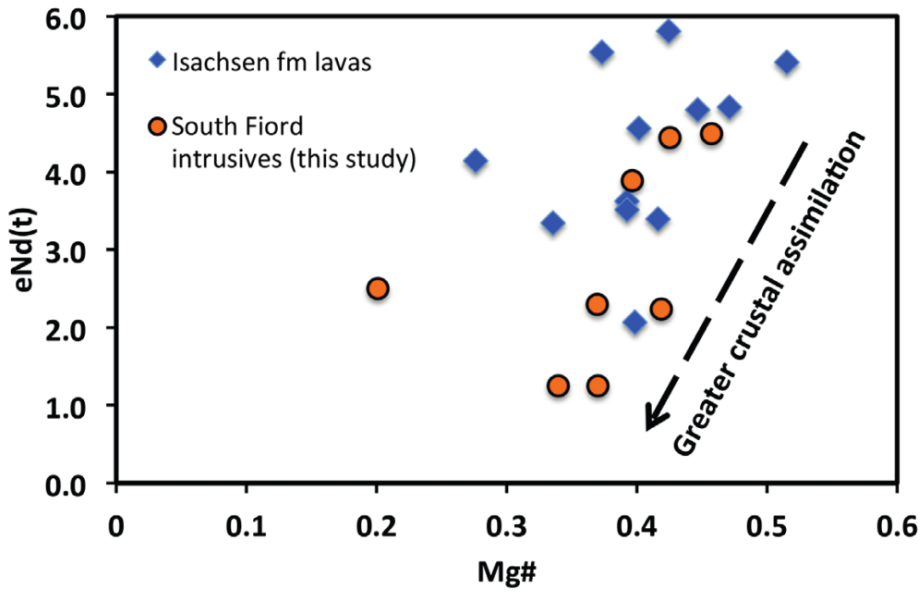

Figure 3.7: Mg# vs. ε_{Nd}-diagram from Kingsbury et al. (2016) showing crustal influence in mafic rocks. The correlation between Mg# and ε_{Nd} for the south fjord intrusives indicates that assimilation with crust was an important process in formation of these rocks (Kingsbury et al., 2016).

Even though variation diagrams may be useful for depicting differentiation processes, they should primarily be seen as a test for a specific hypothesis (Winter, 2010; Rollinson, 1993). Field criterion will be important for determining the process responsible for the composition of a melt. Partly melted xenoliths, for instance, may support a hypothesis involving assimilation (Winter, 2010).

Chapter 4

Methods

4.1 Fieldwork and sampling

The Umbukta gabbro extends approximately 15 km from east to west and 4 km from north to south, crossing the Swedish border. The examined area for this project was restricted to the western part of the pluton, due to the inaccessibility of the easternmost areas. In total, 14 days of fieldwork were conducted in 2015 and 2016 and altogether 67 samples were collected for geochemical analysis and thin section studies. A tablet equipped with ArcMap and a GPS connected by bluetooth, were used during fieldwork in order to coordinate field descriptions with GPS points. Strike and slip were measured using a Silva geologist compass. In 2015, 54 samples were collected from an area of $\sim$8 km^2, extending 2 km from west to east, and 4 km from north to south, between Umbukta fjellstue and the Swedish border. In 2016, the northern, magmatic contact received most of the attention, especially the area around Austre Sauvatnet. A total of 13 samples were collected around Austre Sauvatnet and along the northern margin of the pluton, close to Hukerten, in 2016. As the whole field area is located above 535 m of altitude, the vegetation is scarce, thus the outcrops are easily accessible. Most outcrops around Austre Sauvatnet are completely free of soil and vegetation, which eases the mapping of subtle variations. A sample list comprising coordinates and the methods applied, are presented in appendix A. In addition, the 11 samples analysed for Sm-Nd isotope compositions or mineral chemistry by LA-ICP-MS, were sampled by others: 9 were sampled by Anne Høyen for her master thesis in 2016 and two (MO-28771 and MO-28770) were sampled by Trond Slagstad from NGU, during fieldwork in 2008. The coordinates and chemistry of these samples are

presented in appendix J.

4.2 Petrography

All thin sections were analysed by polarized light microscopy using a Nikon petrographic microscope to identify textures and mineral phases. 19 thin polished thin sections were also analysed by reflected light microscopy. Thin sections of the igneous rocks present in the study area are described as groups in the result chapter, and an overview of the minerals present in each thin section is presented in appendix L.

4.3 Geochemical analysis

In autumn 2015, LA-ICP-MS analyses of mineral trace element chemistry were conducted at the geological survey of Norway, whereas mineral major element chemistry was achieved by Electron Microprobe Analysis at NTNU, in autumn 2016. Samples collected during the field season in 2015, were analysed for whole-rock major and trace element chemistry by XRF and LA-ICP-MS at the geological survey of Norway. Samples collected during the field season in 2016, were milled at NTNU before analysed for whole-rock major and trace element chemistry by ICP-AES and LA-ICP-MS, at ALS geochemistry in Mala, Sweden. The software, IGPET, have been used for plotting and presenting geochemical data. For the heterogenous samples chosen for analysis, only homogenous sections were cut out and selected for further analysis. The rest of the samples selected for whole-rock chemical analysis, were generally homogenous.

4.3.1 Mineral chemistry

LA-ICP-MS for mineral trace element analysis

Laser ablation LA-ICP-MS was used to quantitatively determine the trace element concentrations in clinopyroxene, orthopyroxene and olivine from two samples of olivine gabbro (P19.2 UM) and gabbro (P5.2), sampled by Anne Høyen. The thin sections were polished at the geological survey of Norway before interesting zones were marked with a permanent marker.

These zones were photographed in detail with a camera connected to a Nikon petrographic microscope. The olivines were analysed with a spotsize of 75 micrometer, whereas the pyroxene crystals were analysed with a spotsize of 50 micrometer. The laser pulse rate was set to 7 Hz and the laser energy was set to 5,5 mJ (millijoul). A minimum detection limit for each element is associated with each analysis. Thus, an average detection limit for each element was calculated from 5 analyses of the standard NIST 612, which is presented in appendix F. During some of the analysis, the laser beam drilled through the thin section, which may lead to contamination from the glass slide. To prevent this, the laser signal was cut off prior to contamination in the signal.

Electron Probe Micro Analyser (EPMA), for mineral major element analysis

To quantitatively determine the major element compositions of minerals, 10 thin polished thins sections with a thickness of 40 μm were analysed using a JEOL JXA-8500F electron probe micro-analyser (EPMA), at the geological department at NTNU. The instrument is equipped with five wavelength dispersive spectrometers (WDS) and one energy dispersive spectrometer (EDS). While the EDS record and counts x-ray signals for all elements simultaneously the WDS counts the emitted x-rays from one element at a time (Petruk, 2000). Detectable wavelengths for the JXA-8500F range from 0.087 to 0,93 nm and all elements from Be (4) to U (92) can be analysed. Prior to the analysis interesting zones in the thin sections were marked with a permanent marker. These zones were photographed in detail with a camera connected to a Nikon petrographic microscope. The samples were coated with a thin film of carbon to make the sample conduct the electron beam. The acceleration voltage was set to 15 KeV and the probe current corresponded to 20x10^{-9} A. The beam was defocused to 2 μm to prevent volatilization of the sample surface. The elements which were analysed and the reference standards that were used, are presented in appendix F. The analysed elements were selected according to which elements were expected to be present, based on thin section studies. The results from the EPMA show that analyses often exhibit total concentrations which are above and below 100 %. A possible explanation for the low totals is that elements present in the analysed mineral were not included in the list of analysed elements. The elevated totals could be the result of overestimating the counting in a particular mineral.

4.3.2 Whole-rock geochemistry from NGU, Trondheim

Of the 54 samples collected in 2015, 49 were prepared and analysed for major elements by X-ray fluorescence, and analysed for trace elements by XRF and LA-ICP-MS at the Geological Survey of Norway. XRF is suitable for analysis of elements with atomic number of 9 and higher, but has low precision for the REE.

XRF analysis of whole-rock major element oxides

Sample preparation for major element analysis involves melting of 0,6 g sample material (crushed to a fine powder) mixed with 4.2 g lithium borate ($Li_2B_4O_7$) into homogenous glass. For trace element analysis, 9,6 g of powdered sample material is mixed with 2,4 g of wax before compacted into tablets. The XRF-instrument used at the NGU-lab is a PANaluthical Axios 4kW XRF Rh-X-ray tubes. During the melting process certain elements will incinerate, thus corrections are required. In order to measure the loss of ignition the samples were annealed, which involves heating the sample to 1000°C. Also, the weight of the sample was measured before and after annealing.

LA-ICP-MS analysis of whole-rock trace elements

The samples collected in 2015 were analysed using LA-ICP-MS (Laser-Ablation Inductively Coupled Plasma Mass Spectrometer) for trace element chemistry. Sample preparation methods for LA-ICPMS analysis are similar to the preparation methods for XRF major element analysis in which a glass bead is produced. Analyses are performed on annealed samples. The LA-ICP-MS instrument at NGU is a Thermo Fisher Scientific "ELEMENT XR" attached to a New Wave 193 nm laser. The detection limits are presented in appendix F.

4.3.3 Whole-rock geochemistry from ALS minerals, Mala, Sweden

Sample preparation of the 12 samples collected in 2016 was performed at NTNU, where the samples were washed before being crushed in a Reitsch jaw crusher. The instrument was partly dismantled and washed with ethanol between each sample to minimize the risk of contamination. The samples were subsequently grinded to a grain size of 0,3 mm in a Fritsch disk mill.

The crusher jaws and the grinding disks were both made of tungsten carbide (WC) which has a hardness close to diamond. 30 grams of the final product were split out and sent to ALS Geochemistry at Mala in Sweden, where major elements were analysed by ICP-AES and trace elements were analysed by both ICP-AES and ICP-MS. The description of the methods applied by ALS were aqcuired from the website of ALS global (www.alsglobal.com). Detection limits for analyses contucted at ALS, are presented in appendix H.

Inductively Coupled Plasma - Atomic Emission Spectroscopy (ICP-AES)

Analysis of major element oxides was performed after method ME-ICP06. A prepared sample (0.200 g) is added to lithium metaborate/lithium tetraborate flux (0.90 g), mixed well and fused in a furnace at 1000°C. The resulting melt is then cooled and dissolved in 100 mL of 4% nitric acid/2% hydrochloric acid. This solution is then analysed by ICP-AES and the results are corrected for spectral inter-element interferences. Oxide concentration is calculated from the determined elemental concentration and the result is reported in that format. Analysis of trace elements was performed after method ME-ICP61. A prepared sample (0.25 g) is digested with perchloric, nitric, hydrofluoric and hydrochloric acids. The residue is topped up with dilute hydrochloric acid and the resulting solution is analysed by inductively coupled plasma-atomic emission spectrometry. Results are corrected for spectral interelement interferences.

Inductively Coupled Plasma - Mass Spectroscopy (ICP-MS)

Analysis of trace elements was performed after method ME-MS81. A prepared sample (0.200 g) is added to lithium metaborate flux (0.90 g), mixed well and fused in a furnace at 1000°C. The resulting melt is then cooled and dissolved in 100 mL of 4% HNO_3 / 2% HCl_3 solution. This solution is then analyzed by inductively coupled plasma mass spectrometry. Some base metal oxides and sulfides may not be completely decomposed by the lithium borate fusion. Results for Ag, Co, Cu, Mo, Ni, Pb, and Zn will not likely be quantitative by this method.

4.3.4 Sm-Nd isotopes

Samarium (Sm) and neodynium (Nd) isotope compositions were analysed on samples collected by Trond Slagstad, from NGU and Anne Høyen, during her thesis. Unpublished whole-rock

chemistry was also available for these samples, and is presented in appendix J. The trace and major element compositions for the samples analysed for samarium and neodynium compositions were obtained using the same methods as for the other rocks described in this study. Sm-Nd data on samples from the Umbukta gabbro were obtained in the Geology Laboratory of Université Blaise Pascal (Clermont-Ferrand, France) by using isotope dilution thermal-ionisation mass spectrometry (ID–TIMS). Basaltic samples were decomposed by standard acid dissolution procedures with hydrofluoric acid (HF). Isolation of Nd and Sm was carried out by cation exchange and extraction chromatography methods similar to (samples dissolved with HF), or derived from (samples fused with $LiBO_2$), those described by Pin and Zalduegui (1997). Sm and Nd concentrations were measured by isotope dilution TIMS using a mixed 149Sm–150Nd tracer, allowing determination of $^{147}Sm/^{144}Nd$ ratios with a precision of 0.2 %. Sm isotopes were measured in Clermont-Ferrand after loading the sample in a droplet of c. 5 M phosphoric acid on single Ta filaments by using an automated VG54E mass spectrometer operated in single collection mode. Nd isotopic ratios were determined with double Re filament assemblies with a Thermo Finnigan Triton TI instrument at Nîmes University, in the static multicollection mode, with normalisation to $^{146}Nd/^{144}Nd = 0.7219$.

4.4 Trace element modelling

Trace element modelling was performed to test specific hypotheses related to the processes responsible for the variable chemistry of the rocks in relation to the Umbukta gabbro. The equation for Rayleigh fractionation (Eq. 3.5) was used to calculate the trace element concentration of the residual melt (C_L) and the modelling was performed in three stages with different parameters, to accommodate changing partition coefficients and changes in the crystallizing assemblage. The sample chosen to represent the initial composition of the melt (C_0), was a mafic, fine grained rock (127956) with high concentrations of Ni (235 ppm), Cr (464 ppm) and MgO (10 wt%). C_L was calculated for a range of F-values values (F = fraction of remaining melt), representing different steps within each stage, where 1 represents 100% melt remaining, and each stage started with F = 1. The melt concentration of the last step in stage 1 and 2 were used as the initial composition of stage 2 and 3, respectively. For each step, minerals selected to represent the crystallizing phases were based on the minerals observed in thin section, and which were assumed to have been removed by fractional crystallization. As the presence of

olivine was constrained to the olivine gabbros, the most mafic rock group, it was assumed to be part of an early fractionating assemblage. Interstitial phases, such as biotite, ilmenite and amphibole, were interpreted as late crystallizing phases and were thus included in stage 3. The bulk partition coefficient was calculated with selected minerals, selected mineral proportions and partition coefficients obtained from literature. These are presented in appendix K. Partition coefficients are compiled from mostly tholeiitic and sometimes alkaline systems, and were chosen based on consideration of melt composition. To generate a consistent set of partition coefficients for the REE, the Kd for each mineral was obtained from the same study and missing partition coefficients were obtained from interpolation or extrapolation. In appendix K, these values correspond to the numbers without colour. Some partition coefficients are set to zero as they could not be obtained from literature or was expected to be close to zero. These are not marked with colour, either. For minerals that occur in several stages, higher partition coefficients were selected for the more evolved stages compared to the most primitive, if this was available. The partition coefficients were assumed to remain constant during each stage of the fractional crystallization process. Modelled melt compositions were plotted in chondrite-normalized REE-plots and various bivariate plots with Zr on the x-axis plotted against various transition metals, HFSE and LILE, and then compared with the whole rock analyses for all igneous rocks. The mineral proportions and weight fraction of melt (F) were changed and minerals were removed or added to obtain the best fit. The results from the modelling are presented in the discussion chapter and the modelled trace element concentrations are presented in appendix M.

A compilation of partition coefficients used in modelling, is presented in appendix K, and the partition coefficients were obtained from the following studies: *Norman et al. (2005); Fujimaki et al. (1984); Bougault and Hekinian (1974); Ewart et al. (1973); Ewart and Griffin (1994); Nikogosian and Sobolev (1997); Green et al. (2000); Zajacz and Halter (2007); Bacon and Druitt (1988); Irving and Frey (1978); Dostal et al. (1983); Hauri et al. (1994); Pearce and Norry (1979); Severs et al. (2009); Nash and Crecraft (1985); Matsui (1977); Sisson and Bacon (1992); Sisson (1994); Paster et al. (1974); Luhr et al. (1984); Mysen (1978); Villemant et al. (1981); Villemant (1988); McKenzie and O'nions (1991); Stix and Gorton (1990); Stimac and Hickmott (1994)*

Chapter 5

Results

The results from this thesis can be divided into three parts. The first comprise descriptions of field relations. The second part comprise geochemical results, including whole-rock chemistry, obtained by XRF and ICP-MS, and mineral chemistry from selected thin sections, obtained by EPMA and LA-ICP-MS. Results from Sm-Nd isotopes are also included in this section. The third section comprise petrographic descriptions for all thin sections, described as groups based on the main igneous rock groups in the study area.

5.1 Field descriptions

5.1.1 Description of observed lithologies

Metasediment, migmatitic

The main host rock of the Umbukta gabbro comprise metasediments belonging to the Kjerringfjellet group. These rocks have been described as garnet-biotite gneiss by Høyen (2016) and garnet-bearing schist by Sneltvedt (1981) and they extend about 2-3 km north of the Umbukta gabbro according to Høyen (2016). In this thesis the rocks will be referred to as metasediments.

A subvertical lamination or bedding is prominent in these fine to medium grained rocks and there is an alternation between leucocratic and melanocratic layers. The thickness of the layers ranges from a few millimeters up to 3 centimeters. The rock is fine to medium grained. Locally, abundant garnet is associated with the leucocratic layers. North of Austre Sauvatnet, bodies of

quartzite are located within the metasediments and occur either as 10-30 cm thick beds parallel to the lamination of the metasediments or as larger isolated bodies, probably representing quartz-rich zones in the metasediment (Fig. 5.1A). From approximately 1,5 km north of the northern contact, the metasedimentary rocks are migmatitic to diatexitic. The diatexitic zones appear to be discontinuous and local along the northern margin of the pluton. From the northern part of Austre Sauvatnet to the contact, a continuous section of stromatic migmatite with leucosomes of granitoid material is observed. Extraction structures are present in these rocks, seen as felsic irregular veins, perpendicular to the bedding (Fig. 5.1-B).

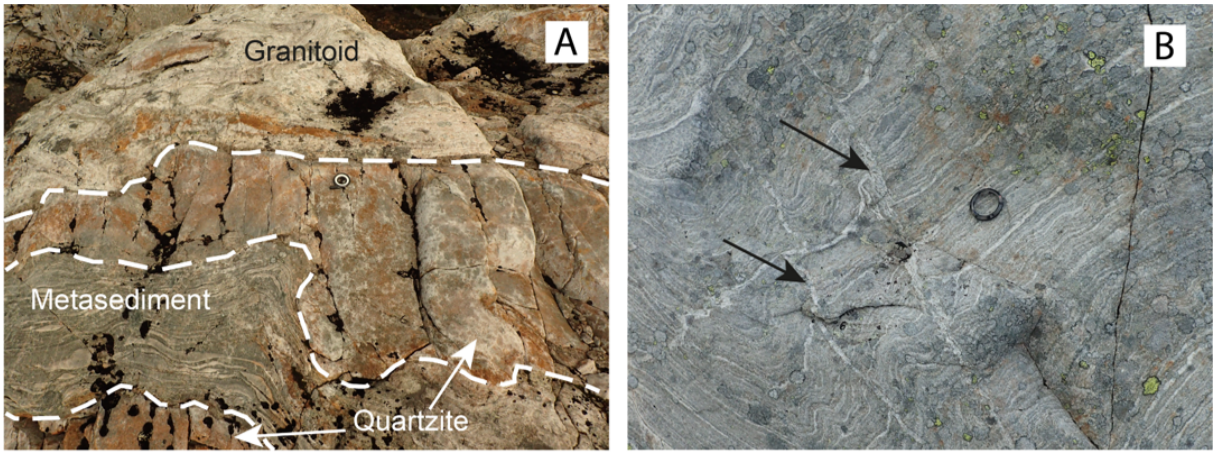

Figure 5.1: A) Quartzite body in between granitic body and stromatic, migmatitic metasediments and B) Extraction structures in migmatitic metasediments. (Both scales are 4 cm in diameter)

Gabbro

The predominant mafic rock in the study area is a medium grained gabbro with an equigranular texture. Fine grained (<1 mm) and coarse grained (>5 mm) varieties are also common. In general, the dominating minerals in the gabbroic rocks are subhedral hornblende and pyroxene, which constitute $>$ 60 % of the modal mineralogy. Plagioclase is an abundant interstitial phase and is commonly lath-shaped. Poikilitic garnet of $<$ 1 cm is rare, but evenly distributed when present. Smaller amounts of garnet is observed within some of the gabbroic rocks. Variations in terms of mineralogy and texture is substantial for the gabbroic rocks in this pluton. In some localities, the texture becomes inequigranular at mesoscale, where pockets of coarse grained minerals occur in rocks dominated by fine to medium grained minerals (Fig. 5.2-B). Inequigranular texture is also seen in the coarser rocks which are composed of larger crystals of hornblende and pyroxene and smaller, interstitial plagioclase. The abundance of homogenous

medium grained gabbro appear to increase when moving away from the northern and western contact. The greater number of gabbroic rocks are melanocratic but leucogabbro are locally observed. An olivine-rich gabbro was observed at three localities in the westernmost part of the study area. The olivine gabbro can be distinguished from the other gabbroic rocks by a brown rusty surface and a darker fresh surface with visible light green olivine grains (Fig 5.2-A). The majority of the gabbroic rocks have a greenish appearance and some pyroxene grains exhibit a lighter green rim, which can be seen in a hand sample. Locally, there is an orientation and elongation of both light and dark minerals in the gabbros.

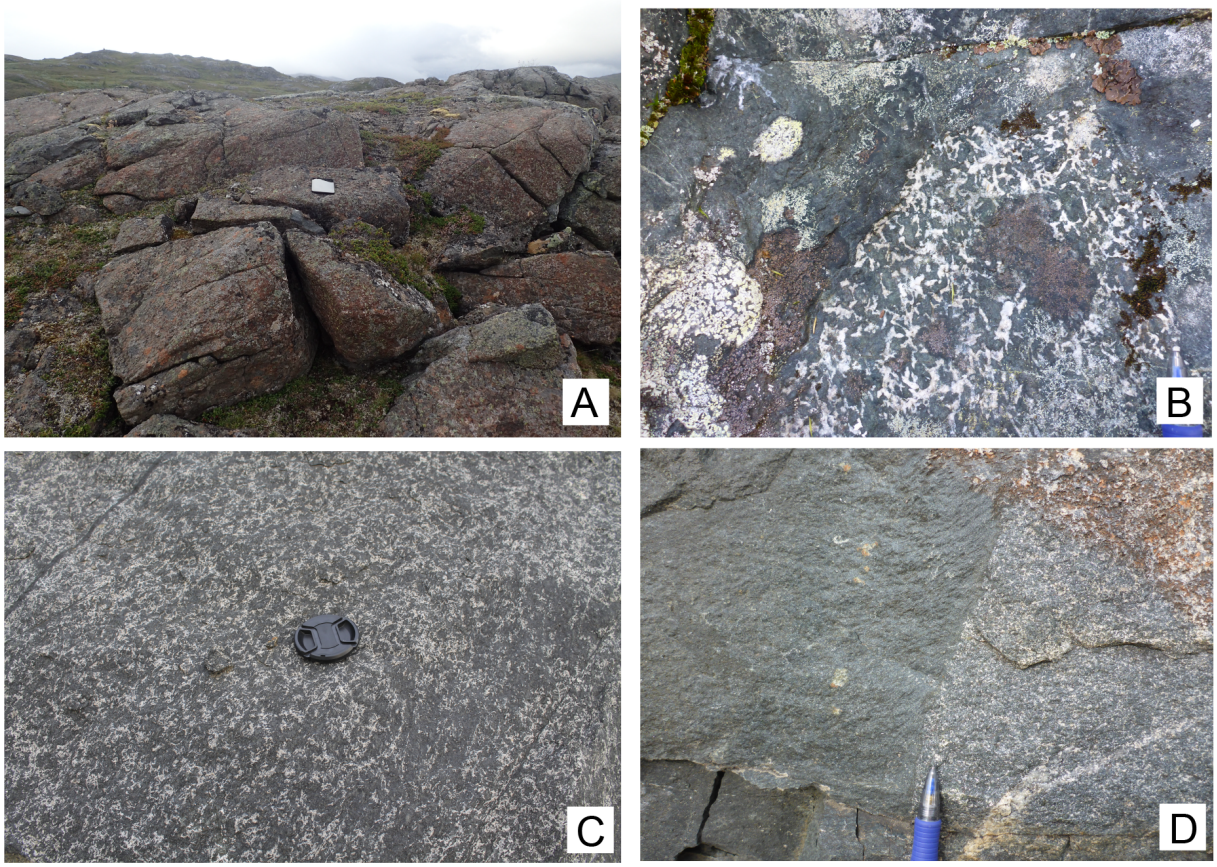

Figure 5.2: A) Outcrop of olivine gabbro. Note the rusty colour of the surface. B) Pocket of coarse grained gabbro enclosed by fine grained gabbro. C) Typical texture of the medium grained gabbro. D) Contact between a fine grained gabbro and a medium grained, more light coloured variety.

Porphyritic diorite

Rocks with an intermediate composition have been named diorite, and like the gabbroic rocks, there are many textural varieties. The most dominant type is a porphyritic diorite comprising subhedral to euhedral feldspar phenocrysts of 0,3-1,5 cm. The abundance differs from a few

scattered phenocrysts to tightly packed. The matrix of this rock is equigranular and dominated by medium grained feldspar and lesser pyroxene and amphibole. In other dioritic rocks, phenocrysts are lacking, and they show equigranular texture with equal amounts of light and dark minerals. There is a substantial difference in colour between the different dioritic rocks. Thus, the leucocratic and melanocratic endmembers are sometimes hard to distinguish from granitoid rocks and gabbros, respectively (Fig. 5.3-A). Poikilitic garnet of 0,5-1,5 cm is associated with the porphyritic diorite (Fig. 5.3-C) and occur in some of the equigranular mafic endmembers. At most localities, the garnets are evenly distributed. In one locality, close to Austre Sauvatnet, the garnets occur as massive aggregates in the diorite (Fig. 5.3-D). However, in some areas the garnet is completely absent. Discontinuous zones of dioritic rocks are observed frequently along the western margin of the gabbro, and occasionally along the northern margin. Commonly, the diorite is observed mingling with gabbro, in which porphyritic diorite encloses rounded to irregular enclaves of fine to medium grained gabbro (Fig. 5.3-B). The contact between the mafic enclaves and the diorite is often sharp, but the enclaves tend to contain a few phenocrysts of feldspar with a similar size and shape as the phenocrysts in the porphyritic diorite.

Felsic granitoid rocks

Felsic leucocratic rocks are found along the western and the northern margins of the pluton and will be referred to as felsic granitoid rocks and contact granitoid rocks, respectively. The contact granitoids are fine grained, equigranular rocks that are dominated by feldspar and quartz with an allotrimorphic texture. Different varieties of mica are also common. At the southern end of Austre Sauvatnet, some felsic rocks contain abundant garnet which appear as 3-6mm poikilitic phenocrysts in a fine-grained matrix composed of quartz, feldspar and a darker mineral (Fig. 5.4-A). Most of the felsic rocks at the northern margin are related to areas where metasediments have been intruded by mafic rocks. Some granitoid bodies are locally connected to leucosomes within the migmatitic metasediments (pic B 216/217). Other, larger outcrops of granitoid rocks contain abundant metasedimentary xenoliths which are randomly oriented (Fig. 5.4-B). The larger bodies commonly contain more dark minerals than the granitoid rocks connected to the leucosomes. At the western margin of the pluton, the granitoid rocks are also dominated by quartz and feldspar and contain minor hornblende and biotite. The texture varies from equigranular to porphyritic with abundant feldspar phenocrysts (Fig. 5.4-D). They are of-

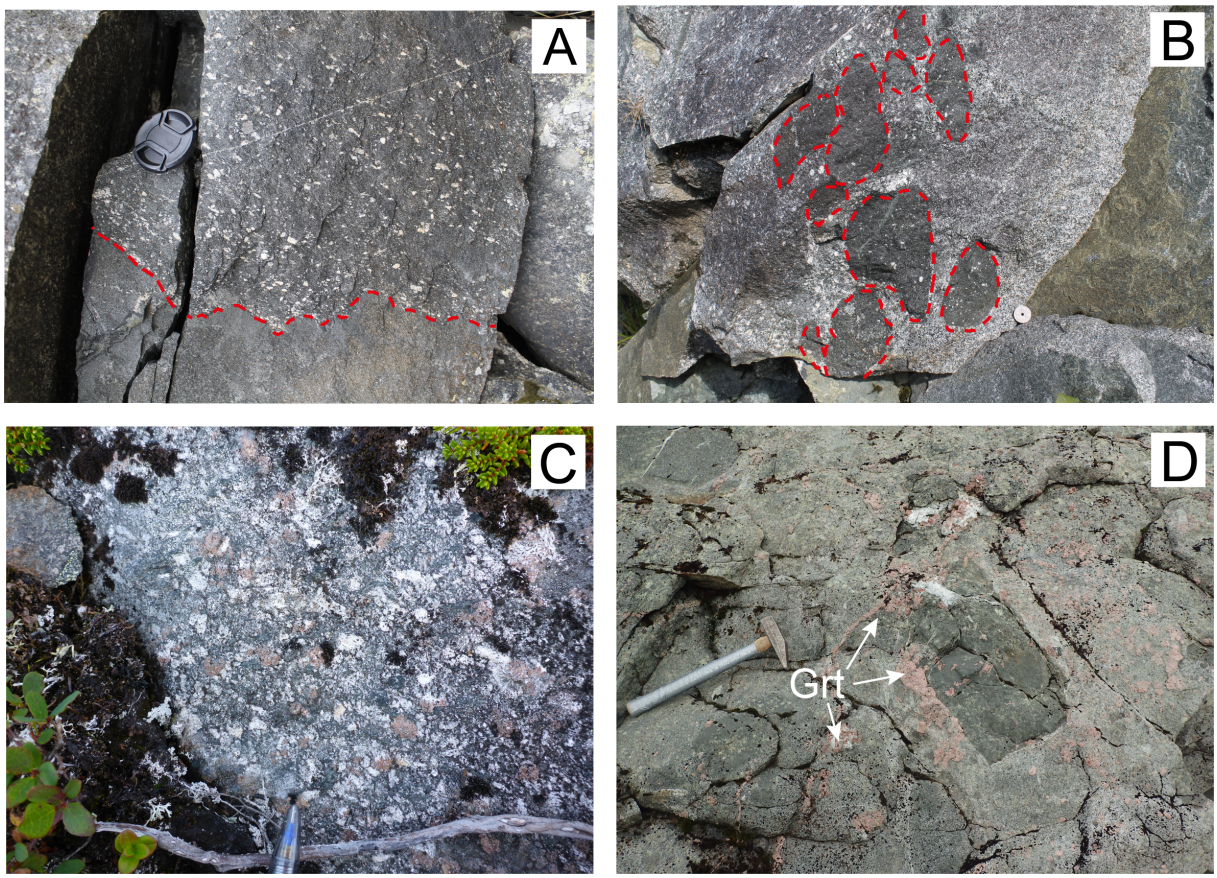

Figure 5.3: A) Contact between fine-medium grained gabbro and a mafic to intermediate, porphyritic rock. B) Mafic, subrounded enclaves containing feldspar phenocryst, enclosed in pophyritic to equigranular diorite. C) Poikilitic garnet evenly distributed in porphyritic diorite. D) Diorite containing massive aggregates of garnet accumulated at the margins of mafic, angular enclaves.

ten net-veining mafic rocks and commonly show a gradual transition towards more intermediate rocks (Fig. 5.12-A). The main distinctions from the granitoids at the northern margin are the lack of metasedimentary xenoliths and a lesser amount of garnet.

5.1.2 Contact relationship between metasediments and gabbro

The northern contact, Austre Sauvatnet

The northern contact of the gabbro towards metasedimentary rocks is exposed at Austre Sauvatnet and can be followed to Umbukta fjellstue. An area of 50x50m north of Austre Sauvatnet comprises outcrops with a rate of 100% exposure with no lichen. The area is characterized by complex contact relationships between migmatitic metasediments, granitoid and mafic material. The migmatitic metasediments display a stromatic structure. The leucosomes are mostly continuous, but some are disrupted and boudined. The thickness of the leucosomes range from a 0,5

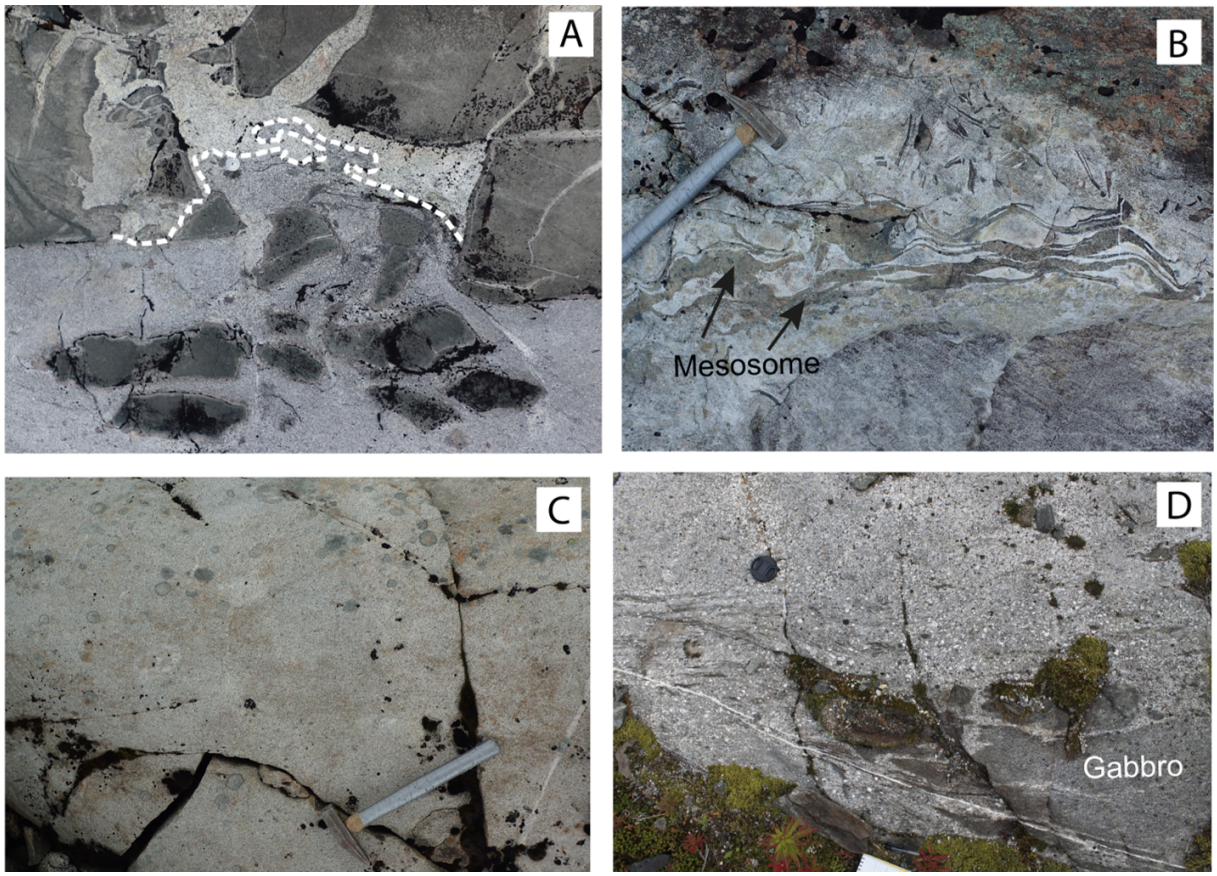

Figure 5.4: A) Contact between two felsic rocks of different composition in the contact zone. The pink-coloured rock at the lower part of the picture contains abundant garnet (sample 132414). Note the light coloured rim and accumulation of garnet along the margins of the mafic enclaves. B) Remnants of mesosomes (metasediment) in contact granitoid. C) Equigranular leucogranitoid (sample 132411). D) Phenocrystic granitoid (sample 127974) from the western margin enclosing lentoid enclaves of fine grained gabbro.

to 5 cm. The same applies for the mesosomes. Granitoid rocks are leucocratic and occur mostly as leucosomes or as smaller bodies spatially associated with mafic material. They contain abundant xenoliths of metasediments and often display a ghost stratigraphy, in which remnants of metasediments occur within granitoid with slightly visible lamination (Fig. 5.8). Interfingering occurs between the migmatitic metasediments and granitoid rocks (Fig. 5.4-B). Sharp contacts are observed locally, in which granitic material cut the layering or folds in the migmatites The granitoid is sometimes hard to distinguish from quartzite as the occurrence of dark coloured minerals is regularly very low in the granitoid. In the same area, mafic fine grained rocks cut the migmatitic metasediments and the contact relationship is often undulating, indicating hot and ductile conditions during emplacement (Fig. 5.14). They appear as irregular to spherical bodies, fine grained, undisrupted dykes and composite dykes. The latter refers to dykes composed of both a mafic and felsic component in which irregular enclaves of mafic material are

net-veined by granitic material (Fig. 5.6).

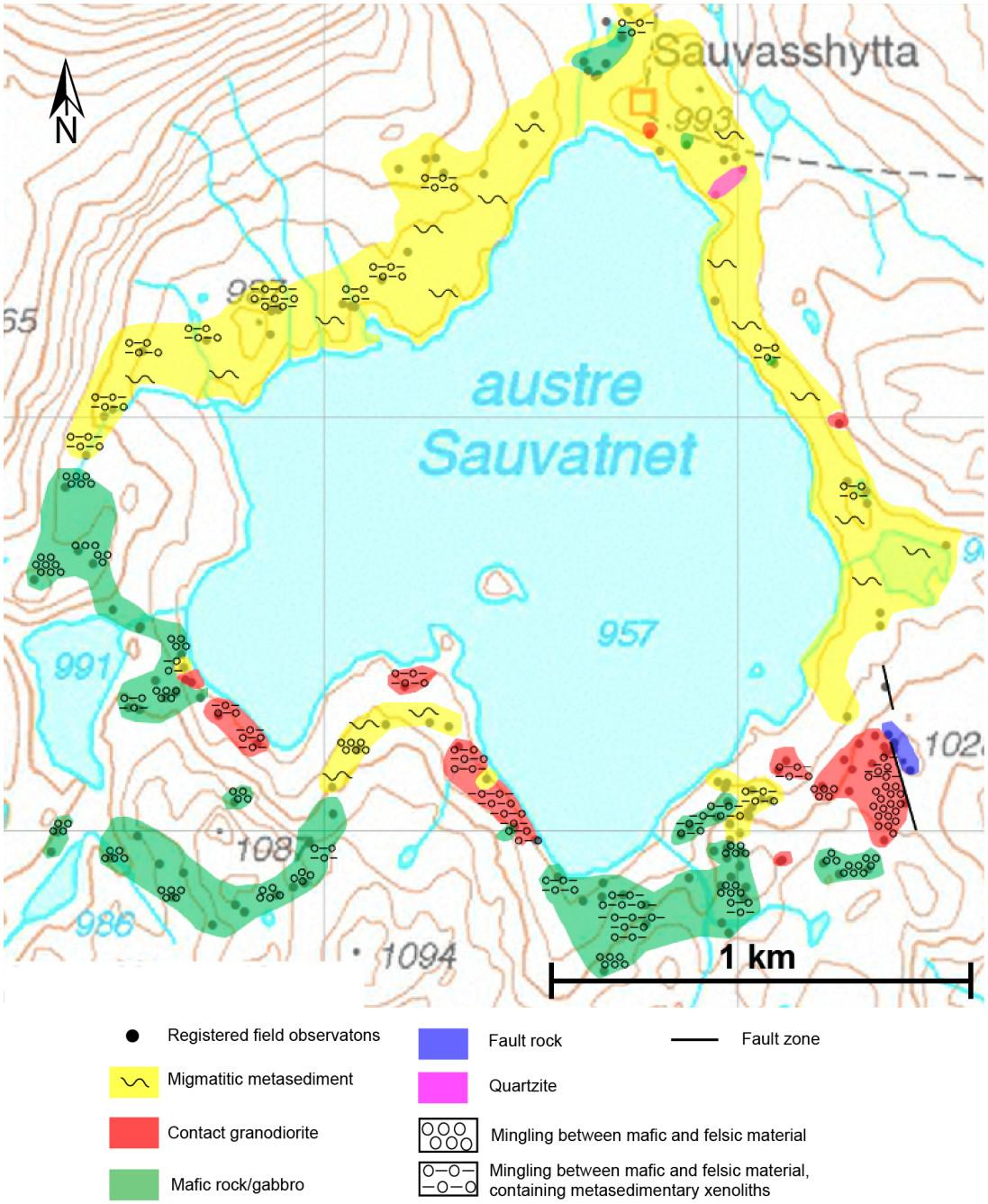

Figure 5.5: A map of the contact zone displaying the distribution of the observed lithologies. The amount of mingling appear to increase and the abundance of metasedimentary xenoliths appear to decrease from north to south.

Contact zone at Austre Sauvatnet

In the migmatitic metasediments around Austre Sauvatnet, mingling is restricted to intermittent composite dykes of 2-10 m width, composed of felsic and mafic rocks. Close to the southern

Figure 5.6: Composite dyke composed of primarily mafic material and net-veined by granitoid. The composite dyke cuts migmatitic metasediments a few 100 m north of Austre Sauvatnet.

end of Austre Sauvatnet a 200-300 m wide zone from north to south, dominated by contact granitoid, represent the transition from migmatitic metasediments to gabbro. This area is characterized by extensive mingling, including a high density of composite dykes, and will be referred to as the contact zone. Most of the granitoid rocks in this zone contain abundant metasedimentary xenoliths that are commonly elongated but may appear more bent or round. The size of the elongated xenoliths varies between 5 and 20 cm in width and 10 to 40 cm in length. Occasionally, granitoid rocks contain rounded xenoliths of < 5 cm which are scarce. Layering is still slightly visible in the xenoliths, and they are mostly leucocratic.

One of the better exposures of the contact between granitoid and mafic rocks in the contact zone is located at the southern end of the lake (Fig. 5.7). In this outcrop, abundant granitoid material are hosting composite dykes. Some of the mafic enclaves are segregated from the composite dykes, indicating that the fragments have been floating in the granitoid rock. The shape of the enclaves is angular to sub-rounded. Most of the enclaves are rimmed by a 1 cm thick garnet corona. The granitoid, the composite dykes and enclaves are crosscut by multiple fine grained

Figure 5.7: Abundant contact granitoid at the southern end of Austre Sauvatnet, hosting mafic enclaves and composite dykes, which are crosscut by three parallel mafic dykes, with sharp contacts to the granitoid host.

mafic dykes with a thickness of 40 to 50 cm that shows sharp contacts (Fig. 5.7).

Another good example of an intrusive contact between mafic and granitoid rocks is exposed at the south-western side of the lake (Fig. 5.9). The granitoid rock is fine to medium grained and rich in metasedimentary xenoliths with no sharp contacts but rather a gradual transition towards granitoid material. Ghost of metasedimentary xenoliths are also observed. The mafic material occurs as pillows within the granitoid rock. The size of the pillows ranges from 10 to 120 cm and the shape is both irregular and rounded. A 0,5 cm chill zone at the margin of the pillows is indicative of a temperature contrast between the felsic and mafic melt. White, acicular feldspar crystals are present in some of the mafic pillows (Fig. 5.9-B). Mingling between intermediate and mafic rocks is observed at several outcrops in the contact zone. One of these outcrops is located at the south-western part of the lake. Mafic, fine grained enclaves are net-veined by medium grained diorite and are locally sheared . In the sheared zone, abundant garnet is distributed in both the enclaves and the diorite. The garnets are poikilitic and vary in size from 0,5 to 3 cm. Only a few meters apart, the garnets are absent, but mafic rounded enclaves are enclosed in a dioritic rock. These enclaves display a light coloured zone of 1 to 2 cm in contact

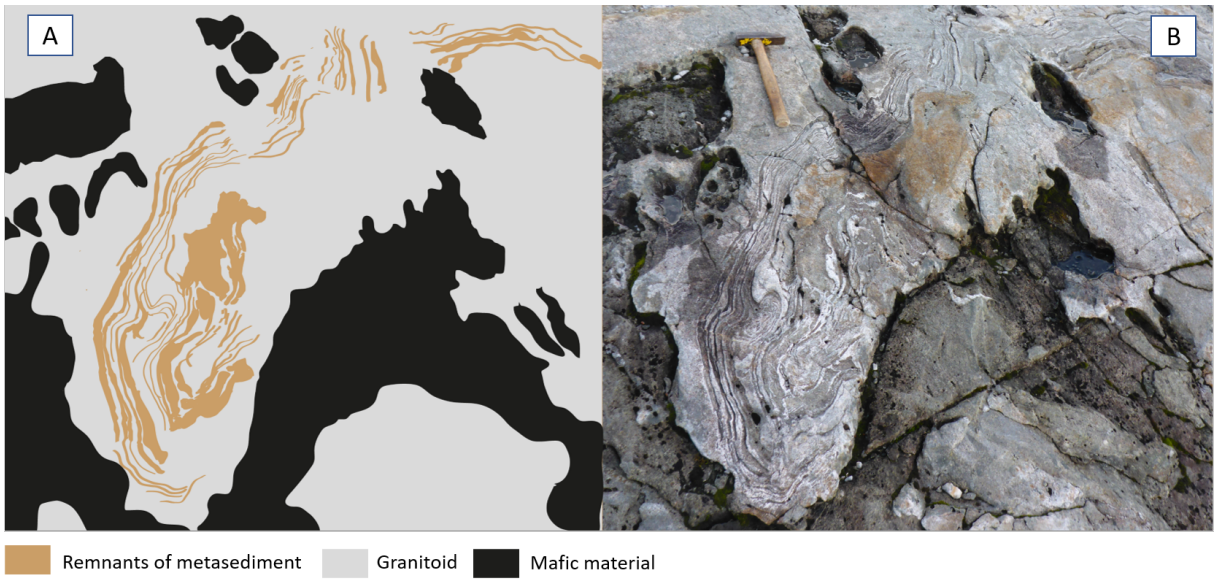

Figure 5.8: A) Sketch displaying the interaction between various lithologic units in the the contact zone. Remnants of metasediments are dislocated and randomly distributed within the granitoid. Irregular mafic enclaves of various size are enclosed in the granitoid. There are internal variations in the abundance of dark minerals in the contact granitoid, which is not displayed in this simplified sketch. B) Picture of the locality which the sketch is based on, with a hammer for scale. Picture was taken a few 100 m north of Austre Sauvatnet.

with the host rock, which is observed in other mafic enclaves in this area. On the south-eastern end of the lake, abundant garnet aggregates occur in a dioritic rock comprising fine grained mafic enclaves of 10 to 40 cm in size (Fig. 5.3-D). Enhanced quantities of garnet are observed at the margins of the enclaves but they also appear more scattered in the diorite.

Exposure of the north-western contact, Hukerten and Krabbfjellet

The outcrops are mostly covered with lichen west of Austre Sauvatnet, thus the width of the contact zone is difficult to determine in this area. Despite this, outcrops between Hukerten and Krabbfjellet display similar features as observed in the contact zone at Austre Sauvatnet. Both areas are characterized by undulate contact relationships and mingling between mafic and granitoid material. At most outcrops in the Hukerten area, several varieties of igneous rocks are present. Mafic, fine grained rocks occur as enclaves in a matrix of medium grained gabbro, but also as disrupted dykes within a granitoid rocks which is spatially associated with migmatitic metasediments (Fig. 5.10-A and B). Most of the enclaves are rounded but some are elongated and oriented parallel to the contact to the metasediments. A few outcrops display more angular mafic fragments resembling magmatic breccia and some of the enclaves are cut by later felsic

veins.

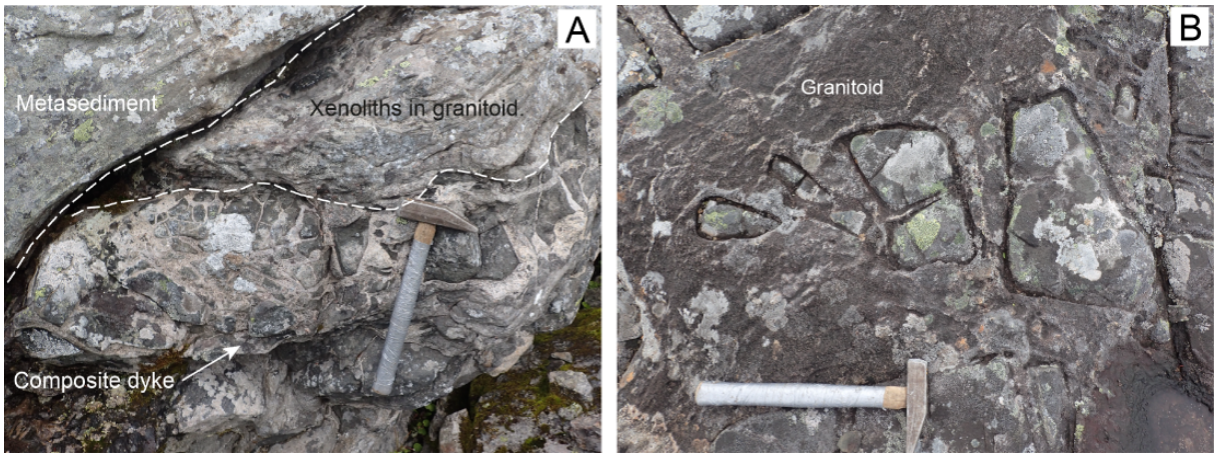

Figure 5.10: A) Composite dyke in contact with migmatitic metasediments at the NW margin of the pluton. B) Disrupted mafic dyke in a granitoid rock, surrounded by a felsic, granitoid rock.

Porphyritic diorite is locally mingling with fine grained mafic material. Garnets are evenly distributed in the dioritic rock but are also present in a light coloured rim at the margins of some of the enclaves. Isolated bodies of homogenous medium grained gabbro, crop out locally in the contact zone. Some are enclosed by migmatitic metasediments. An offshoot of coarse grained gabbro extends 50-100 meters into metasedimentary rocks north of the contact zone. Leucocratic gabbro occurs locally, but the mafic rocks south of the contact zone are generally melanocratic with a grain size ranging from fine to coarse grained. Approximately 1 km south of the northern contact a metasedimentary xenolith of 10 x 5 meter was observed. The xenolith comprises metasediments which are cut by parallel fine grained mafic dykes oriented perpendicular to diffuse, subvertical layering of the metasediments. The adjacent gabbroic rocks, which encloses the xenolith, are homogenous and medium grained.

Summary - the northern contact

Figure 5.5 emphasize the general trends in the area along the northern contact of the gabbro. When approaching the contact between gabbro from the north, the abundance of felsic granitoid material appears to increase. In contrast, the abundance of migmatitic metasediments decreases gradually until they are only present as xenoliths within granitoid material. In general, there are three zones parallel to the margin of the gabbro that are characterized by mingling. The northernmost zone is approximately 1 km wide and is dominated by migmatitic metasediments with

intermittent composite dykes of mafic and felsic material. Further south there is a gradual transition towards the previously described contact zone, dominated by granitoid rocks. Extensive mingling occurs between mafic, intermediate and felsic rocks and the zone extends for 200-300 meter from north to south (Fig. 5.11). The southernmost zone is dominated by gabbro and the content of granite decreases when going further south into the gabbro. Mingling between mafic, intermediate and felsic material can be observed in the gabbroic rocks, several hundred meters from the granite-dominated contact zone. The presence of metasedimentary xenoliths is rare, but is observed in a few places as smaller fragments within the granitoid rocks. As the transition between all three zones is highly gradual, and the rocks in the western part are covered by lichen, the width of each zone is difficult to determine.

The western margin of the pluton

The rocks along the road between Umbukta fjellstue and the Swedish border are highly heterogenous in terms of composition and texture. Most of the roadcuts display a variation from porphyritic diorite through medium grained gabbro and aphyric mafic rocks to felsic medium grained rocks. Where the felsic rock and the porphyritic diorite appear simultaneously, there is no sharp contact between these two rocks, but rather a gradual increase in the abundance of felsic minerals from the diorite to the felsic rock (Fig. 5.12-A). Widespread mingling between rocks of contrasting composition is characteristic of this area. Some outcrops comprise mingling between a fine to medium grained mafic rock and a porphyritic diorite, described previously. The diorite encloses mafic sub-rounded enclaves containing phenocrysts of feldspar. These phenocrysts have the same shape and size as the phenocrysts in the porphyritic diorite (Fig. 5.3-B). The contact between the mafic rock and the diorite is sharp, but undulating. There are no chilled margins associated with the contact between these two rocks.

Mingling between granitoid rocks and aphyric mafic material is also common, in which mafic enclaves are net-veined by granitoid rocks. The shape of the enclaves are commonly rounded and irregular, but when approaching the Swedish border the enclaves exhibit a more angular nature, resembling magmatic breccia (Fig. 5.12-C). However, there are large local variations and angular mafic enclaves are observed right next to sub-rounded mafic enclaves. Some of the rounded enclaves close to the Swedish border are strongly elongated or stretched and deformed (Fig. 5.15-D). A few xenoliths of calc-silicate rocks are observed along the western margin. The

xenoliths range in size from 20 cm to 4 m and comprise zones of massive red garnet and green pyroxene. Angular fragments of calc-silicate rocks and fine grained mafic rocks are enclosed in a dioritic rock. The host rock of the Umbukta gabbro at the southern part is dominated by marble-schist and this contact represents the most strongly deformed part of the gabbro (Fig. 5.15-B). Less than 100 meters east of the roadcuts along the western margin, the amount of mingling declines and the gabbro becomes texturally more homogenous at outcrop scale. Nevertheless, outcrops of coarse grained gabbro are observed very close to outcrops of medium to fine grained gabbro. Locally, sharp contacts can be seen between gabbroic rocks of different grain size. The same can be observed when moving into the gabbro from the northern contact.

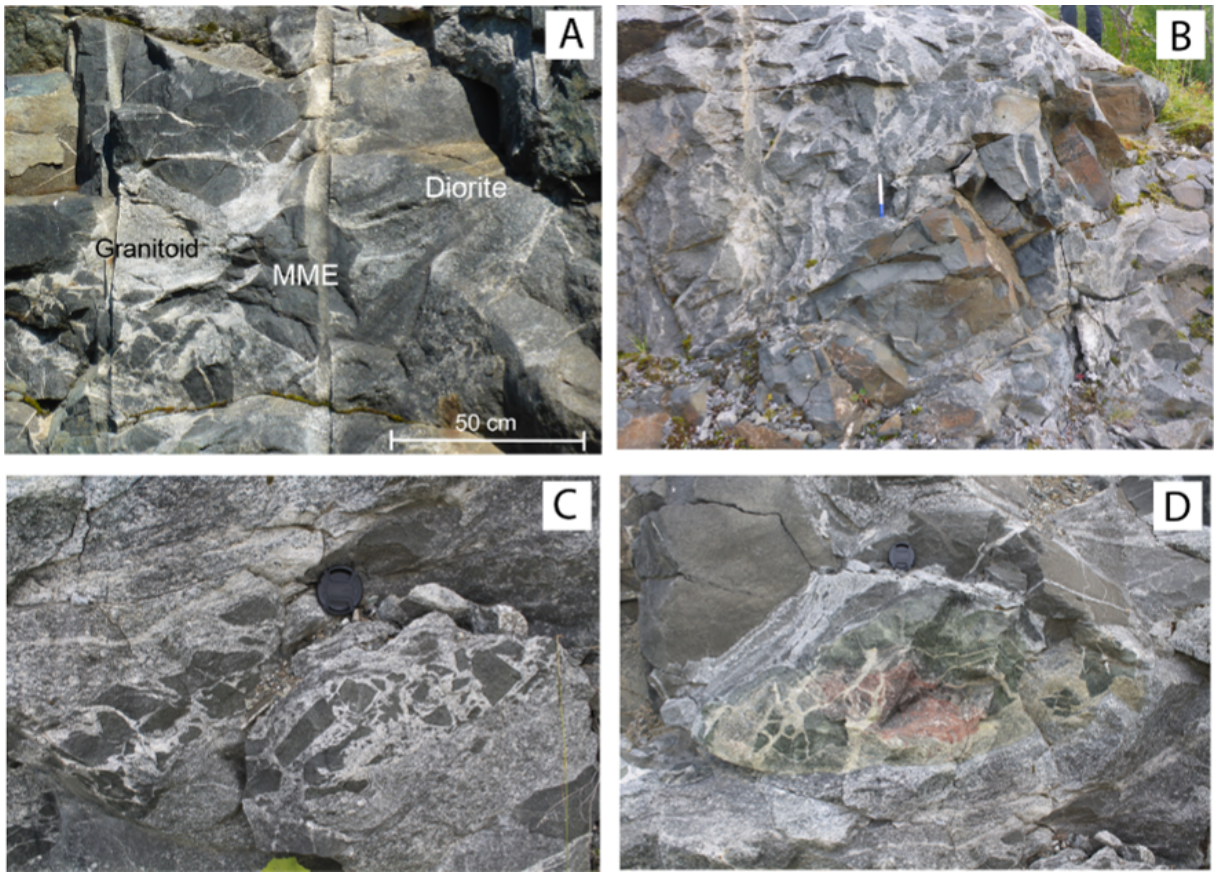

Figure 5.12: A) Mafic magmatic enclaves (MME) enclosed by diorite with a gradual transition to a felsic composition. B) Mafic dyke crosscutting a section of mingled mafic and felsic material. C) Angular mafic clasts enclosed by a porphyritic rock of felsic to intermediate composition. D) Xenolith of calc-silicate enclosed in felsic-intermediate material juxtaposed mafic, fine grained material.

Mafic dykes - Orientation and crosscutting relationship

Mafic fine grained dykes in relation to the Umbukta gabbro are crosscutting gabbro, diorite, granitoid rocks and metasediments. Dykes that cross cut gabbro have a thickness ranging from

2 to 50 cm. A great majority of these dykes are 30-40 cm thick and are steeply dipping (60-90°). There is a large variation in strike, but two trends of N-S and NW-SE are more pronounced for dykes cutting the gabbro (Fig. 5.13). The contact between the dyke and the host rock are sharp and the margins are generally parallel. The dykes are usually more resistant to weathering than the gabbros, making them stand out in the terrain. A few dykes are slightly porphyritic with phenocrysts of 2-4 mm. The phenocrysts are dark green and often have a brown weathered halo. Very often, dykes that are cutting the gabbro are greenish, like most of the gabbroic rocks.

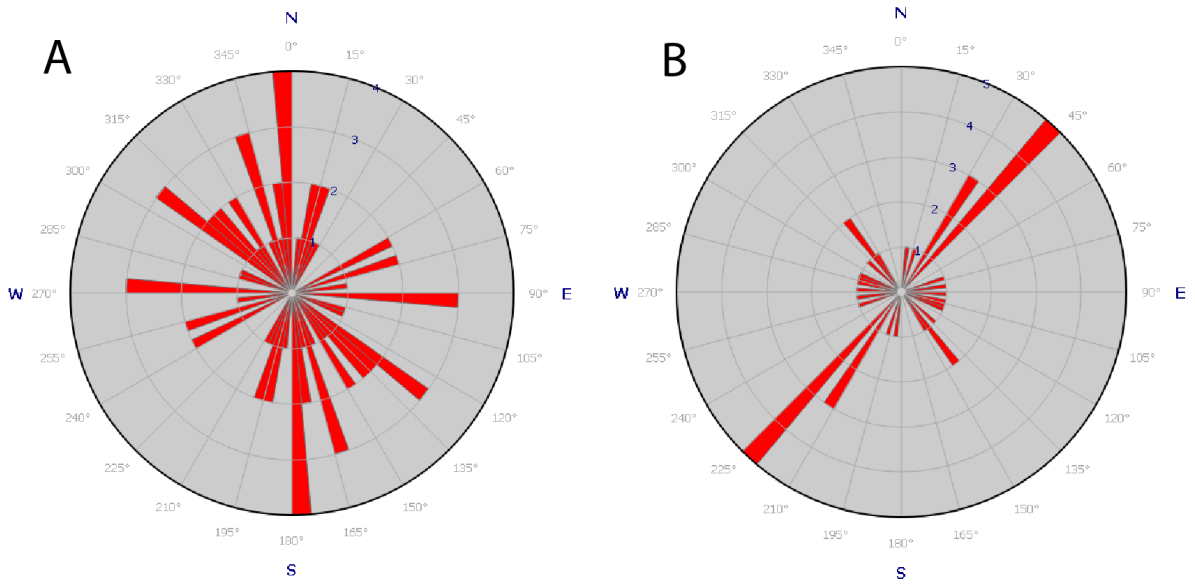

Figure 5.13: A) Rose plot of dykes cutting gabbro. B) Plot of dykes cutting metasediments, granite, and gabbro along the northern contact.

In the contact zone around Austre Sauvatnet, the mafic dykes are mostly cross cutting granitoid rocks and metasediments. In a few localities, the dykes are crosscutting other mafic dykes, both composite and undisrupted dykes. The texture of the crosscutting dykes is mostly fine grained, but some of the dykes exhibit a porphyritic interior with a finer grain size at the margins. Mafic dykes around Sauvatnet have a strike of 210°-220°. A high density of mafic dykes is observed within the contact zone (Fig. 5.14-C) and south-west of Austre Sauvatnet (Fig. 5.14-B) where the sourrounding rocks are predominantly gabbroic. In both localities, the dykes share the same trend of 210-220° as most of the dykes in the contact zone. Most of the dykes are parallel to each other, but oblique crosscutting relationships was also noted. The thickness of the dykes vary from 30 to 50 cm. The textural variations between the dykes range from fine grained aphyric, through porphyritic to coarse grained. The coarse grained rocks cross-cut other dykes sharply with an undulate contact. In the contact zone, mingling between mafic rocks is observed

close to the high-density dykes. Here, aphyric to slightly porphyritic enclaves of fine to medium grained mafic rock are enclosed in a medium grained mafic to intermediate rock.

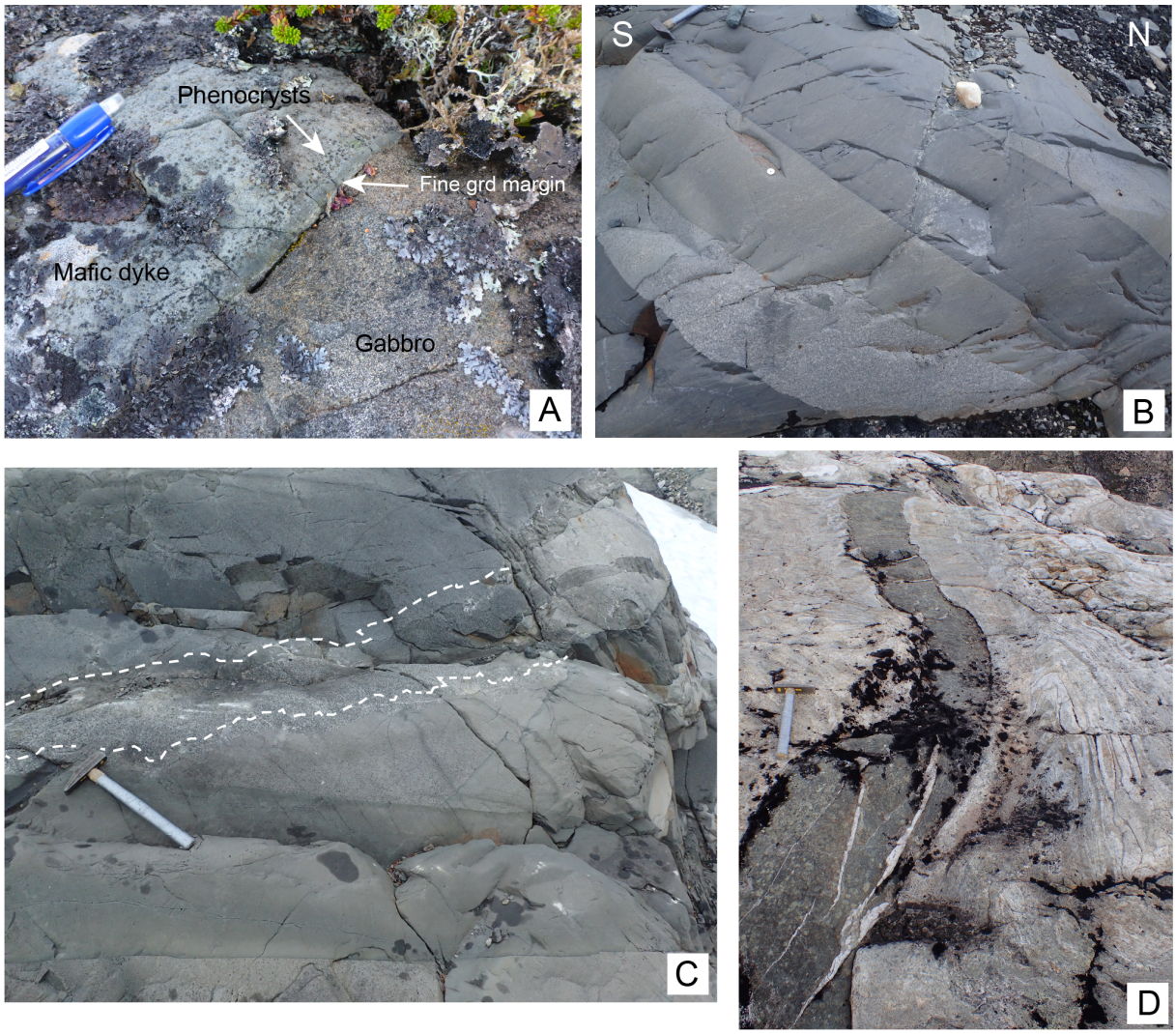

Figure 5.14: A) Mafic dyke with fine grained margins (1cm) and porphyritic interior. Both B) and C) show a high density of mafic dykes in the contact zone and in gabbro, repectively. D) Folded, migmatitic metasediments are cut by a mafic dyke with wavy boundaries.

Observed structures

Deformation within the study area is mostly restricted to smaller zones of localized shear or brittle deformation. The width of these zones varies between 20 centimeters and 10 meters. The gabbro is mostly undeformed except for local foliation at the contact with the mafic dykes and in some localities, close to the southern margin, where the gabbro becomes lineated or foliated. Zones of elongated and oriented mafic enclaves within granitoid material are more frequent from 100 m north of the Swedish border and southwards. Sheared amphibolite is also

observed. The rocks that border the gabbro in the south are very different from the host rock in the north. The meta-carbonates that border the gabbro in the south include marbles and calc-silicates (Fig. 5.15-A). They are strongly deformed, in contrast to the metasediments in the north. The contact between the gabbro and the meta-carbonates is characterized by massive folding, boudinaged lenses of mafic rocks and strongly foliated gabbro. Kinematic indications of dextral shear, oriented NW-SE, is also observed (Fig. 5.15-B). Folded rocks of mafic to intermediate composition is cut by a mafic dyke, indicating that minor post-tectonic magmatism took place (Fig. 5.15-C). The structures along the contact were not mapped in detail as the deformation appear to be mainly post-magmatic.

A zone characterized by extensive fracturing at the south-eastern side of Austre Sauvatnet has an orientation of approximately 340°N. Few oriented structures are visible in this zone, but small shear zones and foliation are observed locally. Boudined lenses of leucocratic material and local shear zones of is observed only meters apart from a darker rock which is clearly fractures by brittle deformation (Fig. 5.16). Areas of both dark and white material are cross cut by light purple veins. A depression of approximately 20 m separates the deformed rocks from abundant contact granitoid. Thus, the deformations zone represents an abrupt transition from migmatitic metasedimentary rocks to contact granite. The zone was followed for at approximately 400 m N-S and aerial photos show a marked depression in the terrain in this exact area, extending 5-6 km in the same direction. North-west of Austre Sauvatnet a 20 meter wide zone of strongly foliated migmatitic metasediments is observed. The foliation is subvertical and the zone is trending roughly west-east. Another deformation zone close to the north-western contact share the same orientation. This zone comprise foliated gabbros, is 10-15 meters wide and possible to follow for at least 1 km.

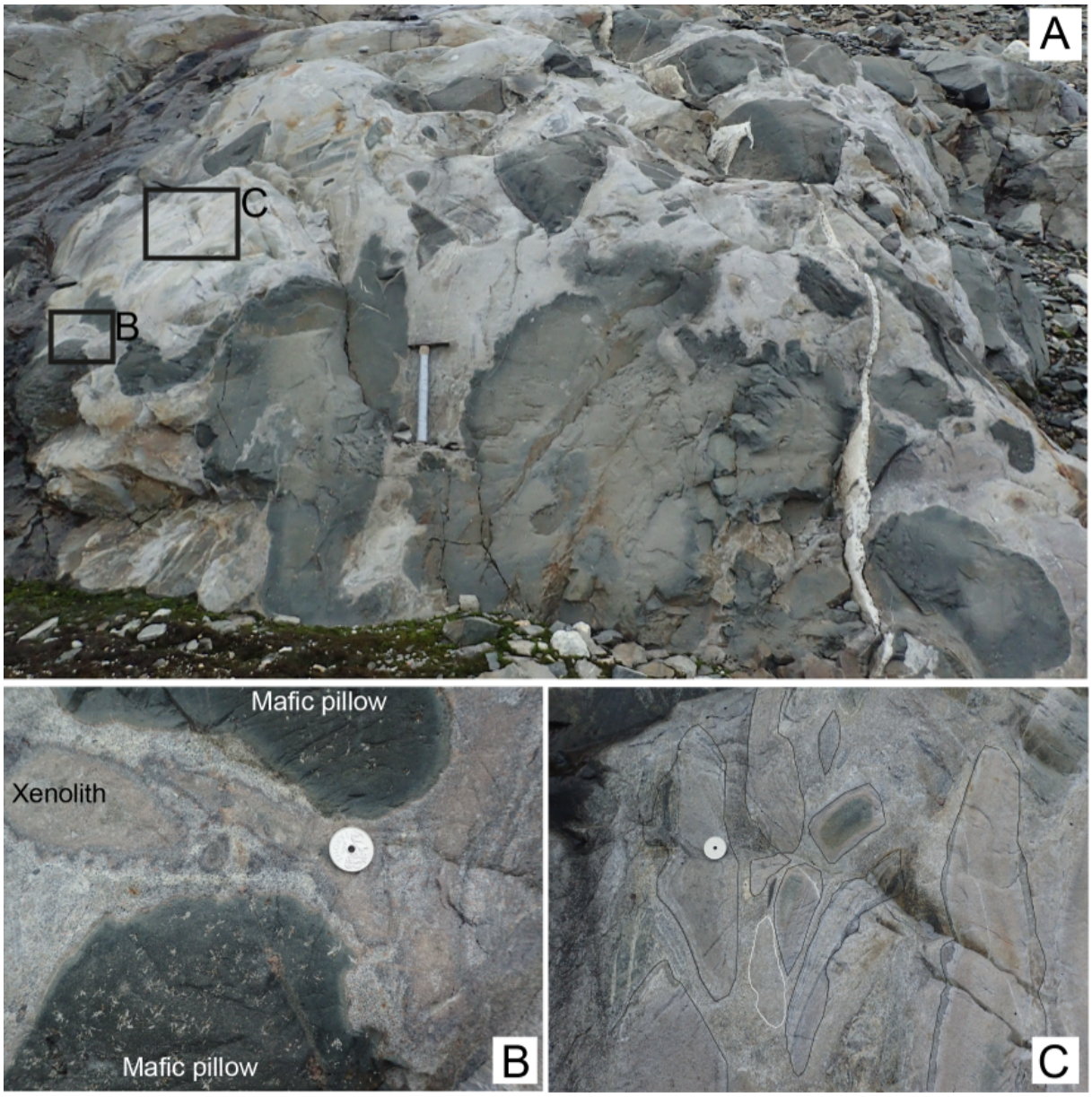

Figure 5.9: A) Mafic pillows and metasedimentary xenoliths in contact granitoid at Austre Sauvatnet. B) Close up of mafic pillows containing acicular feldspar crystals and xenoliths in a granitoid rock. Note the light coloured rim around the mafic pillows. C) Close-up of metasedimentary xenoliths in a granioid rock. Xenoliths are marked with thin black or white lines.

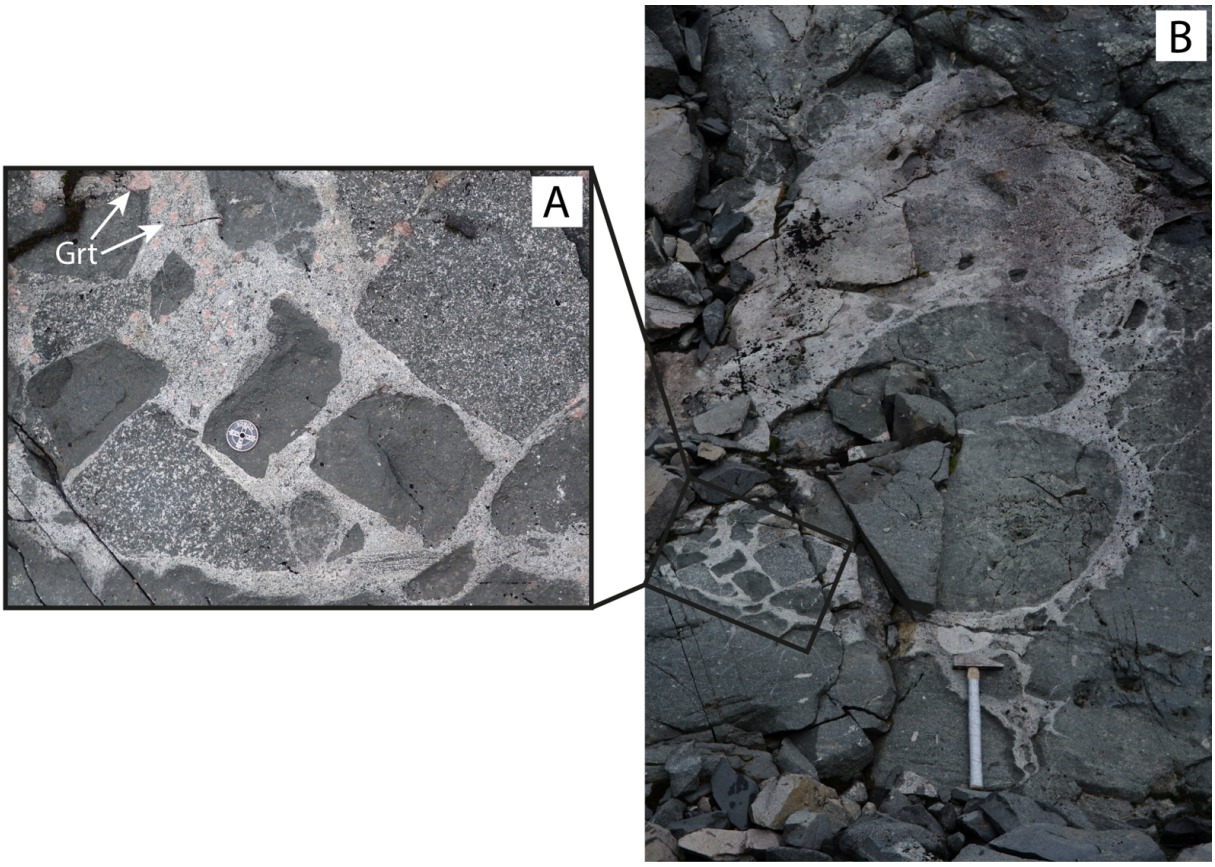

Figure 5.11: A garnet-rich dioritic rock mingles with a fine grained and a coarse grained mafic rock. The diorite is net-veining medium grained gabbro and encapsulates a larger heart-shaped mafic enclave in B).

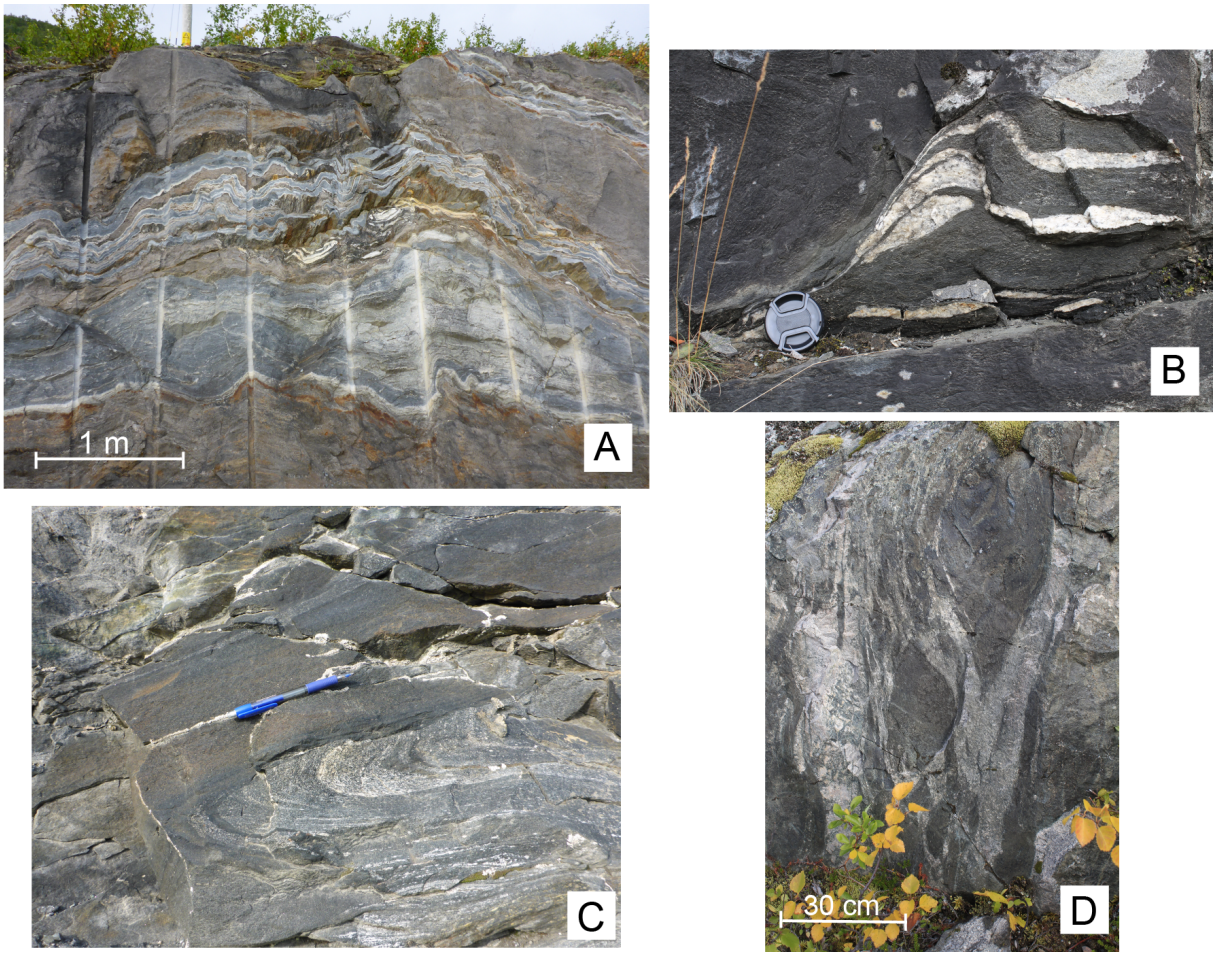

Figure 5.15: A) Folded calc-slicates and marbles south of the Umbukta gabbro. B) Indications of dextral shear in medium grained gabbro with felsic lenses. C) Mafic dyke cross cutting folds in intermediate to mafic rock. D) Stretched and deformed, mafic enclaves in a dioritic rock, close to the swedish border.

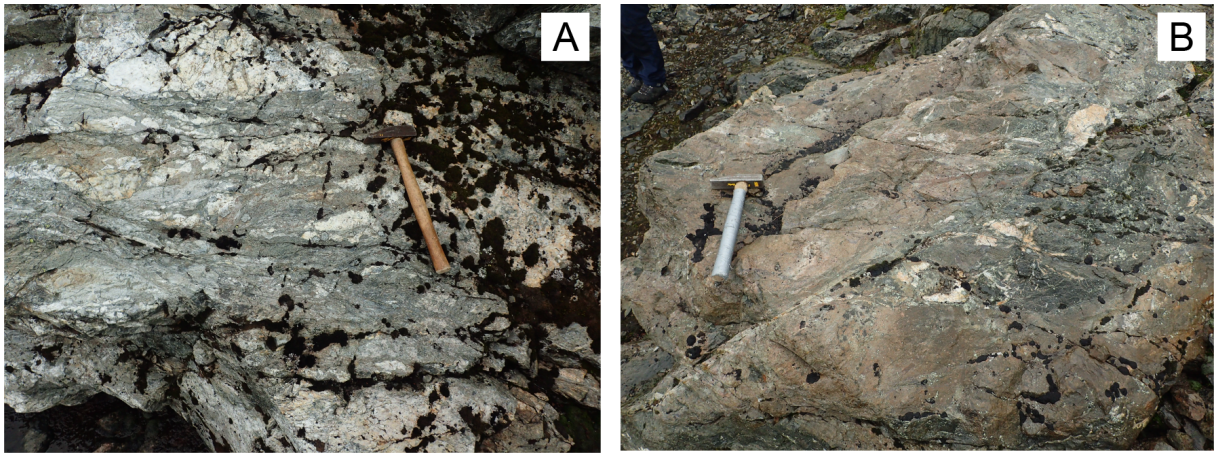

Figure 5.16: A) & B) Fault rock in the contact zone at Austre Sauvatnet.

5.2 Whole-rock geochemistry

A total of 63 samples have been analysed for major- and trace element chemistry, in which 49 samples aquired in 2015 were analyzed by XRF and ICP-MS at NGU and 14 samples acquired in 2016 were analyzed by ICP-AES and ICP-MS at ALS in Sweden.

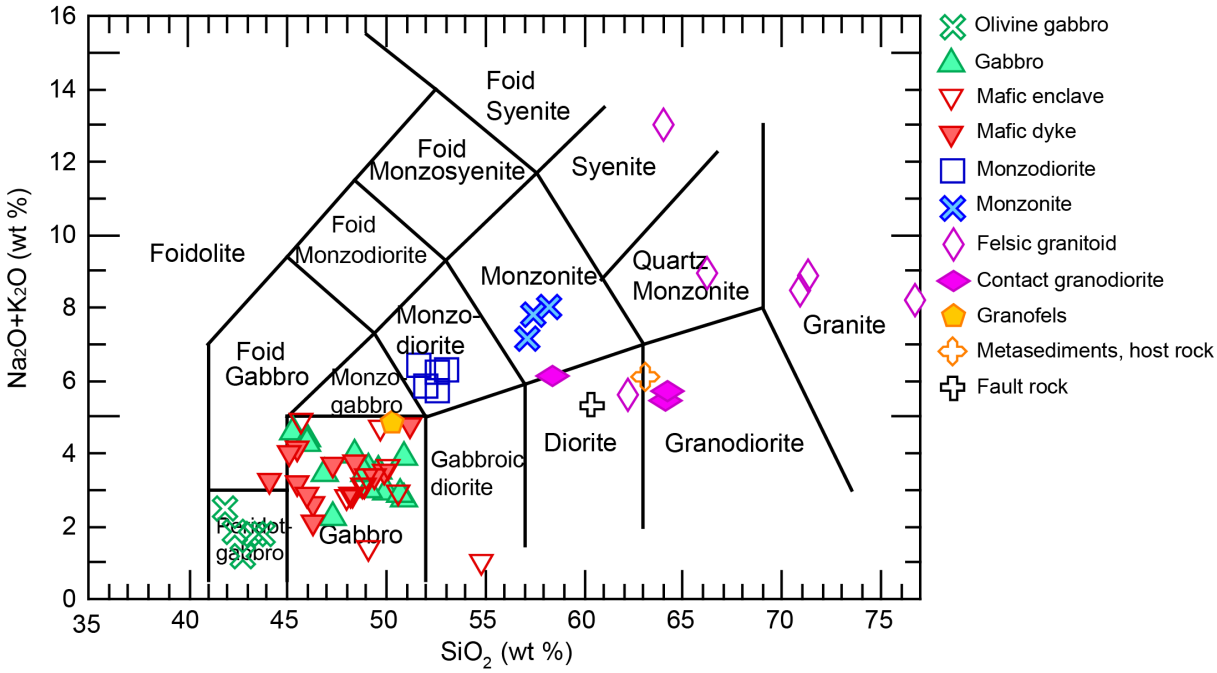

Figure 5.17: Classification of all samples including non-igneous rocks. Diagram after Middlemost (1994)

5.2.1 Classification

The classification of the different lithologic units in the study area is based on the classification diagram for intrusive, igneous rocks by Middlemost (1994) and the rock's occurrence in field (see Fig. 5.17). For example, the contact granodiorites correspond to the felsic rocks observed in the complex contact north of the gabbro, whereas the felsic granitoids are sampled along the western part where there was no observed relationship with metasediments. This distinction has been made since these two rock groups show very different chemical signatures, as will be shown below. Five gabbroic rocks plot in the peridot gabbro-field and these are further referred to as olivine-gabbros.

According to the classification of igneous rocks by Winter (2010), the olivine-gabbros may be classified as ultramafic rocks with SiO_2 = 41,9-43,8 wt%. The gabbros and the mafic dykes

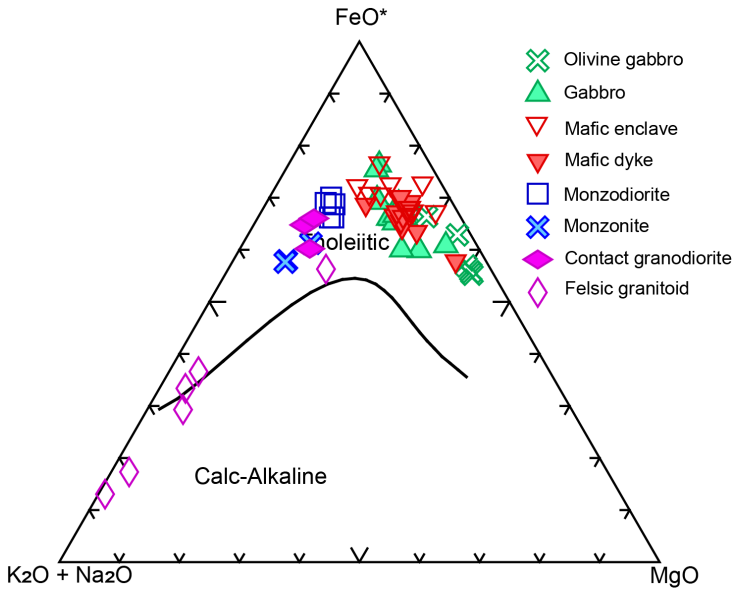

Figure 5.18: AFM diagram for all igneous rocks, which define a strong tholeiitic trend.

and enclaves are classified as mafic rocks with SiO_2 = 44-51 wt% whereas the monzodiorites and contact granodiorites may be classified as intermediate with SiO_2 = 52-58 wt. The felsic granitoids are regarded as felsic with SiO_2 = 64-77 wt%. The only exception is sample 127964 which is classified as diorite, with SiO_2 of 62 wt%. As the classification diagram is intended for igneous rocks, the fault rock and migmatitic metasediments cannot be classified using this diagram. However, it should be noted that their alkali-silica relationship is very similar to the contact granitoids'.

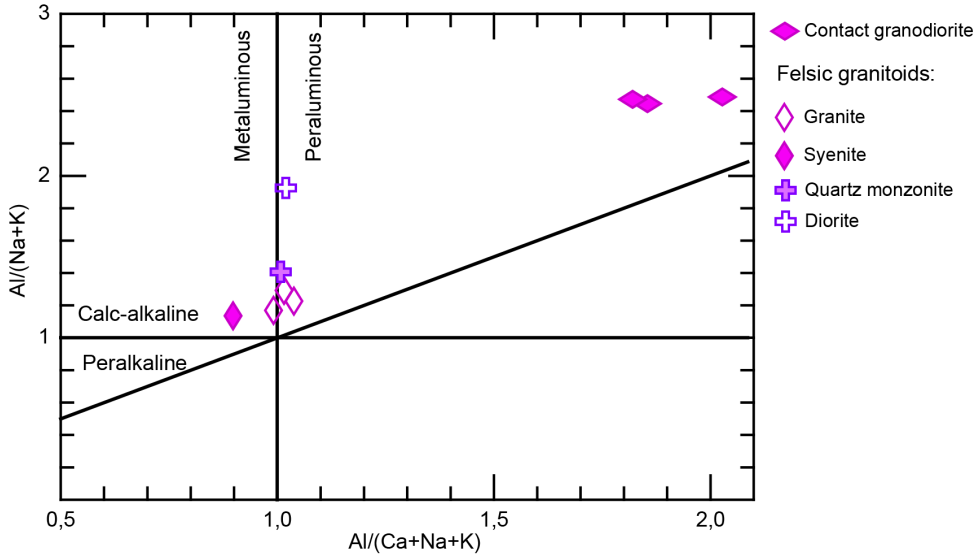

Figure 5.19: Classification of granitoid rocks after Shand (1943).

All mafic and intermediate samples plot in the tholeiitic field in the AFM-diagram (Fig. 5.18). The data define a curved trend towards the FeO∗ corner, with an increasing concentration in the

mafic rocks (Fe_2O_3 = 9-16 wt%), followed by a decreasing concentrations in the intermediate (Fe_2O_3 = 12-8 wt%) and felsic rocks (Fe_2O_3 = 1-3 wt%). Three felsic granitoids plot under the division line in the calc-alkaline field. It should be noted that the AFM is better suited for classifying mafic rocks as the diagram parameters are generally low in felsic rocks (Rollinson, 1993).

The aluminum saturation index (ASI = Al/(Na+K+Ca)) can be used to discriminate between peraluminous (ASI $>$ 1) and metaluminous (ASI $<$ 1) granitoids (Shand, 1943). Metaluminous rocks may be subdivided in to calc-alkaline (Al/(Na+K) $>$ 1) and peralkaline (Al/(Na+K) $<$ 1) granitoids. The contact granodiorites which was sampled along the northern margin of the Umbukta gabbro are chemically distinct from the felsic granitoids observed along the south-western margin, and they plot in two separate clusters in discrimination diagram for granitoids by Shand (1943) in figure 5.19. The contact granodiorites are strongly peraluminous (ASI $>$1,82), have high values of Al_2O_3 (17,6-20,1 wt%) CaO values 0,9-1,6 wt% and relatively low concentration of alkalis (Na_2O+K_2O $<$ 6,1 wt%). The felsic granitoids straddle the metaluminous/peraluminous boundary and the most felsic sample, the syenite, can be classified as calc-alkaline according to Shand (1943). They have slightly lower Al_2O_3-concentrations (1,9-18,1 wt%), and slightly higher concentrations of CaO (1,0-3,9 wt%) and alkalis (Na_2O+K_2O $>$ 8,2 wt%).

5.2.2 Harker diagrams

In figure 5.20 the most common rock forming oxides are plotted in Harker diagrams, where all igneous rock samples from the study are represented. The silica levels range from 42 wt% in the olivine gabbros to 76,7 wt% in the most felsic granitoid. The data define continuous trends in most plots, which may imply that the rocks are genetically related. The only exception is the Harker plot of P_2O_5, in which the data are more scattered, especially the mafic rocks which have P_2O_5 concentrations ranging from 0,09 to 0,98 wt%. In the plot of CaO and Na_2O the contact granodiorites appear to slightly deviate from the trends defined by the other samples. With increasing silica, the concentration of Fe_2O_3, MnO, TiO_2 and MgO decreases continuously, in which Fe_2O_3 and MnO show almost linear trends. Both Al_2O_3 levels and Na_2O levels increase in the mafic samples, from the olivine gabbros to the monzonites, before they decrease continuously in the samples with more than 55 wt% silica. The CaO levels slightly increase in

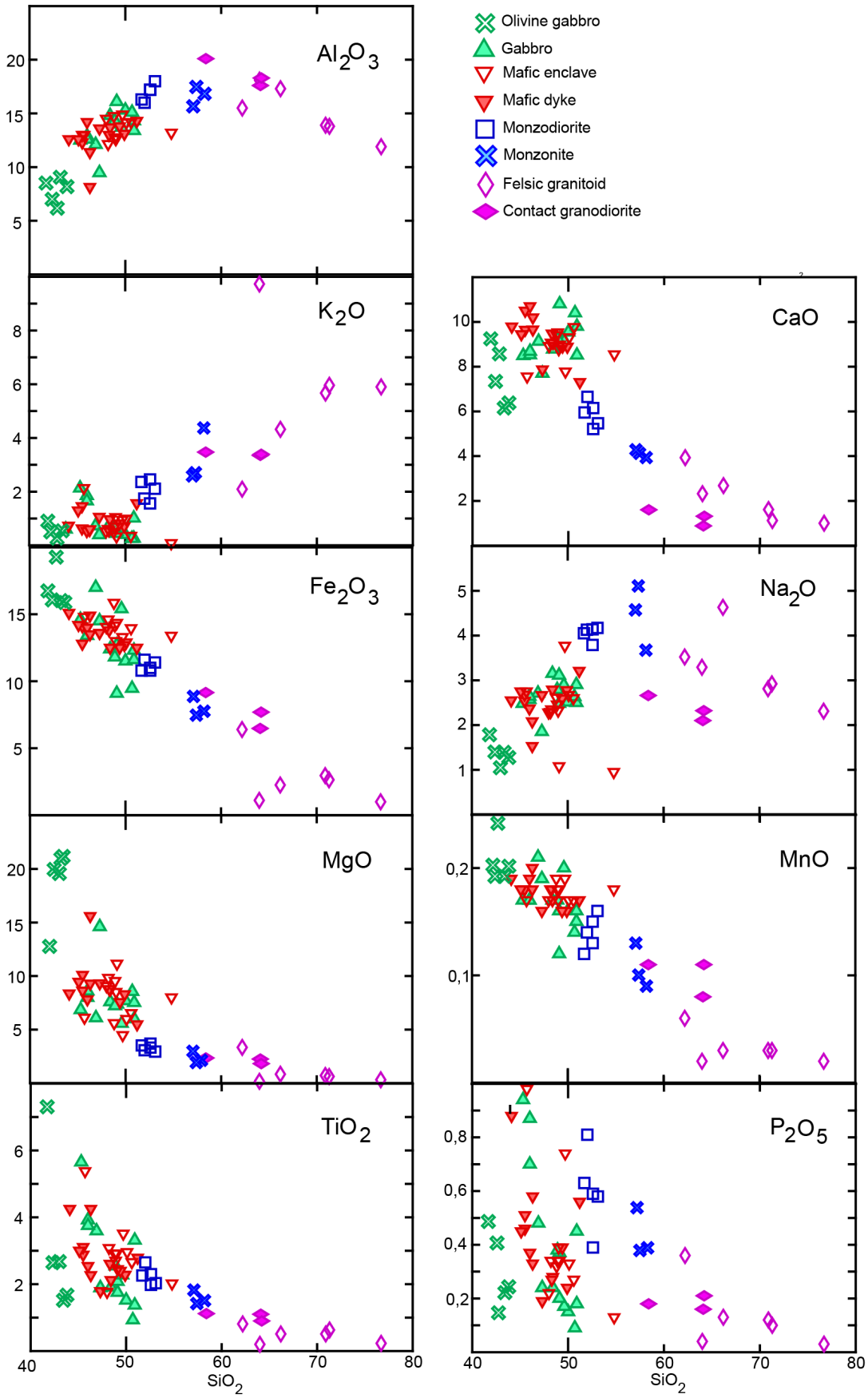

Figure 5.20: Harker diagrams for all analyzed, igneous rocks. Oxides are given in Wt%. See text for more detailed explanation.

the mafic samples for silica levels < 45 wt% and decreases in samples with silica levels > 45 wt%. The only strictly positive correlation is seen in the Harker plot for K_2O.

The olivine gabbros are the most primitive rocks and can be distinguished from the mafic rocks by higher concentrations of Fe_2O_3 (15,9-19,2 wt%), MnO (0,19-0,24 wt%) and MgO (12,6-21 wt%), in addition to lower concentrations of Al_2O_3, K_2O, Na_2O. The olivine-free gabbros have moderately high concentrations of Fe_2O_3 (9,5-15,4 wt%), MnO (0,12-0,20 wt%) and MgO (5,6-8,6 wt%, except one of 14,6 wt%). The mafic dykes and mafic enclaves overlap to a large extent, and are thus described as one group. They have a SiO_2-content of 44,1-51,2 wt% (except for one sample of 54,8 wt%). Their major element concentrations are not too different from the gabbros with Fe_2O_3 of 12,5-15,6 wt%, MnO of 0,16-0,20 wt% and MgO of 5,5-11,2 wt% (and one sample of 15,6 wt%). The most evolved rocks are the felsic granitoids which show variable, but high concentrations of K_2O (2,1-9,7 wt%) and the lowest concentrations of Fe_2O_3 (1-6,4 wt%), MgO (0,6-3,3 wt%), CaO (1-3,9 wt%), MnO (0,02-0,06 wt%) and TiO_2 (0,2-0,8 wt%). Monzodiorites and monzonites have intermediate concentrations of SiO_2 (51,7-53,1 wt% and 57,1-58,2 wt%, respectively) and they mostly plot in between the mafic and felsic granitoid rocks in distinct clusters. The contact granodiorites have SiO_2 concentrations of 58,1-64,2 wt%, mostly plot in between the monzonites and felsic granitoids, but they slightly deviate from the trend seen in the Na_2O and the K_2O plot.

5.2.3 Trace elements in bulk rock

Trace element analyses normalized to mid-ocean ridge basalt (MORB), show that the majority of gabbros, mafic dykes and mafic enclaves are enriched in most trace elements, except for Y and Yb , which are depleted with respect to MORB (Fig. 5.21-A & -B). There is a large variation in the abundance of trace elements between samples, with a range of 1,5-30 times MORB concentration for the most abundant element, Th, while there is a range of 0,2-1 times MORB concentration for the least abundant element, Yb. The general trend for all mafic rocks is characterized by a convex-shaped positive slope from Sr to Th followed by a gently negative slope to Zr. This is followed by an enrichment in Sm and a distinct depletion in Y and Yb. Some exceptions include sample 127992, a gabbro, which is depleted in most elements except for the LILE, and sample 132416, a mafic enclave, which show strong depletion in K, a distinct Ta-Nb trough followed by a sublinear trend until Ti.

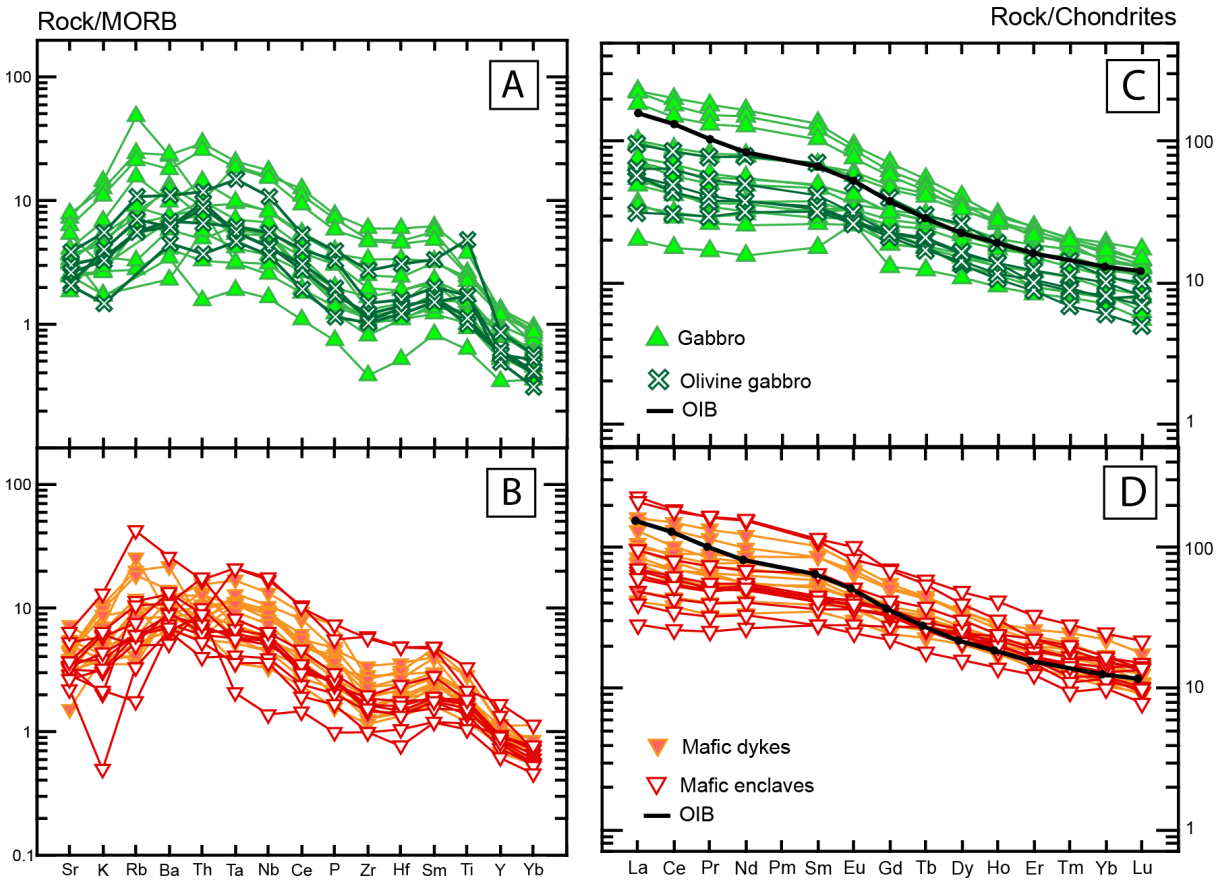

Figure 5.21: A) & B) Spider diagrams normalized to MORB with values from Pearce (1983) A) Ol-gabbros and normal gabbros. B) mafic dykes and mafic enclaves. C) & D) Chondrite-normalized REE-patterns with normalizing values from Sun and McDonough (1989). Chemistry for typical ocean island basalt (OIB) from Sun and McDonough (1989) have been plotted for comparison and is shown in black. C) Ol-gabbros and normal gabbros. D) Mafic dykes and mafic enclaves.

Olivine gabbros show LREE abundances of 30-100 times chondrite, whereas olivine-free gabbros show a slightly wider range of 20-250 times chondrite. The two rock groups show a similar range in HREE abundances with 5-20 times chondrite. Mafic dykes and enclaves show a similar range in REE concentrations. REE patterns for all mafic and ultramafic rocks, (Fig. 5.21), exhibit a small LREE enrichment ($(La/Sm)_N$ = 0,99-2,06) with a shallow negative trend from La to Sm, followed by a steeper negative trend from Sm to Lu with a moderate HREE depletion ($(Gd/Yb)_N$ = 1,79-4,40). Eu-anomalies are absent in most of the mafic rocks but some samples display a small positive Eu-anomaly (Eu/Eu^* = 0,92-1,73).

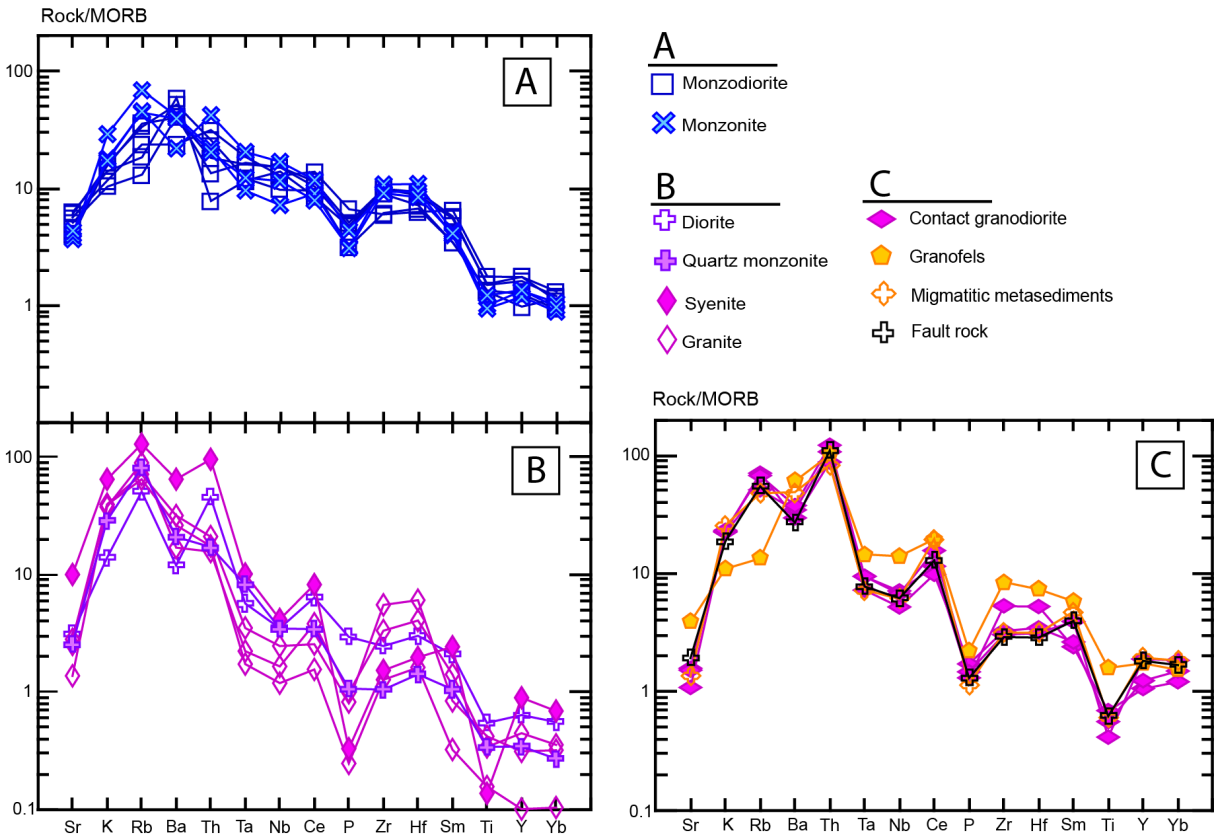

Figure 5.22: MORB-normalized spider diagrams for A) monzodiorites and monzonites, B) felsic granitoid rocks (subdivided into granite, syenite, quartz monzonite and diorite based on the classification in Fig. 5.17), C) migmatitic metasediments, fault rock, granofels and the contact granodiorites. Normalizing values for MORB from Pearce (1983)

The monzodiorites and monzonites show higher concentrations of all trace elements compared to the mafic rocks and there is a narrow range of compositions in the MORB-normalized spider-diagram (Fig. 5.22-A). They show a more pronounced LILE-enrichment (K, Rb and Ba) compared to the mafic rocks, but there is a distinct negative P-anomaly in these analyses. There is also a distinct enrichment of Zr and Hf followed by a relative depletion of Ti, Y and Yb, with concentrations similar to MORB. Monzonites and monzodiorites show the highest REE abundances of all igneous rocks, with LREE = 55-290 times chondrite and HREE = 15-80 times chondrite. They also show a similar REE-pattern as the mafic rocks, with a general decrease from LREE to HREE, where the LREE are slightly enriched, with $(La/Sm)_N$ = 1,83-2,79, and the HREE are moderately depleted, with $(Gd/Yb)_N$ = 1,79-3,14. There is a small, but hardly visible positive Eu-anomaly in some monzonites and monzodiorites (Eu/Eu^* = 0,78 and 1,24).

Analyses of felsic granitoids display the strongest enrichment of LILE, compared to the other rock groups, with abundances up to 100 times MORB. There are some variation in abundance

between samples, but they mostly display similar trends (Fig. 5.22).Ta and Nb are depleted in all samples relative to Th and and Ce, creating a trough shape, and the syenite and the granites display a distinct, negative P-anomaly, similar to the monzonites and monzodiorites. Other Similar features include a relative Zr and Hf enrichment, although not as pronounced, and that Ti, Y and Yb are depleted with repsect to MORB. The felsic granitoids show lower concentrations of all REE compared to the remaining igneous rocks, with LREE abundances of 48-160 times chondrite and HREE abundances of 5-12 times chondrite. Even though there is a large variation between the samples, all felsic granitoids show enrichment in LREE, with $(La/Sm)_N$ = 2,76-6,94, and depletion in the HREE, with $(Gd/Yb)_N$ = 1,68 - 2,52. Distinct positive Eu-anomalies occur in the granites (Eu/Eu^* = 1,05-5,57) and the quartz-monzonite (Eu/Eu^* = 2,19), while the diorite and the syenite display flat or negative Eu-anomalies (Eu/Eu^* = 0,97 and 0,34).

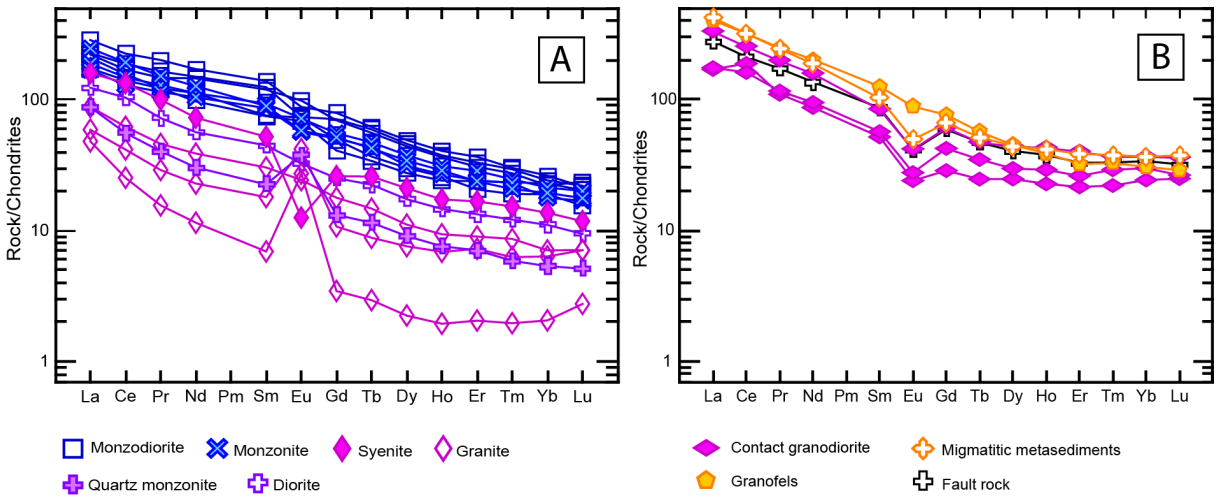

Figure 5.23: A) Chondrite-normalized REE patterns for monzodiorites, monzonites and felsic granitoid rocks B) Chondrite nomalized REE patterns for migmatitic metasediments, fault rock, granofels and the contact granodiorites. Normalizing values for chondrite from Sun and McDonough (1989)

The trace element pattern for the contact granodiorites in the MORB-normalized spider diagram overlap with the host rock and fault rock to a large extent. Similar to the felsic granitoids they show a strong enrichment in LILE, a negative trough-shaped trend for Ta and Nb, distinct, negative P- and Ti-anomalies and the Y and Yb are slightly enriched compared to MORB, the mafic rocks and the felsic granitoids. REE-abundances of the contact granitoids are similar to the monzonite and monzodiorite's with LREE abundances of 169-332 times chondrite and HREE abundances of 25-36 times chondrite values. The chondrite normalized REE patterns for the contact granodiorites show a strong LREE-enrichment with $(La/Sm)_N$ = 3,3-3,9 and

a moderate HREE-enrichment with $(Gd/Yb)_N$ = 1,2-1,7. They exhibit a distinct Eu-anomaly (Eu/Eu^* = 0,56-0,62), which is also seen in the fault rock and the metasediments, whereas the granofels exhibit no anomaly.

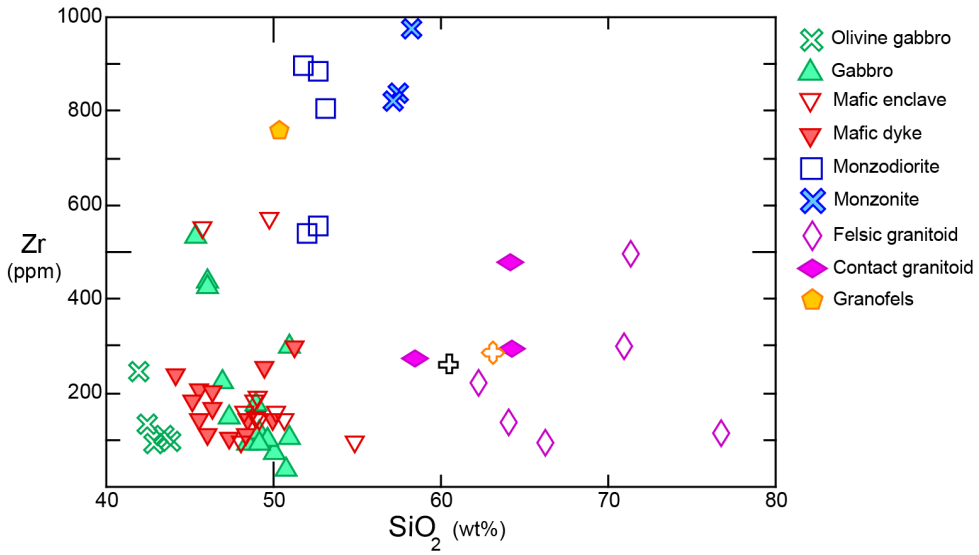

Figure 5.24: Zr (in ppm) is plotted versus SiO2 (in wt%). Note the strong Zr enrichment in the monzonites and monzodiortes compared to the felsic granitoids nad granodiorites.

Figure 5.24 displays the relationship between Zr and silica content in all analysed rocks. From the olivine gabbros, through the gabbros and monzodiorites to the monzonites there is a slight positive correlation between Zr and silica content. Felsic granitoid rocks have Zr concentrations of 94-496 ppm, similar to the gabbros (73-532 ppm), thus the felsic rocks deviates from the positive trend seen in the data from mafic to intermediate rocks. This is also reflected in the plots in figure 5.25, where Zr, a common differentiation index, is plotted against various transition metals and HFSE, as these are most likely immobile during alteration. Compared to the Harker diagram, there is more scatter in these plots, but the data still define trends in all diagrams. The concentration of Co, Cr, and Ni generally decrease in a curved fashion with increasing Zr. There is a declining trend in the plot for Sc, but this is more shallow dipping. Olivine gabbros exhibit a distinct enrichment in Co (74-99 ppm) and Ni (320-674 ppm), and a moderate enrichment in Cr (453-698 ppm) relative to the other rocks, whereas the Sc levels (14-22 ppm) of the olivine gabbros is within the range of the remaining mafic rocks (14-26 ppm). The Ni content and Mg# for the olivine gabbros (Mg# $>$ 0,66 for all samples except 127983 with Mg# = 0,60) is as high as for primitive melts, but the Cr level is more than 300 ppm too low to give them this designation (Winter, 2010). The olivine-free gabbros have moderate to high concentrations of Sc (15-22 ppm), Cr (52-466 ppm), Ni (47-202 ppm) and Co (34-70 ppm). The Sc content is

somewhat higher in the mafic enclaves (mostly 22-26 ppm) compared to the gabbros and mafic dykes (mostly 17-21 ppm), whereas the Cr content is slightly lower in the mafic enclaves (36-333 ppm) compared to the mafic dykes (mostly 168-464 ppm). The Co content of the mafic dykes and mafic enclaves are similar (29-68 ppm). Except for one mafic dyke with sample number 127995 (Mg# = 0,70, Cr = 1130, Ni = 444) none of the mafic dykes, mafic enclaves or olivine-free gabbros can be classified as primitive. Y show a positive correlation with Zr, and the rock group with the highest Y content is monzodiorite with concentrations up to 53 ppm. In the Zr-plot for Ti and V, there is an increasing trend from 34 ppm to 245 ppm Zr where there is a shift towards a decreasing trend. For Nb, there is positive correlation with Zr up to 552 ppm Zr, followed by a weak declining trend defined by the monzodiorites and the monzonites. The felsic granitoids and contact granodiorites deviates from the trends in, more or less, all of these plots as their concentration of Zr is generally as low as in the more mafic rocks, but their concentration of transition metals and HFSE are generally much lower compared to the intermediate and mafic rocks (Fig. 5.24).

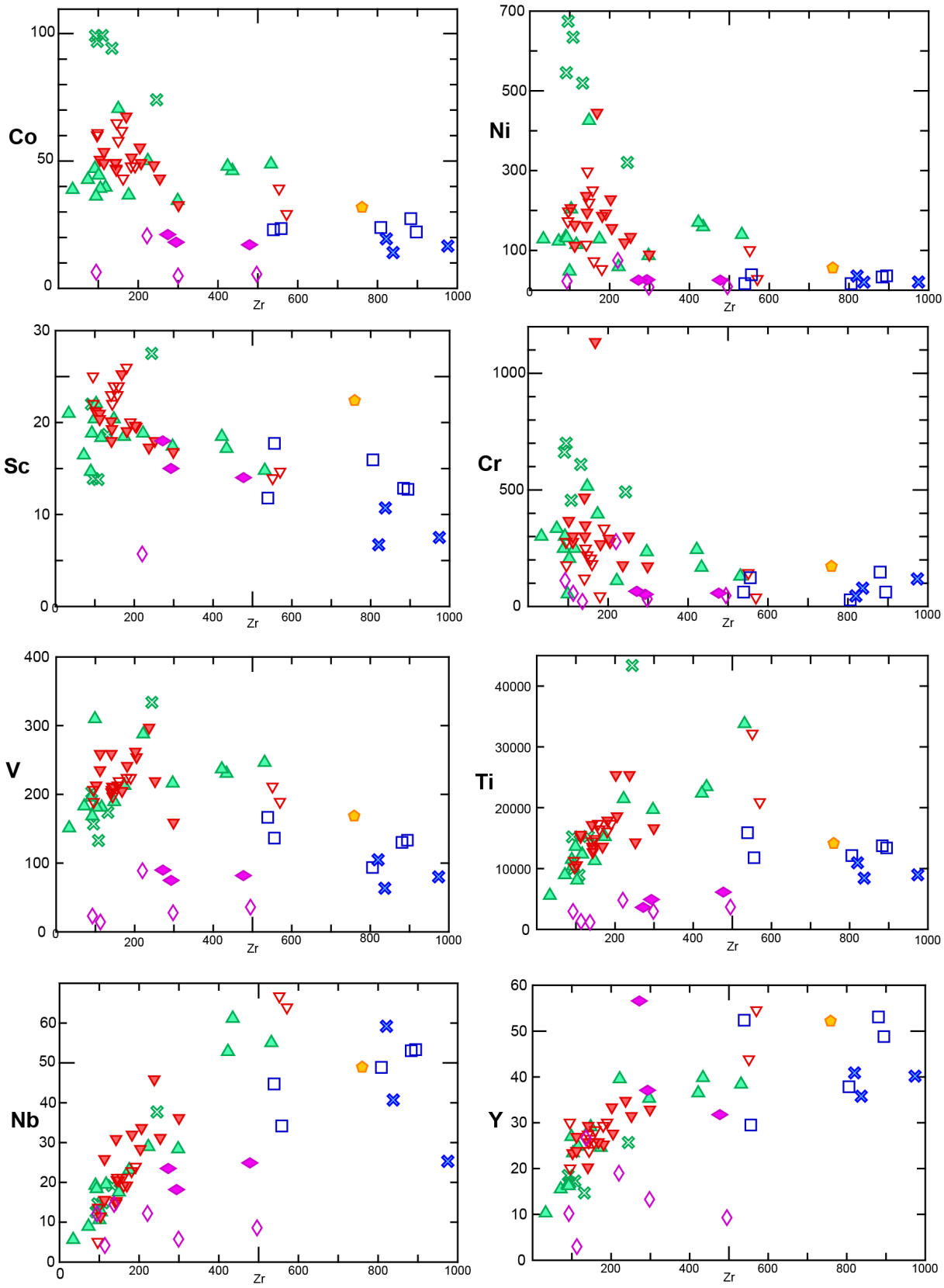

Figure 5.25: Various trace elements plotted against Zr. All concentrations are given in ppm. See figure 5.24 for legend.

5.3 Mineral chemistry

10 polished thin sections were analyzed by Electron Probe Microanalyzer (EPMA). Two sections from each rock group were analysed (except contact granodiorites, which were sampled the following year), and the thin sections were selected based on the abundance of primary igneous minerals. For all mineral formula calculations, FeO is assumed to represent total iron, thus Fe^{3+} have been calculated. Unfortunately, most of the analyses report totals which deviate from 100% and range between 94 % (in amphibole) and 112 % (in apatite). There seems to be a correlation between the total and SiO_2, in which the totals appear to increase with increasing SiO_2 content. However, when comparing the EPMA-results with the chemistry of minerals listed in Deer et al. (1992) the concentrations of all oxides from the analyses appear to be in the correct range, even though the data are not possible to use for any detailed studies. Accessory phases that were analysed by EPMA, include apatite, scapolite, calcite, zircon, clinozoisite, epidote, rutile and titanite and analyses are presented in appendix E. Olivine, clinopyroxene and orthopyroxene from two polished thin sections of an olivine gabbro (P19.2UM) and an olivine-free gabbro (P5.2) were analysed by LA-ICP-MS. Analyses are presented in appendix D.

5.3.1 Olivine

Analyses are presented in appendix E and the totals are somewhat high, with a range of 99,3-104,5 %. Forsterite contents are calculated based on 4 oxygens following the method by Deer et al. (1992). All analyzes of olivine grains are from thin sections of olivine gabbro and there is little chemical variation difference between samples. The forsterite content of the olivines from sample P19.2UM range from $Fo_{68,2}$ to $Fo_{70,1}$. The forsterite content of the olivines from sample 127988 range from $Fo_{69,8}$ to $Fo_{71,3}$. The concentration of MnO range from 0,25 to 0,33 wt% and is slightly higher in sample P19.2 UM (Fig. 5.26). The olivine grains are mantled by a Corona that appear to be divided in two chemically distinct zones, amphibole, and orthopyroxene (see section 5.3.3 and 5.3.6).

Trace elements were analysed by LA-ICP-MS in thin section P19.2 UM. Olivine from this sample show high concentrations of Ni (1208-1431 ppm) and moderately high concentrations of Co (214-247 ppm) and Zn (138,3-305,5 ppm). They show quite low concentration of Cr (0,47-

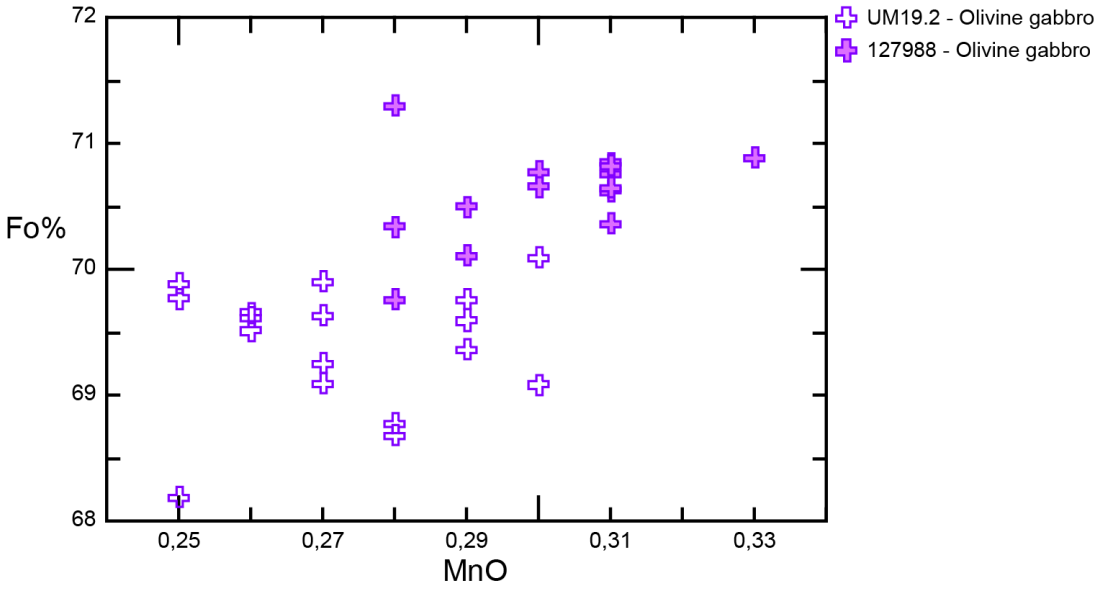

Figure 5.26: Results of EPMA analysis of olivine. Calculated forsterite content in olivine is plotted against concentration of MnO (wt%).

31,09 ppm) and Sc (1,03-2,65 ppm). Figure 5.27 shows there is a slight positive correlation between Ni and Cr, while there is slight negative correlation between Ni and Sc. Several olivine grains were analysed on both core and rim, but there were no signs of chemical zoning in these minerals, neither from the EPMA or the LA-ICP-MS analyses.

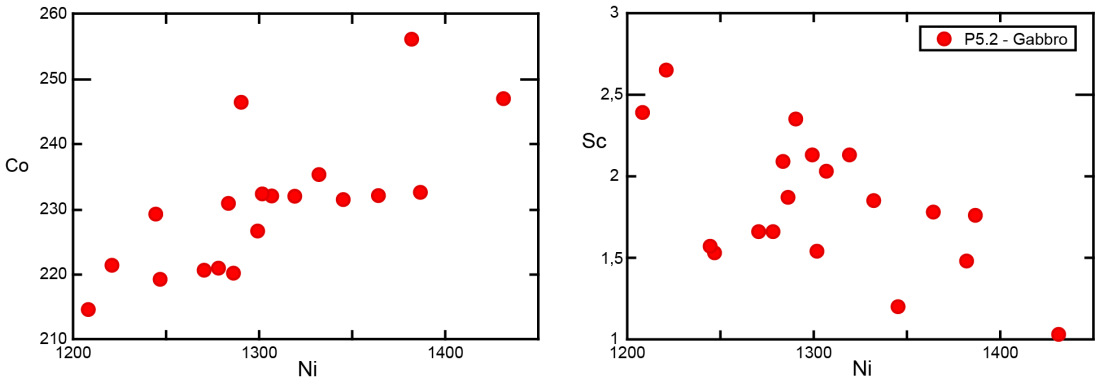

Figure 5.27: Results from LA-ICP-MS analysis of olivine from sample P5.2. All elements are given in ppm.

5.3.2 Clinopyroxene

Analyses are presented appendix E and they report totals within the range of 95 %-102 %. The mineral classification is based on the method by Morimoto (1988) where the composition is normalized to Ca + Mg + ΣFe = 100 with $\Sigma Fe = Fe^{2+} + Fe^{3+} + Mn^{2+}$, assuming 6 oxygens in the structural formula. Clinopyroxene is present in ultramafic to felsic rocks. Most of the

clinopyroxenes plot close to the divison line between the diopside and augite field, while some plot in the augite field in the classification diagram by Morimoto (1988). The pyroxenes of augitic composition represent analyses of crystals in which exsolution was observed. Clinopyroxene from the syenite are classified as hedenbergite with a range in Mg# from 0,31 to 0,34. Eight analyses of minerals denoted clinopyroxene based on thin section observations showed Al_2O_3 concentration of 6,9-15,6 wt% and their composition were more similar to amphibole. The analyses come from a gabbro, monzodiorites and olivine gabbros and they are presented in appendix E.

The Cr2O3 values of clinopyroxene from the olivine gabbros range from 0,237 to 0,634 wt% which is close to the value of the standard that was used (0,58 wt%) and way above the detection limit (200 ppm). For the other samples, the Cr_2O_3-values are less than 0,04 wt%. Trace elements were analysed by LA-ICP-MS in thin section P19.2 UM and P5.2. Clinopyroxene from the olivine gabbro, P19.2 UM, show high Mg# (0,82-0,83), high concentrations of Cr (2002,8-4646,2 ppm) and moderate concentrations of Co (34,3-37,6 ppm) Ni (167,1-198,5 ppm) and Sc (72,3-82,9 ppm). Clinopyroxene from the gabbro, P5.2, show slightly lower Mg# (0,73-0,84) and more moderate concentrations of Cr (453-954 ppm), Co (32,3-44 ppm), Ni (86,4-102,3 ppm) and Sc (63,6-104,5 ppm).

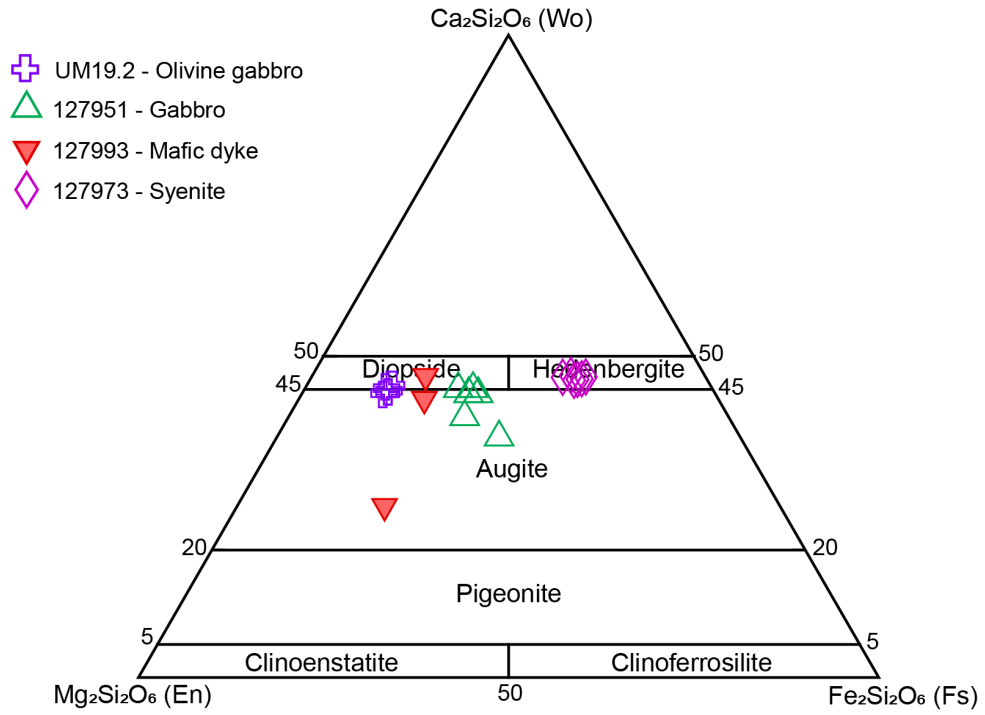

Figure 5.28: Classification of clinopyroxene based on analyses from EPMA. Classification diagram after Morimoto (1988).

The REE-analyses for clinopyroxene are normalized to chondrite and plotted in figure 5.29. The clinopyroxenes show a convex REE pattern, with LREE enrichment relative to HREE. Crystals from the olivine gabbro (P19.2 UM) have a slightly negative or no Eu-anomaly ($Eu/Eu^* = 0{,}64\text{-}1.09$). One group of crystals from the gabbro (P5.2) show distinct negative Eu-anomalies ($Eu/Eu^* = 0{,}22\text{-}0{,}35$), whereas the rest of the crystals in P5.2 show slightly negative or no Eu-anomalies (with $Eu/Eu^* = 0{,}64\text{-}0{,}99$). Several clinopyroxene grains were analysed on both core and rim, but there was no signs of chemical zoning in these minerals, neither from the EPMA or the LA-ICP-MS results.

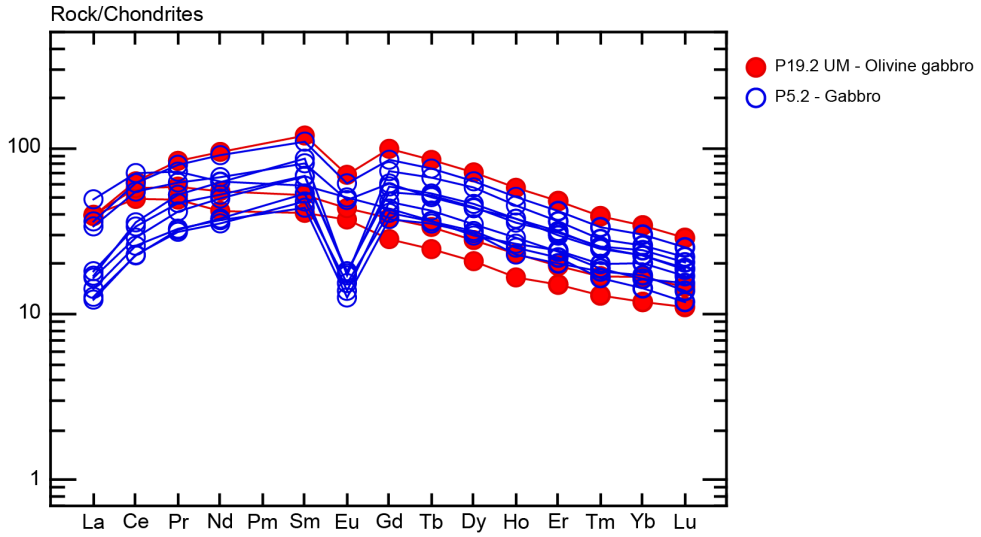

Figure 5.29: REE pattern of clinopyroxene from LA-ICP-MS. Normalization values for chondrite from Sun and McDonough (1989).

5.3.3 Orthopyroxene

Analyses are presented in appendix E and and they report totals within the range of 96 %-104 %. The mineral classification is based on the method by Morimoto (1988), as with clinopyroxene. The analyzed orthopyroxenes come from a gabbro, a mafic dyke and olivine gabbros and they plot in three distinct clusters, where analyses from the olivine-coronas overlap with the analyses from the olivine gabbros. Orthopyroxenes from olivine gabbros and the mafic dyke can be classified as enstatite, whereas orthopyroxene from the gabbro can be classified as ferrosolite according to the classification diagram by Morimoto (1988)(Fig. 5.30). However, both the mafic dyke and gabbro have orthopyroxene compositions close to the division line between the enstatite and ferrosilite field. The orthopyroxene show small variations in silica content between

samples and their MgO content range from 14,3 wt% in gabbro 127951 to 27,8 wt% in olivine gabbro UM19.2.

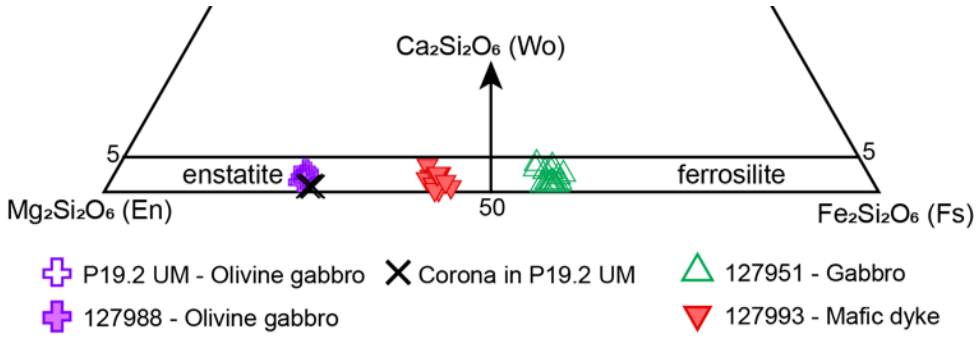

Figure 5.30: Classification of oprthopyroxene based on analyses from EPMA. Classification diagram after Morimoto (1988).

Trace elements were analysed by LA-ICP-MS in thin section P19.2 UM and P5.2. The orthopyroxene show moderately high concentrations of Cr (108-575,6 ppm), Co (68,5-87 ppm), Ni (100-311,3 ppm), Sc (9,8-58,7 ppm), V (51,9-249 ppm) and Zn (193,5-518,3 ppm). The Mg# for the orthopyroxenes (0,56-0,78) are slightly lower than for the olivines and the clinopyroxenes. Several orthopyroxene grains have been analysed on both core and rim, but from the EPMA and LA-ICP-MS analyses, there are no signs of chemical zonation in these minerals.

5.3.4 Feldspar

Analyses are presented in appendix E and end-member calculations are based on 8 oxygens in the formula (Ribbe and Hofmeister, 1983). Feldspar have been found in all thin sections analysed by EPMA and their composition is presented in ternary feldspar diagrams (Fig. 5.31 after Deer et al. (1992)). Feldspar from mafic and intermediate rocks are classifed as plagioclase, and olivine gabbros, which display the highest proportion of anorthite (An_{41-66}) are classified as labradorite, according to Deer et al. (1992). Plagioclase from the monzodiorites plot closer to the albite corner rather than the anorthite corner (Ab_{52-73}, An_{27-53}) and can be classified as andesine and labradorite, whereas plagioclase from the gabbro and mafic dykes and enclaves have compositions between feldspar from olivine gabbros and monzodiorites (with Ab_{48-76}, An_{23-56}). These feldspars are classified as oligoclase, andesine and labradorite. A common feature for all the mafic rocks is that the orthoclase (K) component is close to zero. The felsic granitoids comprise both plagioclase with compositions between albite and oligo-

clase ($Ab_{71-97}An_{2-97}$) and K-feldspar (Or_{85-92}, Ab_{8-14}). Several zoned plagioclase crystals occur in mafic, intermediate and felsic rocks. A plagioclase displaying concentric zoning was analyzed with five points from core to rim, but no notable variation was detected.

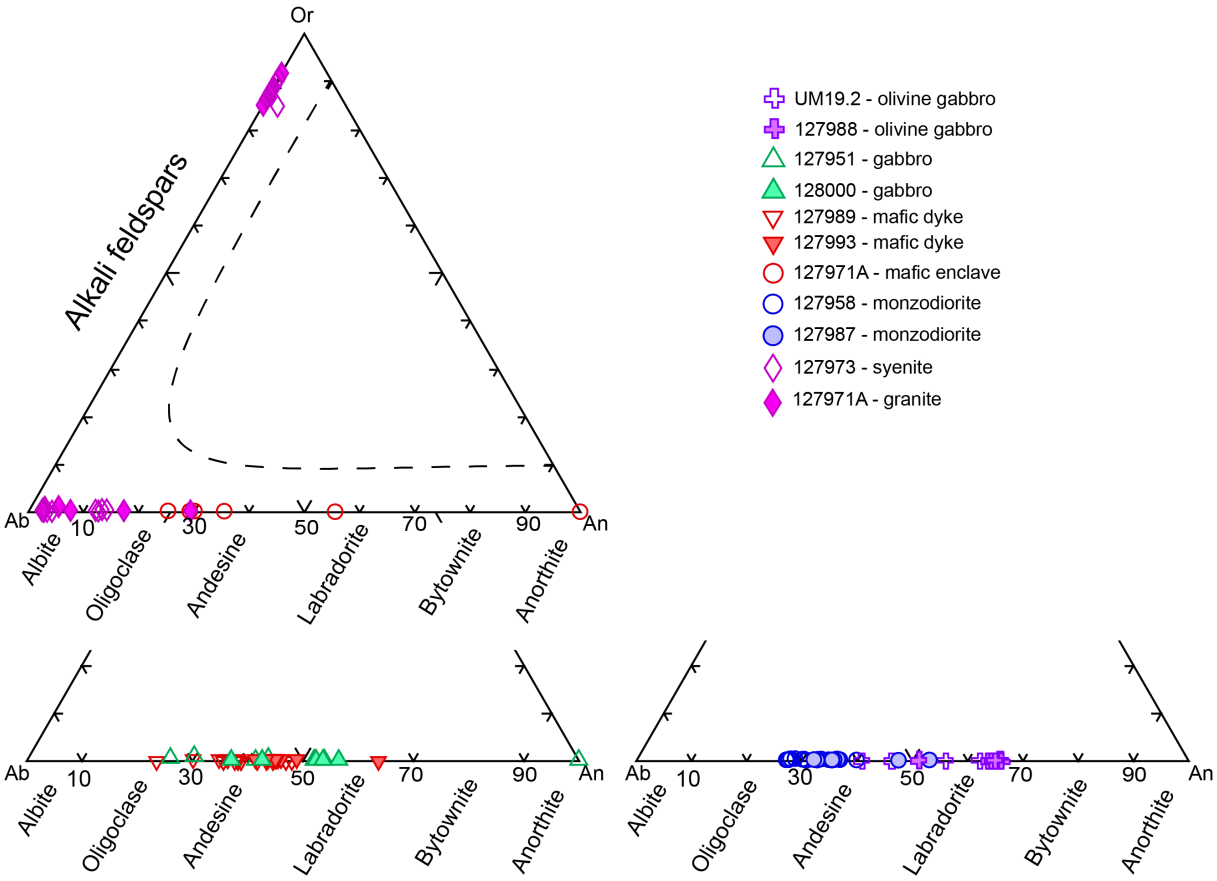

Figure 5.31: Ternary feldspar diagram for feldspar after Deer et al. (1992) with results from the EPMA analysis.

5.3.5 Garnet

Analyses are presented in appendix E. Calculation of elements in the X site and end-members were based on 12 oxygens in the formula (Grew et al., 2013). Garnet occurs in gabbro 127951 and in the monzodiorites of the thin sections analysed by EPMA. Garnets from the monzodiorites have compositions of $Gr_{15-21,5}$ $Py_{10,3-14,9}$ $Alm_{57,5-66,5}$ $Sp_{4,1-8,2}$ $And_{0,2-3,5}$. Garnets from the gabbro have compositions of $Gr_{16-23,8}$ $Py_{6,9-13}$ $Alm_{64,1-68,3}$ $Sp_{2-3,9}$ $And_{1,8-3,1}$. The nomenclature diagram by Grew et al. (2013) shows that all samples can be classified as almandine, which is due to the high iron content (29,7-34,5 wt%). No chemical differences were detected between the rim and the core of garnets.

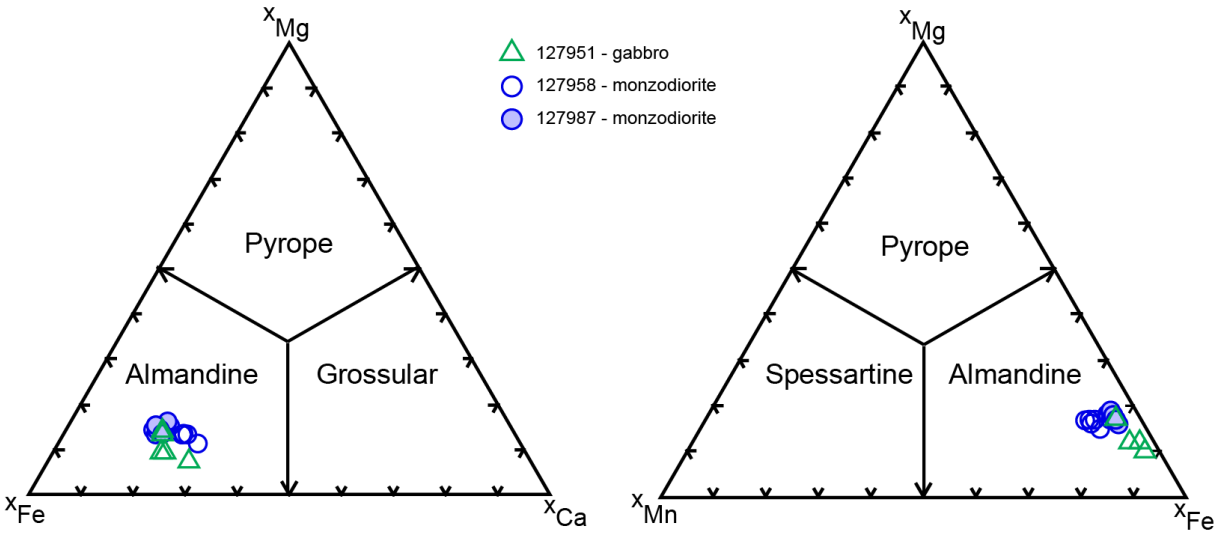

Figure 5.32: Classification of garnet based on the occupancy of the X site, after Grew et al. (2013)

5.3.6 Amphibole

Analyses are presented in appendix E. The calculations for classification follow the method by Leake (1978) which is based on 23 oxygens with adjustments of the cations, assuming 13 cations in total. As (Ca+Na)$_B \geq$ 1,00 and $Na_B <$ 0,5 for all analysed amphiboles, they are all members of the calcic amphibole group (Leake et al., 1997). All amphiboles have Ca$_B >$ 1,50, while the (Na+K)$_A$-values, however, are both above and below 0,5. Thus, they are plotted in two different diagrams, Fig. 5.33-A and -B, respectively. As $^{VI}Al < Fe^{3+}$ for all amphiboles, all mafic and intermediate samples of Fig. 5.33-A can be classified as magnesiohastingsite, except for one gabbro sample which can be classified as hastingsite and amphibole from the mafic enclave which is close to edenite. The intermediate rocks plot along the division line between magnesiohastingsite and hastingsite and amphibole from the syenite sample is classified as hastingsite. The amphiboles with (Na+K)$_A <$ 0,5 in Fig. 5.33-B are all from mafic samples and plot both in the magnesiohornblende and tschermakite field. Mg# in amphibole range from 0,51 to 0,72 in the mafic rocks, and from 0,50 to 0,51 in the monzodiorites,

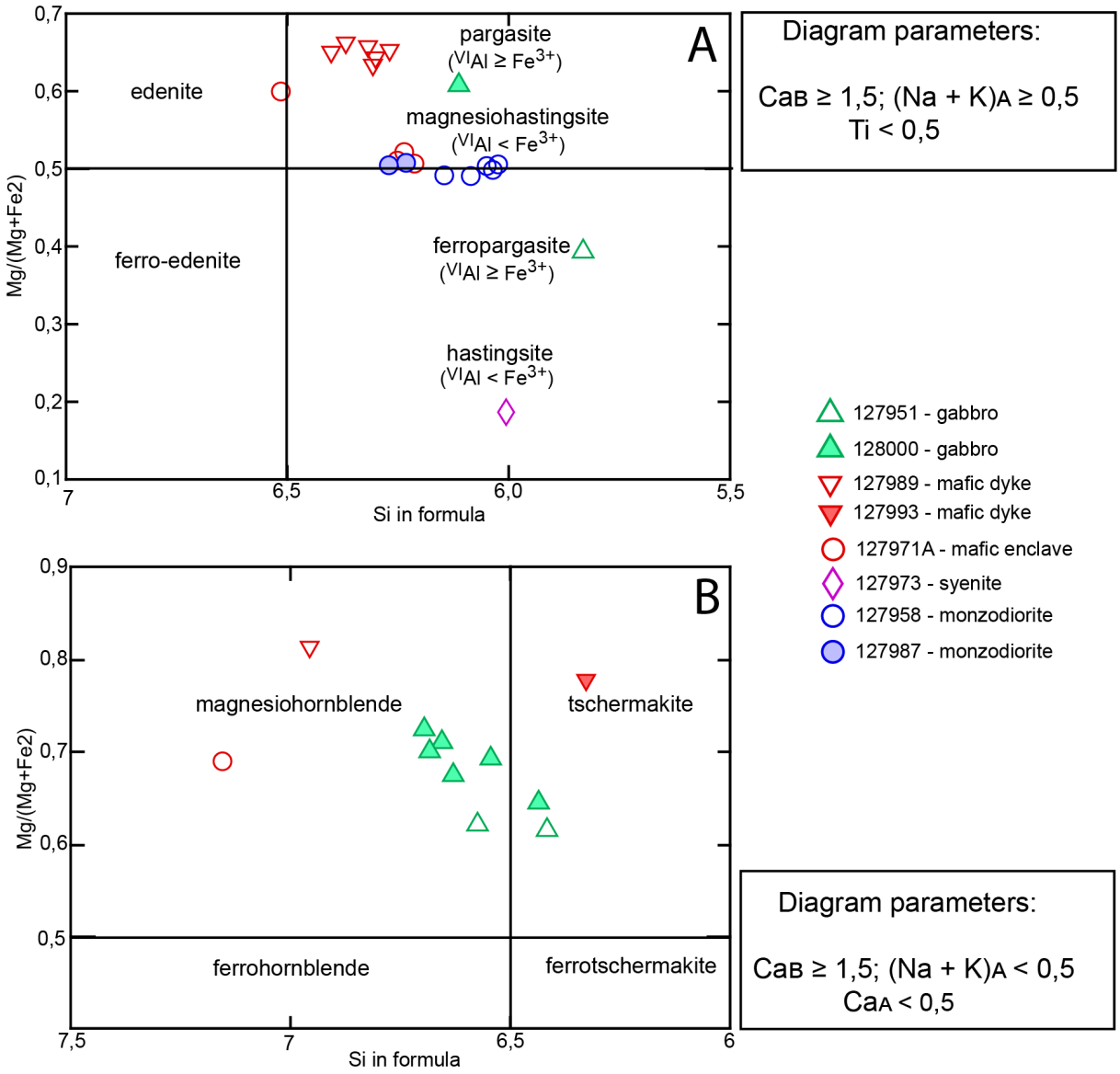

Figure 5.33: Classification diagram for calcic amphibole, after (Leake et al., 1997). A) Classification of calcic amphibole with (Na+K)$_A \geq 0,5$. B) Classification of calcic amphibole with (Na+K)$_A <$ 0,5.

5.3.7 Biotite

Analyses are presented in appendix E. Li_2O and H_2O calculations were performed following the method of Tindle and Webb (1990). Mica from gabbros, mafic dykes, monzodiorites and felsic rocks plot in the biotite field of the classification diagram and have Fe/(Fe+Mg)-values of 0,35-0,61. Mica from olivine gabbros can be classified as phlogopite with lower Fe/(Fe+Mg)-values of 0,17-0,27.

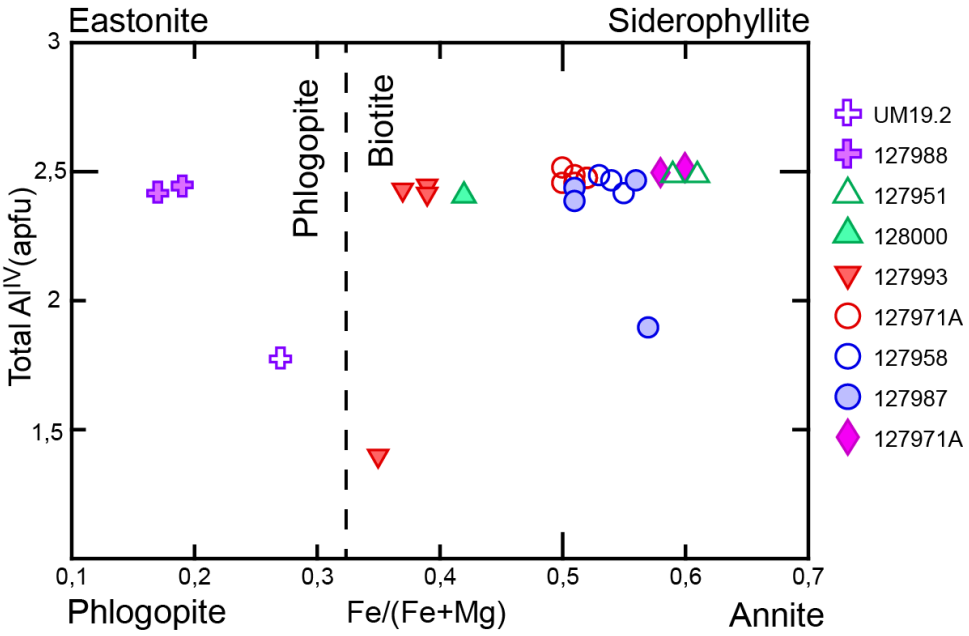

Figure 5.34: Classification of biotite, after Deer et al. (1992).

5.4 Sm-Nd isotopes

Sample	Rock description	ε_{Nd}
MO-28771	Garnet mica schist, host rock	-8,2
P6.3	Gabbro	-2,5
P5.2	Gabbro	-1,7
UM-46	Gabbro	4,4
P9.4	Gabbro	4,8
UM-1D	Gabbro	5,4
UM-61	Gabbro	5,6
P5.1	Mafic dyke	2,8
UM-1A	Mafic dyke, cutting gabbro	3,3
MO-28770	Mafic dyke, cutting host rock	4,5

Table 5.1: Table for samples analysed for Sm-Nd isotopes. ε_{Nd} values have been calculated with a decay constant of 6,54 x 10^{-12} and the following values for present day CHUR: $^{143}Nd/^{144}Nd$ = 0,512638, $^{147}Sm/^{144}Nd$ = 0,1967 (DePaolo and Wasserburg, 1976).

Isotopic ratios and Sm-Nd concentrations are presented in appendix I and the chemistry of samples analysed for Sm-Nd isotopes is presented in appendix J. Calculated ε_{Nd} values are listed in table 5.1. Figure 5.35 shows ε_{Nd} plotted against two differentiation indices, Mg# and Th (ppm) and in both diagrams, the data define a linear trend with the host rock as one end-members. Two samples of gabbro, P6.3 and P5.2 plot in the middle between the host rock and the other mafic rocks, displaying negative ε_{Nd}-values of -2,5 and -1,7. The other gabbros show

ε_{Nd}-values of +4,4-5,6 and the mafic dykes show values between +2,8 and +4,5.

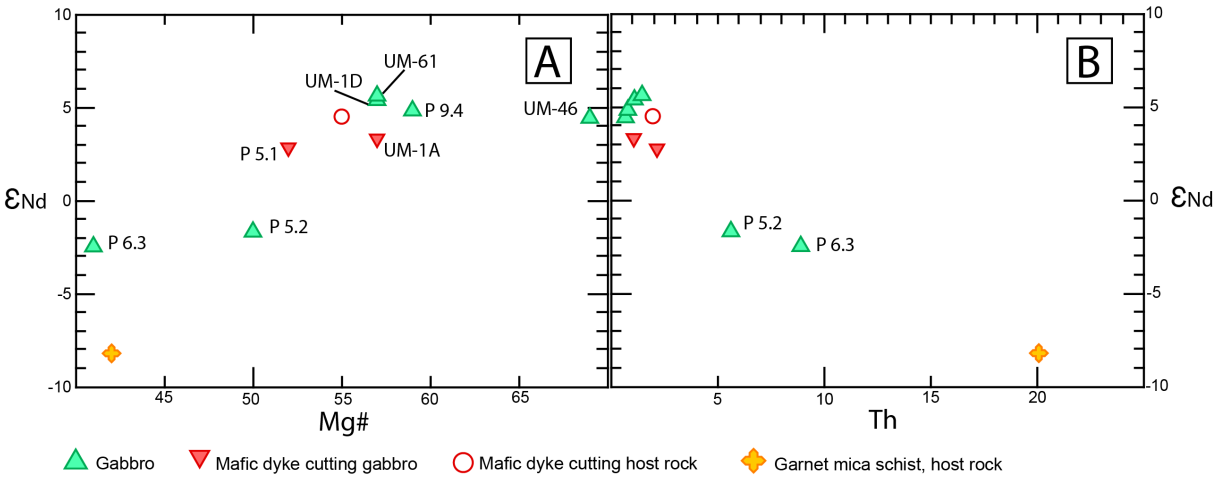

Figure 5.35: Epsilon-Nd vs Mg# and Th. Note that sample P.6.3 and P5.2 plot on a line in particular in the Th-plot.

5.5 Petrographic descriptions

In the following section, each of the rock groups described in the previous section, will be described in terms of mineralogy and textures, based on observations in a petrographic microscope. An overview of the minerals observed in each specific thin section, is presented in appendix L.

Rock group: Gabbro

Thin sections: 127951 (P), 127963 (P), 127965, 127972, 127980 a&b, 127984, 127985, 127992, 127996 a (P), 127996b, 127999 a&b, 128000 (P), 132402 a&b, 132403. Polished thin sections were made for thin sections marked with (P).

Main minerals: Amphibole (20-50%), plagioclase (20-40%), orthopyroxene (15-20%), clinopyroxene (10-15%), biotite (5-10%), opaque minerals (3-10%), actinolite (0-40%).

Opaque, accessory (total 100%): Ilmenite (70%), pyrrhotite (20%), pentlandite (7%), chalcopyrite (3%)

Accessory minerals: Apatite (<1-3%), epidote (<1-2%), clinozoisite (<1-5%) titanite (<1-3%), rutile (<1-3%), chlorite (<1-2%), garnet (<1-3%), scapolite (<1-3%), calcite (<1%), quartz (<1-3%)

In thin section, the gabbroic rocks commonly have a green appearance due to the abundance of green to blue amphibole. Primary igneous textures are only preserved in a minority of the samples. The least altered samples have a seriate texture, are fine- to medium-grained and contain mainly plagioclase, orthopyroxene and clinopyroxene. Plagioclase occurs as subhedral, elongate crystals with a size of 0,2-6 mm and curved grain boundaries. Polysynthetic twinning is well developed in most crystals and some exhibit discontinuous zoning, dividing the mineral into a rim and a core. Both clinopyroxene and orthopyroxene are mostly anhedral, 0,1-4 mm in size, and show replacement by light green amphibole, particularly along the margins of the minerals (Fig. 5.36-A&B). The pyroxenes have a dusty appearance and inclusions of fine grained plagioclase and amphibole are observed in some crystals. Twinning is a common feature in clinopyroxene and some pyroxene grains exhibit lamellaes of either exsolution of Fe-Ti oxides along the cleavage. The primary contacts between plagioclase and pyroxene grains are generally obscured by the secondary growth of amphibole. Biotite is red-brown in plane polarized light and occurs as an interstitial phase, encompassing pyroxene grains (Fig. 5.36-D). Subhedral garnet is variably present, is 0,1 to 2 mm in size and can contain inclusions of plagioclase, biotite and opaque minerals (Fig. 5.36-A&E). Euhedral epidote of 0,2-0,6 mm occurs along the grain boundaries of plagioclase in a few samples. Interstitial quartz of up to 2,5 mm with slightly wavy grain boundaries occurs in a few samples. Plagioclase and interstitial biotite are variably poikilitic with inclusions of subhedral to euhedral apatite and rounded opaque minerals. The opaque minerals are anhedral to subhedral and fine to medium grained, and are often mantled by a corona of green amphibole. The more altered samples are dominated by fine grained, light green amphibole, which probably is actinolite. The amphibole appears to have replaced pyroxene, as a core of pyroxene with irregular grain boundaries is observed within some of the amphibole grains. The larger, green amphibole grains exhibit a poikiloblastic texture with inclusions of fine grained anhedral plagioclase crystals. Light green, actinolitic amphibole occur regularly alongside the poikiloblastic amphibole. In some samples (127972, 127999) amphibole appears as independent, subhedral crystals of 0,1-0,4 mm with distinct cleavage (Fig. 5.36-F). Rutile is present as anhedral to subhedral crystals of 0,1-0,3 mm and is commonly surrounded by amphibole with distinct cleavage (Fig. 5.36-E). Plagioclase appears as anhedral crystals of 0,1-0,5 mm with poorly developed polysynthetic twinning between the amphibole and as inclusions within amphibole crystals. Except for a few larger plagioclase crystals of 2-3 mm, the plagioclase and amphibole crystals exhibit an equigranu-

lar texture. The plagioclase crystals commonly have a sericitic core. Needle shaped crystals and medium grained subhedral crystals of clinozoisite, appear inside larger plagioclase crystals together with anhedral scapolite. Clinozoisite is characterized by its distinct anomalous blue interference colour (Fig. 5.36-E). The opaque minerals are less abundant in the altered samples and they are often mantled by a 0,06 mm irregular rim of titanite. In all gabbroic samples, ilmenite is the dominating opaque phase and show lamellar twinning oriented at 45 degrees to each other. Most of the ilmenite crystals are anhedral and rounded with a size of 0,2-0,4 mm, but some are elongated and up to 6 mm in size. Magnetite is present as individual subhedral grains and commonly exhibits a trellis texture in which ilmenite occurs as laths in magnetite. Magnetite contains microcrystalline inclusions of anhedral silicates, whereas ilmenite is more homogenous. Regularly, ilmenite displays an intergrowth with orthopyroxene in a vermicular fashion and constitute aphanitic needles in biotite. Pyrrhotite is an accessory phase and contain inclusions of chalcopyrite and is penetrated by laths of pentlandite. Small subhedral grains of pyrrhotite, pentlandite and chalcopyrite is situated along the margins of some of the ilmenite crystals.

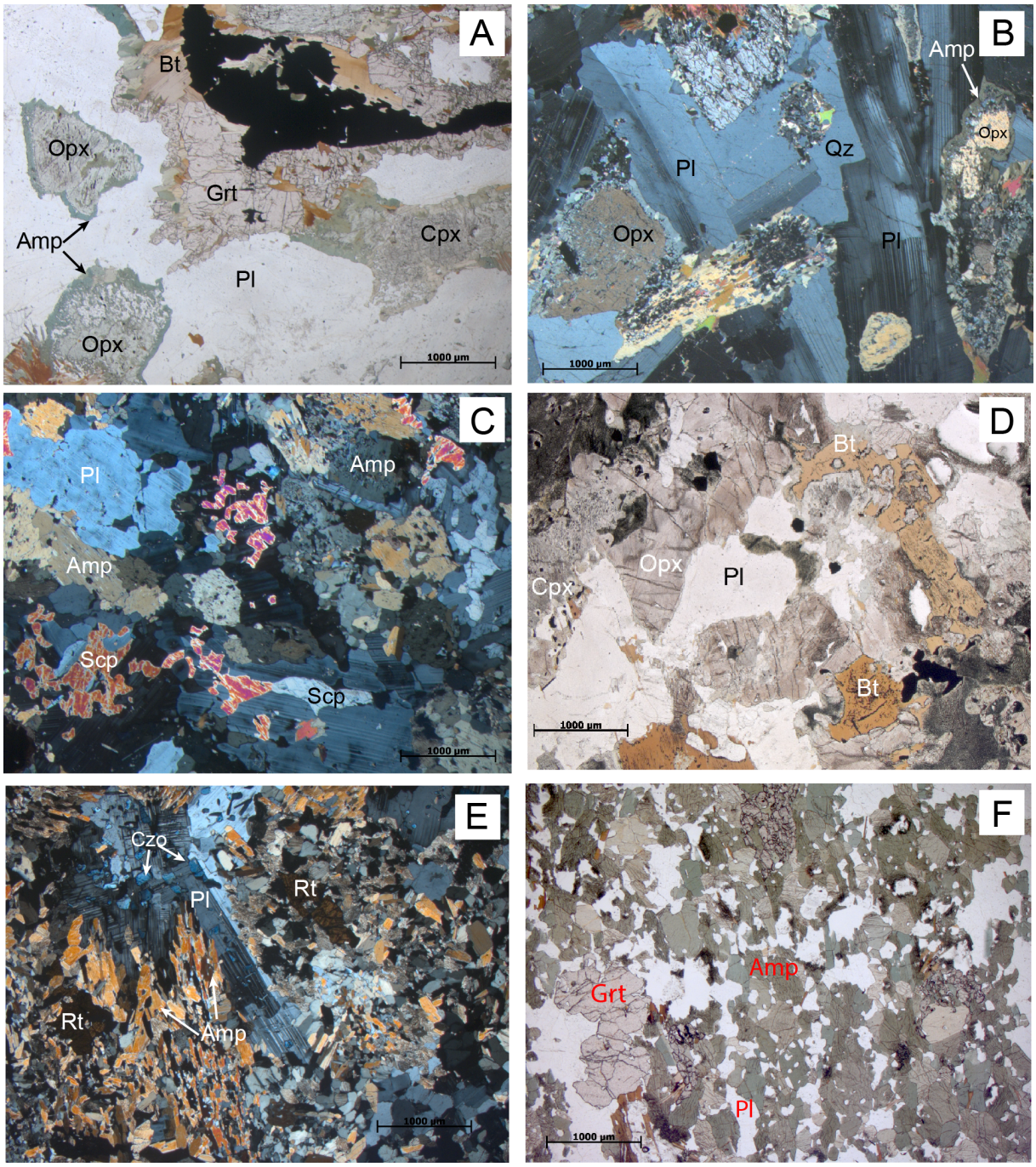

Figure 5.36: Photomicropraphs of five different gabbros. Both A and B are from thin section 127951. A) Crystals of pyroxene are mantled by light green amphibole. B) Individual crystals of orthopyroxene surrounded by elongated plagioclase crystals C) Scapolite inclusions in plagioclase and dark green amphibole. From thin section 128000 in xpl. D) From thin section 127996a in ppl. E) From thin section 127992 in xpl. F) From thin section 127996b in ppl.

Rock group: Olivine gabbro

Thin sections: 127955, 127991, 127983, 127988 (P), 127998 (P), P19.2UM (P). Polished thin sections were made for thin sections marked with (P).

Main minerals: Olivine (5-30%), orthopyroxene (20-30%), clinopyroxene (15-25%), plagioclase (10-20%), orange-brown amphibole (5-10%), green amphibole (5-10%), biotite (10-15%), ilmenite (3-5%)

Accessory minerals: Apatite, calcite, amphibole-pyroxene coronas, pyrrhotite, pentlandite.

Olivine gabbros display a fine to medium grained, seriate texture with a main mineral assemblage of olivine, clinopyroxene, orthopyroxene and plagioclase. Anhedral plagioclase occurs as an interstitial phase which varies between 0,2 and 1 mm in size. Oscillatory zoning is observed in a few interstitial crystals. Larger crystals (up to 5-6mm) of poikilitic plagioclase enclose subhedral olivine and clinopyroxene grains (Fig. 5.37-C). Pyroxene grains are typically 0,2 to 2 mm large and simple twinning is a common feature in clinopyroxene. The interference colour of clinopyroxene is commonly second order pink to blue, whereas the interference colour of orthopyroxene range from first order grey to second order blue. Pyroxene exhibit wavy grain boundaries and they are commonly affected by exsolution which give them a dusty appearance. Regularly, pyroxene is completely replaced by an aphanitic phase with second order interference colour. Some larger, poikilitic pyroxenes contain inclusions of smaller olivine grains (Fig. 5.37-B). Subhedral olivine of 0,2-1 mm is often mantled by a 0,06 mm wide corona of fibrous, radially oriented light green actinolite or colourless pyroxene. Anhedral, medium grained amphibole is orange-brown in plane polarized light and sometimes difficult to distinguish from red-brown biotite, as both minerals are typically interstitial between olivine and pyroxene grains (Fig. 5.37-A). Orange-brown amphibole occurs regularly as partial reaction rims on orthopyroxene and as patchy inclusions within the pyroxene. The size of the biotite crystals varies between 0,1 and 4 mm, where the larger crystals are enclosing medium grained pyroxene and olivine grains. Thin veins of serpentine (or actinolite) cut some of the samples. Opaque minerals are often mantled by green amphibole and occur as anhedral, embayed crystals at the margins of the major mineral phases or as inclusions in biotite. Ilmenite is the most abundant phase in the olivine gabbros. However, there are more subhedral pyrrhotite with rounded inclusions and flame-like exsolution of pentlandite in these samples compared to the olivine-free gabbros. Ilmenite occur in an interstitial fashion as homogenous grains of 0,4-1,4 mm and regularly as fine-grained inclusions in biotite and pyroxene.

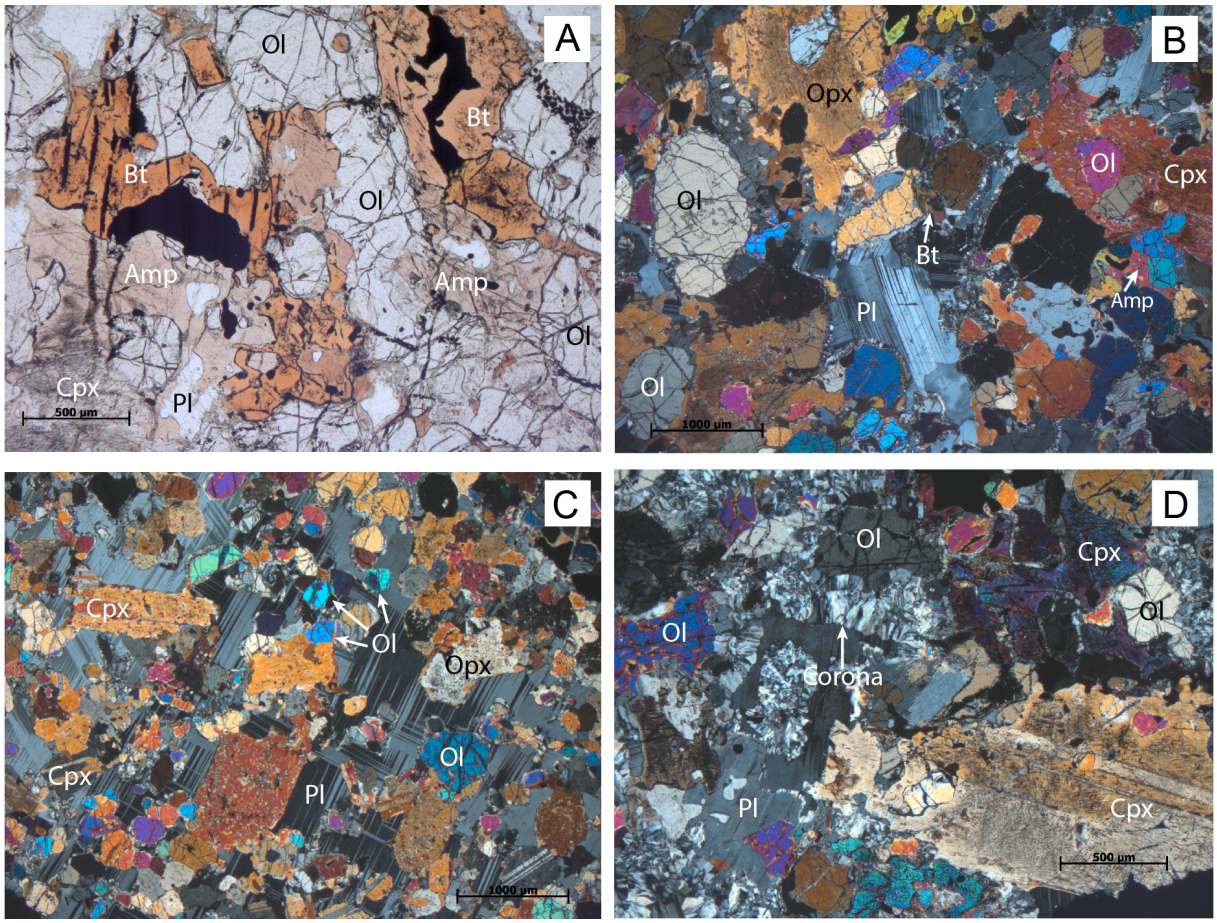

Figure 5.37: Photomicrographs of three olivine gabbros, where A and B are from thin section 127988. C) Poikilitic plagioclase with inclusions of olivine and pyroxene, from thin section 127998 in xpl. D) Olivine mantled by fibrous coronas in thin section 127991 in xpl.

Rock group: Aphyric, mafic dykes and mafic, magmatic enclaves.

Thin sections: 127969, 127970, 127979, 127993 (P), 127994 (P), 127959, 127978, 127981, 127982, 127986, 127989 (P), 127995, 132401, 132402. Polished thin sections were made for thin sections marked with (P).

Main minerals: Green amphibole (30-40%), pyroxene (0-20%), plagioclase (30-40%), biotite (5-10%), ilmenite (5-10%)

Accessory minerals: Titanite (1-3%), epidote (<1%), rutile (<1%), apatite (<1%), zircon (<1%), calcite (<1%), rutile (<1%), pyrrhotite (<1%), pentlandite (<1%), chalcopyrite

Green amphibole and plagioclase dominate the minerals assemblage of the mafic enclaves and dykes. Some of the thin sections display an equigranular texture with a grain size ranging from 0,1 to 0,4 mm. Subhedral, elongated crystals of light green amphibole have distinct cleavage and are slightly oriented, indicating a weak foliation. The plagioclase crystals are subhedral to

anhedral. Biotite is both interstitial and prismatic and sometimes exhibit kink banding. Other samples have a seriate texture, with grains between 0,1 mm and 1 mm in size. The amphibole occurs either as poikiloblastic grains with fine grained inclusions of anhedral plagioclase, or as irregular rims around anhedral pyroxene grains, which have interference colours between first order yellow and second order blue. Subhedral pyroxene phenocrysts reach up to 1 mm in a fine-grained matrix (0,1 mm) of plagioclase and pyroxene. They only occur in inequigranular samples and are spatially associated with amphibole and regularly biotite. Plagioclase occur as randomly oriented laths and oscillatory zoning occurs in some of the crystals (Fig. 5.38-B). In a few samples elongated plagioclase phenocrysts, up to 4 mm in size, occur in a matrix composed of poikiloblastic amphibole and randomly oriented plagioclase and biotite. Biotite occur both as prismatic, stubby crystals and as an interstitial phase in between the pyroxene grains (Fig. 5.38-A). Apatite occurs both as subhedral-to euhedral medium grained crystals and acicular crystals of 0,05-0,15 mm. Opaque minerals are present in both equigranular and inequigranular samples as anhedral, slender or embayed crystals. Ilmenite occurs as anhedral inclusions in biotite and more rarely in plagioclase. The crystals are 0,06-0,6 mm in size and most of them are homogenous. In pyroxene, ilmenite occurs in almost a vermicular fashion as slender, rounded inclusions or as microcrystalline inclusions. Subhedral pyrrhotite is present in small commodities with pentlandite lamellaes and inclusions of chalcopyrite. Titanite, which is an accessory mineral, is rimming the opaque minerals and is variably present as individual crystals.

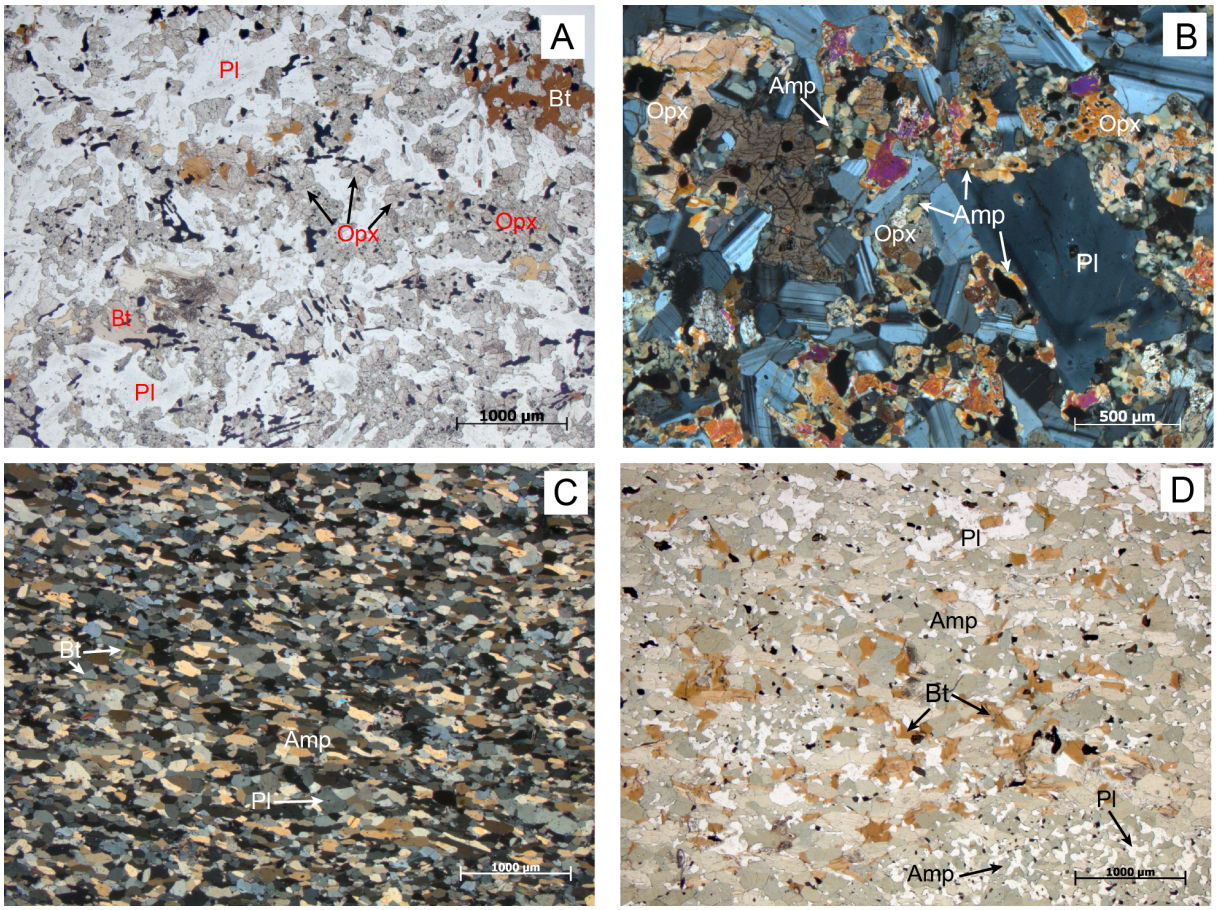

Figure 5.38: Photomicrographs of four mafic, fine grained rocks. A) Interstitial biotite and opaque minerals between pyroxene in thin section 127993. B) Seriate texture and plagioclase zoning thin section 127994. C) From thin section 127956. Note the orientation of the amphibole grains. D) From thin section 127959. Note the poikiloblastic amphibole in the lower right corner.

Rock group: Monzodiorite and monzonite

Thin sections: Monzodiorite: 127952, 127958 (P), 127960, 127961, 127987 (P). Monzonite: 132404a (P), 132404b (P), 127968, 127977. Polished thin sections were made for thin sections marked with (P).

Monzodiorites

Main minerals: Amphibole (15-20%), plagioclase (30-40%), K-feldspar (5-10%), quartz (5-10%), biotite (10-15%), ilmenite (5-10%), garnet (0-5%)

Accessory minerals: Epidote, chlorite, apatite, calcite, zircon, titanite, pentlandite, chalcopyrite

The monzodiorites are inequigranular and dominated by plagioclase, K-feldspar, biotite and amphibole. Plagioclase crystals are anhedral to subhedral with a size range of 0,1-4 mm, have

a dusty appearance and are often sericitic. The grain boundaries are often bulging and small recrystallized grains of $< 0{,}1$ mm commonly occur at the grain boundaries. Scapolite occur as inclusions in some of the larger feldspar grains and myrmekite is a widespread texture in many samples (Fig. 5.39-D). Recrystallized quartz with undulous extinction occur throughout the samples. Green poikiloblastic amphibole crystals are common and they contain fine-grained plagioclase and quartz inclusions (Fig. 5.39-A). Other green and blue-green hornblende forms networks of anhedral crystals with a size range of 0,1-0,4 mm. Large phenocrysts of poikilitic garnet, with a size of 4-8 mm, contain inclusions of mainly plagioclase and quartz but also minor biotite and hornblende. Brown-red biotite occur both as interstitial, anhedral grains and as stubby, prismatic crystals. The latter display kink banding and indicate a weak orientation in some of the samples. Opaque minerals are interstitial and occur in small commodities. Ilmenite is the dominating opaque phase, exhibit lamellar twinning and has a grain size of 0,06-0,3 mm. It is often anhedral and contain inclusions of smaller silicates. Pentlandite and chalcopyrite are present as minor accessory phases. Interstitial chlorite and serpentine veins are present is some of the samples.

Monzonites

Main minerals: Amphibole (5-10%), plagioclase (15-20%), K-feldspar (15-20%), quartz (10-15%), biotite (10-15%), pyroxene (5-10%)

Accessory minerals: Epidote, apatite, calcite, zircon, titanite, epidote, scapolite, ilmenite

The most pronounced difference between monzodiorites and monzonites is that K-feldspar and quartz is more abundant in the latter. In addition to smaller recrystallized grains, quartz occur as anhedral to subhedral crystals of 0,3-1 mm. Phenocrysts of K-feldspar and plagioclase crystals are subhedral with a size of 1-4 mm. Flame perthite and antiperthite is widespread and oscillatory zoning is observed in plagioclase (Fig. 5.39-C&D). Myrmekite is also abundant in these rocks. Subhedral clinopyroxene and orthopyroxene of 0,2-0,8 mm large are present in small commodities and are often rimmed by blue-green amphibole. Compared to the monzodiorites, the content of green amphibole is lower (5-10%) in the monzonites and occurs mostly as rims or inclusions in biotite and pyroxene. However, some subhedral crystals of green amphibole occur as individual, homogenous crystals with a size of 0,2 to 2 mm. Some of these comprise minor inclusions of anhedral pyroxene or opaque minerals. Red-brown biotite occur in a chaotic, radiating fashion and is often enclosing smaller blue-green amphibole grains. Anhedral

to subhedral ilmenite occur commonly as homogenous grains of 0,04-0,4mm, but also appears as microcrystalline inclusions within pyroxene grains.

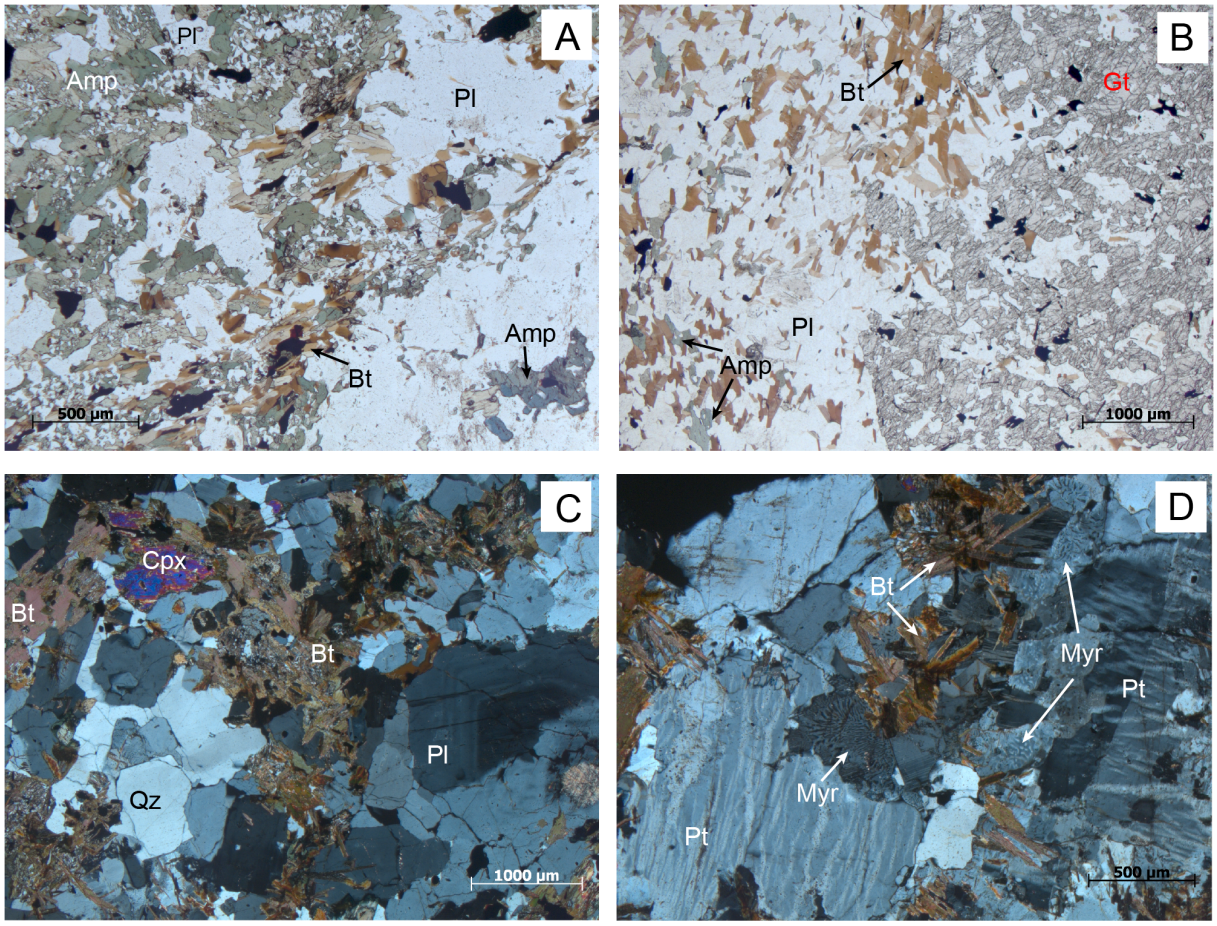

Figure 5.39: Photomicrographs of monzodiorites (A & B) and monzonites (C & D) A) Poikiloblastic amphibole from thin section 127987. B) Phenocrystic and poikilitic garnet from thin section 127958. C) Oscilllatory zoning in plagioclase and radiating biotite from thin section 132404. D) Myrmekite and flame perthite in thin section 132404.

Rock group: Felsic granitoid

Thin sections: Granite: 127966, 127971a (P), 127971b, 127974. Syenite: 127973 (P), 127990. Polished thin sections were made for thin sections marked with (P).

Main minerals: Quartz (20%), K-feldspar (30%), plagioclase (15-20%), biotite (3-20%), green clinopyroxene (0-5%)

Accessory: Scapolite, actinolite, chlorite, serpentine, ilmenite, pyrrhotite, pentlandite, chalcopyrite.

According to the TAS-diagram by Middlemost (1994), three of the felsic granitoid plot in the field of granite and two plot in the field of syenite. Sample 127964 plot in the diorite field.

The felsic graniotoids are medium grained and equigranular, except for some smaller (<1 mm) recrystallized quartz grains and some phenocrystic K-feldspar up to 1 cm in size. Quartz, K-feldspar and plagioclase dominate the mineral assemblage. The K-feldspar is mostly anhedral with wavy grain boundaries, but is sometimes subhedral and elongated. Plagioclase occurs as subhedral to euhedral, nearly rectangular crystals and exhibit wavy grain boundaries. Both feldspars have a dusty appearance and contain inclusions of fine grained muscovite and, less commonly, scapolite. Perthite is present in all samples and occur both as flame perthite and in a more patchy fashion, with inclusions or anhedral plagioclase in K-feldspar. Anhedral quartz encapsulates euhedral plagioclase and the larger quartz grains (1-2 mm) exhibit undulous extinction. Myrmekite is widespread and occur in isolated zones of 0,4 mm along the margins of K-feldspar grains and sometimes as inclusions within them (Fig. 5.40-B). Biotite varies with respect to abundance and colour. While the colour is more green-brown in the most felsic samples, it changes to red-brown in the less felsic sample where biotite is more abundant (127964). The biotite is generally interstitial, but also occur as stubby prismatic crystals in a radiating fashion and is often spatially associated with titanite. Kink banding and replacement rims of green amphibole around biotite is observed in some of the samples. One sample (127973) contain light green, pleochroic clinopyroxene which appear as isolated subhedral crystals and exhibit partial overgrowth of blue-green, anhedral amphibole (Fig. 5.40-D). *Opaque phases* In the granite, most of the ilmenite grains contain inclusions of microcrystalline silicates and occur as individual, anhedral grains mantled by a 0,4 mm wide rim of titanite. A few anhedral to subhedral grains of pyrrhotite and pentlandite are also present in the sample. In the syenite, there are only scarce amounts of pyrrhotite of 0,02-0,1 mm in size, occurring along the grains boundaries of the major mineral phases, in addition to a few grains or chalcopyrite which are below 0,04 mm in size.

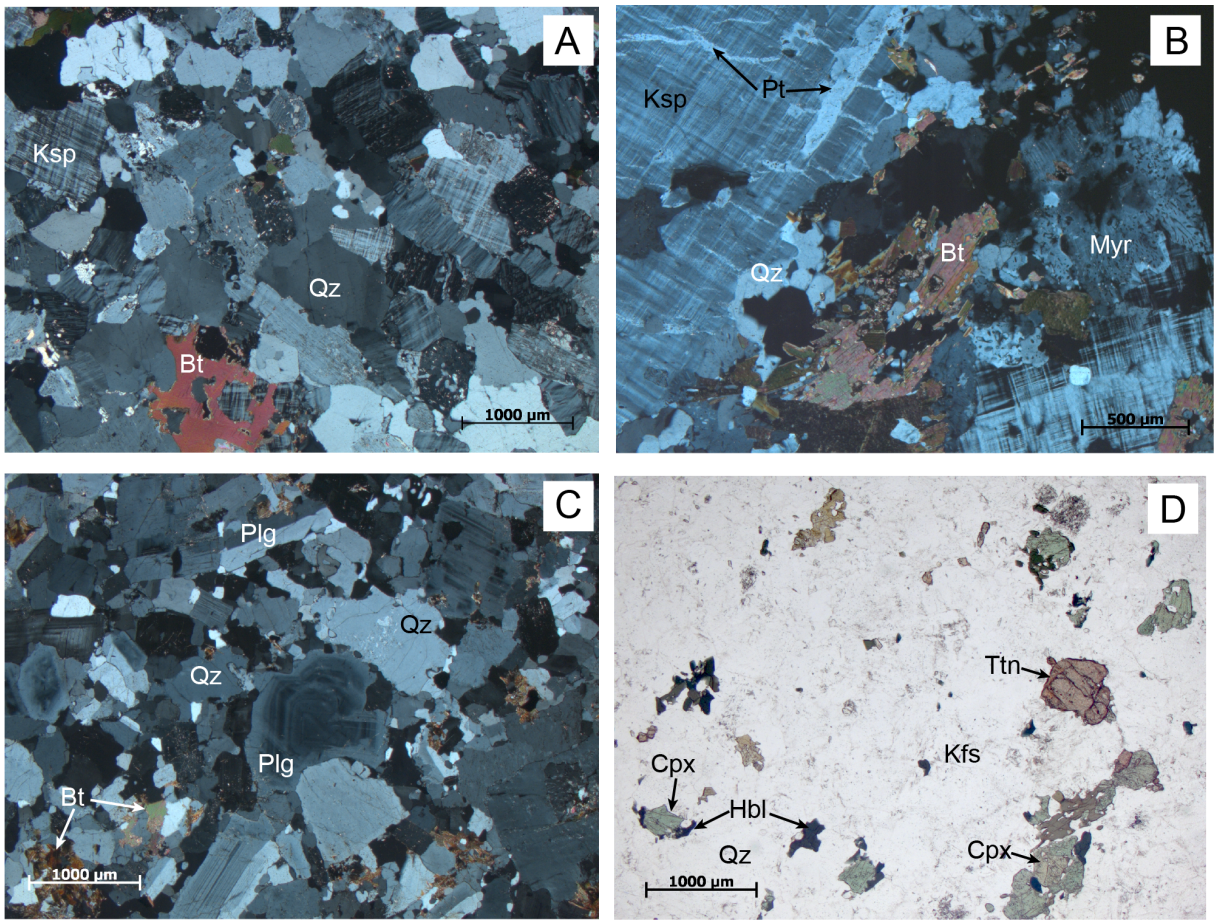

Figure 5.40: A) and B) are both from thin section 127974 where B) displays perthite in K-felspar. C) From thin section 127990 in xpl. Note the oscillatory zoning in plagioclase. D) From thin section 127973 in ppl. The rock is dominated by K-feldspar and contain titanite and light green clinopyroxene, which is discontinuously mantled dark green hornblende.

Rock group: Contact granodiorite

Thin sections: 132410, 132411, 132414. No polished section were made for the contact granodiorites.

Main minerals: Quartz (40-50%), muscovite (15-20%), biotite (10-15%), garnet (5-10%), plagioclase (5-15%).

Accessory minerals: Chlorite, rutile, apatite, rutile

The contact granodiorite is fine to medium grained with a seriate texture with a mineral assemblage dominated by quartz, muscovite and biotite. Anhedral quartz have undulous extinction and irregular grain boundaries. The crystals range in size from <0,1 to 0,8, mm, where the smaller appear as subgrains. Minor myrmekite has developed along the grain boundaries of the quartz and is restricted to smaller patches of 0,4 mm. Anhedral plagioclase is medium grained

and contain needles of muscovite in addition to dark exsolution, which give the mineral a dusty appearance. Individual muscovite grains are either flaky or anhedral and poikilitic, with inclusions of quartz. They occur between the quartz and plagioclase grains and are often spatially associated with biotite (Fig. 5.41). The biotite is red-brown, but some places slightly green, and is both interstitial and lath shaped. Subhedral garnet is present in small abundances, and some are poikilitic, enclosing fine grained biotite and quartz (Fig. 5.41-C and D). Green chlorite, with anomalous blue interference colour, is present in one sample, where it occurs as an interstitial phase.

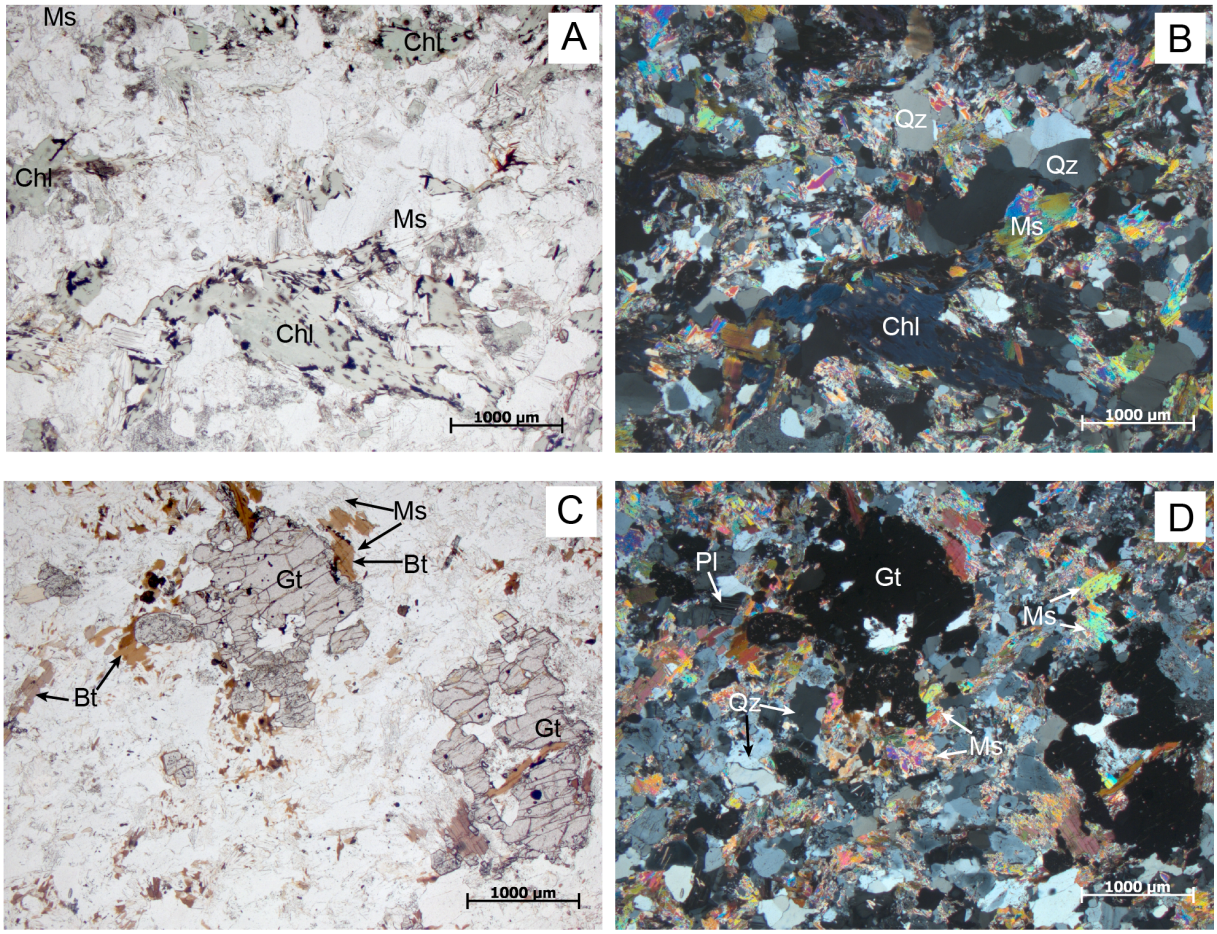

Figure 5.41: Photomicrographs of contact granodiorite. A) & B) Muscovite and quartz together with abundant chlorite in thin section 132410. C) & D) Garnet, biotite and muscovite in thin section 132414.

Chapter 6

Discussion

6.1 Petrogenesis of the Umbukta gabbro

Geochemical and petrographic studies of the Umbukta gabbro, as well as field observations from the study area, reveal that several differentiation processes may have been responsible for the formation of the Umbukta gabbro. The associated igneous rocks of the study area represent various rock types with a broad range of compositions. In the following sections, magmatic differentiation processes, which may explain the varieties of these igneous rocks, will be discussed.

6.2 Fractional crystallization

6.2.1 Whole-rock major element chemistry

Continuous trends in the whole-rock major element and trace element plots, imply that the rocks could be related by a process of fractional crystallization (Winter, 2010), which is particularly evident in the Harker plots 5.20. The negative correlation between silica and Fe_2O_3, MnO, TiO_2 and MgO reflects extraction of these oxides as the magma evolves. Depletion of MnO and MgO is consistent with progressive crystallization of olivine and pyroxene (Winter, 2010; Juteau and Maury, 1999) which are abundant in the olivine gabbros. Regularly, olivine gabbros display a cumulate texture in which olivine, and pyroxene to a certain degree, constitute the cumulus

phases. As olivine is absent in the more evolved rocks, including gabbro, this suggests that the olivine was likely removed by fractional crystallization from the evolving melt. Depletion of Fe_2O_3 and TiO_2 with increasing silica is consistent with fractionation of Fe-Ti-oxides such as ilmenite, which is present in most samples from olivine gabbros to felsic granitoids. There is an increasing trend in the CaO-plot, from 40 to 45 wt% silica, followed by a decreasing trend, where the peak could reflect the onset of clinopyroxene fractionation or Ca-plagioclase. Both Al_2O_3 and Na_2O display a positive trend up to 55% silica, followed by a negative trend. The peak marks the onset of fractionation of phases controlled by Al_2O_3 and Na_2O. Na-plagioclase, which is increasingly more abundant when going from olivine gabbros (An $>$ 34), through the mafic rocks, to felsic granitoid (An $<$ 97), may represent a phase responsible for the extraction of Al_2O_3 and Na_2O from the melt (Fig. 5.31). A positive correlation between SiO_2 and K_2O is expected for increasingly evolved rocks in a system subjected to fractional crystallization. As P is an essential structural component in the apatite, the scatter in the P_2O_5 plot for the mafic rocks may be related to variable proportions of this accessory mineral (Deer et al., 1992).

6.2.2 Whole-rock trace element chemistry

As REE patterns for igneous rocks are in part controlled by the chemistry of their source, the strong resemblance between the REE pattern for all mafic rocks, the monzonites and monzodiorites can be taken as an indication that these rocks are genetically linked to the same parental magma (Rollinson, 1993). The increased abundance of REE from the mafic rocks to the monzonites may reflect that these rocks represent more and less evolved melt compositions, respectively, as the abundance of REE in the melt are expected to increase with increasing silica content (Brophy et al., 2011). However, the felsic granitoids are depleted in REE relative to the monzonites and most of the samples show distinct positive europium anomalies, which may indicate accumulation of plagioclase (Winter, 2010). Particularly the syenite (sample 127973), shows very high concentrations of Sr and Ba (1200 ppm and 1370 ppm), known to substitute for K, which is consistent with the abundance of K-feldspar, observed in thin section (Best, 2003).

In the bivariate trace elements plots with Zr as the differentiation index, there appear to be continuous trends defined by the mafic rocks, the monzonites and monzodiorites. The felsic granitoids strongly deviate from these trends, due to very low concentrations of transition metals, REE and HFSE and generally high concentration of LILE, relative to the mafic and

intermediate rocks. The enhanced scatter in these plots, compared to the major element plots, may reflect the presence of accessory phases such as apatite (observed in ultramafic to felsic rocks) and zircon (observed in mostly intermediate and felsic rocks). These minerals can be extremely enriched in certain elements, which may obscure the effects produced by the major phases during fractional crystallization (Bea, 1996). As Zr is an essential structural constituent in zircon, even small concentrations of zircon may strongly elevate the Zr concentration of the whole-rock analyses (Hoskin and Schaltegger, 2003). The same applies for other elements that tend to concentrate in certain accessory minerals.

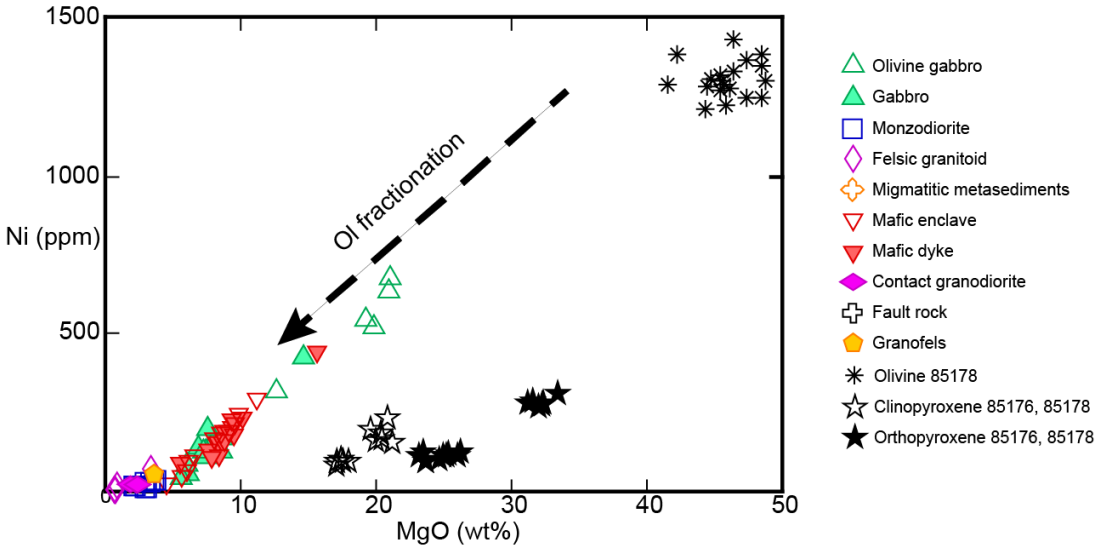

Figure 6.1: Whole-rock analyzes of mafic rocks show a strong positive correlation between Ni and MgO, moving away from olivine, indicative of olivine fractionation. Whole-rock compositions are obtained from XRF and olivine compositions are obtained from LA-ICP-MS.

In figure 6.1 and 6.2 mineral chemistry data from LA-ICP-MS have been combined with whole-rock data from XRF and LA-ICP-MS. Figure 6.1 illustrate olivine's strong control on the Ni content, where whole-rock analyses show a linear correlation between the Ni and MgO content. The fact that more evolved rocks plot successively further away from the composition of the analysed olivine crystals, give strong indications for removal of olivine from the evolving melt, by fractional crystallization.

A similar trend, however less pronounced, can be seen in figure 6.2, displaying the relationship between the Sc and MgO content. The figure illustrates that the range of Sc concentration in the mafic to intermediate rocks, are likely related to the removal of clinopyroxene from the evolving melt, by fractionation crystallization. Thus, selection of the fractionating assemblage for stage 1 in the fractional crystallization modelling were based on these findings.

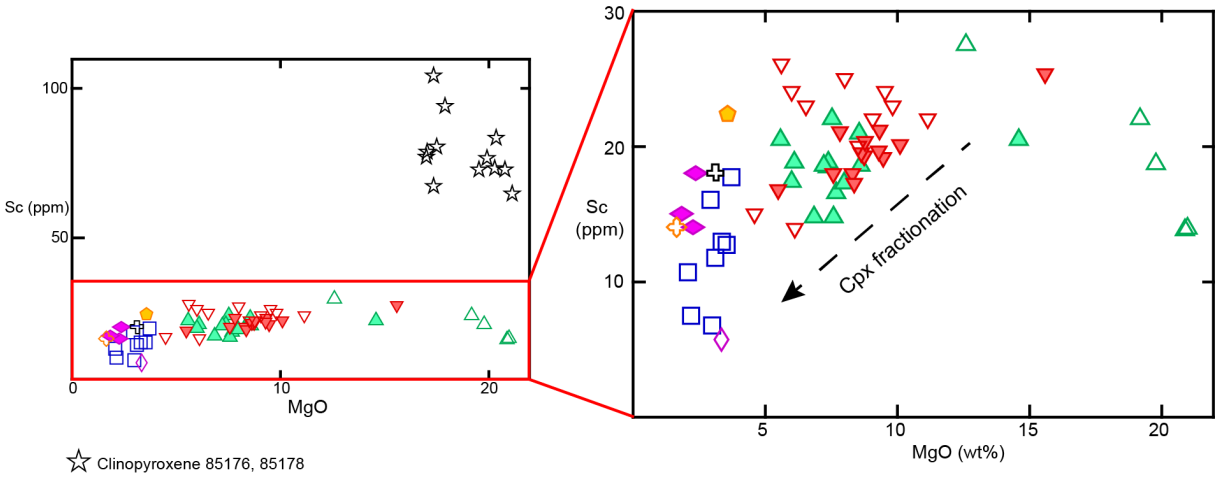

Figure 6.2: Whole-rock analyzes of mafic and intermediate rocks show a positive correlation between Sc and MgO, moving away from the clinopyroxene composition, indicating clinopyroxene fractionation. Whole-rock compositions are obtained from XRF and clinopyroxene compositions are obtained from LA-ICP-MS. See figure 6.1 for legend.

6.2.3 Fractional crystallization modelling

Based on the Harker and trace element plots, there are reason to believe that the range of compositions and continuous compositional trends may in part be explained by fractional crystallization. Thus, a residual melt composition produced by fractional crystallization have been modelled. The dyke chosen to represent the parental magma composition, sample 127956, was the second most mafic, fine grained sample, and exhibit moderate to high concentrations of Cr, Ni and MgO. Sample 127995 is an ultramafic dyke with primitive magma compositions, but it has slightly higher concentrations of Zr (169 ppm compared to 142 ppm in sample 127956) which made it impossible to reproduce the trend defined by the mafic rocks, by modelling. Modelled trace element concentrations of the restite melt was obtained from the equation for Rayleigh fractionation (Eq.3.5), where C_L represents the concentration of a certain element in the melt. The modelled concentrations which gave the best correlation with observed trends are plotted together with the whole-rock data from XRF and LA-ICP-MS in chondrite normalized REE plots (Fig. 6.5) and in bivariate trace element plots with Zr as the differentiation index (Fig. 6.3 and 6.4). The fractionating assemblage and the amount of crystallization for each stage is presented in the figures.

The modelled trends for Cr, Ni, Co and Sc versus Zr show a good correlation with the mafic rock analyses and display steep declining trends, reflecting fractionation of olivine (mostly Ni and Co) and pyroxene (mostly Cr and Sc) during the first and second stage (Hollings and Wyman,

2005; Foley et al., 2013). This is supported by high mean concentrations of Ni and Co in olivine ($Ni_{1305}Co_{231}$ in ppm), high mean concentrations of Cr and moderate concentrations of Ni, Co and Sc in clinopyroxene ($Cr_{1979}Ni_{142}Co_{39}Sc_{78}$ in ppm) and moderate concentrations of Cr, Ni, Co and Sc in orthopyroxene ($Cr_{327}Ni_{179}Co_{76}Sc_{34}$ in ppm), obtained from LA-ICP-MS analysis.

Sharp peaks are characteristic for the modelled trends of Nb and V, and represent the transition between different stages in the modelling. As V is strongly included in oxide minerals, but rarely included in silicate minerals, the melt concentration of V is generally controlled by fractionation of oxides (Jang et al., 2001). Ti-rich phases such as ilmenite tend to accommodate both Nb and V (Green and Pearson, 1987; Best, 2003). Thus, the change from a positive to a negative slope for these elements, may reflect the beginning of fractionation of ilmenite, which is present in thin sections from ultramafic to felsic rocks in decreasing abundances. The distinct depletion of Ti in the MORB-normalized spider diagram for monzonite and monzodiorite (Fig. 5.22) may reflect that these rocks crystallized from the restite melt after most Fe-Ti oxides was removed by fractionation.

The concentration of Ba is generally controlled by the abundance of K-feldspar, whereas Sr is controlled by plagioclase (Severs et al., 2009; Best, 2003). Neither modelled concentrations of Ba or Sr gave a good fit. As Sr and Ba are regarded as mobile elements, the concentration of these elements may not represent the original igneous composition if the rocks have been subjected to alteration (Rollinson, 1993; Hastie et al., 2007).

Amphibole and ilmenite may influence the Y concentration with Kd of 1,47 and 1,6, in the trace element modelling. However, small concentrations of assumed igneous amphibole and ilmenite were present in thin section. Apatite, which are present in most mafic and intermediate rocks in the study area, commonly accomodate Y, although the concentrations may vary (Bea, 1996). If apatite saturation was reached at the beginning of stage two, fractionation of apatite could have explained the inclined positive trend defined by the mafic and intermediate rocks Y plot. Garnet occur in gabbros and more commonly in monzodiorites from the study area. It was included in the modelling to test whether garnet is likely to represent a fractionating phase. The resulting pattern (Fig. 6.5-B) show that even when garnet is present in small amounts (stage 2: 5 %, stage 3: 4 %) the HREE is strongly depleted, which is not consistent with the observed trends. Thus, garnet is highly unlikely to be a magmatic phase. When excluding garnet, however, the modelled REE pattern provide a very good correlation with the composition of monzodiorites

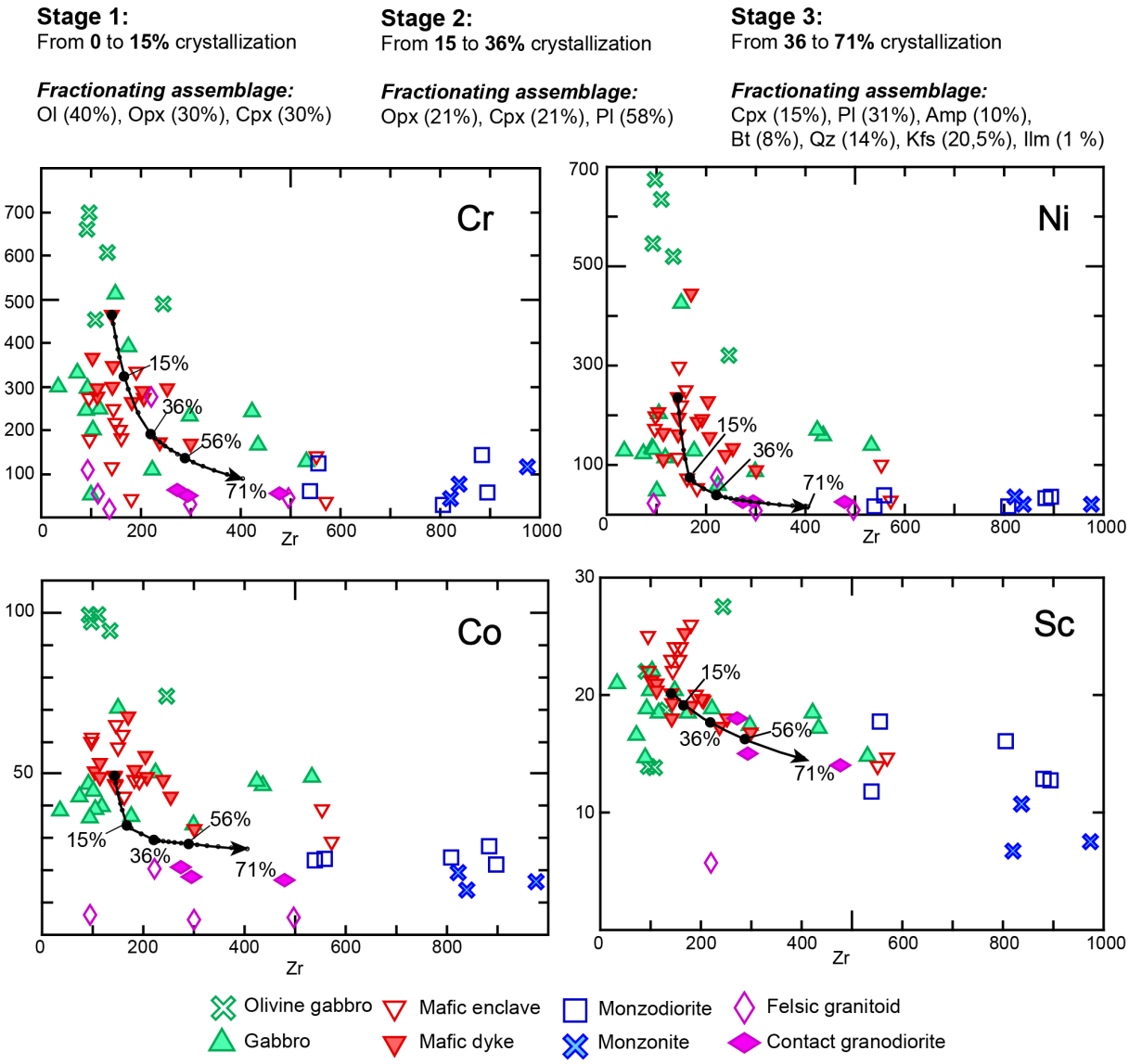

Figure 6.3: Modelled trend (black line) plotted together with whole-rock data obtained from XRF and LA-ICP-MS for all igneous rocks. The arrow indicate the direction of fractional crystallization and black dots along the modelled trend indicate the concentration in the melt at various % of fractional crystallization. 15% is the last step of stage 1, 36% is the last step of stage 2, whereas stage 3 involves up to 71% fractional crystallization.

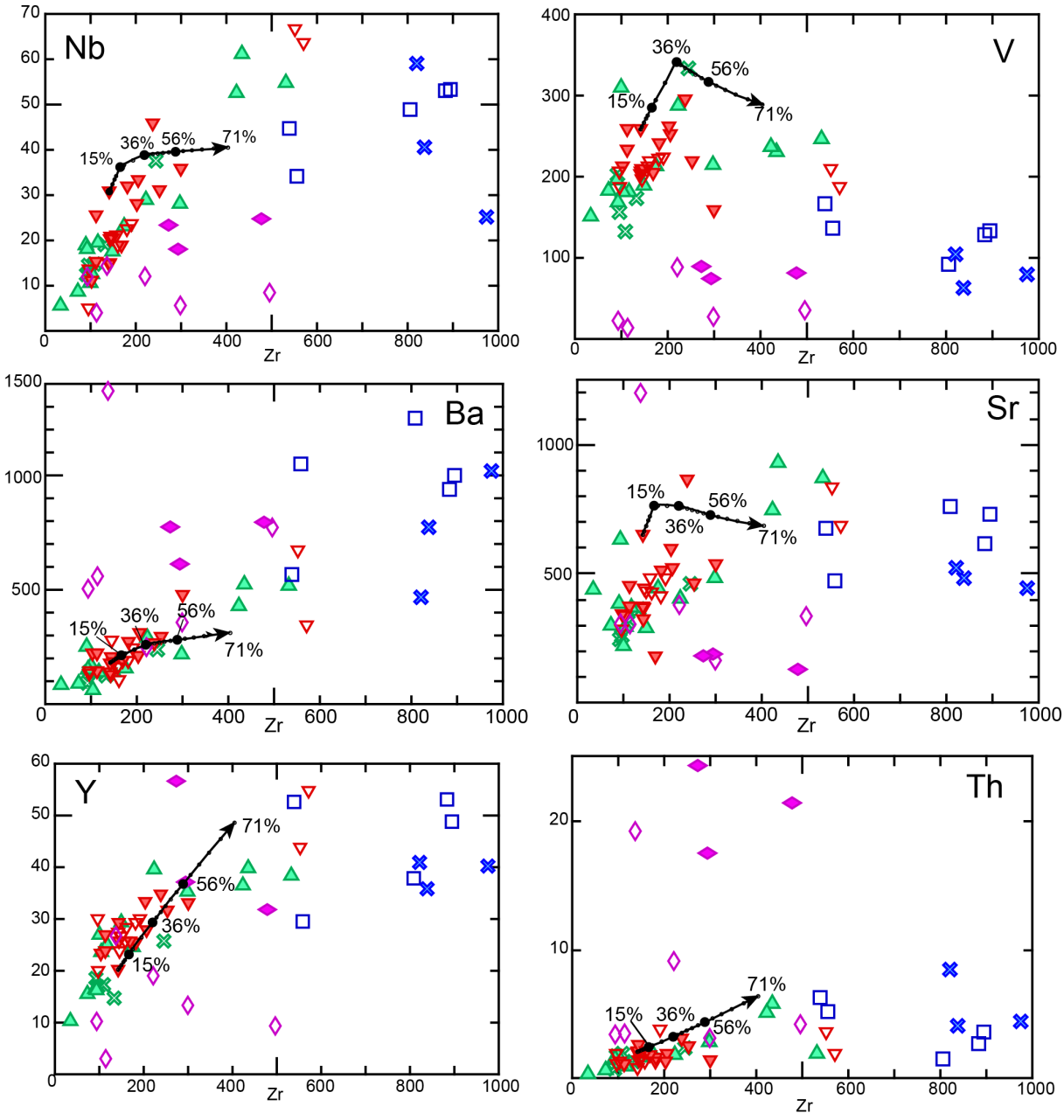

Figure 6.4: Modelled trend (black line) plotted together with whole-rock data obtained from XRF and LA-ICP-MS for all igneous rocks.

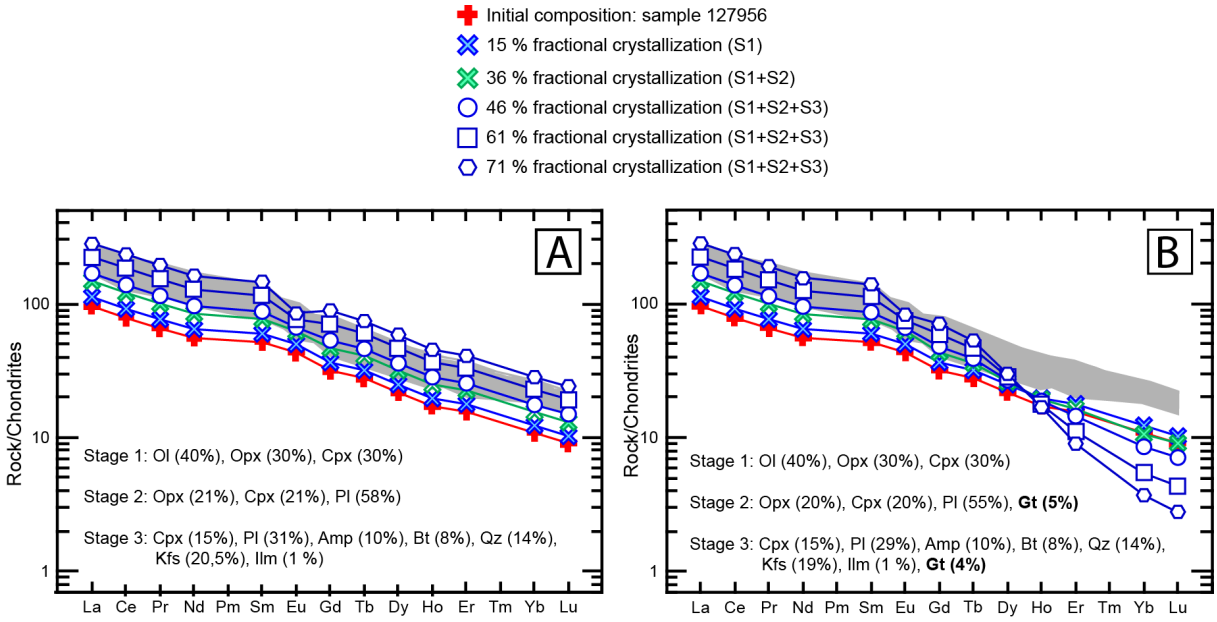

Figure 6.5: Chondrite-normalized REE diagram showing the modelled composition of residual melts produced by fractional crystallization compared with the the assumed parental magma (red line) as well as the composition of the monzonites and monzodiorites (shaded area). Normalization values are from Sun and McDonough (1989). S1 = stage 1, S2 = stage 2 and S3 = stage 3. The fractionating assemblage for each stage is given inside each diagram. A) REE diagram displaying the modelled trend which gave the best fit to the REE-trend for the monzonites and monzodiorites. B) Garnet is included in stage 2 and 3, to test if garnet is likely to be a part of the fractionating assemblage. Note how the modelled HREE strongly deviates from the trends from monzonites and monzodiorite analyses.

and monzonites between 55 and 71 % fractional crystallization. Composition of contact granodiorites deviate from both modelled and observed trend, which strongly suggest a different source and evolution for these rocks. This will be further discussed in section 6.3.

The results from the trace element modelling are slightly ambiguous. REE patterns for the modelled melt composition show that compositions very similar to the monzodioritic rocks can be produced by 55 to 71 % fractional crystallization. In the bivariate plots, on the other hand, the modelled trend cover only the mafic rocks, whereas the intermediate rocks and the felsic granitoids, in particular, are more difficult to attain by modelling, which may suggests that fractional crystallization is responsible for the compositional variation in the mafic rocks. The best trends were seen in the plots for transition metals, implying that removal of major phases such as olivine and pyroxene by fractional crystallization was an important process in differentiating the magma. Trends for elements controlled by minor and accessory phases cannot be easily recreated by modelling, which is expected.

In order to obtain the compositions of the monzonites and monzodiorites by modelling, the concentration of Zr must be strongly elevated. The monzonites and monzonites are strongly

enriched in Zr with concentrations of 537-975 ppm, whereas the felsic granitoids display Zr levels of only 4-15 ppm. In comparison, the concentration in typical crustal rocks is approximately 100-200 ppm, where most of it is contained in zircon (Taylor and McLennan, 1985; Bea et al., 2006). Zircon were observed in thin section, although they occurred in small abundances. However, the accumulation of zircon may strongly influence the REE pattern as zircon tends to accommodate high concentrations of HREE (Hoskin et al., 2000; Bea et al., 2006). Therefore, it is considered unlikely that zircon accumulation is the main cause of the elevated Zr levels. It has been shown that high concentrations of Zr may occur in minerals such as titanite, ilmenite, rutile, amphibole and garnet (Bea, 1996) which are all present in mafic rocks from Umbukta. According to (Kamber and Collerson, 2000) the maximum possible degree of enrichment in Zr through fractional crystallization may be calculated from the equation of Rayleigh fractionation, where D_i is set to zero, in which case the formula can be simplified to

$$C_L = \frac{C_0}{F} \tag{6.1}$$

For an initial concentration, C_0, of 142 ppm Zr (sample 127956 used in the modelling) and a remaining liquid fraction, F, of 0,15 (85 % fractional crystallization) the maximum possible enrichment is $\frac{142}{0,15}$ = 947 ppm, which roughly correspond to the concentration of the monzonites and monzodiorites. Another possible explanations for the elevated Zr levels, may be that monzodiorites and monzonites experienced interaction with Zr enriched crustal material, at depth. As the primary igneous contact along the south-western border is not exposed, due to the presence of a tectonic contact, there is little information of the interaction between the host rock and the gabbro in this area, making it difficult to conclude upon the source of the Zr enrichment.

There are several pitfalls related to trace elements modelling, including: variation in published partition coefficients, the assumption that investigated rocks represent melt composition and the effect of accessory phases (Slagstad, 2003). While this method is based on the assumption of perfect fractional crystallization, textural observations imply that other processes operated simultaneously. The presence of poikilitic plagioclase and interstitial plagioclase, amphibole and biotite in the olivine gabbros imply that some liquid was trapped between the cumulus crystals and eventually crystallized to form plagioclase, biotite, amphibole. If magmatic liquid is trapped between cumulus crystals, incompatible trace elements (with Kd < 1) become increasingly more enriched in the trapped liquid (Jackson, 1961). As the cumulus minerals continue

to grow from the intercumulus melt, they will acquire increasingly higher concentrations of incompatible elements (Paster et al., 1974). The modelling is also based on the assumption that the igneous analyzed rocks represent melt composition. Most of the mafic dykes and enclaves are fine grained, and are thus good candidates, but some are slightly porphyritic, reflecting they have experienced some degree of crystal accumulation, which may affect the chemistry, particularly the trace element concentrations.

6.3 Mingling and mixing

Evidence for mingling and minor mixing is mostly constrained to the western and northern margin of the gabbro. However, the appearance of the felsic end members in the respective areas, are distinctly different in terms of chemical signature, composition and texture.

6.3.1 Felsic granitoids along the western margin

Along the western margin of the gabbro mingling occurs between various igneous rocks, with a predominance of mafic rocks. Where mingling occur between mafic and a dioritic rock containing abundant feldspar phenocrysts, the mafic enclaves appear to have inherited feldspar phenocrysts (Fig. 5.3-A and B). A gradual transition from felsic granitoid to intermediate rocks suggest that mixing occurred, at least at a small scale (Fig. 5.12-A). The presence of rounded to irregular, mafic pillows enclosed in a felsic to intermediate rocks, point to the co-existence of a felsic and mafic magma. Yet, the mostly sharp contacts between them suggest that mixing was inhibited by a large property contrasts between the melts (Kokfelt et al., 2015). Magmatic breccia, observed as angular mafic enclaves enclosed in leucocratic felsic rocks, is present at the south-western margin of the gabbro. Their occurrence could be related to overpressure during intrusion of the mafic magma, or that the felsic melts intruded when the mafic melt was partly solidified (Best, 2003). The origin of the felsic granitoids is not certain, but their calc-alkaline signature (Fig. 5.19) imply they were likely derived from a mixed origin of both mantle-derived and crustal components (Barbarin, 1999). Similar features are observed in the trace element patterns for the felsic granitoids and the metasedimentary host rock(figure 5.22-B), such as distinct Nb-Ta, P and Ti troughs, which is indicative of crustally derived rocks (Kirsch and Svenningsen, 2015).

The rocks which are denoted diorite in the field descriptions, are found along both the western and the northern margin. However, the samples analysed for major and trace element chemistry were aquired only from the western margin and these are classified as monzonites and monzodiorites, based on chemistry. Trace element patterns for monzonites and monzodiorites lack the distinct Nb-Ta anomaly, but show pronounced P and Ti anomalies similar to the host rock and the various felsic rocks (figure 5.22-A). They can mostly be characterized by abundant garnet, even though some are completely garnet-free. Regularly, garnet is evenly distributed in the rocks, while they are accumulated along margins of mafic enclaves in others. Barnes et al. (2012) found that mixing between a dioritic and a granitic magma may result in a garnet-bearing hybrid rock, in a system that is not too different from Umbukta. To verify or reject the hypothesis that garnet stability was promoted by mixing, more extensive studies of mineral chemistry would be required. In some of the major element plots, the monzonites and monzodiorites plot directly between the mafic rocks and the felsic granitoid. However, the break point observed in the Harker plot for Al_2O_3, CaO and Na_2O, rule out mixing between the felsic and mafic rocks of the study area as a likely mechanism forming the monzonites and monzodiorites. Neither are they likely to be a product of mixing between mafic rocks and contact granodiorites, as the latter regularly plot between the mafic rocks and the monzodiorites.

6.3.2 Contact granodiorites at Austre sauvatnet

Along the northern margin of the gabbro, there is a 200-300 m wide zone (north to south), extending in the east-west direction, with field evidence of substantial interaction between the gabbro and the metasedimentary host rock. The zone is characterized by the presence of metasedimentary xenoliths and abundant contact granodiorite, which is commonly seen mingling with mafic, fine grained material. Observations of stromatic migmatite, and undulating contacts of mafic dykes cutting the metasediments, indicate that the host rock was ductile when the gabbro intruded. Interfingering between leucosomes in the migmatitic metasediment and the granodioritic rock (Fig. 5.17), containing abundant metasedimentary xenoliths, suggest that the contact granodiorite formed as a result of anatexis. The peraluminous character of the contact granodiorite (Fig. 5.19) and their abundance of muscovite, which is characteristic of S-type granites, support this interpretation (Chappell and White, 2001; Barbarin, 1996). MORB-normalized trace element patterns for the contact granodiorites are almost identical to the trace element

patterns of the metasedimentary host rock, which emphasize their genetic relationship (figure 5.22-C).

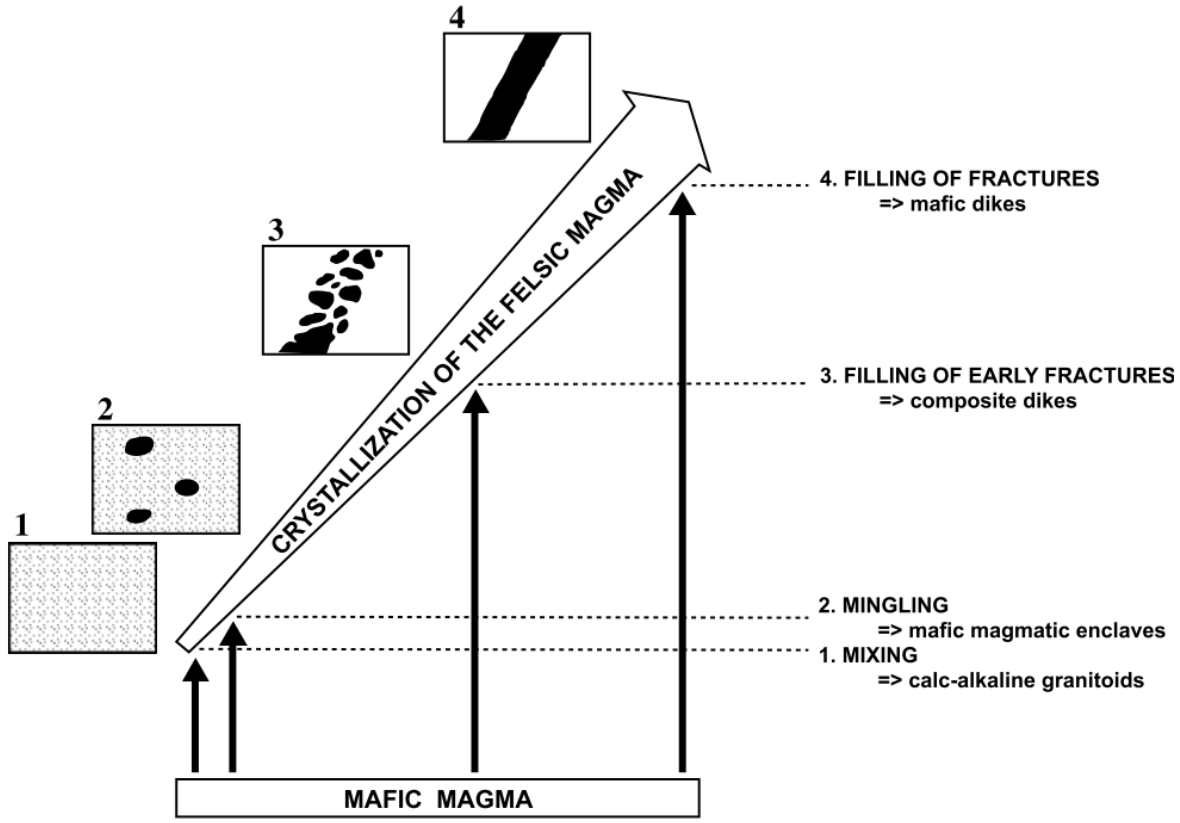

Figure 6.6: Sketch of the various types of hybridization processes resulting from intrusion of mafic magma into granitoid magma at various stages of crystallization of the latter. From Barbarin and Didier (1992)

The northern contact zone display individual mafic pillows, abundant composite dykes, which occur alongside and are sometimes crosscut by undisrupted mafic dykes with parallell margins (see Fig. 5.7). Barbarin and Didier (1992) proposed that the various appearances of mafic rocks intruded in granitoid rocks, depend on the degree of crystallization of the granitoid. This relationship is illustrated in figure 6.6. According to Barbarin and Didier (1992), the field observations along the northern contact zone favours injection of mafic magma at different degrees of crystallisation of the felsic magma. This implies that mafic pillows represent intrusion of mafic magma into molten granodiorite, the composite dykes represent mafic magma intruding a slightly cooler granitoid magma and eventually mafic magma were injected in a more or less completely crystallized granitoid represented by the mafic dykes with parallell margins. As dioritic rocks were observed regularly in the contact zone, these intermediate rocks may in fact be the result of mixing between mafic melts and crustal melt derived from partial melting of

host rock. However, sampling and chemical analyses would be required to be able to conclude whether these dioritic rocks have a similar composition as the monzodiorites and monzonites and whether they are the result of hybridization.

6.4 Assimilation

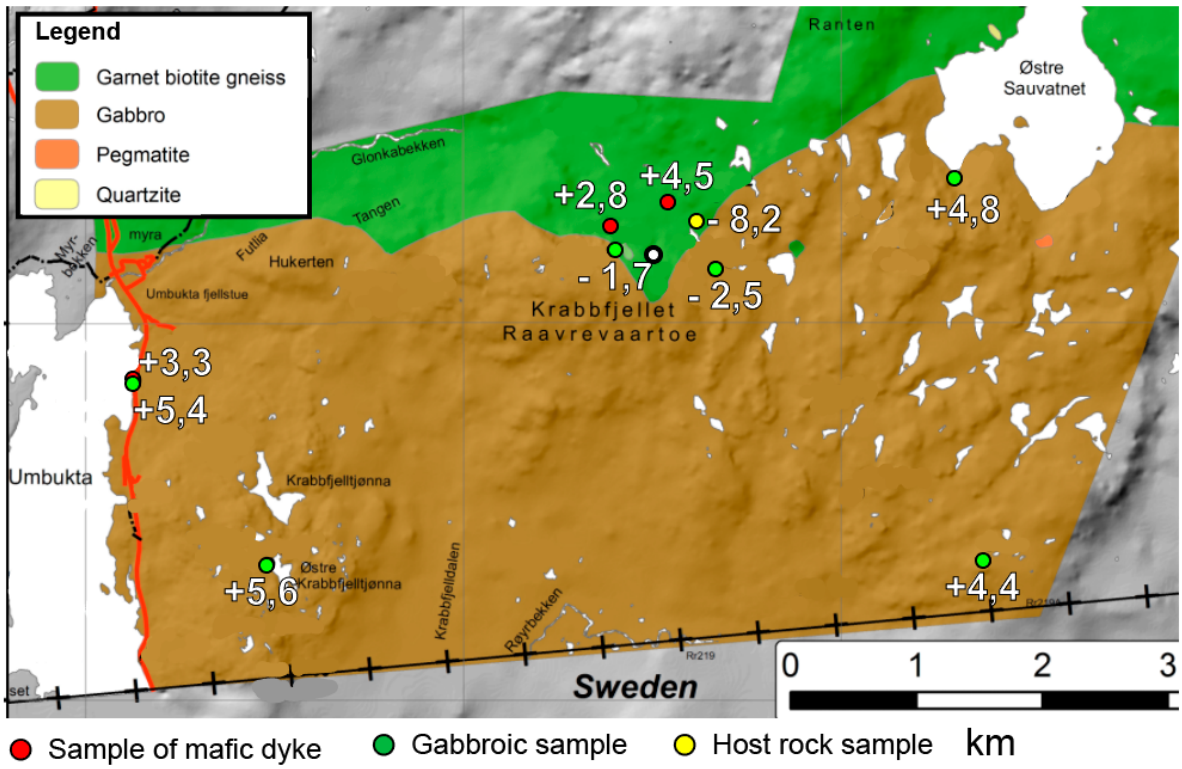

Figure 6.7: On the map of the Umbukta gabbro, the position of samples analyzed for Sm-Nd isotopic compositions are indicated with their respective ε_{Nd} values written in white text, on map from Høyen (2016).

The host rock of the Umbukta gabbro are composed of crustal rocks, including garnet biotite gneiss and quartzites in the north (Høyen, 2016). This is favourable when investigating the degree of assimilation, as crustal rocks exhibit distinctly different isotopic compositions compared to mantle derived, mafic rocks (DePaolo, 1988). Most of the mafic rocks (gabbros and mafic dykes) analyzed for Sm-Nd isotopic compositions, display positive ε_{Nd} values, but the gabbroic samples P6.3 and P5.2 have ε_{Nd}-values of -2,5 and -1,7. Th, an element strongly enriched in the continental crust relative to the mantle and oceanic crust (Winter, 2010), show a negative correlation with ε_{Nd} in figure 5.35, while there is a positive correlation between Mg# and ε_{Nd}. In both diagrams the gabbroic samples P6.3 and P5.2 plot on a line directly in between the host

rock and the other gabbros (Fig. 6.7). This correlation strongly suggest that interaction with the host rock is responsible for the negative and ε_{Nd} values in the gabbroic rocks. Figure 6.8 shows that the trace element pattern for these samples can be distinguished from the remaining rocks by distinct enrichment of incompatible trace elements, particularly the LILE, followed by a troughs for Nb-Ta and negative anomalies of P and Ti, implying they were subjected to contamination of a crustal component (Ernst et al., 2005; Li et al., 2000). Even small amounts of contamination may strongly enhance the concentration of elements such as K, Rb and Th, because their concentrations are distinctly higher in crustal rocks compared to tholeiitic basalt and due to their incompatible nature, which make them partition into melt at small degrees of partial melting (DePaolo, 1981).

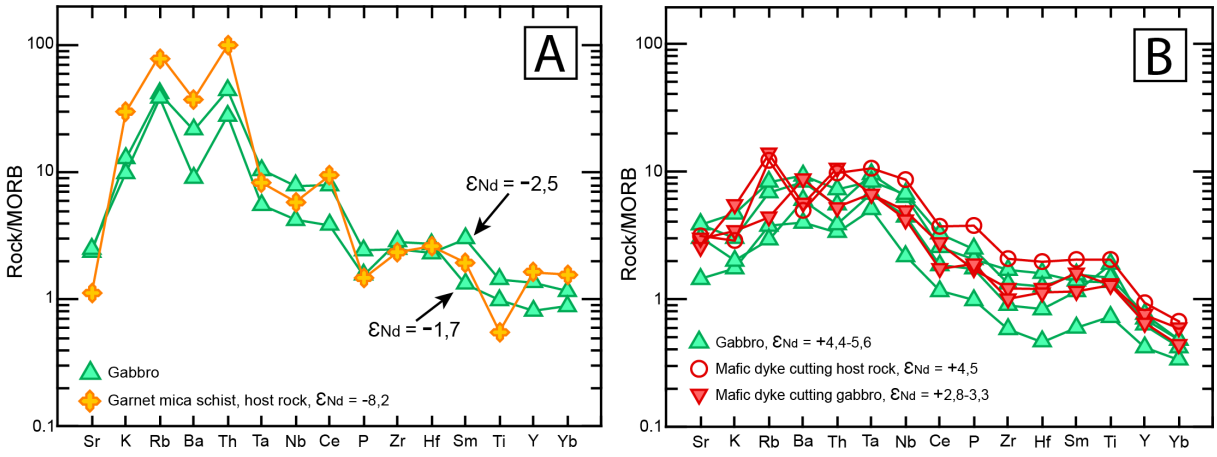

Figure 6.8: MORB normalized trace element patterns for samples analysed for Sm-Nd isotopic compositions. A) The gabbroic samples, P5.2 and P6.3, which show negative ε_{Nd} values, are plotted together with the host rock. Note the similarity between the trace element patterns. B) Samples which showed positive ε_{Nd}-values show very little enrichment in LILE.

The rocks displaying negative ε_{Nd} values also stand out in terms of major element chemistry, with a more felsic composition (SiO_2 = 55,1 and 58,4 wt%, MgO = 3,9 and 4,02 wt %) compared to the samples displaying positive ε_{Nd} values (SiO_2 = 45,4-49,4 wt%, MgO = 7,1-18,9 wt%). This is also consistent with chemical interaction between a basalt and continental crust (Juteau and Maury, 1999). Sample P5.1, mafic dyke cutting the host rock, also show a more felsic composition (SiO_2 = 57 wt%, MgO = 5,66 wt%) and exhibit the lowest positive ε_{Nd} value (+2,8), implying that some interaction crustal material may have occurred.

Figure 6.7 show the location of the samples analyzed for Sm-Nd isotope compositions, where the ε_{Nd} values are denoted in white text. The map show that the gabbroic samples displaying negative ε_{Nd} values are located very close to the intrusive contact towards the host rock, whereas

the gabbroic samples displaying positive ε_{Nd} values are all but one located much further away from the contact. Observations of host rock xenoliths along the northern margin appear to decrease gradually southwards and disappear at a distance of 1 km from the margin, indicating that assimilation mainly affected the northern margin of the intrusion, whereas the interior remained unaffected. The 10x5m large xenolith, observed 1 km south of the northern margin, may have represented a stoped block as it was cut by parallell mafic dykes, suggesting a piece of metasediment loosened from the roof of the magma chamber after being intruded by dykes.

Samples from the two mafic dykes (P5.1 and MO 28770) cutting the host rock show positive ε_{Nd} values (+2,8 and +4,5). Crustal contamination of mantle-derived magmas mainly takes place in large magma chambers, where latent heat is released from fractional crystallization (Bowen, 1928; DePaolo, 1981) and residence time for the magma is long. Magma which rises through dykes, forcing aside country rocks, have low heat capacity and will crystallize fast. Thus, it is expected that these dykes will be subjected to a limited amount of assimilation (Philpotts, 1990). Sample (P9.4), described by Høyen (2016) as a medium grained, heterogenous gabbro, was also located very close to the margin of the pluton (Fig. 6.7), but based on the ε_{Nd}-value (+4,8) and trace element composition (Fig. 6.8B) it did not show any signs of contamination. The lack of detailed field descriptions make it difficult to conclude, but there is a chance that this gabbro represent a batch of magma which intruded at a later stage, where the heat required for assimilation was absent (DePaolo, 1981).

Of the samples analysed for Sm-Nd, sample P6.3 is the most enriched in REE and exhibit the lowest ε_{Nd}-value of the all the mafic samples (-2,5), implying there could be a correlation betweeen REE-concentration and assimilation. Thus, the REE variations seen in the gabbroic and mafic rocks may be attributed to various degrees of assimilation. In general, the trace element chemistry of the olivine gabbros, olivine-free gabbros, mafic enclaves and dykes do not appear to be strongly influenced by crustal contamination: The samples are slightly enriched in LREE and show no signs of negative Nb, Ta and Ti anomalies (Ernst et al., 2005; Li et al., 2000). However, three gabbroic samples, acquired during this thesis, show distinct enrichment in incompatible trace elements, up to 30 times MORB, and enriched LREE patterns with a mean La/Sm_N = 1,8 (Fig. 5.21-A and B). Although there are no marked Nb-Ta or Ti anomaly, the samples show similar chemical features as the rocks that display negative ε_{Nd} values. Common for all three samples is that they are located very close to the margins of the gabbro (sample 127963 along the western and sample 127979 and 127980 along the southern.) The elevated

trace element concentrations may be related to contamination, but may also be related to variable enrichment in the source region of the gabbro. Due to the compatible nature of Ti, Y and Yb, these elements will not partition from the crust into the melt, and thus do not modify the original basalt pattern (Winter, 2010).

The monzonites and monzodiorites on the other hand, display very similar trace element patterns as the rocks with a distinct crustal isotopic signature (P6.3 and P5.2). This includes strong enrichment in incompatible trace elements, particularly LILE (K, Rb and Ba) and Th, negative P anomaly and small relative depletion of Ti, Y and Yb. In addition, the silica content is quite high (52-58,2 wt%) for the monzonites and monzodiorites, similar to the rocks with crustal isotopic signatures (sample P5.2 and P6.3). The monzonites and monzodiorites acquired along the south-western contact contain xenoliths composed of calc-silicates with abundant diopside and garnet. Therefore, it appears likely that the monzodiorites exhibit a crustal component, even though the observed number of xenoliths are few. In fact, in the contact zone along the northern margin, the presence of xenoliths appear to decrease in the contact zone when moving from the metasediments and into the gabbro, even though the mingling persists. Thus, host rock xenoliths may have been present further west, either in the lake of Umbukta or at the other side. Few observations of these intermediate rocks more than 500 m east of the road along the western margin support the hypothesis that the monzonites and monzodiorites were a product of interaction between the gabbro and the host rock. To verify this interpretation, isotopic studies of these rocks with associated detailed sample descriptions are required.

For the medium grained gabbroic rocks, there appear to be some correlation between ε_{Nd} values and the distance to the northern intrusive contact to the host rock. ε_{Nd} values combined with trace element composition of rocks acquired during this thesis suggest that contamination was constrained to the margins of the pluton. This is further supported by the observations by (Høyen, 2016) and (Sneltvedt, 1981) who reported the presence of host rock xenoliths up to 1 km from the northern margin. If assimilation occurred at greater depths than at the level of exposure, a correlation between contamination and distance to the intrusive contacts would be unlikely, and contaminated rocks would be distributed in a more random fashion. Based on the available data, it appears as though assimilation occurred close to or at the level of exposure.

6.5 Tectonic and magmatic setting

The assignment of a tectonic setting to a suite of igneous rocks, cannot be based on tectonic discrimination diagrams alone, but should be based on all geochemical data as well as other geological information (Li et al., 2015). In figure 6.10 and 6.9 the mafic enclaves and dykes from Umbukta are plotted in various tectonic discrimination diagrams. As the mafic dykes and mafic enclaves are mostly fine grained, they correspond more closely to the composition of the melt, than the more coarse grained and porphyritic rocks, which are likely to be derived from a magma that has experienced crystal accumulation (Best, 2003). Considering the various tectonic discrimination diagrams in figure 6.9 and 6.10, there are implications for a within plate setting, which is supported by the lack of negative Nb and Ta anomalies (Li et al., 2000). The data also plot in the fields for continental basalts and continental rift alkaline basalts in figure 6.10.

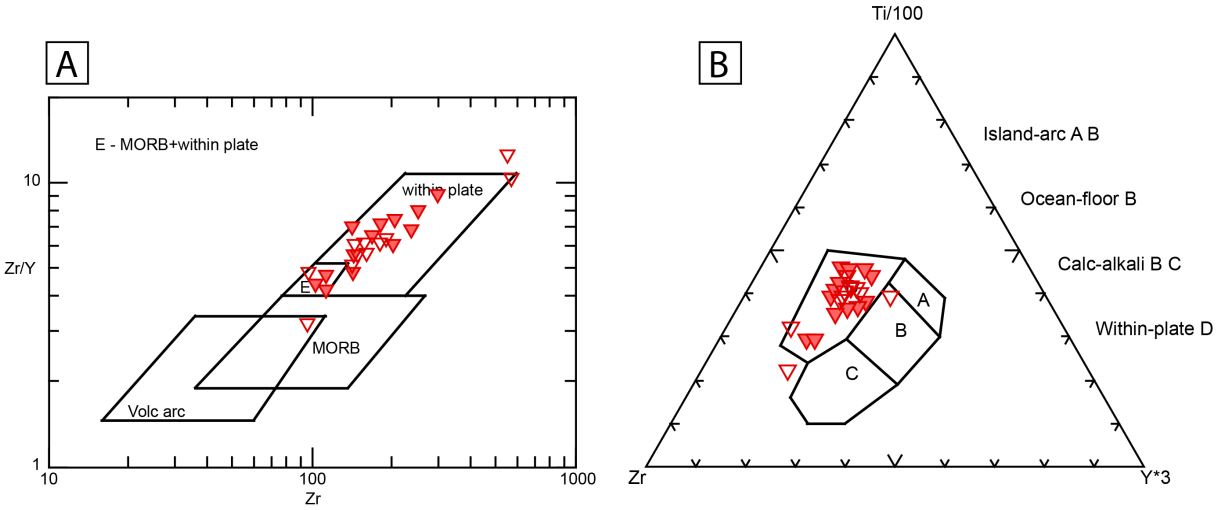

Figure 6.9: A) Zr/Y versus Zr binary discrimination diagram from Pearce and Norry (1979). B) Zr-Ti-Y discrimination diagram from Pearce and Cann (1973). The data from the fine grained mafic dykes and enclaves are mostly constrained to the within-plate field in both diagrams.

Based on the AFM diagram (Fig. 5.18) and the Zr-Nb-Y by Meschede (1986) the mafic and gabbroic rocks exhibit a tholeiitic signature, related to the enrichment of Fe relative to Mg. Such magmas are water-poor and evolve under low oxygen fugacities, resulting in late crystallization of Fe-Ti oxides. Thus, the concentration of Fe and Ti is increased in the successive liquids before crystallization (Juteau and Maury, 1999). Tholeiitic rocks are commonly related to widespread magmatism in extensional settings (Marzoli et al., 1999) and makes up most of the oceanic crust produced at oceanic spreading ridges (MORB: Mid Ocean Ridge Basalt) (Best,

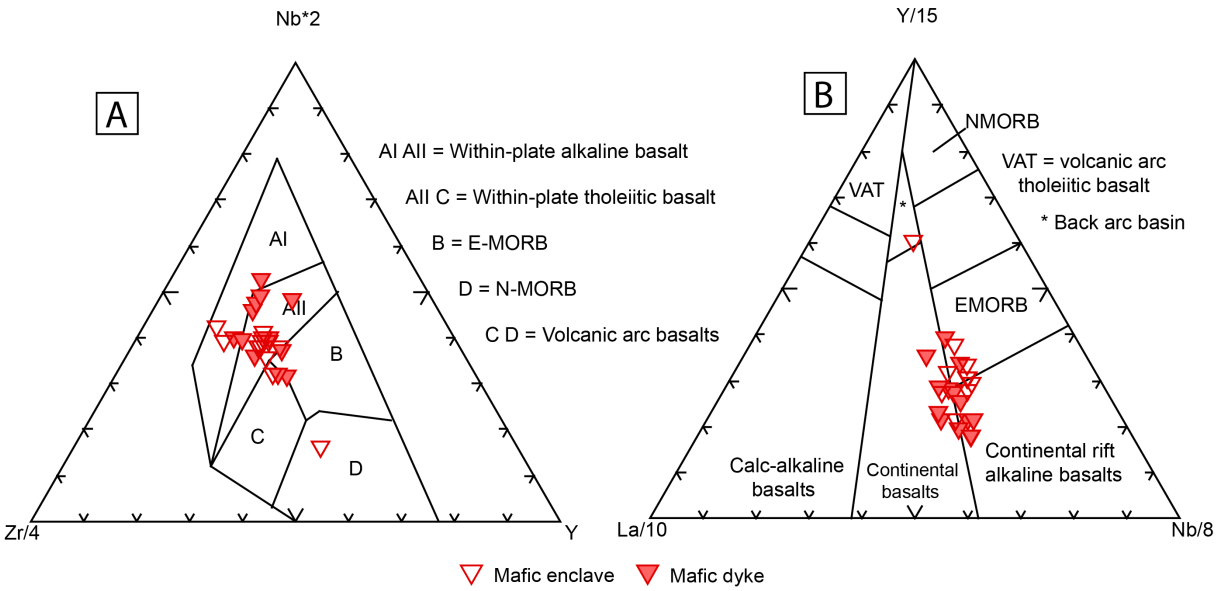

Figure 6.10: A) Zr-Nb-Y discrimination diagram from Meschede (1986). The data plot in the fields for within-plate tholeiitic basalt and within-plate alkaline basalt, except for one sample that plot in the N-morb field B) Th-Hf-Ta discrimination diagram from Cabanis (1989). The data straddle the division line between the field for continental basalts and E-MORB/continental rift alkaline basalts.

2003). Many large igneous provinces, such as the Skaergård intrusion, Bushveld complex and Sept iles, are largely composed of tholeiitic rocks (Namur et al., 2010).

The mafic rock rocks of Umbukta are strongly enriched in all trace element, except Y and Yb, with respect to MORB (Fig. 5.21). The enriched LREE relative to HREE are typical of both ocean island and continental basalts (Henderson, 1984). In fact, the REE abundances of the mafic rocks in Umbukta strongly resemble those seen in ocean island basalts (OIB), which is illustrated in figure 5.21. This pattern is typical of melts generated from relatively undepleted mantle in intraplate settings (Winter, 2010).

Chilled margins, or a finer grain size observed at the margins of dykes, is a common feature for dykes which have been emplaced into cool country rocks (Huppert and Sparks, 1989). There are few dykes in the study area which exhibit a finer grain size along the margins, and from the dykes that do, this can probably be ascribed to accumulation of phenocrysts a few cm from the margin, rather than fast cooling. However, the predominantly parallel and sharp margins between gabbro and mafic dykes, between some contact granitoid rocks and mafic dykes and between individual dykes in the contact zone, may indicate that the dykes crystallized relatively fast, suggesting emplacement at higher levels in the crust. Another possibility is that the timespan between increments of mafic intrusions were long enough for previously emplaced magma to crystallize before they were intruded by new magma. The fact that parts of the intrusion have

been affected by crustal assimilation may have implications for the level of emplacement. As the potential for assimilation is greatly reduced going from the middle to upper crust, as the country rocks are cooler, this points to emplacement at possibly medium-upper crustal depths (Tegner et al., 2005). However, to be able to constrain the emplacement depth, more detailed studies of the contact aureole would be advantageous.

The ratio $(Tb/Yb)_N$, which is plotted against Mg# in figure 6.11, can be used to depict depth of partial melting. Due to garnets strong preference for the HREE, melts in equilibrium with garnet will exhibit high Tb/Yb values (Kingsbury et al., 2016). A $(Tb/Yb)_N$ ratio of $>$ 1,8 is interpreted to indicate melting under garnet stability, whereas $(Tb/Yb)_N < 1{,}8$ is interpreted to indicate melting under shallower (<75km) spinel lherzolite (Wang et al., 2002). Analyses from mafic dykes and enclaves from Umbukta, show $(Tb/Yb)_N$ ratios $>$ 1,8, implying they were derived from partial melting under garnet stability, corresponding to a depth of $>$ 75 km (Wang et al., 2002).

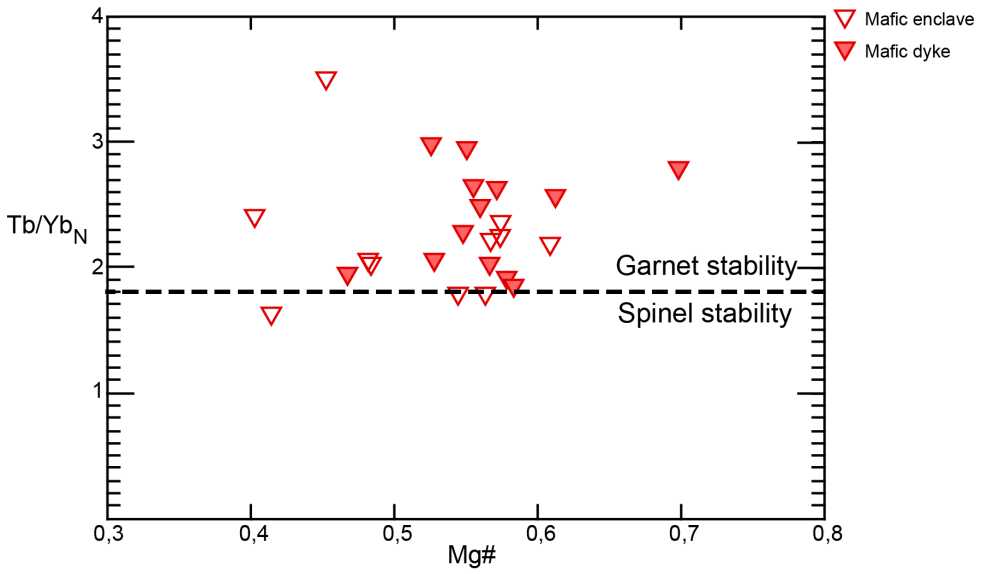

Figure 6.11: Tb/Yb vs Mg# for fine grained igneous rocks, mafic dykes and mafic enclaves. Chondrite normalized values from (Sun and McDonough, 1989)

The discrimination diagrams and trace element plots strongly suggest that the rocks were produced in a within-plate setting from a relatively enriched mantle. The high abundance of mafic dykes in the study area, is consistent with the formation in an extensional environment (Kingsbury et al., 2016). The fact that enrichment of incompatible elements is also seen in the fine grained mafic rocks, with little ability to assimilate, support the interpretation that the parental magma was derived from an enriched mantle source from quite large depths.

6.6 The role of alteration and metamorphism

Few primary igneous textures are preserved in the Umbukta gabbro and the associated igneous rocks. As the intrusion is interpreted to be a part of the Uppermost Allochton, a far travelled unit in the Scandinavian Caledonides, it is highly likely to have been affected by regional metamorphism. Most samples have experienced secondary alteration, including sericitization, extensive replacement of pyroxene by calcic amphibole, local recrystallization of plagioclase as well as growth of secondary phases. Almandine, which occurs in mafic to felsic rocks from the study area, are mostly characteristic of metamorphic rocks (Deer et al., 1992). It has also been shown by fractional crystallization modelling that garnet is highly unlikely to represent a magmatic phase. Scapolite, an ubiquitous phase in gabbroic rocks from the study area, is uncommon in igneous parageneses and generally occur in regionally metamorphosed rocks from greenschist to granulite facies (Deer et al., 1992). These observations, combined with the common occurrence of calcic amphibole and the presence of epidote, suggest that the rocks were affected by metamorphism of at least amphibolite grade (Winter, 2010), which correspond to the deformation of the adjacent nappe units in the Uppermost Allochton (Melezhik et al., 2015).

As several minerals occur as secondary, it is difficult to establish a certain fractionating mineral assemblage. Textural observations in thin section suggest that the green amphibole is secondary, whereas the brown-red amphibole, which occur interstitially in olivine gabbros, is regarded as primary. The origin of other phases, such as biotite, was more difficult to determine. Planar textures are only seen in thin sections of samples from the south-western and southern margin. This area is clearly affected by deformation with evidence of folding and faulting. Sneltvedt (1981) reported a north dipping fault (50-70 degrees) in this area, seperating the gabbro from the calc-silicates and marble-schists, belonging to the underlying nappe unit.

Evidence of secondary alteration and metamorphism likely caused mobilization of LILE and silica to varying degrees (Kingsbury et al., 2016). As elevation in LILE is small in mafic rocks, except for contaminated sampled (indicated by ε_{Nd}-values), and there are clearly defined trends in the Harker plots and bivariate trace element plots, the effect of metamorphism on the primary composition appears to be small. Yet, this study relies more heavily on the elements considered to be the most immobile, including Zr, Hf, Nb, Y, Ti, Cr, Sc, Th and the REE, apart from Eu (Hastie et al., 2007).

6.7 Summary of the evolution

Most large igneous intrusions do not form from a single pulse of magma, but are the result of repetitive intrusions, which may have variable compositions (Philpotts, 1990; Namur et al., 2010). The nonsystematic grain size distribution as well as the high density of dykes with slightly variable content of dark minerals and variable grain size, suggest that the Umbukta gabbro formed through a series of smaller intrusions. The lack of pronounced igneous structures, indicate that convecting processes were minor. The similar and enriched trace element pattern for most mafic rocks, imply that the intrusions originated from the same enriched source and evolved through fractional crystallization. Pulses of mafic magma may have crystallized at slightly various depths and under slightly different temperature conditions, thus we find cumulate rock of olivine gabbro alongside more evolved gabbro, and coarse grained varieties adjacent fine grained dykes. Magma emplaced at the margin of the swarm of intrusions were partly subjected to assimilation with contamination of metasedimentary material. The heat from the gabbro probably led to migmatization of the hostrock and subsequent anatexis, resulting in a granodioritic melt. It is considered likely that this melt initially mingled but also mixed with the mafic melt. The variation from mafic pillow, through composite dykes to undisrupted dykes in the contact zone, suggest that mafic magma intruded the granodiorite at various degrees of crystallization of the granodiorite.

It should be noted that the field work and sampling for chemical analysis during this thesis have been constrained to the north-western and western part of the pluton and large areas of the pluton have not been reached. According to Sneltvedt (1981), who performed extensive mapping of both the pluton and the Kalvatn area, the heterogenous nature of the gabbro is constrained to the margins of the pluton, whereas more homogenous gabbro is present further into the pluton, consistent with the observations from this study. Sneltvedt (1981) describes the eastern margin of the gabbro as complex, including fine grained gabbros with coarse grained xenoliths which are particularly abundant at the southern side of Melkfjellet. Based on these findings, it can be suggested that enhanced heat in the interior of the pluton might have led to the homogenization in the central parts of the intrusion.

Presence of metasedimentary xenoliths in the gabbro, south of the northern contact are also reported by Høyen (2016) and Sneltvedt (1981). The Sm-Nd isotopic compositions, trace element data and field relations strongly suggets that assimilation was operating along the northern

margin of the pluton and possibly along other margins, implying that assimilation occurred at the level of emplacement. The fact that the trace REE pattern of the monzonites and monzodiorites is possible to produce by fraction crystallization modelling from the composition of a mafic dyke, strongly imply that the intermediate rocks are genetically related to the more mafic rocks. However, the similarities between the trace element pattern of the intermediate rocks and the rocks displaying isotopic, crustal signatures, combined with presence of host rock xenoliths, provide strong indications for a crustal component in these rocks. From this, a likely explanation is that these monzonites and monzodiorites stem from a mixed source, representing mantle-derived melts which later assimilated material along the margins of the pluton.

6.8 Comparison with synchronous igneous intrusions

The Seiland igneous province (SIP) records a period of magmatism between 560 and 570 Ma (Roberts et al., 2006, 2010) and comprise numerous mafic intrusions with a range of compositions from calc-alkaline to tholeiitic and alkaline (Robins, 1996). The surface outcrops of the SIP cover an area of 5400 km^2, dominated by gabbro (50 %), which commonly host later ultramafic intrusions (35 %), and are often accompanied by a significant volume (10 %) of felsic to intermediate rocks (monzodioritic, dioritic and granitoid) (Roberts, 2007). Alkaline intrusions comprise only 5 % of the surface outcrops and are believed to represent the last igneous event in SIP (Roberts, 2007). The extensive and short-lived magmatism, suggests that the emplacement occurred in an extensional, tectonic regime, probably during intracontinental rifting or back-arc spreading (Daly et al., 1991; Andréasson et al., 1998; Roberts et al., 2006; Roberts, 2007). A general conception is that SIP represents the deep roots of igneous plutons, probably a large igneous province (LIP), which were likely emplaced at mid- to deep crustal depths (Griffin et al., 2013; Grant et al., 2016).

6.8.1 Gabbroic intrusions

Gabbroic intrusions are dominating the province and they commonly host later intrusions of alkaline and ultramafic composition (Roberts, 2007). According to Robins and Gardner (1974) the gabbroic intrusions may be divided into three groups: i) Tholeiitic gabbro displaying a stratiform layering, ii) Syenogabbro - an igneous complex with interlayered gabbroic rocks together

with more evolved rocks such as syenite, monzonite and diorite, iii) Clinopyroxene gabbros, which are nepheline normative, and contain Al-rich clinopyroxene and calcic plagioclase. Currently, most of the gabbros are classified as syneogabbros, after the scheme of Robins and Gardner (1974), but the Hasvik gabbro, as well as the Lille Kufjord intrusion and presumably other less studied intrusions, display a tholeiitic composition (Roberts, 2007).

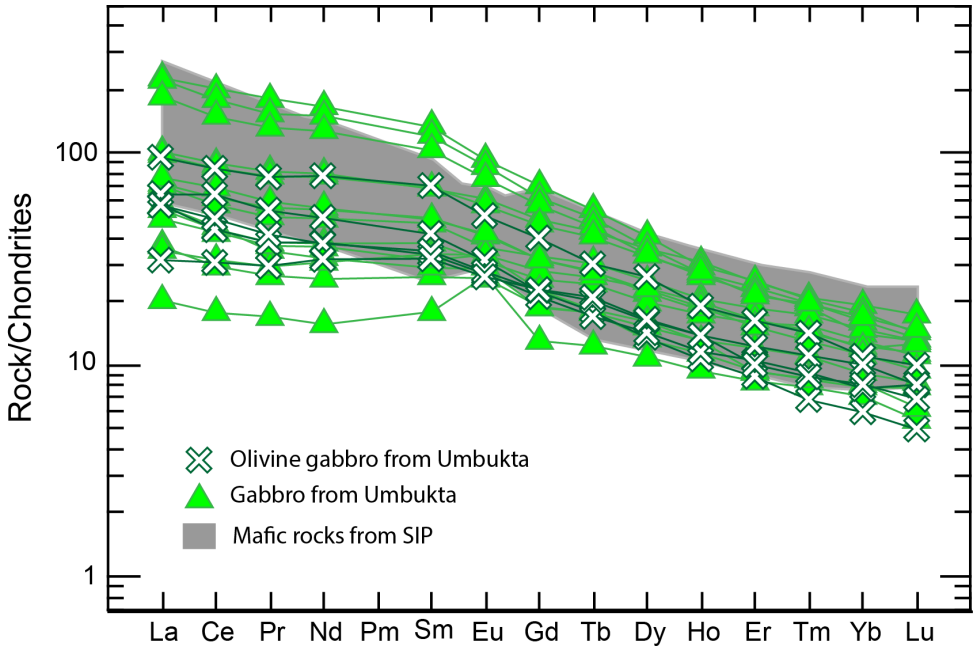

Figure 6.12: Chondrite-normalized REE pattern displaying the chemical similarities between gabbros and olivine gabbros from Umbukta and mafic rocks from the Seiland igneous province. Data from Roberts (2007)

6.8.2 Trace element chemistry

Figure 6.12 reflect the similar chemistry of the mafic rocks from SIP (marked by the shaded area) and the gabbroic rocks from Umbukta. Mafic rocks from both regions show a generally declining trend from La to Lu, but a small negative Eu-anomaly is present in the rocks from Seiland. Of the available normalizing values, EMORB showed the most similar values to the analyses from Umbukta, and was thus chosen as normalization values when comparing trace element values from SIP with those from Umbukta. Figure 6.13 show that there are overlap between the trace element compositions, which is particularly apparent in the HREE, with a steady decline from Sm through Ti to Lu. Both regions display a slight negative Zr anomaly, but the rocks from Umbukta are somewhat enriched in LILE, particularly Cs and Rb, relative to the SIP gabbros, which may reflect a higher degree of alteration. However, this is also consistent

with increased chemical interaction between the mafic magma and continental crust (Juteau and Maury, 1999). There are several peaks in the data from Seiland which cannot be seen in the data from Umbukta, including La, Sr and Pb, but in general there is a great deal of overlap, particularly in the REE pattern (Fig. 6.12). Nevertheless, the Umbukta gabbros display a more flat trend for the LREE compared to the SIP gabbros. Roberts (2007), who acquired these chemical data, compared the chemistry of gabbroic rocks from Seiland to various other large igneous provinces and concluded that the REE pattern for SIP was strongly enriched compared to these other igneous complexes.

Similar to Umbukta, there are several intrusions of granitic and monzodioritic composition associated with some of the gabbroic intrusions in Seiland (Roberts, 2007). Thus, the REE composition of felsic rocks from Umbukta ($SiO_2 > 63$ %) have been compared with the REE composition from various felsic rocks from Seiland ($SiO_2 > 61$ %). Figure 6.14 show that the REE patterns of the felsic rocks from the two regions show similar charactersitics. However, the range of compositions are large for both regions, thus overlapping compositions are very likely. Syenitic intrusions are commonly associated with gabbroic intrusions and interpreted as differentiates (Robins, 1996).

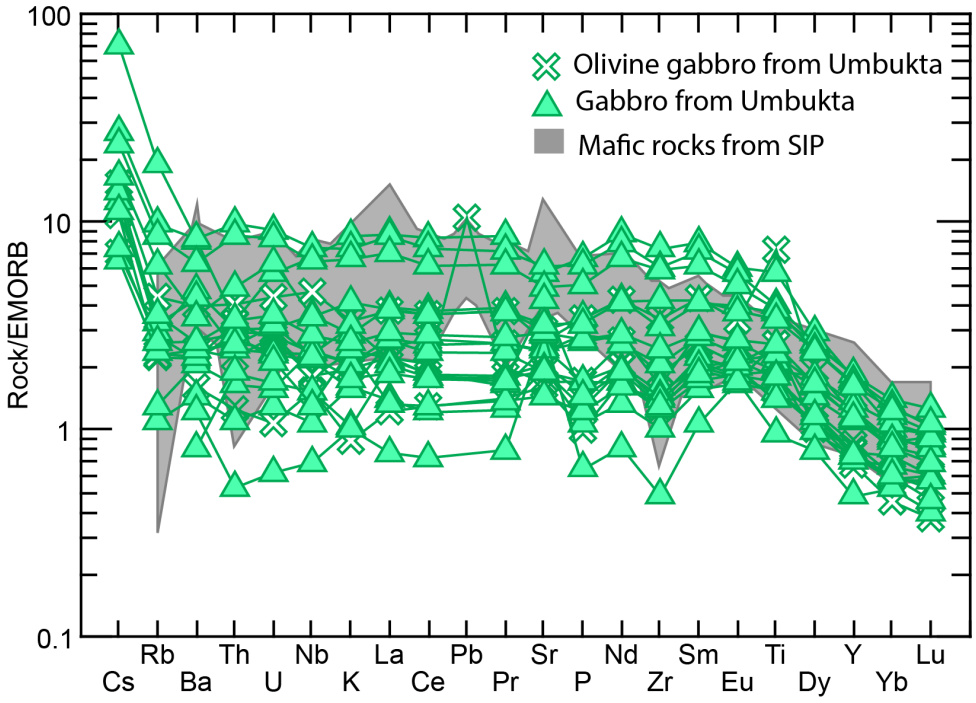

Figure 6.13: Trace element pattern normalized to EMORB (Sun and McDonough, 1989) displaying the chemical similarities between gabbros and olivine gabbros from Umbukta and mafic rocks from the Seiland igneous province. Data from Roberts (2007)

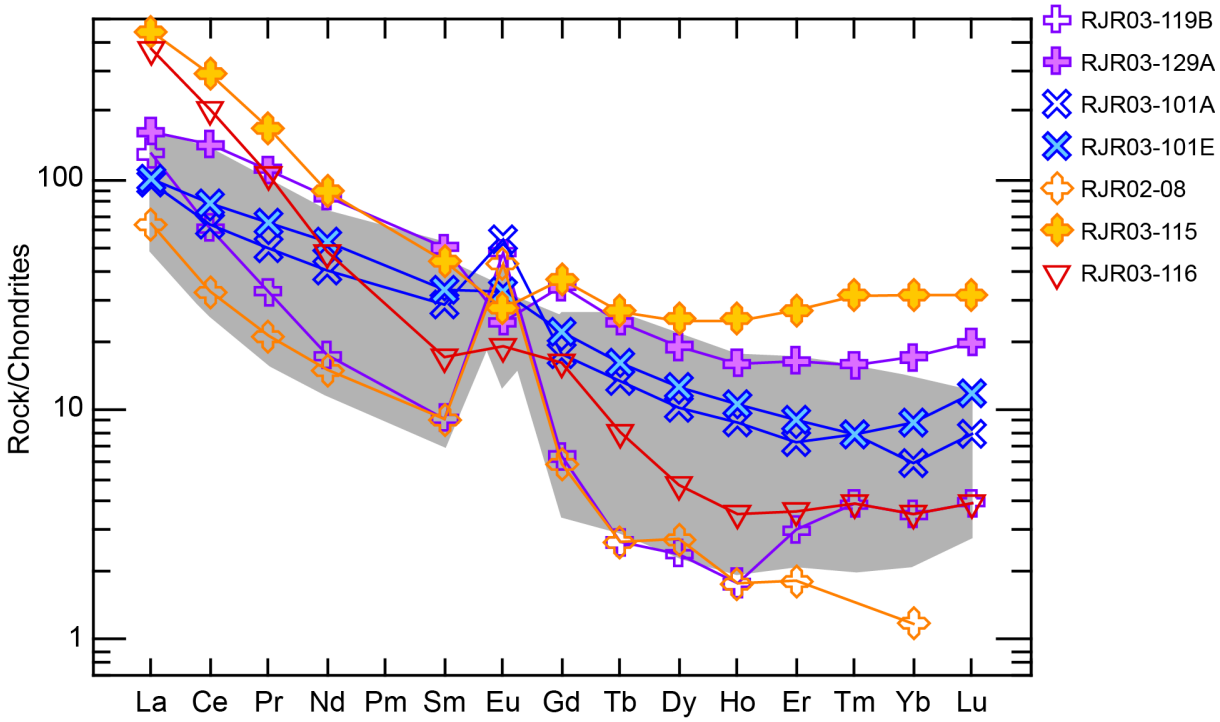

Figure 6.14: Chondrite-normalized REE pattern displaying the chemical similarities between the felsic granitoids from Umbukta (SiO_2 = 62,7-76,7), represented by the shaded area, and various felsic rocks from the Seiland igneous province, obtained from Roberts (2007). RJR03-119B is a diorite (SiO_2 = 60,6 %), RJR03-129A is a granite (SiO_2 = 78,7 %), RJR03-101A is a monzodiorite (SiO_2 = 62,25 %), wehereas RJR03101E and RJR02-08 are monzonites (SiO_2 = 63,3 and 63,8 %).

6.8.3 Sm-Nd isotope chemistry

The similar age of the rocks from Seiland and Umbukta enable us to compare their isotopic ratios. Figure 6.15 display ε_{Nd} values obtained from various gabbroic rocks in SIP. The ε_{Nd} values have been calculated from measured isotopic ratios based on the most recent geochronology (Roberts et al., 2006). The most extensive dataset of Sm-Nd was acquired from the Hasvik gabbro located on Sørøy (Tegner et al., 1999). The two hornblende gabbros analysed by Mørk and Stabel (1990), and a sample from the Storvik intrusion analysed by Daly et al. (1991) were acquired from the Øksfjord peninsula. Two metagabbro, hosting the later Lillebukt alkaline intrusion, analysed by Cadow (1993), and a sample from the Kvalfjord intrusion, analysed by Daly et al. (1991) were all acquired from Stjernøya.

The Sm-Nd data show that the gabbroic rocks from Seiland display a range of isotopic compositions, reflecting crustal signatures to primitive, mantle-like signatures (Fig. 6.15).

The most primitive isotopic composition is represented by the Kvalfjord intrusion, an olivine metagabbro with a ε_{Nd} value of +5,4 (Daly et al., 1991). At the other end of the scale there are

rocks from the Hasvik gabbro, with the lowest ε_{Nd} values of -6,7 from the Upper Border Series, which was interpreted to represent the roof of the magma chamber (Tegner et al., 1999). The samples from the layered series, systematically collected and covering all series of the layered intrusion, reveal a distinct correlation between the degree of contamination and the level in the magma chamber. Despite some erratic ε_{Nd} values, there is a general decreasing trend upsection through the layered series from +3,6 in the Lower zone to -3,7 in the Upper zone, reflecting an increased amount of assimilation closer to the roof of the magma chamber (Tegner et al., 1999). The ε_{Nd} values also decrease with decreasing Mg# and decreasing anorthite component in plagioclase , which suggests that concurrent assimilation and fractional crystallization took place (Tegner et al., 1999).

The Hasvik gabbro as well as the Kvalfjord and Storvik olivine gabbros are layered intrusions (Daly et al., 1991). The former cut previously deformed metasediments of the Sørøy succession, while the latter two cut "basement" paragneisses (Daly et al., 1991). A large variation in ε_{Nd} values is seen throughout the province, which may reflect that assimilation processes that have been reported from the Hasvik gabbro were also effective in the remaining plutons (Roberts, 2007). The gabbroic rocks from Umbukta show ε_{Nd} values between -2,5 and +5,6, which correspond to nearly the same range displayed by gabbros from SIP, suggesting that the least contaminated rocks from Umbukta were derived from a mantle source which was just as primitive as the source of the SIP.

The intrusion with the strongest resemblance to Umbukta is the Hasvik gabbro, which show a tholeiitic signature (Robins and Gardner, 1975; Roberts et al., 2006) and is believed to be extensively affected by assimilation of crustal material (Tegner et al., 1999). One of the samples included in the shaded area (representing the lowest REE concentrations) in figure 6.12 and 6.13 is an olivine gabbro from the upper zone. In resemblance to Umbukta gabbro, the Hasvik intrusion is characterized by composite mafic-granitoid dykes, with an inner contact aureole composed of massive granitic to granodioritic rocks with angular to rounded inclusions of country rocks cut by mafic dykes (Tegner et al., 1999; Robins, 1996). These breccias are believed to have been formed by disruption of the banded metasediments during extensive partial melting (Robins, 1996). This description is somewhat applicable to the contact zone around Austre Sauvatnet, with strong evidence for partial melting of metasediments. These observations combined with the range of isotopic compositions and the overlapping trace element patterns suggest that the Umbukta gabbro was formed through similar processes as those

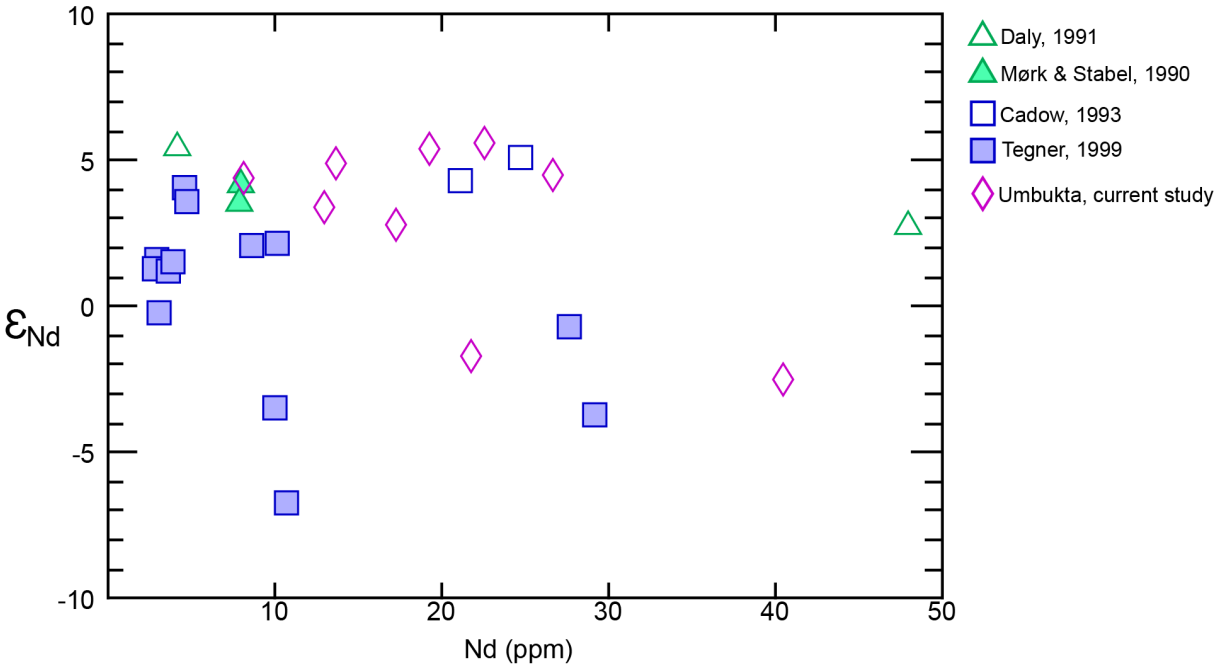

Figure 6.15: ε_{Nd} values for gabbroic rocks from SIP and Umbukta. The analyses from Daly et al. (1991) represent The Storvik gabbro and the Kvalfjord gabbro, the analyses from Cadow (1993) represent two metagabbros from Lillebukt alkaline complex, the analyses from Mørk and Stabel (1990) represent two hornblende gabbros and the analyses from Tegner et al. (1999) represent samples from all zones within the Hasvik gabbro. The ε_{Nd} values have been calculated on the basis of the most recent ages from Roberts et al. (2006), assuming a decay constant of 6,54 x 10^{-12} and the following values for present day CHUR: $^{143}Nd/^{144}Nd$ = 0,512638, $^{147}Sm/^{144}Nd$ = 0,1967 (DePaolo and Wasserburg, 1976).

responsible for the Hasvik gabbro, including a significant amount of assimilation. However, the sample with the strongest crustal signature have a ε_{Nd} value of -2,5 compared to -3,7 for the Layered series in the Hasvik gabbro, implying the amount of assimilation was smaller. The range of ε_{Nd} values from both regions is displayed in figure 6.16. The AFC modelling of the Hasvik gabbro suggest that up to 21 % of assimilant contaminated the layered intrusion, which is in fact unusually high (Tegner et al., 1999). Currently, there have been no observations of primary igneous structures such as layering in the Umbukta, which is pronounced in many, but not all, rocks from SIP. In addition, trace element and isotopic studies from Umbukta suggest that assimilation was constrained to the margins of the pluton. Nevertheless, modal layering in the Hasvik gabbro is generally inconspicious, and the cryptic variations is defined by variations in the cumulus mineral assemblage (Robins, 1996). To be able to determine the presence or lack of modal layering, systematic, detailed sampling and petrographic studies of the Umbukta intrusion is required.

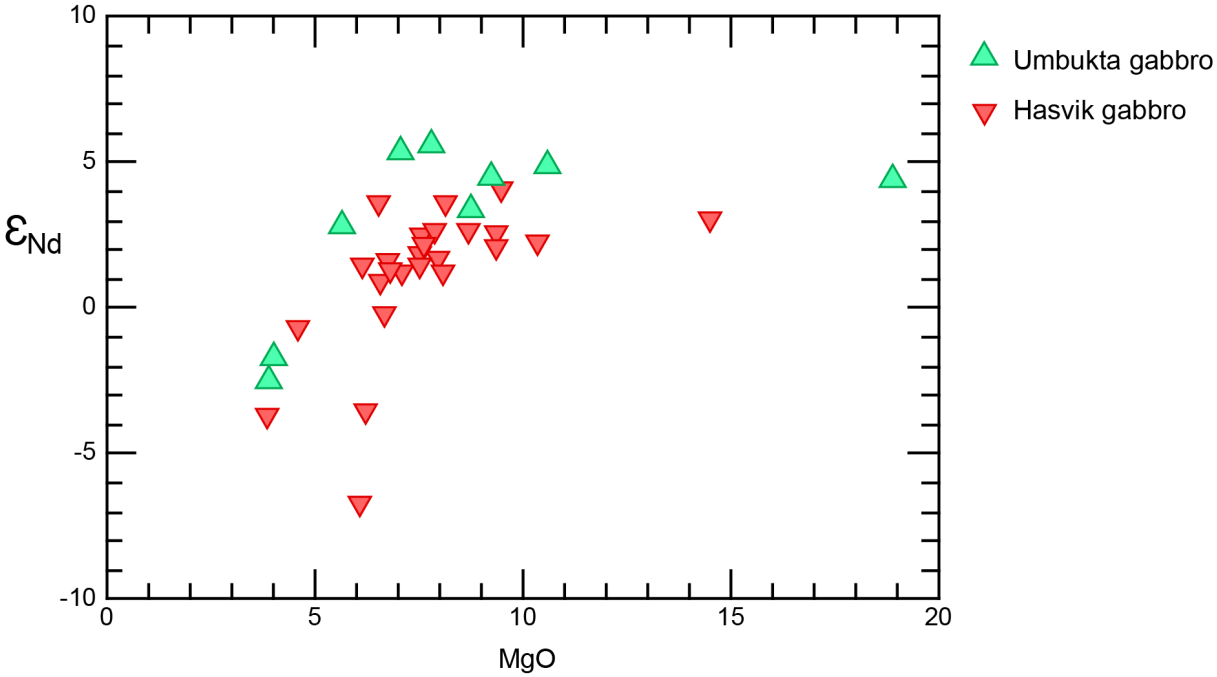

Figure 6.16: ε_{Nd} values for mafic rocks from Umbukta and mafic samples from the Hasvik gabbro. The values from the Hasvik gabbro are recalculated, on the basis of the most recent ages from Roberts et al. (2006), following the procedure described in figure 6.15.

6.8.4 Comparison SIP and Umbukta

As pointed out by Høyen (2016), recent U-Pb dating of the Umbukta gabbro display exactly similar age as those obtained from Seiland igneous province (Høyen, 2016; Roberts et al., 2007, 2010). Despite the lack of alkaline bodies and a less significant volume of ultramafic rocks, the Umbukta gabbro compare with gabbroic rocks in SIP with respect to age, trace element chemistry, isotopic signature, and many field relations. Umbukta share a tholeiitic signature with many of the gabbroic rocks and there are strong indications for a within plate setting, similar to SIP. Roberts et al. (2007) tentatively suggested that monzodiorites associated with mafic rocks in the Seiland igneous province were related to partial melting of pre-existing mafic rocks. This may be a possible explanation for the formation of monzonites and monzodiorites in Umbukta. However, to achieve the composition of the monzodiorites, with silica levels from 52 %, would require unrealistically high degrees of partial melting. The similarity between the most primitive isotopic values from Umbukta and those obtained from Seiland, combined with the overlapping trace element patterns, imply that a similar, enriched mantle source gave rise to these intrusions, located over 500 km apart, linking these two igneous systems to a widespread magmatic event.

Chapter 7

Conclusion and future work

7.1 Conclusion

- The most abundant rock in the study area is a medium grained gabbro, with a mineral assemblage dominated by calcic amphibole, plagioclase, orthopyroxene and clinopyroxene. There are variations in terms of composition and grain size throughout the pluton, where the largest variations are constrained to the margins of the pluton. These findings, combined with the high density of mafic dykes, are thought to reflect that the Umbukta gabbro formed through a series of smaller intrusions.

- In accordance with previous studies (Sneltvedt, 1981; Høyen, 2016), the Umbukta gabbro is thought to have been formed in an intra-plate extensional setting, based on tectonic discrimination diagrams, major and trace element chemistry, and the high density of mafic dykes in the study area. The enriched REE pattern of the mafic dykes, the mafic enclaves and the gabbroic rocks is thought to stem from an enriched source.

- Trace element modelling has shown that the compositional variation in the mafic rocks may be explained by fractional crystallization, where fractionation of olivine, and likely other major phases, were important. The results from the modelling suggest that the REE composition of the monzodiorites and monzonites is possible to produce after 55-71 % fractional crystallization. As these rocks also show evidence for crustal interaction, they are believed to stem from a mixed source. However, the source of the strong Zr enrichment in these rocks remains questionable.

- A contact zone between the gabbro and the metasedimentary host rock in the north, provide evidence for substantial crustal anatexis in the aureole of the pluton. This is indicated by abundant peraluminous granodiorite with a crustal geochemical signature, and observations of mingling between mafic and felsic rocks. The strong correlation between negative ε_{Nd} values and the distance to the margin of the pluton, suggest that assimilation occurred primarily at the level of emplacement.
- The high rate of good exposures along the intrusive contact of the gabbro, makes Umbukta an excellent locality for studying the interaction between crustal rocks and mantle-derived magmas. As there is also a strong correlation between trace elements and isotopic compositions, the Umbukta gabbro provide both direct and indirect evidence for assimilation, which may enhance the understanding of these subsurface processes.
- Comparison of isotopic and chemical data from Umbukta and the Seiland igneous province suggest they were both derived from a relatively enriched mantle source and were both affected by assimilation, although this was more extensive in Seiland. Umbukta can be distinguished from the tholeiitic intrusions of SIP by the apparent lack of layering and alkaline intrusions. However, their similarities are linking them to the same widespread, magmatic event.

7.2 Future work

- As the origin of the felsic granitoids remains questionable, isotopic studies on these rocks would likely give a more certain indication of the source. Isotopic studies would also help constrain the origin of the monzonites and monzodiorites, and to determine whether the rocks represent the product of substantial fractional crystallization or if they resulted from concurrent fractional crystallization and assimilation. Chemical analyses of the calc-silicate rocks, present as xenoliths in intermediate rocks, would reveal if assimilation of calc-silicates are likely to have been affecting the chemistry of the monzonites and monzodiorites. To get a better understanding of the relationship between the distance to the host rock and degree of assimilation, samples, acquired along a profile, perpendicular to the northern contact could be analysed for Sm-Nd isotopes.
- More detailed studies of the contact metamorphic aureole, could provide information

about the temperature and depth of emplacement. Textural and mineralogical changes in the country rock may record contact metamorphic overprint related to emplacement (Annen et al., 2006).

- Although there were few indications of primary igneous structures, zones or layers within the Umbukta gabbro, more detailed and systematic mapping and sampling covering a larger area of the pluton with subsequent petrographic studies, may reveal zones or layers defined by variation in terms of grain size, modal mineralogy or chemistry.

Bibliography

Andréasson, P.-G., Svenningsen, O. M., Albrecht, L., 1998. Dawn of Phanerozoic orogeny in the North Atlantic tract; Evidence from the Seve-Kalak Superterrane, Scandinavian Caledonides. Gff 120 (2), 159–172.

Annen, C., Scaillet, B., Sparks, R., 2006. Thermal constraints on the emplacement rate of a large intrusive complex: the Manaslu Leucogranite, Nepal Himalaya. Journal of Petrology 47 (1), 71–95.

Augland, L. E., Andresen, a., Gasser, D., Steltenpohl, M. G., 2013. Early Ordovician to Silurian evolution of exotic terranes in the Scandinavian Caledonides of the Ofoten-Troms area - terrane characterization and correlation based on new U-Pb zircon ages and Lu-Hf isotopic data. Geological Society, London, Special Publications 390 (1), 655–678.

Bacon, C. R., Druitt, T. H., 1988. Compositional evolution of the zoned calcalkaline magma chamber of Mount Mazama, Crater Lake, Oregon. Contributions to Mineralogy and Petrology 98 (2), 224–256.

Barbarin, B., 1996. Genesis of the two main types of peraluminous granitoids. Geology 24 (4), 295–298.

Barbarin, B., 1999. A review of the relationships between granitoid types, their origins and their geodynamic environments. Lithos 46 (3), 605–626.

Barbarin, B., Didier, J., 1992. Genesis and evolution of mafic microgranular enclaves through various types of interaction between coexisting felsic and mafic magmas. Geological Society of America Special Papers 272, 145–154.

Barnes, C. G., Frost, C. D., Nordgulen, Ø., Prestvik, T., 2012. Magma hybridization in the

middle crust: Possible consequences for deep-crustal magma mixing. Geosphere 8 (2), 518–533.

Barnes, C. G., Memmeti, V., Coint, N., 2016. Deciphering magmatic processes in calc-alkaline plutons using trace element zoning in hornblende. American Mineralogist 101 (2), 328–342.

Bea, F., 1996. Residence of REE, Y, Th and U in Granites and Crustal Protoliths; Implications for the Chemistry of Crustal Melts. Journal of Petrology 37 (3), 521–552.

Bea, F., Montero, P., Ortega, M., 2006. A LA–ICP–MS evaluation of Zr reservoirs in common crustal rocks: Implications for Zr and Hf geochemistry, and zircon-forming processes. The Canadian Mineralogist 44 (3), 693–714.

Best, M. G., 2003. Igneous and metamorphic petrology. John Wiley & Sons.

Bingen, B., Demaiffe, D., Van Breemen, O., 1998. The 616 Ma Old Egersund Basaltic Dike Swarm, SW Norway, and Late Neoproterozoic Opening of the Iapetus Ocean. The Journal of Geology 106, 565–574.

Bougault, H., Hekinian, R., 1974. Rift valley in the Atlantic Ocean near 36 50 N: Petrology and geochemistry of basaltic rocks. Earth and Planetary Science Letters 24 (2), 249–261.

Bowen, N. L., 1928. The evolution of the igneous rocks. Princeton University Press.

Brophy, J. G., Ota, T., Kunihro, T., Tsujimori, T., Nakamura, E., 2011. In situ ion-microprobe determination of trace element partition coefficients for hornblende, plagioclase, orthopyroxene, and apatite in equilibrium with natural rhyolitic glass, Little Glass Mountain Rhyolite, California. American Mineralogist 96 (11-12), 1838–1850.

Cabanis, B., 1989. Le diagramme La/10-Y/15-Nb/8: unoutil pour la discrimination des series volcaniques et la mise en evidence des processus de melande et/ou de contamination crustale. CR Acad. Sci. Ser. II 309, 2023–2029.

Cadow, R., 1993. Sm-nd and rb-sr ages of hornblende clinopyroxenite and metagabbro from the lillebukt alkaline complex, seiland igneous province. Norsk geologisk tidsskrift 73 (4), 243–249.

Chappell, B. W., White, A. J. R., 2001. Two contrasting granite types: 25 years later. Australian Journal of Earth Sciences 48 (4), 489–500.

Chu, M. F., Wang, K. L., Griffin, W. L., Chung, S. L., O'Reilly, S. Y., Pearson, N. J., Iizuka, Y., 2009. Apatite composition: Tracing petrogenetic processes in Transhimalayan granitoids. Journal of Petrology 50 (10), 1829–1855.

Claesson, S., 1980. Pre-Silurian orogenic deformation in the north-central Scandinavian Caledonides. Geol. Fören. Stockh. Förh 101, 353–356.

Claesson, S., Roddick, J., 1983. 40Ar/39Ar data on the age and metamorphism of the Ottfjället dolerites, Särv Nappe, Swedish Caledonides. Lithos 16 (1), 61–73.

Cocks, L. R. M., Torsvik, T. H., 2005. Baltica from the late Precambrian to mid-Palaeozoic times: The gain and loss of a terrane's identity. Earth-Science Reviews 72 (1-2), 39–66.

Corfu, F., Andersen, T. B., Gasser, D., 2014a. The Scandinavian Caledonides: main features, conceptual advances and critical questions. Geological Society, London, Special Publications 390 (1), 9–43.

Corfu, F., Gasser, D., Chew, D. M., 2014b. New perspectives on the Caledonides of Scandinavia and related areas: introduction. Geological Society, London, Special Publications 390 (1), 1–8.

Corfu, F., Roberts, R. J., Torsvik, T. H., Ashwal, L. D., Ramsay, D. M., 2007. Peri-Gondwanan elements in the Caledonian Nappes of Finnmark, Northern Norway: Implications for the paleogeographic framework of the Scandinavian Caledonides. American Journal of Science 307 (2), 434–458.

Daly, J., Aitcheson, S., Cliff, R., Gayer, R., Rice, A., 1991. Geochronological evidence from discordant plutons for a late Proterozoic orogen in the Caledonides of Finnmark, northern Norway. Journal of the Geological Society 148 (1), 29–40.

Davì, M., De Rosa, R., Barca, D., 2009. A LA-ICP-MS study of minerals in the Rocche Rosse magmatic enclaves: Evidence of a mafic input triggering the latest silicic eruption of Lipari Island (Aeolian Arc, Italy). Journal of Volcanology and Geothermal Research 182 (1-2), 45–56.

Deer, W. A., Howie, R. A., Zussman, J., 1992. An introduction to the rock-forming minerals. Vol. 696. Longman London.

DePaolo, D., Wasserburg, G., 1976. Nd isotopic variations and petrogenetic models. Geophysical Research Letters 3 (5), 249–252.

DePaolo, D. J., 1981. Trace element and isotopic effects of combined wallrock assimilation and fractional crystallization. Earth and planetary science letters 53 (2), 189–202.

DePaolo, D. J., 1988. Neodymium isotope geochemistry: an introduction. Springer Science & Business Media.

Dobosi, G., Jenner, G. A., 1999. Petrologic implications of trace element variation in clinopyroxene megacrysts from the Nograd volcanic province, north Hungary: A study by laser ablation microprobe-inductively coupled plasma-mass spectrometry. Lithos 46 (4), 731–749.

Dostal, J., Dupuy, C., Carron, J., De Kerneizon, M. L. G., Maury, R., 1983. Partition coefficients of trace elements: application to volcanic rocks of St. Vincent, West Indies. Geochimica et Cosmochimica Acta 47 (3), 525–533.

Ernst, R. E., Buchan, K. L., Campbell, I. H., 2005. Frontiers in large igneous province research. Lithos 79 (3), 271–297.

Ewart, A., Bryan, W., Gill, J., 1973. Mineralogy and geochemistry of the younger volcanic islands of Tonga, SW Pacific. Journal of Petrology 14 (3), 429–465.

Ewart, A., Griffin, W., 1994. Application of proton-microprobe data to trace-element partitioning in volcanic rocks. Chemical Geology 117 (1), 251–284.

Foley, S. F., Prelevic, D., Rehfeldt, T., Jacob, D. E., 2013. Minor and trace elements in olivines as probes into early igneous and mantle melting processes. Earth and Planetary Science Letters 363, 181–191.

Fujimaki, H., Tatsumoto, M., Aoki, K.-I., 1984. Partition coefficients of Hf, Zr, and REE between phenocrysts and groundmasses. In: Lunar and Planetary Science Conference Proceedings. Vol. 14. pp. B662–B672.

Gee, D. G., 1975. A tectonic model for the central part of the Scandinavian Caledonides.

Gee, D. G., Fossen, H., Henriksen, N., Higgins, A. K., 2008. From the early Paleozoic platforms of Baltica and Laurentia to the Caledonide orogen of Scandinavia and Greenland. Episodes 31 (1), 44–51.

Gee, D. G., Ladenberger, A., Dahlqvist, P., Majka, J., Be'eri-Shlevin, Y., Frei, D., Thomsen, T., 2014. The baltoscandian margin detrital zircon signatures of the central scandes. Geological Society, London, Special Publications 390 (1), 131–155.

Gill, R., 2010. Igneous rocks and processes: a practical guide. John Wiley & Sons.

Grant, T. B., Larsen, R. B., Anker-Rasch, L., Grannes, K. R., Iljina, M., McEnroe, S., Nikolaisen, E., Schanche, M., Øen, E., 2016. Anatomy of a deep crustal volcanic conduit system; The Reinfjord Ultramafic Complex, Seiland Igneous Province, Northern Norway. Lithos 252-253, 200–215.

Green, T., Blundy, J., Adam, J., Yaxley, G., 2000. SIMS determination of trace element partition coefficients between garnet, clinopyroxene and hydrous basaltic liquids at 2–7.5 GPa and 1080–1200 C. Lithos 53 (3), 165–187.

Green, T., Pearson, N., 1986. Rare-earth element partitioning between sphene and coexisting silicate liquid at high pressure and temperature. Chemical Geology 55 (1-2), 105–119.

Green, T. H., Pearson, N. J., 1987. An experimental study of Nb and Ta partitioning between Ti-rich minerals and silicate liquids at high pressure and temperature. Geochimica et Cosmochimica Acta 51 (1), 55–62.

Grew, E. S., Locock, A. J., Mills, S. J., Galuskina, I. O., Galuskin, E. V., H??lenius, U., 2013. IMA report: Nomenclature of the garnet supergroup. American Mineralogist 98 (4), 785–810.

Griffin, W. L., Sturt, B. A., O'Neill, C. J., Kirkland, C. L., O'Reilly, S. Y., 2013. Intrusion and contamination of high-temperature dunitic magma: The Nordre Bumandsfjord pluton, Seiland, Arctic Norway. Contributions to Mineralogy and Petrology 165 (5), 903–930.

Harker, A., 1909. The natural history of igneous rocks. Macmillam.

Hastie, A. R., Kerr, A. C., Pearce, J. A., Mitchell, S., 2007. Classification of altered volcanic island arc rocks using immobile trace elements: development of the Th–Co discrimination diagram. Journal of petrology 48 (12), 2341–2357.

Hauri, E. H., Wagner, T. P., Grove, T. L., 1994. Experimental and natural partitioning of Th, U, Pb and other trace elements between garnet, clinopyroxene and basaltic melts. Chemical Geology 117 (1-4), 149–166.

Henderson, P., 1984. Rare earth element geochemistry. Elsevier.

Higgins, M. D., van Breemen, O., 1998. The Age of the Sept Iles Layered Mafic Intrusion, Canada: Implications For the Late Neoproterozoic/Cambrian History of Southeastern Canada. The Journal of Geology 106 (4), 421–432.

Hollings, P., Wyman, D., 2005. The geochemistry of trace elements in igneous systems: principles and examples from basaltic systems. Rare-Element Geochemistry and Mineral Deposits: Geological Association of Canada, GAC Short Course Notes 17, 1–16.

Hoskin, P. W. O., Kinny, P. D., Wyborn, D., Chappell, B. W., 2000. Identifying Accessory Mineral Saturation during Differentiation in Granitoid Magmas: an Integrated Approach. Journal of Petrology 41 (9), 1365–1396.

Hoskin, P. W. O., Schaltegger, U., 2003. The composition of zircon and igneous and metamorphic petrogenesis. In: Hanchar, J M and Hoskin, P W O (eds.) Zircon. Reviews in mineralogy and geochemistry 53 (1), 27–62.

Høyen, A. B., 2016. Within plate gabbroic intrusion at 565 Ma in the Uppermost Allochthon - A regional, geochemical and geochronological study of the Umbukta gabbro, north-central Norway. Master's thesis, NTNU.

Huppert, H. E., Sparks, R. S. J., 1989. Chilled margins in igneous rocks. Earth and Planetary Science Letters 92 (3-4), 397–405.

Irvine, T., Baragar, W., 1971. A guide to the chemical classification of the common volcanic rocks. Canadian journal of earth sciences 8 (5), 523–548.

Irving, A. J., Frey, F. A., 1978. Distribution of trace elements between garnet megacrysts and host volcanic liquids of kimberlitic to rhyolitic composition. Geochimica et Cosmochimica Acta 42 (6), 771–787.

Jackson, E. D., 1961. Primary textures and mineral associations in the ultramafic zone of the Stillwater complex, Montana. Geological Survey Professional Paper 358, 103.

Jang, Y. D., Naslund, H. R., McBirney, A. R., 2001. The differentiation trend of the Skaergaard intrusion and the timing of magnetite crystallization: Iron enrichment revisited. Earth and Planetary Science Letters 189 (3-4), 189–196.

Juteau, T., Maury, R., 1999. The oceanic crust, from accretion to mantle recycling. Vol. 390. Springer.

Kamber, B., Collerson, K., 2000. Zr/nb systematics of ocean island basalts reassessed—the case for binary mixing. Journal of Petrology 41 (7), 1007–1021.

Kamo, S. L., Gower, C. F., 1994. U-Pb baddeleyite dating clarifies age of characteristic paleomagnetic remanence of Long Range dykes, southeastern Labrador. Atlantic Geology 30 (3), 259–262.

Kamo, S. L., Gower, C. F., Krogh, T. E., 1989. Birthdate for the Iapetus Ocean? A precise U-Pb zircon and baddeleyite age for the Long Range dikes, southeast Labrador. Geology 17 (7), 602–605.

Kingsbury, C. G., Ernst, R. E., Cousens, B. L., Williamson, M.-C., 2016. The High Arctic LIP in Canada: Trace element and Sm-Nd Isotopic evidence for the role of mantle heterogeneity and crustal assimilation. Norwegian Journal of Geology 96 (2), 97–118.

Kirkland, C., Stephen Daly, J., Whitehouse, M., 2007. Provenance and Terrane Evolution of the Kalak Nappe Complex, Norwegian Caledonides: Implications for Neoproterozoic Paleogeography and Tectonics. The Journal of Geology 115 (1), 21–41.

Kirkland, C. L., Daly, J. S., Whitehouse, M. J., 2005. Early Silurian magmatism and the Scandian evolution of the Kalak Nappe Complex, Finnmark, Arctic Norway. Journal of the Geological Society 162 (6), 985–1003.

Kirkland, C. L., Daly, J. S., Whitehouse, M. J., 2006. Granitic magmatism of grenvillian and late neoproterozoic age in Finnmark, Arctic Norway - Constraining pre-Scandian deformation in the Kalak Nappe Complex. Precambrian Research 145 (1-2), 24–52.

Kirsch, M., Svenningsen, O., 2015. Root zone of a continental rift: the Neoproterozoic Kebnekaise Intrusive Complex, northern Swedish Caledonides. Gff 5897 (October), 1–23.

Kokfelt, T. F., Weatherley, S. M., Keiding, J. K., Árting, T. B., 2015. Magma mixing, mingling and hybridisation at different crustal levels: snapshots from 1.9 billion years of magmatism in south-eastern greenland. Geological Survey of Denmark and Greenland Bulletin 33, 45–48.

Kumarapeli, P. S., 1993. A plume-generated segment of the rifted margin of Laurentia, Southern

Canadian Appalachians, seen through a completed Wilson Cycle. Tectonophysics 219 (1-3), 47–55.

Le Bas, M. J., Le Maitre, R. W., Streckeisen, A., Zanettin, B., 1986. A chemical classification of volcanic rocks based on the total alkali-silica diagram. Journal of petrology 27 (3), 745–750.

Leake, B. E., 1978. Nomenclature of amphiboles. The Canadian Mineralogist 16 (4), 501–520.

Leake, B. E., Woolley, A. R., Arps, C. E., Birch, W. D., Gilbert, M. C., Grice, J. D., Hawthorne, F. C., Kato, A., Kisch, H. J., Krivovichev, V. G., et al., 1997. Report. nomenclature of amphiboles: Report of the subcommittee on amphiboles of the international mineralogical association commission on new minerals and mineral names. Mineralogical magazine 61 (2), 295–321.

Li, C., Arndt, N. T., Tang, Q., Ripley, E. M., 2015. Trace element indiscrimination diagrams. Lithos 232, 76–83.

Li, X. H., Sun, M., Wei, G. J., Liu, Y., Lee, C. Y., Malpas, J., 2000. Geochemical and Sm-Nd isotopic study of amphibolites in the Cathaysia Block, southeastern China: Evidence for an extremely depleted mantle in the Paleoproterozoic. Precambrian Research 102 (3-4), 251–262.

Luhr, J. F., Carmichael, I. S., Varekamp, J. C., 1984. The 1982 eruptions of El Chichón Volcano, Chiapas, Mexico: mineralogy and petrology of the anhydritebearing pumices. Journal of Volcanology and Geothermal Research 23 (1-2), 69–108.

Marker, M., Bjerkgård, T., Slagstad, T., Solli, A., 2012. Berggrunnsgeologisk kart over Storakersvatnet 2027-3, M 1:50 000. Norges geologiske undersøkelse.

Marzoli, A., Renne, P. R., Piccirillo, E. M., Ernesto, M., Bellieni, G., De Min, A., 1999. Extensive 200-million-year-old continental flood basalts of the central atlantic magmatic province. Science 284 (5414), 616–618.

Matsui, Y., 1977. Crystal structure control in trace element partition between crystal and magma. Bull. Soc. Fr. Mineral. Cristallogr. 100, 315–324.

McArthur, K. L., Frost, C. D., Barnes, C. G., Prestvik, T., Nordgulen, Ø., 2014. Tectonic reconstruction and sediment provenance of a far-travelled oceanic nappe, helgeland nappe

complex, west-central norway. Geological Society, London, Special Publications 390 (1), 583–602.

McIntire, W. L., 1963. Trace element partition coefficients—a review of theory and applications to geology. Geochimica et Cosmochimica Acta 27 (12), 1209–1264.

McKenzie, D., O'nions, R., 1991. Partial melt distributions from inversion of rare earth element concentrations. Journal of Petrology 32 (5), 1021–1091.

McKerrow, W. S., Mac Niocaill, C., Dewey, J. F., 2000. The Caledonian orogeny redefined. Journal of the Geological Society 157 (6), 1149–1154.

Melezhik, V. A., Ihlen, P. M., Kuznetsov, A. B., Gjelle, S., Solli, A., Gorokhov, I. M., Fallick, A. E., Sandstad, J. S., Bjerkgård, T., 2015. Pre-Sturtian (800-730Ma) depositional age of carbonates in sedimentary sequences hosting stratiform iron ores in the Uppermost Allochthon of the Norwegian Caledonides: A chemostratigraphic approach. Precambrian Research 261, 272–299.

Meschede, M., 1986. A method of discriminating between different types of mid-ocean ridge basalts and continental tholeiites with the Nb–Zr–Y diagram. Chemical geology 56 (3), 207–218.

Middlemost, E. A. K., 1994. Naming Materials in the Magma Igneous Rock System. Earth-Science Reviews 37 (1994), 215–224.

Morimoto, N., 1988. Nomenclature of Pyroxenes. Mineralogy and Petrology 39 (1), 55–76.

Mørk, M. B. E., Stabel, A., 1990. Cambrian Sm-Nd dates for an ultramafic intrusion and for high-grade metamorphism on the Øksfjord peninsula, Finnmark, North Norway. Norsk Geologisk Tidsskrift 70 (4), 275–291.

Mysen, B., 1978. Experimental determination of nickel partition coefficients between liquid, pargasite, and garnet peridotite minerals and concentration limits of behavior according to Henry's law at high pressure and temperature. American Journal of Science 278 (2), 217–243.

Namur, O., Charlier, B., Toplis, M. J., Higgins, M. D., Liégeois, J. P., vander Auwera, J., 2010. Crystallization sequence and magma chamber processes in the ferrobasaltic Sept Iles layered intrusion, Canada. Journal of Petrology 51 (6), 1203–1236.

Nash, W., Crecraft, H., 1985. Partition coefficients for trace elements in silicic magmas. Geochimica et Cosmochimica Acta 49 (11), 2309–2322.

Nikogosian, I., Sobolev, A., 1997. Ion-microprobe analysis of melt Inclusions in olivine: experience in estimating the olivine-melt partition coefficients of trace elements. Geochemistry International 35 (2), 119–126.

Nordgulen, O., Bickford, M. E., Nissen, A. L., Wortman, G. L., 1993. U-Pb zircon ages from the Bindal Batholith, and the tectonic history of the Helgeland Nappe Complex, Scandinavian Caledonides. Journal of the Geological Society 150 (1990), 771–783.

Norman, M., Garcia, M. O., Pietruszka, A. J., 2005. Trace-element distribution coefficients for pyroxenes, plagioclase, and olivine in evolved tholeiites from the 1955 eruption of Kilauea Volcano, Hawaii, and petrogenesis of differentiated rift-zone lavas. American Mineralogist 90 (5-6), 888–899.

Paster, T. P., Schauwecker, D. S., Haskin, L. A., 1974. The behavior of some trace elements during solidification of the Skaergaard layered series. Geochimica et Cosmochimica Acta 38 (10), 1549–1577.

Pearce, J. A., 1983. Role of the sub-continental lithosphere in magma genesis at active continental margins. In: Hawkesworth, C., Norry, M. (Eds.), Continental Basalts and Mantle Xenoliths. Shiva, Nantwich, pp. 230–249.

Pearce, J. A., Cann, J., 1973. Tectonic setting of basic volcanic rocks determined using trace element analyses. Earth and planetary science letters 19 (2), 290–300.

Pearce, J. A., Norry, M. J., 1979. Petrogenetic implications of Ti, Zr, Y, and Nb variations in volcanic rocks. Contributions to mineralogy and petrology 69 (1), 33–47.

Philpotts, A., 1990. Principles of igneous and metamorphic petrology. Prentice Hall.

Pin, C., Zalduegui, J., 1997. Sequential separation of light rare-earth elements, thorium and uranium by miniaturized extraction chromatography: application to isotopic analyses of silicate rocks. Analytica Chimica Acta 339 (1), 79–89.

Ramsay, D., Sturt, B., Zwaan, K., Roberts, D., 1985. Caledonides of northern Norway. In: Gee, D., Sturt, B. (Eds.), The Caledonian Orogen: Scandinavia and related areas. Wiley, Chichester, UK, pp. 163–184.

Ribbe, P. H., Hofmeister, A. M., 1983. Chapter 1: ”Chemistry, structure and nomenclature of feldspars” in Feldspar mineralogy. Vol. 2. Mineralogical Society of Amer.

Robb, L., 2005. Introduction to ore-forming processes. John Wiley & Sons.

Roberts, D., 1990. Geochemistry of mafic dykes in the Corrovarre nappe, Troms, North Norway. Norges geologiske undersøkelse 419, 45–54.

Roberts, D., 2003. The Scandinavian Caledonides: Event chronology, palaeogeographic settings and likely modern analogues. Tectonophysics 365 (1-4), 283–299.

Roberts, D., Gee, D. G., 1985. An introduction to the structure of the Scandinavian Caledonides. In: Gee, D. G., Sturt, B. A. (Eds.), The Caledonide Orogen - Scandinavia and Related Areas. John Wiley & Sons Ltd, pp. 55–68.

Roberts, D., Nordgulen, Ø., Melezhik, V., 2007. The Uppermost Allochthon in the Scandinavian Caledonides: From a Laurentian ancestry through Taconian orogeny to Scandian crustal growth on Baltica. Geological Society of America Memoirs 200, 357–377.

Roberts, R., Corfu, F., Torsvik, T., Hetherington, C., Ashwal, L., 2010. Age of alkaline rocks in the Seiland Igneous Province, Northern Norway. Journal of the Geological Society 167 (1), 71–81.

Roberts, R. J., 2007. The Seiland Igneous Province, northern Norway: age, provenance, and tectonic significance. Ph.D. thesis.

Roberts, R. J., Corfu, F., Torsvik, T. H., Ashwal, L. D., Ramsay, D. M., 2006. Short-lived mafic magmatism at 560–570 Ma in the northern Norwegian Caledonides: U–Pb zircon ages from the Seiland Igneous Province. Geological Magazine 143, 887–903.

Robins, B., 1996. Field Trip Guidebook: The Seiland Igneous Province, North Norway.

Robins, B., Gardner, P., 1974. Synorogenic layered basic intrusions in the Seiland petrographic province, Finnmark. Norges geologiske undersøkelse 312, 91–130.

Robins, B., Gardner, P., 1975. The magmatic evolution of the Seiland Province, and Caledonian plate boundaries in northern Norway. Earth and Planetary Science Letters 26 (2), 167–178.

Rollinson, H. R., 1993. Using geochemical data: evaluation, presentation, interpretation. Longman Scientific & Technical; Copublished in the US with J. Wiley & Sons.

Severs, M. J., Beard, J. S., Fedele, L., Hanchar, J. M., Mutchler, S. R., Bodnar, R. J., 2009. Partitioning behavior of trace elements between dacitic melt and plagioclase, orthopyroxene, and clinopyroxene based on laser ablation ICPMS analysis of silicate melt inclusions. Geochimica et Cosmochimica Acta 73 (7), 2123–2141.

Shand, S. J., 1943. Eruptive Rocks: Their Genesis, Composition, Classification, and Their Relation to Ore-deposits. Wiley, New York.

Sisson, T., 1994. Hornblende-melt trace-element partitioning measured by ion microprobe. Chemical Geology 117 (1-4), 331–344.

Sisson, T., Bacon, C., 1992. Garnet/high-silica rhyolite trace element partition coefficients measured by ion microprobe. Geochimica et Cosmochimica Acta 56 (5), 2133–2136.

Slagstad, T., 2003. Geochemistry of trondhjemites and mafic rocks in the Bymarka ophiolite fragment, Trondheim, Norway: Petrogenesis and tectonic implications. Norsk Geologisk Tidsskrift 83 (3), 167–185.

Sneltvedt, H. S., 1981. En berggrunnsgeologisk og strukturgeologisk undersøkelse av Kalvatnområdet, Rana, Nordland. Master's thesis, University of Oslo.

Sparks, R., Marshall, L., 1986. Thermal and mechanical constraints on mixing between mafic and silicic magmas. Journal of Volcanology and Geothermal Research 29 (1-4), 99–124.

Stephens, M. B., Gustavson, M., Ramberg, I., Zachrisson, E., 1985. The Caledonides of central-north Scandinavia – a tectonostratigraphic overview. In: Gee, D. G., Sturt, B. A. (Eds.), The Caledonide Orogen - Scandinavia and Related Areas. John Wiley & Sons Ltd, pp. 135–162.

Stimac, J., Hickmott, D., 1994. Trace-element partition coefficients for ilmenite, orthopyroxene and pyrrhotite in rhyolite determined by micro-PIXE analysis. Chemical Geology 117 (1-4), 313–330.

Stix, J., Gorton, M. P., 1990. Variations in trace element partition coefficients in sanidine in the Cerro Toledo Rhyolite, Jemez Mountains, New Mexico: Effects of composition, temperature, and volatiles. Geochimica et Cosmochimica Acta 54 (10), 2697–2708.

Sturt, B. A., Pringle, I. R., Ramsay, D. M., 1978. The Finnmarkian phase of the Caledonian orogeny. Journal of the Geological Society 135 (6), 597–610.

Sun, S. S., McDonough, W. F., 1989. Chemical and isotopic systematics of oceanic basalts: im-

plications for mantle composition and processes. Geological Society, London, Special Publications 42 (1), 313–345.

Svenningsen, O. M., 2001. Onset of seafloor spreading in the Iapetus ocean at 608 Ma: Precise age of the Sarek Dyke Swarm, northern Swedish Caledonides. Precambrian Research 110 (1-4), 241–254.

Taylor, S. R., McLennan, S. M., 1985. The continental crust: its composition and evolution.

Tegner, C., Robins, B., Reginiussen, H., Grundvig, S., 1999. Assimilation of Crustal Xenoliths in a Basaltic Magma Chamber: Sr and Nd Isotopic Constraints from the Hasvik Layered Intrusion, Norway. Journal of Petrology 40 (3), 363–380.

Tegner, C., Wilson, J. R., Robins, B., 2005. Crustal assimilation in basalt and jotunite: Constraints from layered intrusions. Lithos 83 (3-4 SPEC. ISS.), 299–316.

Thompson, G., Malpas, J., 2000. Mineral/melt partition coefficients of oceanic alkali basalts determined on natural samples using laser ablation-inductively coupled plasma-mass spectrometry (lam-icp-ms). Mineralogical Magazine 64 (1), 85–85.

Tindle, A. G., Webb, P. C., 1990. Estimation of lithium contents in trioctahedral micas using microprobe data: application to micas from granitic rocks. European Journal of Mineralogy, 595–610.

Torsvik, T. H., Cocks, L. R. M., 2004. Earth geography from 400 to 250 Ma: a palaeomagnetic, faunal and facies review. Journal of the Geological Society 161 (4), 555–572.

Torsvik, T. H., Cocks, L. R. M., 2005. Norway in space and time: A Centennial cavalcade. Norsk Geologisk Tidsskrift 85 (1-2), 73–86.

Torsvik, T. H., Smethurst, M. A., Meert, J. G., Van der Voo, R., McKerrow, W. S., Brasier, M. D., Sturt, B. A., Walderhaug, H. J., 1996. Continental break-up and collision in the Neoproterozoic and Palaeozoic - A tale of Baltica and Laurentia. Earth-Science Reviews 40 (3-4), 229–258.

Van Staal, C. R., Dewey, J. F., Mac Niocaill, C., McKerrow, W. S., 1998. The Cambrian-Silurian tectonic evolution of the northern Appalachians and British Caledonides: history of a complex, west and southwest Pacific-type segment of Iapetus. Geological Society, London, Special Publications 143 (1), 197–242.

Van Staal, C. R., Whalen, J. B., Valverde-Vaquero, P., Zagorevski, A., Rogers, N., 2009. Pre-carboniferous, episodic accretion-related, orogenesis along the laurentian margin of the northern appalachians. Geological Society, London, Special Publications 327 (1), 271–316.

Villemant, B., 1988. Trace element evolution in the Phlegrean Fields (Central Italy): fractional crystallization and selective enrichment. Contributions to Mineralogy and Petrology 98 (2), 169–183.

Villemant, B., Jaffrezic, H., Joron, J.-L., Treuil, M., 1981. Distribution coefficients of major and trace elements; fractional crystallization in the alkali basalt series of Chaine des Puys (Massif Central, France). Geochimica et Cosmochimica Acta 45 (11), 1997–2016.

Wang, K., Plank, T., Walker, J. D., Smith, E., 2002. A mantle melting profile across the Basin and Range, SW USA. Journal of Geophysical Research: Solid Earth 107 (B1).

Wilcox, R. E., 1999. The Idea of Magma Mixing: History of a Struggle for Acceptance. The Journal of Geology 107 (4), 421–432.

Wilson, M., 1993. Magmatic differentiation. Journal of the Geological Society 150 (4), 611–624.

Winter, J. D., 2010. An introduction to igneous and metamorphic petrology. New York: Prentice Hall.

Yoshinobu, A. S., Barnes, C. G., Nordgulen, Ø., Prestvik, T., Fanning, M., Pedersen, R. B., 2002. Ordovician magmatism, deformation, and exhumation in the Caledonides of central Norway: An orphan of the Taconic orogeny? Geology 30 (10), 883–886.

Zajacz, Z., Halter, W., 2007. LA-ICPMS analyses of silicate melt inclusions in co-precipitated minerals: Quantification, data analysis and mineral/melt partitioning. Geochimica et Cosmochimica Acta 71 (4), 1021–1040.

Appendix

A: Overview of samples and methods applied

Sample#	Description	UTM E33	UTM N33	Thin section	XRF	ICP-MS	ICP-AES	EPMA
127951	Gabbro, medium	481389	7337534	x (pol)	x	x		x
127953	Mafic rock, porphyritic	481375	7336672	x	x	x		
127954	Mafic rock, porphyritic	481375	7336672	x	x	x		
127955	Ol-gabbro	481376	7336684	x	x	x		
127956	Mafic dyke	481395	7336540	x	x	x		
127957	Mafic dyke, porphyritic	481405	7336500	x	x	x		
127958	Diorite, porphyritic	481415	7336419	x (pol)	x	x		x
127959	Mafic rock	481415	7336419	x	x	x		
127960	Gabbro, fine	481427	7336357	x	x	x		
127961	Diorite, porphyritic	481433	7336137	x	x	x		
127962	Mafic dyke	481435	7336129	x	x	x		
127963	Gabbro, fine	481424	7336084	x (pol)	x	x		
127964	Felsic granitoid, cutting gabbro	481421	7335994	x	x	x		
127965	Gabbro, medium	481428	7335928	x	x	x		
127966	Felsic granitoid	481488	7335608	x	x	x		
127967	tonalite with small enclaves	481488	7335608	x				
127968	Diorite, porphyritic	481489	7335613	x	x	x		
127969	Mafic dyke	481489	7335490	x	x	x		
127970	mafic enclaves in tonalite	481489	7335490	x				
127971	Felsic granitoid	481480	7335459	x (pol	x	x		x
127972	Gabbro, medium, foliated	481471	7335431	x	x	x		
127973	Felsic granitoid	481485	7335322	x (pol)	x	x		x
127974	Felsic granitoid, porphyritic	481506	7335206	x	x	x		
127975	Foliert tonalite og fine grd gabbro	481951	7334512	x				
127976	Pegmatitic vein in Gabbro	484330	7334162	x				
127977	Felsic granitoid, porphyritic	484403	7334115	x	x	x		
127978	Mafic dyke	484403	7334115	x	x	x		
127979	Gabbro, fine and medium	484438	7334092	x	x	x		
127980	Gabbro, medium	484438	7334092	x	x	x		
127981	Mafic dyke	485202	7333749	x	x	x		
127982	Mafic dyke	485202	7333749	x	x	x		
127983	Ol-gabbro	481473	7336705	x	x	x		
127984	Gabbro, fine to medium	481609	7336731	x	x	x		
127985	Gabbro, coarse	481733	7336784	x	x	x		
127986	Mafic dyke	481721	7336758	x	x	x		
127987	Diorite, porphyritic	481867	7336575	x (pol)	x	x		x
127988	Gabbro	482210	7336809	x (pol)	x	x		x
127989	Mafic dyke	482309	7336992	x (pol)	x	x		x
127990	Felsic granitoid	482211	7336932	x	x	x		

127991	Ol-gabbro, medium	482151	7336962	x (pol)	x	x		
127992	Gabbro, coarse	482261	7337486	x (pol)	x	x		
127993	Mafic dyke, porphyritic	482384	7337409	x (pol)	x	x		x
127994	Mafic dyke	482616	7337106	x (pol)	x	x		
127995	Ultramafic dyke	482782	7336896	x	x	x		
127996	Gabbro, medium to coarse	482741	7336947	x (pol)	x	x		
127997	Granofels	482871	7337750	x	x	x		
127998	Olivine gabbro			x (pol)	x	x		
127999	Gabbro, medium, lineated	483037	7338181	x	x	x		
128000	Gabbro, coarse	481792	7336306	x (pol)	x	x		x
132401	Mafic dyke	482417	7335670	x	x	x		
132402	Gabbro, medium	482455	7335549	x	x	x		
132403	Gabbro, medium	481881	7335610	x	x	x		
132404	Diorite, porphyritic	481721	7335632	x (2 x pol)	x	x		
127952	Diorite	481328	7337047	x		x	x	
132409	Migmatitic Gt Bt gneiss	489267	7339844	x		x	x	
132410	Granitoid	489356	7339205	x		x	x	
132411	Granitoid	489259	7339172	x		x	x	
132413	Fault rock	489380	7339214	x		x	x	
132414	Granitoid	488460	7339005	x		x	x	
132415	Mafic enclave	481499	7335505	x		x	x	
132416	Mafic enclave	482790	7338747	x		x	x	
132417	Mafic enclave	482790	7338747	x		x	x	
132418	Mafic enclave	482941	7338680	x		x	x	
132420	Mafic enclave	482935	7338660	x		x	x	
132421	Mafic enclave	483609	7338467	x		x	x	
132423	Mafic enclave	483695	7338093	x		x	x	
132424	Mafic enclave	483982	7338145	x		x	x	

B: Whole-rock major- and trace element analyses from XRF

	Sample	127951	127953	127954	127955	127956	127957	127958	127959	127960	127961
	Rock type	Gabbro, medium	Mafic rock, porphyritic	Mafic rock, porphyritic	Ol-gabbro	Mafic dyke	Mafic dyke, porphyritic	Diorite, porphyritic	Mafic rock	Gabbro, fine	Diorite, porphyritic
	UTM E33	481389	481375	481375	481376	481395	481405	481415	481415	481427	481433
	UTM N33	7337534	7336672	7336672	7336684	7336540	7336500	7336419	7336419	7336357	7336137
SiO2	[%]	46.9	49.7	45.7	42.4	45.5	51.2	52.6	49.0	52.0	51.7
Al2O3	[%]	12.1	14.9	13.0	6.91	12.3	14.3	17.2	12.6	16.0	16.3
Fe2O3	[%]	17.0	13.3	14.8	15.9	12.8	12.5	10.8	13.0	11.6	10.8
TiO2	[%]	3.59	3.51	5.38	2.56	2.88	2.79	1.98	2.92	2.65	2.26
MgO	[%]	6.09	4.48	6.11	19.8	10.1	5.48	3.69	8.51	3.07	3.52
CaO	[%]	9.13	7.78	7.56	7.27	10.5	7.31	5.21	8.78	6.65	5.95
Na2O	[%]	2.71	3.77	2.75	1.38	2.54	3.21	3.79	2.32	4.13	4.05
K2O	[%]	0.724	0.949	2.13	0.521	0.629	1.57	2.45	1.05	1.74	2.36
MnO	[%]	0.214	0.187	0.170	0.187	0.177	0.166	0.134	0.169	0.139	0.120
P2O5	[%]	0.482	0.744	0.977	0.400	0.506	0.558	0.386	0.390	0.811	0.632
LOI	[%]	-0.135	0.120	0.235	1.81	0.794	0.400	0.550	0.720	0.360	1.65
Sum	[%]	98.9	99.4	98.8	99.1	98.7	99.5	98.8	99.4	99.1	99.3
As	ppm	<10	<10	<10	<10	<10	<10	<10	<10	<10	<10
Ba	ppm	261	289	566	136	180	429	1040	235	472	807
Cd	ppm	<10	<10	<10	<10	<10	<10	<10	<10	<10	<10
Ce	ppm	39	80	87	35	43	60	69	38	103	89
Co	ppm	50.1	29.1	39.1	94.4	49.4	32.7	23.5	47.8	23.0	22.0
Cr	ppm	108	36.1	141	607	464	168	123	333	60.6	57.7
Cu	ppm	48.9	23.1	20.0	15.9	65.4	15.6	21.6	38.1	25.9	18.6
Ga	ppm	21.1	24.2	24.5	11.6	18.7	22.7	25.3	19.4	26.3	26.4
La	ppm	21	37	35	<15	<15	34	42	16	48	43
Mo	ppm	<3	<3	4.9	<3	3.0	<3	<3	<3	<3	<3
Nb	ppm	25.7	50.8	58.3	22.1	33.7	37.4	32.9	23.1	35.8	47.8
Nd	ppm	34	52	54	28	22	39	37	23	58	60
Ni	ppm	59.6	27.7	101	519	235	90.2	39.5	191	16.6	36.7
Pb	ppm	<5	<5	5.6	<5	<5	<5	10.2	<5	6.7	6.2
Rb	ppm	14.7	16.4	90.8	11.3	8.0	39.7	67.4	22.8	47.1	71.7
Sb	ppm	<15	<15	<15	<15	<15	<15	<15	<15	<15	<15
Sc	ppm	18.8	14.7	13.9	18.7	20.1	16.8	17.7	20.0	11.8	12.7
Sn	ppm	<5	<5	5.7	<5	<5	<5	<5	<5	<5	<5
Sr	ppm	406	688	835	363	651	539	474	483	677	732
Th	ppm	<3	<3	<3	<3	<3	<3	3.8	3.0	3.5	3.1
U	ppm	<5	<5	<5	<5	<5	<5	<5	<5	<5	<5
V	ppm	288	189	211	174	259	159	137	225	167	134
W	ppm	i/a	i/a	i/a	i/a	i/a	i/a	i/a	i/a	i/a	i/a
Y	ppm	36.8	46.5	37.3	19.7	24.3	39.7	31.5	29.5	43.8	44.6
Yb	ppm	<5	<5	<5	<5	<5	<5	<5	<5	<5	<5
Zn	ppm	158	151	157	110	115	129	133	121	112	126
Zr	ppm	148	350	375	158	160	295	517	169	355	591
Cl	[%]	0.064	0.044	0.033	0.049	0.062	<0.02	0.044	0.033	0.094	<0.02
F	[%]	<0.2	<0.2	<0.2	<0.2	<0.2	<0.2	<0.2	<0.2	<0.2	<0.2
S	[%]	0.13	<0.1	<0.1	<0.1	<0.1	<0.1	<0.1	<0.1	<0.1	<0.1
Cs	ppm	<10	<10	<10	<10	<10	<10	<10	<10	<10	<10
Hf	ppm	<5	9.8	10.8	<5	<5	8.3	14.9	<5	9.3	16.3
Sm	ppm	<10	12	12	<10	<10	<10	<10	<10	13	14
Ta	ppm	<5	<5	<5	<5	<5	<5	<5	<5	<5	<5

	Sample	127962	127963	127964	127965	127966	127968	127969	127971	127972	127973
	Rock type	Mafic dyke	Gabbro, fine	Felsic granitoid	Gabbro, medium	Felsic granitoid	Diorite, porphyritic	Mafic dyke	Felsic granitoid	Gabbro, medium, foliated	Felsic granitoid
	UTM E33	481435	481424	481421	481428	481488	481489	481489	481480	481471	481485
	UTM N33	7336129	7336084	7335994	7335928	7335608	7335613	7335490	7335459	7335431	7335322
SiO2	**[%]**	47.3	45.3	62.2	50.0	71.3	58.2	49.9	76.7	48.4	64.0
Al2O3	**[%]**	13.6	12.5	15.5	15.3	13.8	16.9	13.1	11.9	14.8	18.1
Fe2O3	**[%]**	13.6	14.6	6.39	11.5	2.64	7.76	12.7	0.988	12.4	1.10
TiO2	**[%]**	1.79	5.65	0.814	1.52	0.626	1.51	2.28	0.233	1.91	0.204
MgO	**[%]**	9.32	6.84	3.33	7.68	0.623	2.15	8.29	0.312	7.58	0.169
CaO	**[%]**	7.87	8.49	3.93	9.54	1.12	3.98	8.89	0.996	8.78	2.32
Na2O	**[%]**	2.67	2.48	3.52	2.51	2.92	3.65	2.78	2.31	3.15	3.29
K2O	**[%]**	1.06	2.13	2.09	0.396	5.96	4.37	0.714	5.90	0.785	9.73
MnO	**[%]**	0.160	0.172	0.064	0.155	0.026	0.091	0.164	0.019	0.166	0.016
P2O5	**[%]**	0.185	0.943	0.355	0.152	0.102	0.391	0.240	0.029	0.242	0.041
LOI	**[%]**	1.81	0.235	1.02	0.710	0.160	0.480	0.320	0.365	0.585	0.335
Sum	**[%]**	99.4	99.4	99.2	99.6	99.3	99.5	99.4	99.8	98.7	99.3
As	**ppm**	<10	<10	<10	<10	<10	<10	<10	<10	<10	<10
Ba	**ppm**	167	461	239	81	637	829	110	526	241	1300
Cd	**ppm**	<10	<10	<10	<10	<10	<10	<10	<10	<10	<10
Ce	**ppm**	18	96	60	15	24	62	30	20	30	60
Co	**ppm**	50.7	48.9	20.5	42.7	5.4	16.5	46.9	<4	46.9	<4
Cr	**ppm**	366	128	276	330	44.7	116	298	54.2	244	19.3
Cu	**ppm**	<5	46.9	29.3	35.9	<5	7.3	40.0	<5	34.5	<5
Ga	**ppm**	16.9	21.9	24.8	17.2	18.7	26.0	19.1	15.5	19.1	23.0
La	**ppm**	<15	43	27	<15	<15	29	<15	<15	<15	33
Mo	**ppm**	<3	<3	<3	<3	<3	<3	<3	<3	<3	<3
Nb	**ppm**	11.0	44.1	13.6	8.8	8.1	23.8	13.2	4.5	18.1	13.9
Nd*	**ppm**	11	70	26	10	10	32	15	<10	<10	24
Ni	**ppm**	205	140	74.4	122	8.8	20.1	161	<5	134	<5
Pb	**ppm**	<5	<5	<5	<5	11.9	9.3	<5	13.0	<5	7.6
Rb	**ppm**	51.3	94.9	102	5.5	143	138	19.8	130	16.2	259
Sb	**ppm**	<15	<15	<15	<15	<15	<15	<15	<15	<15	<15
Sc	**ppm**	21.2	14.8	5.7	16.5	<5	7.5	18.0	<5	14.7	<5
Sn	**ppm**	<5	6.2	<5	<5	<5	<5	<5	<5	<5	5.3
Sr	**ppm**	338	868	379	301	336	444	327	304	382	1200
Th	**ppm**	<3	<3	8.6	<3	<3	<3	<3	<3	<3	17.1
U	**ppm**	<5	<5	<5	<5	<5	<5	<5	<5	<5	<5
V	**ppm**	213	247	89.1	183	36.1	80.2	207	14.5	196	<5
W	**ppm**	i/a	i/a	i/a	i/a	i/a	i/a	i/a	i/a	i/a	i/a
Y	**ppm**	21.0	34.2	20.1	16.8	5.9	35.0	24.6	<3	19.1	20.1
Yb	**ppm**	<5	<5	<5	<5	<5	<5	<5	<5	<5	<5
Zn	**ppm**	132	137	66.0	97.1	24.7	91.7	113	33.9	116	18.1
Zr	**ppm**	88.3	368	207	66.9	346	657	107	94.2	93.3	133
Cl	**[%]**	0.034	0.032	0.033	0.030	<0.02	0.031	0.021	0.060	0.128	0.030
F	**[%]**	<0.2	<0.2	<0.2	<0.2	<0.2	<0.2	<0.2	<0.2	<0.2	<0.2
S	**[%]**	<0.1	<0.1	<0.1	<0.1	<0.1	<0.1	<0.1	<0.1	<0.1	<0.1
Cs	**ppm**	<10	<10	<10	<10	<10	<10	<10	<10	<10	<10
Hf	**ppm**	<5	11.6	5.9	<5	9.4	18.0	<5	<5	<5	<5
Sm	**ppm**	<10	16	<10	<10	<10	<10	<10	<10	<10	<10
Ta	**ppm**	<5	<5	<5	<5	<5	<5	<5	<5	<5	<5

	Sample	127974	127977	127978	12797 9	127980	127981	127982	127983	127984	127985
	Rock type	Felsic granitoid , porpyr.	Felsic granitoid, porphyr.	Mafic dyke	Gabbro, fine and medium	Gabbro, medium	Mafic dyke	Mafic dyke	Ol-gabbro	Gabbro, fine to medium	Gabbro, coarse
	UTM E33	481506	484403	484403	484438	484438	485202	485202	481473	481609	481733
	UTM N33	7335206	7334115	7334115	733409 2	7334092	7333749	7333749	7336705	7336731	7336784
SiO2	[%]	70.9	57.4	48.4	46.0	46.0	45.5	45.1	41.9	49.1	50.9
Al2O3	[%]	13.9	17.4	13.7	12.9	12.6	13.0	12.6	8.40	14.0	14.3
Fe2O3	[%]	2.95	7.46	12.5	13.4	13.4	14.1	14.2	16.6	12.7	11.6
TiO2	[%]	0.508	1.42	2.12	3.92	3.75	3.11	3.00	7.25	2.08	1.37
MgO	[%]	0.710	2.06	8.74	7.98	8.60	8.63	9.46	12.6	7.36	7.52
CaO	[%]	1.61	4.11	9.06	8.52	8.68	9.65	9.45	9.19	9.24	9.80
Na2O	[%]	2.81	5.10	2.79	2.57	2.64	2.68	2.75	1.71	2.48	2.50
K2O	[%]	5.67	2.71	0.965	1.85	1.65	1.46	1.30	0.833	0.518	0.259
MnO	[%]	0.027	0.095	0.167	0.166	0.171	0.183	0.184	0.201	0.158	0.152
P2O5	[%]	0.123	0.380	0.280	0.866	0.701	0.457	0.451	0.475	0.373	0.184
LOI	[%]	0.200	1.15	0.400	0.630	0.484	0.434	0.420	0.450	0.680	0.609
Sum	[%]	99.4	99.3	99.1	98.8	98.7	99.3	98.9	99.5	98.7	99.2
As	ppm	<10	<10	<10	<10	<10	<10	<10	<10	<10	<10
Ba	ppm	339	790	180	466	357	279	220	221	116	46
Cd	ppm	<10	<10	<10	<10	<10	<10	<10	<10	<10	<10
Ce	ppm	40	67	26	88	69	22	39	30	31	23
Co	ppm	4.7	13.9	46.4	46.3	47.8	49.1	51.3	74.1	39.7	39.1
Cr	ppm	29.9	76.2	348	165	243	273	264	489	248	202
Cu	ppm	<5	11.4	42.0	36.6	40.0	31.6	32.1	35.3	32.3	41.6
Ga	ppm	21.2	26.0	18.1	21.5	19.9	19.3	18.4	15.7	18.8	17.5
La	ppm	20	34	<15	47	33	<15	<15	<15	<15	<15
Mo	ppm	<3	<3	<3	3.2	3.2	<3	<3	<3	<3	<3
Nb	ppm	6.2	39.4	18.4	49.7	43.1	30.1	28.5	33.4	17.4	11.7
Nd*	ppm	14	39	19	53	44	19	21	28	24	15
Ni	ppm	7.3	19.9	195	158	169	156	185	320	114	202
Pb	ppm	10.2	7.5	<5	<5	<5	<5	<5	<5	<5	<5
Rb	ppm	179	89.0	23.8	48.3	42.4	36.6	19.0	21.6	6.5	<5
Sb	ppm	<15	<15	<15	<15	<15	<15	<15	<15	<15	<15
Sc	ppm	<5	10.7	19.3	17.2	18.5	19.5	19.1	27.5	18.4	22.0
Sn	ppm	<5	<5	<5	<5	<5	<5	<5	<5	<5	<5
Sr	ppm	164	483	368	932	744	522	512	461	367	296
Th	ppm	<3	3.4	<3	3.8	3.4	<3	<3	<3	<3	<3
U	ppm	<5	<5	<5	<5	<5	<5	<5	<5	<5	<5
V	ppm	28.0	63.6	211	231	237	254	242	334	182	182
W	ppm	i/a	i/a	i/a	i/a	i/a	i/a	i/a	i/a	i/a	i/a
Y	ppm	11.4	35.3	23.8	32.6	29.1	23.5	23.6	24.4	24.3	21.9
Yb	ppm	<5	<5	<5	<5	<5	<5	<5	<5	<5	<5
Zn	ppm	34.5	87.1	105	129	126	121	125	124	148	96.8
Zr	ppm	241	610	113	298	276	160	150	199	89.3	80.2
Cl	[%]	0.024	0.022	<0.02	0.051	0.032	0.030	0.032	0.062	0.113	0.087
F	[%]	<0.2	<0.2	<0.2	<0.2	<0.2	<0.2	<0.2	<0.2	<0.2	<0.2
S	[%]	<0.1	<0.1	<0.1	<0.1	<0.1	<0.1	<0.1	<0.1	<0.1	<0.1
Cs	ppm	<10	<10	<10	<10	<10	<10	<10	<10	<10	<10
Hf	ppm	5.7	16.9	<5	9.0	7.3	<5	5.0	5.5	<5	<5
Sm	ppm	<10	<10	<10	12	<10	<10	<10	<10	<10	<10
Ta	ppm	<5	<5	<5	<5	<5	<5	<5	<5	<5	<5

	Sample	127986	127987	127988	127989	127990	127991	127992	127993	127994	127995
	Rock type	Mafic dyke	Diorite, porphyritic	Gabbro	Mafic dyke	Felsic granitoid	Ol-gabbro, medium	Gabbro, coarse	Mafic dyke, porphyr.	Mafic dyke	Ultramafic dyke
	UTM E33	481721	481867	482210	482309	482211	482151	482261	482384	482616	482782
	UTM N33	7336758	7336575	7336809	7336992	7336932	7336962	7337486	7337409	7337106	7336896
SiO2	**[%]**	49.4	52.6	43.4	44.1	66.2	43.8	50.7	46.3	46.0	46.3
Al2O3	**[%]**	13.8	17.2	8.88	12.6	17.3	8.00	15.1	11.4	14.2	8.15
Fe2O3	**[%]**	12.5	11.0	15.9	15.1	2.25	15.7	9.46	14.9	14.0	13.5
TiO2	**[%]**	2.40	2.30	1.50	4.25	0.507	1.68	0.931	4.25	2.54	2.27
MgO	**[%]**	7.57	3.31	20.9	8.36	0.825	21.0	8.55	9.29	7.82	15.6
CaO	**[%]**	8.90	6.15	6.11	9.79	2.68	6.37	10.4	9.66	10.7	10.2
Na2O	**[%]**	2.59	4.14	1.35	2.55	4.63	1.24	2.63	2.08	2.37	1.53
K2O	**[%]**	0.811	1.56	0.488	0.734	4.32	0.595	0.254	0.574	0.528	0.604
MnO	**[%]**	0.163	0.148	0.194	0.188	0.030	0.199	0.144	0.196	0.185	0.177
P2O5	**[%]**	0.385	0.592	0.208	0.877	0.126	0.242	0.087	0.579	0.369	0.329
LOI	**[%]**	0.550	0.245	-0.020	0.718	0.325	0.480	0.570	0.290	0.380	0.605
Sum	**[%]**	99.0	99.3	99.0	99.2	99.2	99.4	98.9	99.6	99.1	99.2
As	**ppm**	<10	<10	<10	<10	<10	<10	<10	<10	<10	<10
Ba	**ppm**	249	827	124	238	417	122	68	208	188	168
Cd	**ppm**	<10	<10	<10	<10	<10	<10	<10	<10	<10	<10
Ce	**ppm**	38	73	22	76	33	29	<15	46	27	28
Co	**ppm**	42.9	27.5	99.4	48.2	6.2	97.1	38.6	55.5	49.0	67.6
Cr	**ppm**	297	143	453	173	109	698	300	290	276	1130
Cu	**ppm**	39.5	21.4	23.0	34.7	6.7	51.3	16.1	42.8	57.4	32.2
Ga	**ppm**	20.6	26.6	11.9	20.6	25.7	11.6	15.3	20.6	19.6	12.7
La	**ppm**	22	36	<15	30	20	<15	<15	19	16	17
Mo	**ppm**	<3	<3	<3	<3	<3	<3	<3	<3	<3	<3
Nb	**ppm**	24.0	41.4	13.3	42.3	11.0	15.0	6.8	26.5	21.3	17.3
Nd*	**ppm**	28	52	<10	49	14	14	12	37	26	23
Ni	**ppm**	134	33.5	634	119	22.2	674	128	229	110	444
Pb	**ppm**	<5	7.9	<5	<5	14.9	6.2	<5	<5	<5	<5
Rb	**ppm**	17.1	26.3	11.1	11.7	163	14.1	<5	8.1	7.0	16.6
Sb	**ppm**	<15	<15	<15	<15	<15	<15	<15	<15	<15	<15
Sc	**ppm**	18.0	12.9	13.8	17.3	<5	13.9	20.9	19.6	21.0	25.3
Sn	**ppm**	<5	<5	<5	<5	<5	<5	<5	<5	<5	<5
Sr	**ppm**	463	615	314	865	307	259	441	596	454	183
Th	**ppm**	<3	<3	<3	<3	<3	<3	<3	<3	<3	<3
U	**ppm**	<5	<5	<5	<5	<5	<5	<5	<5	<5	<5
V	**ppm**	220	130	133	297	23.1	157	151	263	259	205
W	**ppm**	i/a	i/a	i/a	i/a	i/a	i/a	i/a	i/a	i/a	i/a
Y	**ppm**	26.6	42.4	14.5	33.1	7.0	18.0	12.0	33.9	23.3	22.8
Yb	**ppm**	<5	<5	<5	<5	<5	<5	<5	<5	<5	<5
Zn	**ppm**	108	121	119	140	24.2	128	73.3	130	106	115
Zr	**ppm**	163	545	82.1	214	72.0	90.8	35.3	181	92.0	130
Cl	**[%]**	0.027	0.130	0.025	0.154	<0.02	0.034	0.027	<0.02	<0.02	0.042
F	**[%]**	<0.2	<0.2	<0.2	<0.2	<0.2	<0.2	<0.2	<0.2	<0.2	<0.2
S	**[%]**	<0.1	<0.1	<0.1	<0.1	<0.1	<0.1	<0.1	<0.1	<0.1	<0.1
Cs	**ppm**	<10	<10	<10	<10	11	<10	<10	<10	<10	<10
Hf	**ppm**	<5	15.2	<5	6.7	<5	<5	<5	5.2	<5	<5
Sm	**ppm**	<10	12	<10	11	<10	<10	<10	<10	<10	<10
Ta	**ppm**	<5	<5	<5	<5	<5	<5	<5	<5	<5	<5

C: Whole-rock trace element analyses from LA-ICP-MS

	Sample	127951	127953	127954	127955	127956	127957	127958	127959	127960	127961	127962	127963	127964	127965	127966	127968	127969
	Rock type	Gabbro, medium	Mafic rock, porphyritic	Mafic rock, porphyritic	Ol-gabbro	Mafic dyke	Mafic dyke, porphyritic	Diorite, porphyritic	Mafic rock	Gabbro, fine	Diorite, porphyritic	Mafic dyke	Gabbro, fine	Felsic granitoid, cutting gabbro	Gabbro, medium	Felsic granitoid	Diorite, porphyritic	Mafic dyke
LOI	%	-0.135	0.120	0.235	1.81	0.794	0.400	0.550	0.720	0.360	1.65	1.81	0.235	1.02	0.710	0.160	0.480	0.320
Be	ppm	1.4	2.8	2.8	<1	1.0	1.7	2.0	1.3	2.5	2.4	1.8	1.7	2.5	<1	<1	2.5	1.1
Y	ppm	39.6	54.7	43.9	14.7	20.2	33.0	29.5	30.0	52.5	48.8	23.4	38.3	19.0	15.5	9.32	40.2	29.4
Zr	ppm	223	571	552	133	142	300	557	191	539	895	103	532	221	72.8	496	975	143
Nb	ppm	29.0	63.9	66.8	19.2	30.9	36.1	34.2	23.9	44.8	53.4	11.4	55.0	12.2	8.81	8.60	25.3	15.3
Cs	ppm	0.79	0.54	3.11	0.67	<0.4	0.92	3.00	0.99	2.62	1.16	0.65	4.42	5.37	<0.4	2.24	4.05	0.47
Ba	ppm	289	348	674	125	182	478	1050	245	569	1000	222	516	250	88.9	773	1020	130
La	ppm	24.1	53.6	49.3	15.6	22.7	35.0	49.7	22.5	67.7	54.0	9.73	54.0	29.3	8.60	14.0	44.8	16.7
Ce	ppm	55.0	113	109	40.2	47.9	80.1	96.0	49.2	138	115	23.3	124	63.6	17.9	25.5	90.8	34.3
Pr	ppm	7.80	15.3	15.5	5.24	6.21	10.8	11.7	6.94	19.1	15.6	3.15	17.3	6.88	2.51	2.76	12.3	5.02
Nd	ppm	37.5	71.7	73.0	23.8	25.9	45.9	45.5	31.6	80.1	70.1	15.8	77.7	26.4	11.9	10.7	52.4	24.9
Sm	ppm	10.4	16.8	17.4	6.55	7.89	13.0	11.5	10.0	21.3	19.1	5.36	20.4	6.85	3.99	2.76	14.3	8.18
Eu	ppm	3.54	4.70	5.79	1.86	2.50	3.73	4.01	2.98	5.12	4.27	1.74	5.40	1.89	1.49	2.43	4.17	2.50
Gd	ppm	10.0	14.5	14.0	4.70	6.50	10.3	8.44	8.63	16.3	14.6	5.00	14.5	5.17	3.88	2.21	11.4	6.95
Tb	ppm	1.60	2.19	2.03	0.686	1.04	1.61	1.28	1.39	2.32	2.22	0.849	2.02	0.836	0.661	0.333	1.77	1.17
Dy	ppm	8.98	12.2	9.98	3.52	5.51	8.97	7.02	7.73	12.5	11.7	5.22	10.3	4.42	3.83	1.93	9.57	6.67
Ho	ppm	1.74	2.33	1.73	0.619	0.970	1.63	1.37	1.36	2.30	2.13	0.967	1.66	0.832	0.742	0.394	1.76	1.25
Er	ppm	4.08	5.38	3.68	1.50	2.58	4.31	3.97	3.70	6.06	5.48	2.61	4.14	2.21	1.99	1.20	4.73	3.25
Tm	ppm	0.534	0.720	0.480	0.184	0.331	0.626	0.604	0.507	0.772	0.746	0.356	0.516	0.306	0.275	0.164	0.628	0.442
Yb	ppm	3.26	4.13	2.63	1.05	1.84	3.77	3.91	2.84	4.48	4.11	2.02	3.01	1.88	1.55	1.08	3.63	2.62
Lu	ppm	0.435	0.549	0.339	0.132	0.230	0.448	0.522	0.348	0.549	0.563	0.281	0.362	0.241	0.207	0.176	0.509	0.347
Hf	ppm	5.75	12.5	12.5	3.78	4.34	8.50	16.2	6.16	15.1	22.5	3.20	14.2	7.21	2.62	14.5	26.3	4.60
Ta	ppm	1.69	4.08	4.10	1.11	2.00	2.32	2.20	1.59	3.33	2.90	0.640	3.40	1.02	0.561	0.633	1.73	1.02
W	ppm	0.40	0.50	0.82	0.42	0.91	0.62	0.65	0.51	1.10	0.63	0.51	0.90	0.77	<0.2	0.44	0.72	0.37
Bi	ppm	<0.5	<0.5	<0.5	<0.5	<0.5	<0.5	<0.5	<0.5	<0.5	<0.5	<0.5	<0.5	<0.5	<0.5	<0.5	<0.5	<0.5
Th	ppm	1.80	1.94	3.66	1.31	2.07	1.48	5.18	3.79	6.26	3.65	1.35	1.97	9.12	0.653	4.21	4.43	2.12
U	ppm	0.544	0.777	1.49	0.499	0.830	0.690	1.45	0.875	1.79	1.67	0.304	1.00	2.41	0.229	1.62	2.52	0.643

	Sample	127971	127972	127973	127974	127977	127978	127979	127980	127981	127982	127983	127984	127985	127986	127987	127988
	Rock type	Felsic granitoid	Gabbro, medium, foliated	Felsic granitoid	Felsic granitoid, porphyritic	Felsic granitoid, porphyritic	Mafic dyke	Gabbro, fine and medium	Gabbro, medium	Mafic dyke	Mafic dyke	Ol-gabbro	Gabbro, fine to medium	Gabbro, coarse	Mafic dyke	Diorite, porphyritic	Gabbro
LOI	%	0.365	0.585	0.335	0.200	1.15	0.400	0.630	0.484	0.434	0.420	0.450	0.680	0.609	0.550	0.245	<0
Be	**ppm**	<1	<1	2.8	1.9	2.6	<1	2.4	2.3	1.3	1.2	1.3	<1	<1	1.4	2.1	<1
Y	**ppm**	3.00	16.4	26.7	13.3	35.8	25.8	39.8	36.5	27.8	25.4	25.7	24.9	23.5	31.6	53.0	17.3
Zr	**ppm**	114	90.4	137	299	838	144	435	423	206	182	245	117	104	253	883	109
Nb	**ppm**	4.15	19.1	14.5	5.76	40.7	20.5	61.3	52.8	33.6	32.0	37.7	19.6	12.6	31.2	53.2	14.9
Cs	**ppm**	1.99	0.88	3.63	1.77	2.74	0.98	1.70	1.48	1.34	<0.4	0.95	<0.4	<0.4	<0.4	0.90	<0.4
Ba	**ppm**	560	251	1370	358	774	205	523	431	313	273	239	138	64.4	297	940	141
La	**ppm**	11.4	13.6	38.0	20.9	40.0	17.9	52.9	44.1	24.9	22.4	23.2	17.0	12.8	30.9	52.6	13.9
Ce	**ppm**	15.5	27.9	82.1	38.0	79.1	37.5	110	91.0	52.8	50.1	53.1	37.8	26.7	61.6	104	27.3
Pr	**ppm**	1.48	3.32	9.51	4.36	10.9	4.92	14.6	12.6	7.26	6.85	7.51	5.27	3.60	7.95	14.0	3.68
Nd	**ppm**	5.37	15.1	34.1	18.1	48.8	22.7	70.3	59.5	36.2	32.9	37.4	25.3	17.5	36.6	68.0	18.1
Sm	**ppm**	1.06	4.46	7.99	4.64	13.2	6.98	18.4	15.8	9.89	9.37	11.0	7.58	5.75	9.96	18.3	5.19
Eu	**ppm**	1.58	1.67	0.729	1.41	3.28	2.11	5.06	4.41	2.99	2.83	3.01	2.37	1.79	2.93	5.72	1.60
Gd	**ppm**	0.71	3.87	5.36	3.66	10.4	5.79	12.7	11.7	7.35	7.30	8.37	6.49	5.20	7.79	14.3	4.43
Tb	**ppm**	0.113	0.665	0.969	0.552	1.62	0.967	1.85	1.68	1.22	1.06	1.15	1.04	0.901	1.27	2.09	0.654
Dy	**ppm**	0.57	3.39	5.36	2.82	7.95	5.45	9.15	8.44	6.18	5.86	6.80	5.57	5.03	6.92	11.2	3.70
Ho	**ppm**	0.110	0.645	0.979	0.533	1.52	1.02	1.53	1.49	1.09	1.03	1.10	1.03	0.977	1.27	2.06	0.672
Er	**ppm**	0.336	1.57	2.77	1.49	4.01	2.69	3.84	3.63	2.79	2.55	2.75	2.71	2.61	3.31	5.08	1.78
Tm	**ppm**	0.051	0.220	0.391	0.216	0.593	0.387	0.503	0.478	0.359	0.335	0.368	0.364	0.389	0.482	0.704	0.235
Yb	**ppm**	0.35	1.35	2.33	1.20	3.03	2.38	2.74	2.38	1.88	1.83	1.92	2.09	2.20	2.53	3.77	1.35
Lu	**ppm**	0.065	0.200	0.296	0.178	0.430	0.318	0.341	0.332	0.267	0.255	0.256	0.292	0.284	0.374	0.601	0.211
Hf	**ppm**	3.87	2.67	4.72	9.73	22.8	4.34	11.3	10.7	5.76	5.03	7.38	3.53	3.11	6.94	21.2	3.37
Ta	**ppm**	0.314	1.02	1.82	0.395	2.22	1.30	3.72	3.31	2.03	1.95	2.68	1.12	0.736	1.89	2.99	0.988
W	**ppm**	<0.2	0.35	0.39	0.26	0.31	0.33	0.89	1.02	0.79	0.67	0.57	<0.2	0.52	0.35	0.45	0.33
Bi	**ppm**	<0.5	<0.5	<0.5	<0.5	<0.5	<0.5	<0.5	<0.5	<0.5	<0.5	<0.5	<0.5	<0.5	<0.5	<0.5	<0.5
Th	**ppm**	3.50	1.45	19.2	3.14	4.09	2.65	5.80	5.10	1.94	1.68	2.37	0.972	1.11	2.53	2.71	1.93
U	**ppm**	0.629	0.418	4.29	1.46	2.08	0.828	1.62	1.48	0.603	0.520	0.767	0.277	0.304	0.600	1.14	0.481

	Sample	127989	127990	127991	127992	127993	127994	127995	127996	127997	127998	127999	128000	132401	132402	132403	132404
	Rock type	Mafic dyke	Felsic granitoid	Ol-gabbro, medium	Gabbro, coarse	Mafic dyke, porphyritic	Mafic dyke	Ultramafic dyke	Gabbro, medium to coarse	Granofels	Mafic dyke	Gabbro, medium, lineated	Gabbro, coarse	Mafic dyke	Gabbro, medium	Gabbro, medium	Diorite, porphyritic
LOI	%	0.718	0.325	0.480	0.570	0.290	0.380	0.605	0.829	0.300	<0	0.285	0.680	0.409	1.01	0.355	0.545
Be	**ppm**	1.5	1.9	<1	<1	1.2	<1	<1	<1	5.4	<1	<1	1.3	1.3	1.6	2.7	4.4
Y	**ppm**	34.8	10.2	16.9	10.3	33.4	26.9	25.8	29.2	52.1	18.5	26.9	16.2	23.9	24.5	35.2	40.9
Zr	**ppm**	238	93.6	96.5	34.5	203	113	169	149	760	92.0	100	93.3	113	175	298	821
Nb	**ppm**	46.0	12.1	14.6	5.66	28.3	25.8	19.2	17.6	49.0	12.6	10.7	18.3	15.6	23.2	28.3	59.2
Cs	**ppm**	0.49	8.29	0.44	<0.4	<0.4	<0.4	0.72	0.41	0.76	<0.4	0.47	<0.4	<0.4	0.69	1.04	3.32
Ba	**ppm**	268	505	142	85.7	211	225	189	139	1120	92.5	171	149	147	158	221	468
La	**ppm**	37.9	20.8	13.8	4.79	23.5	20.1	18.6	16.7	94.8	7.59	8.22	11.6	11.5	18.2	23.3	58.6
Ce	**ppm**	91.4	34.1	30.7	10.8	55.5	42.6	41.9	34.9	195	19.1	19.2	25.9	27.0	42.2	52.4	118
Pr	**ppm**	12.6	3.84	4.02	1.61	8.44	5.91	6.23	4.75	23.5	2.85	2.78	3.47	3.84	5.62	7.45	14.4
Nd	**ppm**	57.2	14.2	17.9	7.27	40.2	26.0	29.4	23.0	94.1	15.1	14.3	16.9	19.3	25.7	36.3	59.3
Sm	**ppm**	15.5	3.45	5.41	2.73	13.0	7.90	8.92	7.16	19.2	4.97	5.12	4.79	5.95	7.44	10.6	13.7
Eu	**ppm**	4.32	2.19	1.64	1.53	3.98	2.56	2.60	2.08	5.11	1.55	1.92	1.92	2.18	2.42	3.31	3.37
Gd	**ppm**	11.3	2.71	4.74	2.67	10.6	7.01	7.25	6.70	15.7	4.78	5.72	4.62	5.76	6.47	9.47	10.6
Tb	**ppm**	1.66	0.427	0.771	0.456	1.67	1.11	1.15	1.13	2.12	0.795	0.970	0.675	0.959	1.03	1.51	1.59
Dy	**ppm**	8.53	2.31	4.21	2.77	8.98	6.62	6.20	6.37	11.4	4.28	5.85	4.06	5.61	5.77	8.30	8.70
Ho	**ppm**	1.49	0.430	0.800	0.529	1.60	1.15	1.08	1.16	2.19	0.799	1.12	0.732	0.999	1.06	1.55	1.63
Er	**ppm**	3.63	1.17	2.08	1.39	3.93	3.00	2.72	3.07	5.32	1.70	2.71	1.53	2.31	2.51	3.54	3.94
Tm	**ppm**	0.467	0.150	0.286	0.197	0.528	0.422	0.360	0.442	0.832	0.230	0.366	0.215	0.310	0.325	0.498	0.529
Yb	**ppm**	2.53	0.91	1.75	1.21	2.87	2.45	1.87	2.51	5.20	1.41	2.04	1.39	1.75	1.90	2.88	3.30
Lu	**ppm**	0.317	0.129	0.214	0.140	0.354	0.280	0.270	0.329	0.728	0.182	0.317	0.163	0.240	0.235	0.369	0.453
Hf	**ppm**	7.35	3.37	3.24	1.24	6.39	3.69	5.22	4.49	17.6	2.90	2.85	2.58	3.38	4.49	7.99	20.3
Ta	**ppm**	3.00	1.47	0.995	0.336	1.92	1.68	1.27	1.11	2.61	0.837	0.565	0.957	0.928	1.26	1.77	3.70
W	**ppm**	0.66	2.34	0.25	0.26	0.22	0.20	0.62	0.55	0.33	<0.2	0.38	0.51	0.24	0.49	1.04	1.00
Bi	**ppm**	<0.5	<0.5	<0.5	<0.5	<0.5	<0.5	<0.5	<0.5	<0.5	<0.5	<0.5	<0.5	<0.5	<0.5	<0.5	<0.5
Th	**ppm**	3.09	3.42	1.74	0.311	1.36	1.18	1.83	1.64	20.2	0.740	1.71	1.51	1.11	1.98	2.83	8.46
U	**ppm**	1.10	1.97	0.521	0.113	0.412	0.367	0.709	0.408	0.783	0.193	0.384	0.562	0.327	0.630	1.12	3.09

D: Analyses of mineral chemistry from LA-ICP-MS

		SiO2	Al2O3	FeO	TiO2	MgO	Mg#	CaO
Sample	**Mineral**	**(wt%)**	**(wt%)**	**(wt%)**	**(wt%)**	**(wt%)**		**(ppm)**
P19.2 UM	Ol	39.99	0.00	30.66	0.01	45.77	0.73	0.01
P19.2 UM	Ol	39.99	0.01	30.32	0.01	44.75	0.73	0.02
P19.2 UM	Ol	39.99	0.01	31.61	0.01	46.31	0.73	0.02
P19.2 UM	Ol	39.99	0.00	36.39	0.01	42.20	0.68	0.01
P19.2 UM	Ol	39.99	0.00	32.75	0.01	41.49	0.70	0.01
P19.2 UM	Ol	39.99	0.01	31.18	0.02	45.38	0.72	0.02
P19.2 UM	Ol	39.99	0.00	30.65	0.01	45.68	0.73	0.01
P19.2 UM	Ol	39.99	0.01	32.20	0.01	46.33	0.72	0.01
P19.2 UM	Ol	39.99	0.00	30.13	0.00	46.11	0.73	0.01
P19.2 UM	Ol	39.99	0.00	29.64	0.01	44.37	0.73	0.01
P19.2 UM	Ol	39.99	0.00	29.93	0.00	47.31	0.74	0.01
P19.2 UM	Ol	39.99	0.00	31.22	0.01	45.56	0.72	0.01
P19.2 UM	Ol	39.99	0.00	30.02	0.01	45.42	0.73	0.01
P19.2 UM	Ol	39.99	0.00	31.44	0.01	48.49	0.74	0.01
P19.2 UM	Ol	39.99	0.01	30.75	0.01	48.44	0.74	0.04
P19.2 UM	Ol	39.99	0.01	31.55	0.01	48.69	0.74	0.01
P19.2 UM	Ol	39.99	0.01	32.46	0.01	48.46	0.73	0.01
P19.2 UM	Ol	39.99	0.02	28.60	0.01	44.20	0.74	0.03
P19.2 UM	Ol	39.99	0.00	31.00	0.01	47.28	0.73	0.01
P19.2 UM	Cpx	52.66	2.98	7.80	1.21	19.55	0.82	20.63
P19.2 UM	Cpx	52.66	2.84	7.53	1.13	20.31	0.83	20.02
P19.2 UM	Cpx	52.66	2.47	7.97	0.96	20.38	0.82	20.30
P5.2	Cpx	52.66	3.75	8.25	1.62	20.80	0.82	20.22
P5.2	Cpx	52.66	2.15	8.02	0.80	19.94	0.82	19.97
P5.2	Cpx	52.66	1.60	7.26	0.59	21.15	0.84	19.76
P5.2	Cpx	52.66	0.96	11.30	0.25	17.06	0.73	20.77
P5.2	Cpx	52.66	0.74	10.86	0.17	17.37	0.74	20.85
P5.2	Cpx	52.66	0.74	10.30	0.13	17.02	0.75	21.29
P5.2	Cpx	52.66	0.82	11.77	0.19	17.92	0.73	21.95
P5.2	Cpx	52.66	1.07	10.70	0.21	17.52	0.75	21.34
P5.2	Cpx	52.66	0.91	11.06	0.19	17.37	0.74	21.73
P19.2 UM	Opx	54.93	0.49	16.38	0.12	31.53	0.78	0.75
P19.2 UM	Opx	54.93	0.47	17.55	0.19	33.37	0.77	0.99
P19.2 UM	Opx	54.93	0.47	16.38	0.16	31.95	0.78	0.88
P19.2 UM	Opx	54.93	0.50	16.03	0.12	31.15	0.78	0.56
P19.2 UM	Opx	54.93	0.79	16.65	0.27	32.30	0.78	0.98
P19.2 UM	Opx	54.93	0.60	17.02	0.19	32.21	0.77	0.74
P5.2	Opx	54.93	0.65	32.37	0.13	25.29	0.58	0.69
P5.2	Opx	54.93	0.94	31.40	0.21	23.12	0.57	0.91
P5.2	Opx	54.93	0.57	31.83	0.16	24.62	0.58	0.96
P5.2	Opx	54.93	0.67	33.18	0.14	23.62	0.56	0.62
P5.2	Opx	54.93	0.69	31.25	0.22	23.44	0.57	1.11
P5.2	Opx	54.93	0.73	33.33	0.16	25.97	0.58	0.70
P5.2	Opx	54.93	0.51	29.43	0.13	24.91	0.60	0.83
P5.2	Opx	54.93	0.60	30.21	0.25	26.19	0.61	1.22
P5.2	Opx	54.93	0.50	29.80	0.13	25.14	0.60	0.84
P5.2	Opx	52.66	0.71	28.45	0.21	23.62	0.60	1.29

		Y	Zr	La	Ce	Pr	Nd	Sm	Eu	Gd	Tb	Dy
Sample	**Mineral**	**(ppm)**	**(ppm)**	**(ppm)**	**(ppm)**	**(ppm)**	**(ppm)**	**(ppm)**	**(ppm)**	**(ppm)**	**(ppm)**	**(ppm)**
P19.2 UM	Ol	0.03	0.14	0.00	0.01	0.00	0.00	0.00	0.00	0.00	0.00	0.00
P19.2 UM	Ol	0.04	0.13	0.02	0.06	0.01	0.02	0.01	0.00	0.01	0.00	0.01
P19.2 UM	Ol	0.07	0.22	0.02	0.06	0.01	0.05	0.02	0.00	0.02	0.00	0.01
P19.2 UM	Ol	0.01	0.03	0.00	0.01	0.00	0.00	0.00	0.00	0.00	0.00	0.00
P19.2 UM	Ol	0.01	0.06	0.00	0.00	0.00	0.00	0.00	0.00	0.00	0.00	0.00
P19.2 UM	Ol	0.04	0.87	0.03	0.07	0.01	0.04	0.01	0.00	0.00	0.00	0.00
P19.2 UM	Ol	0.01	0.33	0.01	0.02	0.00	0.01	0.00	0.00	0.00	0.00	0.00
P19.2 UM	Ol	0.00	0.25	0.00	0.01	0.00	0.01	0.00	0.00	0.00	0.00	0.00
P19.2 UM	Ol	0.03	0.11	0.01	0.02	0.00	0.01	0.00	0.00	0.01	0.00	0.00
P19.2 UM	Ol	0.03	0.20	0.00	0.00	0.00	0.00	0.00	0.00	0.00	0.00	0.00
P19.2 UM	Ol	0.01	0.08	0.00	0.00	0.00	0.00	0.00	0.00	0.00	0.00	0.00
P19.2 UM	Ol	0.01	0.14	0.00	0.00	0.00	0.00	0.00	0.00	0.00	0.00	0.00
P19.2 UM	Ol	0.02	0.16	0.07	0.20	0.02	0.06	0.01	0.00	0.00	0.00	0.01
P19.2 UM	Ol	0.01	0.16	0.00	0.01	0.00	0.00	0.00	0.00	0.00	0.00	0.00
P19.2 UM	Ol	0.07	0.39	0.03	0.07	0.02	0.05	0.03	0.01	0.03	0.00	0.01
P19.2 UM	Ol	0.03	0.12	0.00	0.00	0.00	0.00	0.01	0.00	0.00	0.00	0.01
P19.2 UM	Ol	0.08	0.22	0.00	0.00	0.00	0.00	0.00	0.00	0.01	0.00	0.01
P19.2 UM	Ol	0.07	0.26	0.00	0.00	0.00	0.00	0.00	0.00	0.00	0.00	0.00
P19.2 UM	Ol	0.01	0.17	0.00	0.00	0.00	0.00	0.00	0.00	0.00	0.00	0.00
P19.2 UM	Cpx	23.58	85.48	9.38	30.22	4.64	19.48	6.22	2.15	5.80	0.92	5.28
P19.2 UM	Cpx	31.97	140.00	9.37	35.09	5.56	25.69	7.98	2.52	7.79	1.25	7.08
P19.2 UM	Cpx	80.07	199.73	9.22	38.52	7.94	44.18	18.16	4.00	20.32	3.17	18.09
P5.2	Cpx	37.58	159.43	11.62	43.20	6.84	29.32	9.08	2.92	8.87	1.36	7.54
P5.2	Cpx	68.74	215.40	8.56	37.63	7.52	42.27	16.70	3.55	17.45	2.81	16.01
P5.2	Cpx	50.51	148.42	7.99	33.42	5.88	31.16	12.36	2.82	12.55	1.89	11.01
P5.2	Cpx	51.10	26.43	4.29	20.59	4.43	24.44	10.40	1.05	11.12	1.94	11.18
P5.2	Cpx	39.01	9.51	3.01	13.80	3.05	17.55	8.13	0.80	9.74	1.57	8.82
P5.2	Cpx	33.25	15.04	3.36	15.77	3.10	17.17	6.68	0.73	7.66	1.31	7.79
P5.2	Cpx	61.76	15.93	4.03	21.83	4.97	29.07	13.19	0.99	14.91	2.48	14.69
P5.2	Cpx	50.84	16.27	3.92	17.66	3.94	23.19	10.29	1.02	12.04	1.99	11.70
P5.2	Cpx	34.05	14.06	2.89	13.92	2.97	16.41	7.29	0.89	8.36	1.35	8.03
P19.2 UM	Opx	4.09	6.87	0.01	0.05	0.01	0.09	0.13	0.04	0.20	0.07	0.56
P19.2 UM	Opx	4.57	4.61	0.02	0.11	0.03	0.24	0.20	0.06	0.33	0.09	0.69
P19.2 UM	Opx	5.19	5.20	0.02	0.10	0.03	0.22	0.20	0.05	0.36	0.09	0.79
P19.2 UM	Opx	3.29	4.12	0.01	0.06	0.02	0.14	0.10	0.03	0.20	0.06	0.48
P19.2 UM	Opx	5.59	11.84	0.03	0.15	0.03	0.27	0.21	0.07	0.44	0.12	0.88
P19.2 UM	Opx	3.45	2.91	0.01	0.07	0.02	0.13	0.11	0.04	0.22	0.06	0.52
P5.2	Opx	16.11	1.33	0.03	0.17	0.05	0.42	0.37	0.04	1.00	0.28	2.51
P5.2	Opx	17.90	3.40	1.35	3.26	0.49	2.40	1.21	0.14	2.17	0.49	3.55
P5.2	Opx	19.36	1.18	0.09	0.39	0.10	0.67	0.47	0.04	1.06	0.31	2.75
P5.2	Opx	5.28	0.71	0.12	0.41	0.07	0.24	0.14	0.04	0.39	0.11	1.01
P5.2	Opx	17.47	1.90	0.23	1.43	0.24	1.44	0.56	0.06	1.16	0.30	2.88
P5.2	Opx	5.99	1.40	0.29	0.83	0.13	0.65	0.36	0.05	0.57	0.16	1.30
P5.2	Opx	8.34	1.52	0.19	0.74	0.10	0.40	0.22	0.03	0.44	0.14	1.19
P5.2	Opx	10.98	4.31	2.81	5.48	0.44	1.34	0.47	0.06	0.94	0.25	1.85
P5.2	Opx	4.77	0.90	0.07	0.29	0.05	0.29	0.23	0.03	0.44	0.11	1.00
P5.2	Opx	6.00	2.68	1.52	2.75	0.25	0.90	0.33	0.07	0.59	0.13	1.03

		Ho	Er	Tm	Yb	Lu	Hf	Th	U	Mn	Ti
Sample	**Mineral**	**(ppm)**	**(ppm)**	**(ppm)**	**(ppm)**	**(ppm)**	**(ppm)**	**(ppm)**	**(ppm)**	**(ppm)**	**(ppm)**
P19.2 UM	Ol	0.00	0.01	0.00	0.03	0.01	0.00	0.00	0.00	2391.93	46.37
P19.2 UM	Ol	0.00	0.01	0.00	0.01	0.00	0.00	0.01	0.00	2220.74	60.57
P19.2 UM	Ol	0.00	0.01	0.00	0.02	0.01	0.00	0.00	0.00	2286.61	57.95
P19.2 UM	Ol	0.00	0.00	0.00	0.03	0.01	0.00	0.00	0.00	2713.59	30.17
P19.2 UM	Ol	0.00	0.01	0.00	0.02	0.01	0.00	0.00	0.00	2314.10	58.81
P19.2 UM	Ol	0.00	0.02	0.00	0.04	0.02	0.03	0.01	0.00	2240.14	113.04
P19.2 UM	Ol	0.00	0.00	0.00	0.01	0.00	0.02	0.00	0.00	2405.08	78.47
P19.2 UM	Ol	0.00	0.00	0.00	0.00	0.00	0.00	0.00	0.00	2248.80	64.64
P19.2 UM	Ol	0.00	0.01	0.00	0.04	0.01	0.00	0.01	0.00	2594.44	19.06
P19.2 UM	Ol	0.00	0.01	0.00	0.04	0.01	0.01	0.00	0.00	2233.07	50.57
P19.2 UM	Ol	0.00	0.00	0.00	0.01	0.01	0.00	0.00	0.00	2263.03	28.74
P19.2 UM	Ol	0.00	0.00	0.00	0.02	0.01	0.00	0.00	0.00	2218.58	48.64
P19.2 UM	Ol	0.00	0.00	0.00	0.01	0.01	0.00	0.02	0.00	2329.68	49.63
P19.2 UM	Ol	0.00	0.00	0.00	0.01	0.00	0.00	0.00	0.00	2365.40	42.31
P19.2 UM	Ol	0.00	0.02	0.00	0.02	0.01	0.01	0.00	0.00	2489.10	43.73
P19.2 UM	Ol	0.00	0.01	0.00	0.03	0.01	0.01	0.00	0.00	2437.54	35.73
P19.2 UM	Ol	0.00	0.01	0.01	0.06	0.01	0.01	0.00	0.00	2475.98	51.99
P19.2 UM	Ol	0.00	0.02	0.00	0.06	0.02	0.01	0.00	0.00	2168.11	64.68
P19.2 UM	Ol	0.00	0.01	0.00	0.01	0.01	0.00	0.00	0.00	2526.76	79.43
P19.2 UM	Cpx	0.94	2.49	0.33	2.01	0.28	1.64	0.89	0.19	1179.51	7250.26
P19.2 UM	Cpx	1.31	3.23	0.43	2.85	0.37	2.64	0.74	0.17	1232.91	6745.40
P19.2 UM	Cpx	3.26	7.93	0.99	5.80	0.73	6.98	0.63	0.16	1573.73	5779.41
P5.2	Cpx	1.50	3.99	0.51	3.44	0.43	2.90	0.79	0.17	1267.84	9702.67
P5.2	Cpx	2.87	6.90	0.85	5.11	0.64	8.99	0.60	0.15	1385.77	4794.61
P5.2	Cpx	2.12	5.21	0.64	3.83	0.47	5.13	0.41	0.10	1319.34	3553.58
P5.2	Cpx	2.01	5.11	0.65	4.12	0.52	2.07	0.45	0.31	1678.79	1492.82
P5.2	Cpx	1.63	3.93	0.48	2.77	0.39	0.92	0.07	0.31	1559.24	1032.47
P5.2	Cpx	1.29	3.34	0.46	2.91	0.35	1.37	0.08	0.19	1573.39	797.99
P5.2	Cpx	2.55	5.98	0.72	4.40	0.56	1.32	0.08	0.07	1674.54	1120.70
P5.2	Cpx	2.12	4.93	0.63	3.83	0.48	1.55	0.17	0.23	1637.48	1269.35
P5.2	Cpx	1.42	3.62	0.42	2.43	0.30	1.40	0.10	0.13	1727.59	1127.53
P19.2 UM	Opx	0.15	0.60	0.10	0.88	0.14	0.26	0.03	0.01	2295.94	738.28
P19.2 UM	Opx	0.18	0.71	0.12	0.95	0.15	0.18	0.02	0.01	2524.84	1138.74
P19.2 UM	Opx	0.20	0.72	0.12	0.98	0.16	0.19	0.00	0.00	2353.41	934.71
P19.2 UM	Opx	0.13	0.48	0.09	0.77	0.12	0.15	0.01	0.00	2232.53	744.02
P19.2 UM	Opx	0.22	0.77	0.13	1.07	0.16	0.70	0.02	0.01	2364.28	1619.27
P19.2 UM	Opx	0.13	0.49	0.09	0.83	0.13	0.13	0.00	0.00	2433.70	1166.74
P5.2	Opx	0.65	2.48	0.44	3.32	0.52	0.11	0.01	0.01	3696.79	781.86
P5.2	Opx	0.76	2.38	0.35	2.48	0.40	0.34	2.14	0.28	3679.82	1242.86
P5.2	Opx	0.74	2.59	0.45	3.51	0.54	0.13	0.01	0.03	3672.18	944.49
P5.2	Opx	0.25	0.84	0.15	1.24	0.22	0.10	0.01	0.09	4299.18	812.28
P5.2	Opx	0.73	2.62	0.43	3.19	0.51	0.16	0.08	0.06	3495.35	1291.33
P5.2	Opx	0.30	0.90	0.18	1.44	0.26	0.14	0.31	0.17	3961.56	986.61
P5.2	Opx	0.31	1.15	0.20	1.64	0.25	0.14	0.07	0.05	3508.67	780.83
P5.2	Opx	0.45	1.46	0.25	1.94	0.30	0.24	0.86	1.06	3650.73	1508.43
P5.2	Opx	0.22	0.76	0.12	1.00	0.16	0.09	0.04	0.02	3621.37	772.86
P5.2	Opx	0.24	0.94	0.15	1.32	0.23	0.20	0.61	0.71	3528.30	1281.93

Sample	Mineral	Co (ppm)	Cr (ppm)	Ga (ppm)	Ni (ppm)	Sc (ppm)	Sr (ppm)	V (ppm)	Zn (ppm)
P19.2 UM	Ol	221.41	2.50	0.06	1220.92	2.65	0.19	1.57	264.74
P19.2 UM	Ol	232.05	20.84	0.37	1306.76	2.03	0.06	12.30	230.02
P19.2 UM	Ol	235.34	1.47	0.05	1332.17	1.85	0.15	0.60	193.98
P19.2 UM	Ol	256.12	1.21	0.03	1381.96	1.48	0.02	0.58	305.47
P19.2 UM	Ol	246.43	1.76	0.04	1290.38	2.35	0.01	1.24	275.30
P19.2 UM	Ol	232.01	20.40	0.19	1319.16	2.13	0.08	1.04	177.99
P19.2 UM	Ol	220.19	1.53	0.07	1286.21	1.87	0.01	0.37	180.54
P19.2 UM	Ol	246.99	2.75	0.07	1431.33	1.03	0.01	0.14	171.96
P19.2 UM	Ol	220.96	1.20	0.04	1278.19	1.66	0.01	0.29	194.51
P19.2 UM	Ol	230.91	3.71	0.06	1283.51	2.09	0.01	1.07	189.43
P19.2 UM	Ol	232.10	1.12	0.04	1364.12	1.78	0.01	0.29	141.33
P19.2 UM	Ol	232.37	1.14	0.04	1301.72	1.54	0.02	0.72	138.29
P19.2 UM	Ol	220.65	1.47	0.04	1270.48	1.66	0.07	0.45	156.34
P19.2 UM	Ol	231.50	0.47	0.07	1345.24	1.20	0.02	0.20	153.09
P19.2 UM	Ol	219.25	7.25	0.04	1246.82	1.53	0.13	0.98	260.40
P19.2 UM	Ol	226.66	11.74	0.05	1299.24	2.13	0.01	1.37	177.52
P19.2 UM	Ol	232.60	10.47	0.07	1386.69	1.76	0.01	1.09	178.29
P19.2 UM	Ol	214.60	31.09	0.21	1208.21	2.39	0.01	2.93	158.03
P19.2 UM	Ol	229.26	3.53	0.07	1244.47	1.57	0.01	1.30	234.92
P19.2 UM	Cpx	37.62	4154.49	12.20	198.50	72.27	55.00	311.81	73.98
P19.2 UM	Cpx	36.26	3293.90	12.86	186.76	72.52	57.41	332.95	61.96
P19.2 UM	Cpx	34.27	3148.42	15.72	167.10	82.92	51.86	537.21	56.29
P5.2	Cpx	41.34	4646.24	16.11	238.21	72.29	78.15	374.21	77.99
P5.2	Cpx	36.53	2362.25	13.77	166.04	75.92	45.77	469.93	58.01
P5.2	Cpx	32.34	2002.78	10.86	160.69	63.61	49.33	399.14	59.34
P5.2	Cpx	42.00	671.27	6.02	100.87	78.09	17.80	439.51	108.13
P5.2	Cpx	40.04	953.97	5.06	102.26	104.49	15.76	508.48	109.00
P5.2	Cpx	39.59	591.65	4.64	86.37	76.61	16.60	376.43	99.74
P5.2	Cpx	43.98	873.39	5.12	99.08	94.03	17.40	469.49	107.41
P5.2	Cpx	43.17	597.78	5.60	98.97	79.84	16.84	385.56	104.90
P5.2	Cpx	43.31	453.41	5.60	101.55	66.41	17.48	336.12	111.74
P19.2 UM	Opx	75.43	219.11	4.09	289.41	10.18	0.10	51.91	202.75
P19.2 UM	Opx	77.40	234.12	4.84	311.33	11.51	0.13	55.31	213.78
P19.2 UM	Opx	73.75	129.01	4.08	272.06	12.35	0.08	68.95	199.57
P19.2 UM	Opx	75.26	107.99	4.55	280.26	9.78	0.41	56.24	193.52
P19.2 UM	Opx	75.68	437.36	6.15	284.32	14.23	0.18	111.03	204.78
P19.2 UM	Opx	74.48	253.84	5.55	274.52	11.08	0.04	80.94	205.31
P5.2	Opx	81.61	482.66	6.19	124.46	50.73	-0.10	237.44	500.29
P5.2	Opx	76.97	227.11	6.76	116.34	46.84	3.39	198.03	467.76
P5.2	Opx	70.26	424.27	5.51	105.83	54.47	0.07	226.92	483.92
P5.2	Opx	68.99	403.82	6.25	100.77	48.39	0.09	193.19	518.33
P5.2	Opx	76.90	575.57	6.50	125.87	58.76	0.31	248.95	485.91
P5.2	Opx	82.85	482.16	6.66	113.25	39.12	0.19	201.13	477.73
P5.2	Opx	70.31	344.48	4.21	114.79	43.19	0.17	193.34	412.79
P5.2	Opx	87.04	211.40	5.09	130.18	56.87	0.64	191.52	436.26
P5.2	Opx	77.03	358.19	4.76	118.09	41.26	0.07	189.02	444.24
P5.2	Opx	68.51	343.89	5.07	100.30	29.69	0.81	176.43	392.67

E: Analyses of mineral chemistry from EPMA

Olivine analyses

SiO2	TiO2	Al2O3	FeO	MnO	MgO	CaO	Na2O	Cr2O3	F	Cl	P2O5	K2O	ZrO2	Total	Sample.zone.nr
wt%	wt%	wt%	wt%	wt%	wt%	wt%	wt%	wt%	wt%	wt%	wt%	wt%	wt%	wt%	
36.74	0.00	0.02	26.91	0.30	36.57	0.00	0.00	0.00	0.00	0.01	0.14	0.00	0.00	100.68	127988.7.6
37.75	0.00	0.00	27.19	0.31	36.91	0.00	0.03	0.00	0.00	0.01	0.01	0.00	0.00	102.20	127988.1.3
37.73	0.01	0.00	26.96	0.31	36.77	0.01	0.00	0.00	0.00	0.00	0.02	0.01	0.00	101.82	127988.3.1
37.91	0.04	0.00	26.95	0.33	36.82	0.03	0.00	0.00	0.00	0.00	0.12	0.00	0.00	102.20	127988.3.2
37.70	0.02	0.01	27.00	0.31	36.77	0.03	0.01	0.00	0.00	0.01	0.02	0.00	0.00	101.86	127988.3.3
37.57	0.00	0.00	26.52	0.28	36.96	0.02	0.01	0.00	0.00	0.01	0.21	0.00	0.00	101.58	127988.5.1
36.68	0.01	0.00	27.11	0.31	36.58	0.00	0.02	0.00	0.00	0.00	0.08	0.01	0.00	100.80	127988.5.2
37.61	0.00	0.00	27.03	0.31	36.50	0.00	0.00	0.00	0.00	0.00	0.00	0.00	0.00	101.45	127988.5.3
37.49	0.00	0.00	27.00	0.30	36.49	0.02	0.00	0.00	0.00	0.01	0.00	0.00	0.00	101.30	127988.6.1
37.40	0.05	0.00	27.26	0.29	36.54	0.00	0.00	0.00	0.00	0.00	0.03	0.00	0.00	101.57	127988.6.2
37.28	0.00	0.00	27.31	0.28	36.33	0.00	0.00	0.00	0.00	0.02	0.00	0.00	0.00	101.21	127988.6.3
37.63	0.00	0.00	28.06	0.28	36.30	0.07	0.02	0.00	0.00	0.02	0.08	0.00	0.00	102.45	127988.6.4
37.27	0.04	0.00	27.33	0.31	36.41	0.03	0.00	0.00	0.00	0.00	0.08	0.00	0.00	101.46	127988.8.2
37.71	0.01	0.00	27.62	0.29	36.33	0.00	0.00	0.00	0.00	0.01	0.00	0.02	0.00	101.99	127988.9.3
34.59	0.02	0.02	28.54	0.30	35.79	0.00	0.00	0.00	0.00	0.00	0.04	0.00	0.03	99.34	19.2UM.1.1
35.80	0.00	0.00	28.23	0.26	36.12	0.00	0.00	0.00	0.00	0.01	0.11	0.00	0.05	100.58	19.2UM.1.6
35.87	0.00	0.01	29.20	0.28	35.93	0.01	0.00	0.00	0.00	0.00	0.00	0.00	0.11	101.41	19.2UM.2.4
37.32	0.00	0.00	29.15	0.28	36.02	0.00	0.00	0.00	0.00	0.01	0.11	0.00	0.00	102.87	19.2UM.2.5
36.56	0.00	0.00	29.56	0.25	35.56	0.01	0.00	0.00	0.00	0.02	0.05	0.00	0.00	102.01	19.2UM.2.7
37.96	0.00	0.00	28.60	0.27	36.80	0.01	0.01	0.00	0.00	0.00	0.22	0.01	0.02	103.89	19.2UM.3.1
37.71	0.00	0.00	29.02	0.27	36.40	0.01	0.00	0.02	0.00	0.01	0.16	0.01	0.20	103.80	19.2UM.3.2
37.81	0.01	0.00	28.69	0.29	36.45	0.01	0.03	0.00	0.00	0.01	0.15	0.02	0.00	103.45	19.2UM.3.3
37.69	0.00	0.00	28.42	0.26	36.54	0.04	0.02	0.00	0.00	0.01	0.00	0.00	0.17	103.15	19.2UM.3.6
37.28	0.00	0.00	28.30	0.25	36.64	0.00	0.06	0.01	0.00	0.08	0.00	0.03	0.08	102.70	19.2UM.4.1
37.47	0.02	0.00	28.77	0.27	36.36	0.00	0.05	0.01	0.00	0.02	0.04	0.00	0.00	103.01	19.2UM.4.2
36.39	0.00	0.01	27.83	0.30	36.59	0.05	0.03	0.00	0.00	0.01	0.18	0.02	0.00	101.40	19.2UM.6.4
35.88	0.00	0.01	28.26	0.29	36.29	0.00	0.00	0.00	0.00	0.00	0.18	0.00	0.25	101.16	19.2UM.6.5
36.99	0.00	0.01	28.12	0.25	36.62	0.00	0.04	0.00	0.00	0.02	0.10	0.00	0.06	102.21	19.2UM.7.1
37.17	0.01	0.00	28.20	0.27	36.76	0.01	0.00	0.02	0.00	0.00	0.00	0.00	0.14	102.57	19.2UM.7.2
35.35	0.00	0.00	28.21	0.29	36.49	0.04	0.05	0.00	0.00	0.00	0.11	0.00	0.00	100.53	19.2UM.8.4
38.56	0.43	0.00	28.47	0.26	36.67	0.04	0.01	0.01	0.00	0.00	0.10	0.00	0.00	104.55	19.2UM.8.6

Clinopyroxene analyses

MgO	F	Cl	MnO	Al2O3	Na2O	P2O5	FeO	SiO2	K2O	CaO	TiO2	Cr2O3	ZrO2	Total	Sample.zone.nr
wt%	wt%	wt%	wt%	wt%	wt%	wt%	wt%	wt%	wt%	wt%	wt%	wt%	wt%	wt%	
5.94	0.00	0.00	0.26	1.40	1.29	0.00	20.56	50.78	0.02	21.24	0.06	0.00	-	101.55	127973.1.1
5.63	0.00	0.00	0.27	0.91	1.11	0.00	21.36	50.81	0.00	21.59	0.00	0.03	-	101.70	127973.3.1
5.78	0.00	0.00	0.30	1.17	1.18	0.00	20.83	50.82	0.01	21.39	0.10	0.00	-	101.57	127973.5.2
5.39	0.00	0.01	0.30	1.11	1.18	0.07	21.51	50.54	0.00	21.67	0.05	0.00	-	101.82	127973.6.1
5.95	0.00	0.01	0.25	1.30	1.20	0.02	20.11	51.01	0.03	21.58	0.07	0.00	-	101.51	127973.6.2
15.25	0.00	0.01	0.10	2.25	0.68	0.04	6.53	48.78	0.06	21.80	0.71	0.45	0.00	96.65	19.2UM.6.1
14.79	0.00	0.00	0.18	2.00	0.58	0.00	6.80	48.91	0.03	21.96	0.70	0.38	0.02	96.35	19.2UM.6.2
15.14	0.00	0.00	0.19	2.32	0.67	0.01	6.83	48.23	0.00	21.37	0.94	0.48	0.11	96.28	19.2UM.6.3
14.99	0.00	0.01	0.15	2.61	0.97	0.10	6.72	47.61	0.09	20.94	0.78	0.48	0.00	95.46	19.2UM.8.1
15.38	0.01	0.02	0.13	2.16	0.55	0.13	6.52	47.52	0.02	21.09	0.88	0.26	0.09	94.75	19.2UM.8.3
13.43	0.02	0.02	0.16	1.76	0.39	0.00	9.44	52.56	0.00	23.24	0.54	0.04	0.09	101.67	127993.4.1
14.33	0.00	0.01	0.19	1.11	0.28	0.00	10.57	54.07	0.00	21.95	0.18	0.03	0.05	102.76	127993.6.7
16.89	0.08	0.03	0.11	4.18	0.65	0.00	11.02	53.14	0.26	11.79	0.27	0.01	0.05	98.44	127993.7.3
11.52	0.00	0.03	0.22	1.47	0.80	0.00	13.56	51.47	0.05	21.19	0.19	0.00	0.00	100.50	127951.1.4
11.30	0.00	0.00	0.26	0.52	0.64	0.00	14.60	52.26	0.00	21.78	0.04	0.01	0.00	101.40	127951.2.2
11.38	0.00	0.06	0.25	1.79	0.73	0.00	18.31	48.08	0.08	18.12	4.45	0.00	0.00	103.22	127951.7.4
12.01	0.00	0.02	0.27	2.22	0.86	0.00	13.87	51.48	0.11	19.14	0.28	0.01	0.00	100.26	127951.8.2
11.95	0.00	0.01	0.26	0.92	0.67	0.02	12.46	51.70	0.02	21.86	0.10	0.00	0.00	99.96	127951.8.3
11.31	0.00	0.00	0.31	0.54	0.66	0.01	13.74	52.43	0.00	22.01	0.04	0.00	0.00	101.06	127951.8.4
6.36	0.02	0.01	0.25	1.30	1.32	0.00	19.52	50.90	0.01	21.42	0.20	0.00	0.00	101.30	127973.1.2

Orthopyroxene analyses

MgO	F	Cl	MnO	Al2O3	Na2O	P2O5	FeO	SiO2	K2O	CaO	TiO2	Cr2O3	ZrO2	Total	Sample.zone.nr
wt%	wt%	wt%	wt%	wt%	wt%	wt%	wt%	wt%	wt%	wt%	wt%	wt%	wt%	wt%	
26.60	0.00	0.02	0.31	0.96	0.04	0.00	15.96	52.39	0.00	1.30	0.31	0.07		97.94	127988.3.5
27.04	0.00	0.00	0.31	0.87	0.06	0.00	15.91	53.31	0.00	1.59	0.28	0.02		99.38	127988.4.1
27.11	0.01	0.02	0.31	0.99	0.03	0.01	16.05	53.21	0.00	1.32	0.36	0.04		99.44	127988.4.2
27.19	0.00	0.01	0.32	1.08	0.04	0.03	16.28	53.30	0.00	1.41	0.33	0.04		100.03	127988.4.3
27.20	0.00	0.00	0.32	1.00	0.03	0.00	15.95	52.74	0.00	1.04	0.29	0.02		98.58	127988.5.4
27.65	0.01	0.01	0.27	0.88	0.04	0.00	16.09	53.92	0.00	0.71	0.27	0.03		99.86	127988.8.1
27.55	0.00	0.01	0.32	0.96	0.00	0.02	16.22	54.53	0.00	1.21	0.31	0.04		101.18	127988.9.6
27.27	0.01	0.00	0.32	0.86	0.02	0.03	16.44	53.53	0.00	1.28	0.49	0.02		100.27	127988.9.7
27.50	0.00	0.00	0.29	0.58	0.01	0.04	16.40	51.61	0.02	1.03	0.18	0.03	0.00	97.69	19.2UM.1.3
27.24	0.00	0.00	0.33	0.47	0.03	0.00	16.41	51.10	0.01	1.20	0.16	0.00	0.09	97.04	19.2UM.1.4
27.38	0.00	0.00	0.34	0.49	0.03	0.04	16.31	50.87	0.04	1.06	0.18	0.02	0.19	96.93	19.2UM.1.5
27.82	0.00	0.00	0.27	0.56	0.01	0.00	16.30	52.63	0.00	0.75	0.22	0.01	0.08	98.65	19.2UM.2.1
27.81	0.00	0.00	0.30	0.68	0.03	0.00	16.54	52.13	0.02	0.88	0.24	0.01	0.00	98.63	19.2UM.2.2
27.38	0.00	0.00	0.31	0.58	0.02	0.01	16.38	51.56	0.00	1.11	0.18	0.03	0.08	97.63	19.2UM.2.3
21.01	0.00	0.00	0.42	0.71	0.01	0.03	26.06	53.19	0.00	2.05	0.04	0.00	0.00	103.53	127993.2.1
20.26	0.00	0.00	0.45	0.82	0.03	0.10	27.06	52.87	0.00	1.32	0.18	0.00	0.03	103.12	127993.2.3
20.62	0.00	0.00	0.43	0.93	0.06	0.04	26.81	52.89	0.03	1.22	0.18	0.00	0.00	103.20	127993.2.5
20.50	0.00	0.02	0.46	0.91	0.06	0.01	27.02	53.29	0.00	1.28	0.29	0.01	0.08	103.91	127993.3.1
20.48	0.00	0.03	0.44	0.95	0.06	0.05	26.99	52.29	0.03	1.06	0.16	0.00	0.00	102.54	127993.3.4
21.14	0.00	0.03	0.38	0.87	0.00	0.10	26.34	52.66	0.02	1.07	0.23	0.00	0.00	102.83	127993.5.1
20.89	0.00	0.00	0.46	0.76	0.00	0.00	27.85	52.81	0.00	0.57	0.09	0.00	0.09	103.53	127993.5.2
20.59	0.00	0.00	0.42	0.90	0.03	0.00	27.12	53.05	0.00	1.48	0.22	0.01	0.03	103.84	127993.5.4
20.45	0.00	0.00	0.45	0.95	0.02	0.13	27.21	53.07	0.00	1.30	0.22	0.01	0.00	103.82	127993.5.5
20.82	0.00	0.00	0.46	0.92	0.00	0.00	27.20	53.28	0.00	1.14	0.19	0.01	0.00	104.03	127993.5.6
21.36	0.00	0.02	0.45	0.75	0.02	0.02	27.57	53.18	0.00	0.57	0.15	0.01	0.16	104.25	127993.5.7
21.10	0.00	0.01	0.46	0.75	0.00	0.01	27.33	53.65	0.00	0.51	0.07	0.00	0.00	103.88	127993.6.2
21.05	0.00	0.00	0.50	0.61	0.03	0.13	27.97	53.79	0.00	0.25	0.03	0.00	0.00	104.37	127993.6.3
20.94	0.00	0.01	0.48	1.15	0.06	0.11	27.30	52.48	0.00	0.26	0.00	0.00	0.00	102.79	127993.6.4
20.83	0.00	0.01	0.50	0.69	0.03	0.00	27.26	53.35	0.00	1.34	0.21	0.00	0.00	104.22	127993.6.8
20.32	0.00	0.02	0.44	1.04	0.03	0.02	28.90	53.03	0.00	0.32	0.01	0.00	0.00	104.13	127993.7.2
20.62	0.00	0.01	0.42	0.86	0.05	0.00	27.18	53.27	0.00	1.32	0.19	0.00	0.00	103.92	127993.7.5
20.52	0.00	0.00	0.50	0.89	0.01	0.14	28.26	53.16	0.00	0.69	0.08	0.01	0.00	104.25	127993.7.6
15.05	0.00	0.00	0.84	0.44	0.07	0.00	34.89	50.82	0.00	1.35	0.22	0.00	0.00	103.66	127951.3.2
15.03	0.00	0.01	0.94	0.27	0.06	0.00	35.72	51.12	0.02	0.56	0.00	0.01	0.00	103.74	127951.3.3
14.87	0.00	0.00	0.98	0.28	0.00	0.06	36.13	51.23	0.04	0.45	0.02	0.00	0.00	104.07	127951.3.4
15.59	0.00	0.00	0.75	0.28	0.04	0.00	35.48	50.95	0.00	0.41	0.00	0.00	0.00	103.50	127951.6.1
15.19	0.00	0.02	0.75	0.50	0.09	0.01	33.80	50.59	0.00	1.85	0.00	0.00	0.00	102.78	127951.6.2
15.16	0.00	0.04	0.76	0.48	0.01	0.09	35.44	49.77	0.03	0.58	0.53	0.00	0.00	102.87	127951.6.3
14.96	0.00	0.00	0.76	0.41	0.04	0.02	36.05	51.43	0.00	0.60	0.06	0.00	0.00	104.32	127951.6.4
14.28	0.00	0.00	0.58	0.49	0.03	0.00	36.83	50.95	0.00	1.12	0.19	0.00	0.00	104.46	127951.7.6
14.73	0.00	0.00	0.80	0.36	0.03	0.12	36.39	50.48	0.00	0.41	0.01	0.00	0.00	103.32	127951.10.1
14.69	0.00	0.00	0.82	0.24	0.01	0.00	36.71	50.88	0.00	0.49	0.01	0.00	0.00	103.85	127951.10.2
14.74	0.00	0.00	0.80	0.33	0.04	0.01	35.42	51.05	0.00	1.31	0.01	0.00	0.00	103.71	127951.10.3
14.88	0.00	0.00	0.84	0.30	0.04	0.01	36.08	51.18	0.01	0.44	0.06	0.00	0.00	103.82	127951.10.4
14.94	0.01	0.01	0.80	0.32	0.06	0.00	36.00	50.84	0.02	0.48	0.22	0.00	0.00	103.70	127951.10.5
15.05	0.00	0.01	0.80	0.32	0.04	0.00	35.21	50.60	0.00	0.43	0.00	0.00	0.00	102.45	127951.11.3
15.00	0.00	0.01	0.83	0.51	0.01	0.00	35.59	50.63	0.01	0.45	0.04	0.02	0.00	103.09	127951.11.4
14.44	0.00	0.02	0.74	0.33	0.03	0.09	36.01	50.37	0.00	1.03	0.21	0.00	0.00	103.26	127951.12.1
15.50	0.00	0.01	0.62	0.39	0.07	0.02	34.33	50.78	0.02	1.50	0.15	0.00	0.12	103.50	127951.12.2
14.45	0.00	0.00	0.69	0.44	0.07	0.00	35.07	50.91	0.00	1.67	0.03	0.00	0.00	103.32	127951.12.3
27.39	0.00	0.00	0.30	0.96	0.01	0.10	17.05	53.63	0.04	0.20	0.00	0.00	0.00	99.69	127988.9.4
28.31	0.02	0.01	0.29	0.56	0.03	0.03	17.33	56.11	0.00	0.14	0.00	0.00	0.03	102.86	19.2UM.3.4
27.99	0.00	0.00	0.28	0.79	0.03	0.19	17.74	54.99	0.01	0.13	0.00	0.00	0.13	102.28	19.2UM.4.3

Amphibole analyses

MgO	F	Cl	MnO	Al2O3	Na2O	P2O5	FeO	SiO2	K2O	CaO	TiO2	Cr2O3	ZrO2	Total	Comment
wt%	wt%	wt%	wt%	wt%	wt%	wt%	wt%	wt%	wt%	wt%	wt%	wt%	wt%	wt%	
11.28	0.00	0.25	0.14	11.14	1.98	0.00	15.64	42.79	0.82	11.30	1.24	0.05	0.00	96.57	127989.1.3
14.77	0.01	0.10	0.15	6.23	1.31	0.01	12.74	46.90	0.34	11.18	0.70	0.10	0.00	94.51	127989.2.1
11.33	0.02	0.21	0.14	11.26	1.83	0.00	15.43	42.28	0.90	11.36	1.14	0.01	0.00	95.84	127989.3.3
10.92	0.00	0.32	0.20	11.23	2.09	0.03	16.46	41.70	0.89	11.23	1.20	0.00	0.00	96.18	127989.4.4
11.04	0.04	0.30	0.14	10.87	1.90	0.00	15.90	41.21	0.87	11.19	1.12	0.07	0.00	94.57	127989.4.5
10.93	0.02	0.21	0.18	11.14	2.10	0.07	15.98	40.95	0.79	11.11	1.32	0.05	0.00	94.81	127989.5.4
10.99	0.00	0.29	0.15	11.45	2.17	0.01	16.34	41.94	0.79	11.49	1.10	0.03	0.00	96.67	127989.5.6
12.90	0.00	0.11	0.26	5.17	1.14	0.15	16.14	48.46	0.38	11.11	0.71	0.02	0.00	96.51	127971A.1.6
10.70	0.00	0.13	0.21	10.26	1.49	0.40	16.59	42.74	0.83	11.95	0.60	0.03	0.00	95.88	127971A.2.8
8.86	0.00	0.25	0.21	11.51	2.13	0.05	19.40	40.92	1.28	11.01	1.61	0.02	0.00	97.19	127971A.3.4
8.42	0.00	0.20	0.20	12.16	2.12	0.00	19.60	40.72	1.30	10.89	1.39	0.00	0.00	96.96	127971A.4.5
8.66	0.01	0.21	0.19	12.31	1.74	0.09	19.28	41.12	1.22	11.58	0.91	0.00	0.00	97.26	127971A.4.8
10.79	0.04	0.11	0.10	9.21	1.91	0.16	19.75	44.82	0.86	11.12	0.33	0.02	0.00	99.16	127951.1.3
5.77	0.02	0.20	0.14	16.23	2.28	0.07	23.66	38.91	1.66	10.80	0.26	0.00	0.00	99.96	127951.7.7
9.80	0.04	0.23	0.23	10.63	2.03	0.05	20.40	43.48	0.93	10.52	0.30	0.00	0.00	98.56	127951.11.5
7.97	0.01	0.15	0.18	13.54	2.03	0.08	20.17	39.37	1.12	11.21	0.93	0.05	0.18	96.95	127958.2.4
7.83	0.00	0.15	0.17	13.73	2.06	0.00	20.16	40.15	1.08	11.13	1.03	0.00	0.05	97.49	127958.3.1
7.83	0.01	0.20	0.20	13.57	2.03	0.00	19.88	40.58	1.08	10.96	1.05	0.03	0.15	97.50	127958.4.3
7.84	0.02	0.17	0.17	13.86	2.10	0.12	20.20	39.76	1.08	11.06	1.08	0.02	0.03	97.46	127958.5.4
7.89	0.01	0.18	0.17	14.00	1.96	0.00	20.30	40.11	1.07	11.19	0.95	0.00	0.00	97.78	127958.6.6
11.94	0.00	0.11	0.19	10.79	1.84	0.01	15.19	44.71	0.63	11.16	0.93	0.01	0.00	97.48	128000.1.1
12.22	0.02	0.10	0.18	10.25	1.87	0.02	14.61	45.23	0.65	11.39	1.01	0.04	0.00	97.56	128000.1.2
12.36	0.00	0.08	0.16	9.84	1.62	0.16	14.89	45.53	0.65	11.06	0.99	0.06	0.00	97.37	128000.1.3
13.00	0.00	0.06	0.17	9.54	1.69	0.00	13.87	45.74	0.49	11.40	0.80	0.14	0.00	96.87	128000.3.5
11.10	0.00	0.16	0.16	12.14	1.99	0.03	15.31	43.52	0.68	11.34	0.78	0.00	0.00	97.17	128000.6.1
12.62	0.01	0.08	0.19	9.93	1.74	0.00	14.48	45.91	0.47	11.47	0.81	0.00	0.00	97.67	128000.6.4
8.39	0.03	0.56	0.11	13.37	2.17	0.00	19.40	41.91	1.10	10.92	1.26	0.00	0.00	99.09	127987.9.6
8.41	0.00	0.47	0.14	12.65	2.13	0.00	19.67	41.93	1.04	10.96	1.26	0.06	0.00	98.59	127987.10.5
2.96	0.00	1.74	0.20	12.14	1.67	0.00	29.70	38.07	2.55	10.76	0.79	0.04	0.00	100.22	127973.5.1
9.95	0.00	0.21	0.17	14.26	2.15	0.10	16.06	40.97	1.01	11.28	1.22	0.05	0.00	97.39	128000.5.2
12.71	0.08	0.05	0.10	13.20	1.50	0.13	13.54	43.72	0.89	11.59	0.25	0.00	0.00	97.71	127993.1.4
14.62	0.02	0.03	0.10	30.62	2.10	0.00	13.98	30.07	0.37	7.33	0.00	0.00	0.00	99.22	127988.9.5
14.45	0.03	0.00	0.14	17.80	4.33	0.08	9.51	42.56	0.23	9.65	0.12	0.00	0.00	98.89	19.2UM.3.5
14.95	0.02	0.00	0.14	17.33	4.34	0.00	9.63	42.04	0.17	8.31	0.00	0.00	0.00	96.93	19.2UM.4.4

K-feldspar analyses

MgO	F	Cl	MnO	Al2O3	Na2O	P2O5	FeO	SiO2	K2O	CaO	TiO2	Cr2O3	Total	Sample.zone.nr
wt%	wt%	wt%	wt%	wt%	wt%	wt%	wt%	wt%	wt%	wt%	wt%	wt%	wt%	
0.00	0.02	0.00	0.00	17.50	0.68	0.00	0.02	62.97	15.56	0.00	0.02	0.00	96.76	127971A.6.1
0.00	0.00	0.01	0.00	17.42	0.63	0.00	0.02	61.71	15.29	0.00	0.04	0.00	95.12	127971A.6.3
0.00	0.00	0.00	0.00	17.73	0.81	0.14	0.00	63.10	15.32	0.00	0.00	0.00	97.11	127971A.7.2
0.00	0.01	0.02	0.00	17.59	0.87	0.02	0.01	62.19	15.14	0.00	0.03	0.00	95.87	127971A.7.4
0.00	0.01	0.06	0.00	17.54	0.47	0.01	0.07	62.09	15.86	0.00	0.01	0.00	96.09	127971A.7.5
0.00	0.01	0.02	0.00	17.48	0.66	0.09	0.02	63.13	15.64	0.00	0.00	0.00	97.03	127971A.8.4
0.00	0.00	0.00	0.00	17.73	0.58	0.02	0.06	64.88	15.38	0.00	0.00	0.00	98.66	127973.1.4
0.00	0.00	0.01	0.02	17.81	0.52	0.03	0.02	64.58	15.51	0.00	0.00	0.00	98.49	127973.1.5
0.00	0.02	0.02	0.00	17.79	0.58	0.01	0.03	64.49	15.25	0.00	0.01	0.00	98.20	127973.2.1
0.00	0.03	0.01	0.01	17.76	0.63	0.06	0.04	64.63	15.19	0.00	0.03	0.01	98.38	127973.2.2
0.00	0.00	0.00	0.02	17.40	0.73	0.14	0.01	63.93	15.13	0.29	0.03	0.00	97.67	127973.3.3
0.00	0.00	0.01	0.00	17.78	0.65	0.00	0.03	64.51	15.36	0.00	0.00	0.00	98.33	127973.3.4
0.00	0.00	0.00	0.01	17.75	0.66	0.13	0.00	64.47	15.51	0.00	0.00	0.02	98.53	127973.4.4
0.00	0.02	0.02	0.00	17.86	0.54	0.00	0.02	64.46	15.64	0.00	0.00	0.01	98.55	127973.4.5
0.00	0.00	0.00	0.00	17.82	0.73	0.05	0.00	64.64	15.39	0.00	0.00	0.01	98.64	127973.4.6
0.00	0.00	0.00	0.00	17.77	0.76	0.02	0.05	64.68	15.14	0.00	0.05	0.00	98.47	127973.5.3
0.00	0.00	0.00	0.01	17.80	0.70	0.02	0.09	64.57	15.49	0.00	0.00	0.00	98.67	127973.5.4
0.00	0.03	0.00	0.01	17.74	0.79	0.03	0.03	64.60	15.24	0.00	0.00	0.03	98.49	127973.6.3
0.00	0.00	0.00	0.00	17.78	0.79	0.00	0.00	64.72	15.24	0.00	0.00	0.00	98.52	127973.6.4
0.00	0.00	0.02	0.00	17.80	0.62	0.05	0.04	64.92	15.04	0.00	0.00	0.00	98.49	127973.7.1
0.00	0.00	0.00	0.00	17.71	0.67	0.15	0.00	64.31	15.35	0.00	0.04	0.00	98.22	127973.7.5
0.00	0.00	0.01	0.01	17.73	0.70	0.00	0.01	64.80	15.33	0.00	0.00	0.00	98.59	127973.7.6
0.00	0.00	0.02	0.01	17.78	0.73	0.00	0.00	64.73	15.52	0.00	0.03	0.03	98.84	127973.7.7
0.00	0.00	0.01	0.01	17.75	0.58	0.07	0.32	64.61	15.41	0.00	0.06	0.00	98.82	127973.1.3
0.00	0.00	0.00	0.01	17.81	0.82	0.05	0.03	64.72	15.09	0.00	0.00	0.00	98.53	127973.3.2

Garnet analyses

MgO	F	Cl	MnO	Al2O3	Na2O	P2O5	FeO	SiO2	K2O	CaO	TiO2	Cr2O3	ZrO2	Total	Sample.zone.nr
wt%	wt%	wt%	wt%	wt%	wt%	wt%	wt%	wt%	wt%	wt%	wt%	wt%	wt%	wt%	
3.70	0.00	0.00	2.34	20.13	0.07	0.01	31.14	38.36	0.00	6.39	0.18	0.00	0.00	102.31	127987.1.2
3.52	0.02	0.00	2.23	20.37	0.03	0.00	31.08	38.29	0.01	6.62	0.28	0.00	0.00	102.44	127987.1.3
3.55	0.00	0.00	2.31	20.22	0.01	0.06	30.73	38.27	0.00	6.72	0.24	0.00	0.00	102.11	127987.1.4
3.71	0.00	0.02	2.14	20.52	0.02	0.06	31.43	38.59	0.00	6.44	0.25	0.00	0.00	103.16	127987.5.1
3.85	0.00	0.01	2.03	20.61	0.02	0.00	31.19	38.47	0.01	6.42	0.24	0.00	0.00	102.85	127987.5.2
3.90	0.00	0.00	1.97	21.01	0.00	0.07	31.23	39.61	0.00	5.99	0.13	0.00	0.00	103.91	127987.5.3
3.48	0.00	0.02	2.15	20.72	0.02	0.04	31.68	38.14	0.03	6.27	0.16	0.00	0.00	102.69	127987.9.3
3.54	0.00	0.00	2.06	20.84	0.04	0.00	32.25	38.38	0.02	5.76	0.04	0.01	0.00	102.93	127987.9.4
3.20	0.00	0.00	1.88	20.82	0.05	0.03	32.05	38.68	0.00	6.17	0.07	0.00	0.00	102.95	127987.9.5
3.34	0.00	0.00	1.99	20.73	0.00	0.00	32.26	38.29	0.01	6.06	0.03	0.00	0.00	102.70	127987.10.1
3.71	0.00	0.00	1.98	20.80	0.05	0.00	31.61	38.44	0.01	5.96	0.18	0.00	0.00	102.73	127987.10.2
3.31	0.00	0.00	1.96	20.95	0.00	0.08	31.83	38.44	0.00	6.59	0.10	0.00	0.00	103.27	127987.10.3
3.02	0.00	0.00	3.49	19.82	0.08	0.09	29.77	36.86	0.01	7.28	0.04	0.00	0.00	100.48	127958.6.1
3.07	0.01	0.00	2.98	19.57	0.01	0.01	30.09	36.84	0.00	7.42	0.00	0.01	0.00	100.01	127958.6.2
2.51	0.02	0.01	2.90	19.56	0.07	0.00	29.80	36.40	0.01	8.50	0.09	0.01	0.00	99.87	127958.6.3
2.97	0.00	0.03	3.43	19.66	0.01	0.00	29.69	36.52	0.00	7.64	0.06	0.01	0.03	100.05	127958.7.4
3.00	0.00	0.00	3.58	19.89	0.04	0.00	29.77	36.71	0.03	7.38	0.04	0.00	0.03	100.45	127958.7.5
3.32	0.00	0.00	1.77	20.17	0.00	0.00	33.10	38.01	0.00	6.37	0.05	0.00	0.00	102.79	127951.1.1
3.29	0.00	0.02	1.74	20.37	0.00	0.02	32.61	38.18	0.00	6.68	0.00	0.00	0.00	102.90	127951.1.2
2.15	0.00	0.03	1.60	19.85	0.00	0.00	34.27	37.89	0.00	7.36	0.01	0.00	0.00	103.15	127951.7.1
1.74	0.00	0.00	0.89	19.56	0.06	0.00	32.40	37.42	0.00	9.43	0.15	0.00	0.00	101.65	127951.7.2
2.23	0.00	0.00	1.20	19.74	0.00	0.02	34.85	37.54	0.00	7.07	0.05	0.00	0.00	102.71	127951.7.3

Biotite analyses

MgO	F	Cl	MnO	Al2O3	Na2O	P2O5	FeO	SiO2	K2O	CaO	TiO2	Cr2O3	ZrO2	Total	Sample.zone.nr
wt%	wt%	wt%	wt%	wt%	wt%	wt%	wt%	wt%	wt%	wt%	wt%	wt%	wt%	wt%	
11.07	0.03	0.25	0.12	15.20	0.09	0.05	21.35	35.62	9.42	0.00	2.23	0.03	0.00	95.38	127971A.1.5
11.43	0.01	0.20	0.12	15.40	0.08	0.06	20.04	35.04	9.44	0.00	2.30	0.01	0.00	94.06	127971A.2.9
11.07	0.00	0.20	0.09	15.02	0.07	0.15	20.87	35.00	9.16	0.00	2.21	0.01	0.00	93.80	127971A.3.5
11.29	0.01	0.17	0.11	15.50	0.13	0.00	20.46	35.89	9.33	0.00	2.09	0.00	0.00	94.93	127971A.3.7
10.94	0.00	0.19	0.12	15.30	0.05	0.00	20.56	35.64	9.05	0.00	2.49	0.01	0.00	94.30	127971A.4.4
10.85	0.05	0.18	0.08	15.12	0.10	0.00	21.33	35.28	9.15	0.00	2.12	0.00	0.00	94.22	127971A.4.10
9.20	0.00	0.84	0.19	14.35	0.08	0.13	23.01	34.80	9.53	0.00	3.33	0.00	0.00	95.26	127971A.5.3
8.93	0.00	0.55	0.07	14.35	0.06	0.00	23.95	34.99	9.63	0.00	3.62	0.00	0.00	96.01	127971A.5.6
9.52	0.02	0.43	0.09	14.04	0.14	0.00	24.52	35.78	9.38	0.00	3.73	0.00	0.00	97.53	127951.4.4
9.26	0.02	0.14	0.05	13.57	0.15	0.00	25.63	35.05	9.03	0.00	4.02	0.00	0.00	96.86	127951.7.8
10.00	0.03	0.17	0.07	15.96	0.22	0.00	21.08	36.29	9.40	0.00	3.19	0.01	0.06	96.44	127958.1.5
9.81	0.02	0.16	0.07	16.05	0.24	0.00	21.63	37.00	9.08	0.00	3.12	0.00	0.05	97.17	127958.3.8
10.48	0.03	0.15	0.07	16.19	0.19	0.03	21.06	36.22	9.21	0.00	2.83	0.01	0.00	96.42	127958.4.6
14.16	0.01	0.08	0.05	10.39	3.33	0.10	9.28	40.39	0.92	11.57	4.35	0.37	0.00	94.97	19.2UM.2.6
14.15	0.09	0.08	0.10	8.54	1.40	0.02	13.77	47.22	0.70	11.74	1.33	0.07	0.00	99.13	127993.4.3
14.35	0.15	0.09	0.03	14.77	0.14	0.00	16.41	37.54	9.58	0.00	4.15	0.07	0.09	97.28	127993.4.5
14.27	0.14	0.09	0.02	14.73	0.12	0.00	16.06	37.93	9.56	0.00	4.36	0.08	0.00	97.27	127993.6.9
14.64	0.13	0.09	0.03	14.36	0.11	0.01	15.59	37.75	9.55	0.00	4.60	0.11	0.05	96.94	127993.7.8
19.09	0.05	0.03	0.05	14.93	0.36	0.00	8.09	37.67	8.72	0.00	4.09	0.15	0.00	93.20	127988.3.4
19.53	0.07	0.07	0.03	14.82	0.29	0.00	7.38	38.13	8.89	0.00	4.08	0.30	0.00	93.55	127988.8.3
13.31	0.00	0.17	0.07	15.20	0.22	0.08	17.14	36.76	8.76	0.00	2.89	0.01	0.00	94.56	128000.1.4
11.28	0.01	0.42	0.02	14.40	0.12	0.00	20.95	36.14	8.82	0.00	3.46	0.00	0.00	95.51	127987.1.5
9.83	0.00	0.39	0.06	14.93	0.08	0.10	22.13	35.82	9.08	0.00	3.53	0.00	0.00	95.85	127987.3.4
8.50	0.00	0.37	0.29	12.48	2.11	0.00	20.17	42.01	1.06	10.57	1.11	0.00	0.00	98.59	127987.6.2
11.00	0.04	0.56	0.09	14.54	0.17	0.00	20.74	36.38	8.68	0.00	3.17	0.01	0.00	95.22	127987.10.4
10.32	0.00	0.34	0.08	14.93	0.09	0.00	21.55	36.33	9.01	0.00	3.68	0.00	0.00	96.24	127987.6.3

Plagioclase analyses

MgO	F	Cl	MnO	Al2O3	Na2O	P2O5	FeO	SiO2	K2O	CaO	TiO2	Cr2O3	ZrO2	Total	Sample.zone.nr
0.00	0.03	0.00	0.00	25.39	7.02	0.09	0.11	55.71	0.08	8.06	0.05	0.00	0.00	96.52	127989.1.1
0.02	0.00	0.00	0.02	24.99	7.33	0.08	0.12	55.98	0.16	7.57	0.04	0.00	0.00	96.30	127989.1.4
0.01	0.02	0.00	0.01	24.82	6.99	0.00	0.14	55.37	0.10	8.01	0.05	0.02	0.00	95.52	127989.3.1
0.01	0.00	0.01	0.01	24.29	7.55	0.17	0.07	56.14	0.15	7.29	0.00	0.01	0.00	95.69	127989.3.2
0.02	0.00	0.01	0.02	24.52	7.34	0.07	0.16	55.43	0.12	7.57	0.04	0.00	0.00	95.29	127989.3.4
0.02	0.00	0.00	0.00	25.85	6.32	0.07	0.27	53.06	0.07	9.19	0.08	0.00	0.00	94.91	127989.4.1
0.02	0.01	0.02	0.03	25.39	6.43	0.09	0.20	53.31	0.04	8.93	0.02	0.00	0.00	94.47	127989.4.2
0.00	0.00	0.00	0.03	24.73	7.04	0.14	0.09	54.44	0.10	7.88	0.08	0.00	0.00	94.53	127989.4.3
0.00	0.02	0.01	0.00	25.88	5.95	0.17	0.11	51.54	0.11	9.94	0.05	0.00	0.00	93.76	127989.4.6
0.02	0.02	0.02	0.00	23.22	8.13	0.00	0.08	56.12	0.12	6.32	0.01	0.00	0.00	94.05	127989.4.7
0.01	0.00	0.01	0.00	24.62	7.20	0.02	0.08	54.61	0.11	8.07	0.04	0.02	0.00	94.79	127989.5.1
0.01	0.00	0.00	0.00	25.06	7.38	0.00	0.26	57.99	0.11	7.38	0.19	0.00	0.00	98.38	127989.5.2
0.02	0.01	0.04	0.00	20.92	8.59	0.20	0.23	55.69	0.08	4.77	0.02	0.00	0.00	90.55	127989.5.3
0.01	0.00	0.01	0.01	25.38	6.63	0.00	0.11	54.32	0.08	8.58	0.00	0.00	0.00	95.12	127989.5.5
0.01	0.00	0.00	0.00	25.36	7.15	0.00	0.25	57.75	0.08	7.81	0.09	0.00	0.00	98.49	127989.5.7
0.03	0.02	0.00	0.01	26.15	6.14	0.00	0.21	52.43	0.09	9.83	0.04	0.00	0.00	94.94	127989.5.8
0.02	0.00	0.00	0.02	27.47	5.13	0.02	0.03	51.14	0.06	11.61	0.00	0.01	0.00	95.50	127971A.1.2
0.01	0.00	0.01	0.00	22.68	8.76	0.00	0.10	58.47	0.12	5.35	0.00	0.00	0.00	95.50	127971A.1.7
0.00	0.00	0.00	0.00	23.25	8.11	0.00	0.03	57.30	0.11	6.30	0.00	0.00	0.00	95.09	127971A.2.6
0.00	0.07	0.01	0.02	0.95	0.00	0.08	0.66	29.56	0.08	28.37	37.64	0.00	0.00	97.39	127971A.3.3
0.02	0.00	0.00	0.00	24.75	7.49	0.00	0.02	57.39	0.10	7.45	0.07	0.00	0.00	97.28	127971A.3.6
0.01	0.00	0.00	0.00	23.33	8.19	0.04	0.03	58.40	0.10	6.11	0.01	0.00	0.00	96.20	127971A.4.3
0.00	0.03	0.02	0.00	19.60	9.17	0.08	0.02	69.77	0.36	0.87	0.00	0.00	0.00	99.90	127971A.6.2
0.00	0.00	0.01	0.00	21.46	8.51	0.00	0.02	65.80	0.11	3.20	0.00	0.00	0.00	99.10	127971A.6.5
0.01	0.02	0.00	0.02	19.30	7.61	0.05	0.01	71.46	0.26	0.36	0.03	0.00	0.00	99.09	127971A.7.3
0.00	0.03	0.00	0.00	18.95	11.59	0.00	0.02	65.59	0.09	0.59	0.00	0.01	0.00	96.85	127971A.7.6
0.00	0.00	0.01	0.00	23.76	8.29	0.00	0.00	58.77	0.12	6.22	0.00	0.00	0.00	97.17	127971A.7.7
0.01	0.01	0.00	0.00	19.95	10.98	0.02	0.00	66.36	0.15	1.61	0.00	0.00	0.00	99.09	127971A.8.3
0.01	0.00	0.00	0.01	27.66	5.33	0.05	0.10	53.92	0.09	11.29	0.04	0.00	0.00	98.50	127951.2.4
0.00	0.00	0.00	0.00	23.02	8.63	0.00	0.00	61.44	0.15	5.46	0.00	0.00	0.00	98.69	127951.4.2
0.01	0.00	0.00	0.00	26.30	6.47	0.00	0.01	56.05	0.14	9.10	0.00	0.00	0.00	98.07	127951.8.5
0.00	0.00	0.01	0.00	23.89	8.07	0.00	0.15	60.01	0.25	6.31	0.00	0.00	0.00	98.68	127951.10.6
0.00	0.00	0.00	0.01	27.39	5.52	0.00	0.03	54.18	0.10	10.84	0.01	0.00	0.00	98.07	127951.11.1
0.00	0.00	0.01	0.02	25.72	6.72	0.07	0.05	56.79	0.07	8.60	0.00	0.00	0.00	98.03	127951.11.2
0.00	0.00	0.01	0.00	24.09	8.13	0.00	0.05	59.56	0.17	6.38	0.01	0.00	0.00	98.41	127958.1.1
0.01	0.01	0.02	0.00	24.11	7.60	0.00	0.02	58.69	0.16	6.89	0.00	0.00	0.11	97.61	127958.1.2
0.00	0.00	0.00	0.00	22.86	7.99	0.12	0.07	59.44	0.19	5.80	0.00	0.00	0.00	96.47	127958.1.3
0.00	0.00	0.02	0.00	24.42	7.56	0.07	0.03	57.78	0.12	7.31	0.02	0.01	0.19	97.50	127958.2.1
0.00	0.00	0.01	0.01	23.17	8.47	0.01	0.05	59.66	0.19	5.91	0.04	0.01	0.00	97.53	127958.3.2
0.02	0.00	0.00	0.00	23.56	8.29	0.00	0.19	59.04	0.15	6.41	0.01	0.03	0.13	97.81	127958.4.1
0.00	0.00	0.03	0.00	23.16	8.54	0.00	0.10	59.56	0.13	5.81	0.03	0.00	0.05	97.40	127958.4.2
0.00	0.01	0.00	0.02	24.47	7.57	0.04	0.03	56.76	0.09	7.50	0.01	0.00	0.00	96.49	127958.4.5
0.00	0.01	0.03	0.02	23.21	8.45	0.03	0.04	59.28	0.12	5.79	0.01	0.00	0.06	97.03	127958.4.7
0.01	0.00	0.02	0.00	24.69	7.35	0.10	0.06	55.65	0.12	7.75	0.03	0.01	0.00	95.78	127958.5.1
0.00	0.00	0.01	0.00	24.87	7.01	0.03	0.06	54.90	0.10	8.40	0.00	0.00	0.00	95.38	127958.5.2
0.02	0.00	0.00	0.01	22.74	8.51	0.05	0.08	57.89	0.12	5.84	0.00	0.00	0.19	95.46	127958.5.3
0.00	0.00	0.02	0.00	22.85	8.52	0.00	0.08	58.56	0.11	5.73	0.00	0.00	0.03	95.90	127958.5.5
0.02	0.02	0.00	0.01	23.60	8.23	0.07	0.01	57.79	0.08	6.62	0.00	0.00	0.05	96.47	127958.7.2
0.16	0.00	0.01	0.03	25.89	6.84	0.11	0.31	53.25	0.05	8.57	0.03	0.00	0.00	95.26	19.2UM.6.6
0.57	0.00	0.00	0.03	28.10	5.88	0.12	1.79	49.48	0.04	9.14	0.12	0.00	0.00	95.28	19.2UM.7.3
0.29	0.00	0.00	0.00	28.12	5.02	0.10	0.33	49.36	0.02	11.54	0.04	0.03	0.00	94.83	19.2UM.7.4
0.04	0.00	0.00	0.01	28.07	4.33	0.00	0.12	47.96	0.01	12.87	0.01	0.00	0.16	93.58	19.2UM.8.5
0.00	0.00	0.02	0.00	26.25	6.57	0.00	0.13	56.68	0.16	9.18	0.01	0.00	0.00	99.00	127993.1.1
0.02	0.01	0.00	0.01	26.36	6.50	0.01	0.06	56.65	0.19	9.14	0.00	0.00	0.00	98.95	127993.2.4

Plagioclase analyses, continued

MgO	F	Cl	MnO	Al2O3	Na2O	P2O5	FeO	SiO2	K2O	CaO	TiO2	Cr2O3	ZrO2	Total	Sample.zone.nr
0.00	0.00	0.02	0.03	26.79	6.24	0.02	0.07	56.97	0.18	9.44	0.02	0.00	0.06	99.85	127993.2.6
0.00	0.02	0.00	0.02	26.65	6.37	0.03	0.10	57.11	0.24	9.32	0.01	0.00	0.13	99.99	127993.3.3
0.00	0.01	0.01	0.00	26.64	6.43	0.04	0.09	56.64	0.17	9.28	0.05	0.03	0.00	99.37	127993.4.2
0.01	0.00	0.01	0.00	26.44	6.38	0.00	0.11	56.01	0.17	9.48	0.05	0.00	0.16	98.80	127993.4.6
0.00	0.00	0.00	0.01	26.61	6.43	0.00	0.02	57.13	0.14	9.48	0.04	0.00	0.00	99.85	127993.4.7
0.04	0.01	0.00	0.01	25.94	6.81	0.14	0.17	57.73	0.22	8.69	0.09	0.00	0.00	99.84	127993.5.3
0.00	0.02	0.03	0.00	26.87	6.27	0.01	0.12	57.13	0.17	9.68	0.04	0.00	0.00	100.33	127993.5.8
0.00	0.02	0.00	0.00	26.45	6.45	0.11	0.10	57.10	0.16	9.32	0.03	0.00	0.00	99.74	127993.6.1
0.03	0.02	0.00	0.00	29.22	4.17	0.02	0.20	50.90	0.09	13.27	0.02	0.00	0.00	97.94	127993.6.5
0.00	0.03	0.00	0.01	26.61	6.39	0.00	0.13	57.06	0.15	9.56	0.00	0.02	0.00	99.95	127993.6.10
0.00	0.01	0.02	0.02	27.29	5.90	0.00	0.08	56.23	0.18	10.21	0.02	0.01	0.00	99.95	127993.7.4
0.00	0.01	0.00	0.00	26.47	6.30	0.00	0.11	57.47	0.20	9.32	0.00	0.00	0.10	99.97	127993.7.7
0.01	0.00	0.03	0.00	26.45	6.53	0.04	0.09	57.71	0.20	9.03	0.03	0.02	0.00	100.13	127993.7.9
0.03	0.01	0.01	0.00	29.02	3.85	0.00	0.09	48.88	0.07	13.55	0.06	0.00	0.00	95.55	127988.7.1
0.01	0.00	0.00	0.00	28.83	4.08	0.00	0.07	49.34	0.05	13.07	0.16	0.00	0.00	95.61	127988.7.2
0.05	0.00	0.01	0.00	29.26	3.83	0.00	0.15	48.50	0.05	13.32	0.09	0.00	0.00	95.26	127988.7.3
0.02	0.03	0.00	0.01	29.26	3.85	0.00	0.01	48.76	0.03	13.30	0.08	0.00	0.00	95.33	127988.7.4
0.00	0.01	0.00	0.01	29.38	3.80	0.00	0.01	48.64	0.00	13.49	0.04	0.02	0.00	95.41	127988.7.5
0.00	0.01	0.01	0.02	25.64	6.66	0.03	0.01	55.86	0.10	8.94	0.00	0.00	0.00	97.27	128000.2.6
0.01	0.00	0.03	0.00	27.98	4.93	0.00	0.14	52.71	0.07	11.59	0.09	0.02	0.00	97.56	128000.3.3
0.00	0.00	0.00	0.02	27.30	5.42	0.02	0.08	53.76	0.05	10.79	0.00	0.00	0.00	97.43	128000.3.4
0.00	0.04	0.00	0.01	27.53	5.28	0.00	0.08	53.43	0.04	11.06	0.05	0.00	0.00	97.50	128000.5.5
0.00	0.01	0.02	0.03	24.83	7.23	0.05	0.04	57.48	0.06	7.69	0.02	0.00	0.00	97.44	128000.6.5
0.00	0.02	0.03	0.00	24.68	7.55	0.00	0.07	59.06	0.10	7.47	0.01	0.00	0.00	98.97	127987.2.1
0.02	0.00	0.01	0.01	24.67	7.28	0.08	0.13	58.15	0.17	7.48	0.00	0.00	0.00	97.98	127987.2.2
0.00	0.00	0.07	0.00	24.91	7.22	0.12	0.05	58.59	0.15	7.49	0.00	0.00	0.00	98.59	127987.2.3
0.01	0.00	0.00	0.00	24.43	7.65	0.00	0.08	59.50	0.14	6.75	0.05	0.00	0.00	98.61	127987.3.3
0.02	0.00	0.00	0.00	27.84	5.46	0.03	0.05	54.41	0.10	11.18	0.00	0.00	0.00	99.09	127987.4.1
0.00	0.00	0.00	0.00	24.60	7.36	0.05	0.58	58.43	0.11	7.43	0.27	0.00	0.00	98.81	127987.4.2
0.00	0.00	0.00	0.00	24.82	7.42	0.05	0.06	59.33	0.10	7.36	0.00	0.00	0.00	99.15	127987.6.1
0.01	0.00	0.00	0.00	26.86	6.01	0.03	0.05	55.77	0.08	9.82	0.01	0.00	0.00	98.65	127987.7.1
0.00	0.00	0.00	0.00	24.34	7.83	0.10	0.05	59.68	0.09	6.89	0.00	0.00	0.00	98.97	127987.7.2
0.01	0.00	0.00	0.01	24.51	7.83	0.01	0.07	59.71	0.13	6.69	0.00	0.03	0.00	98.98	127987.9.1
0.00	0.00	0.02	0.01	19.08	11.30	0.07	0.13	70.40	0.14	0.49	0.00	0.00	0.00	101.62	127973.3.5
0.00	0.00	0.00	0.00	19.22	10.34	0.01	0.08	70.16	0.21	0.45	0.05	0.00	0.00	100.52	127973.3.6
0.00	0.00	0.00	0.00	21.16	9.61	0.06	0.02	66.44	0.18	2.85	0.03	0.00	0.00	100.35	127973.3.7
0.00	0.02	0.00	0.02	19.37	11.45	0.00	0.08	69.35	0.08	0.71	0.00	0.01	0.00	101.07	127973.4.1
0.00	0.00	0.01	0.02	20.95	10.27	0.00	0.03	65.98	0.16	2.54	0.00	0.00	0.00	99.95	127973.4.2
0.00	0.03	0.00	0.00	19.59	11.08	0.00	0.04	68.97	0.08	0.88	0.00	0.00	0.00	100.66	127973.4.3
0.00	0.00	0.02	0.00	21.25	10.02	0.00	0.11	65.85	0.20	2.75	0.03	0.00	0.00	100.23	127973.5.6
0.00	0.00	0.00	0.00	19.39	10.66	0.00	0.04	71.09	0.12	0.51	0.00	0.00	0.00	101.82	127973.7.3
0.01	0.00	0.01	0.00	20.94	10.19	0.09	0.00	66.71	0.10	2.66	0.05	0.00	0.00	100.73	127973.7.4
0.07	0.01	0.00	0.00	27.05	5.50	0.06	0.11	52.92	0.07	10.43	0.03	0.00	0.00	96.24	127988.1.2
0.00	0.02	0.01	0.02	29.23	4.15	0.03	0.02	50.54	0.04	13.19	0.03	0.01	0.00	97.27	127988.2.1
0.00	0.02	0.01	0.00	29.46	3.92	0.02	0.05	50.49	0.04	13.26	0.00	0.00	0.00	97.25	127988.2.2
0.01	0.00	0.01	0.00	29.07	4.07	0.04	0.05	49.80	0.05	13.30	0.07	0.00	0.00	96.46	127988.9.1
0.00	0.00	0.00	0.01	29.30	3.89	0.08	0.04	49.68	0.02	13.01	0.05	0.01	0.00	96.10	127988.9.2

Scapolite	MgO	F	Cl	MnO	Al2O3	Na2O	P2O5	FeO	SiO2	K2O	CaO	TiO2	Cr2O3	ZrO2	Total	Sample.zone.nr
	0.00	0.01	0.42	0.01	25.22	4.18	0.00	0.06	46.07	0.13	16.36	0.00	0.00	0.00	92.36	128000.2.1
	0.01	0.03	0.45	0.03	25.12	4.38	0.00	0.05	46.81	0.15	16.06	0.00	0.00	0.00	92.98	128000.2.5
	0.00	0.00	0.37	0.02	25.56	4.07	0.00	0.04	46.49	0.13	16.77	0.01	0.00	0.00	93.37	128000.3.1
	0.01	0.00	0.48	0.01	25.19	4.23	0.01	0.07	46.36	0.18	16.30	0.00	0.00	0.00	92.73	128000.3.2
	0.01	0.00	0.44	0.01	25.62	4.23	0.14	0.05	46.71	0.14	16.64	0.04	0.00	0.00	93.94	128000.5.4
	0.00	0.00	0.67	0.01	24.48	5.10	0.08	0.03	48.25	0.20	14.94	0.00	0.00	0.00	93.60	128000.6.2
Clinozoisite																
	0.06	0.03	0.01	0.09	26.29	0.09	0.07	7.27	38.66	0.02	23.35	0.16	0.00	0.00	96.08	127971A.1.3
	0.06	0.00	0.00	0.09	24.78	0.06	0.00	8.36	36.94	0.00	23.59	0.21	0.00	0.00	94.09	127971A.2.7
	0.01	0.00	0.00	0.11	26.43	0.04	0.16	8.00	38.80	0.00	23.44	0.09	0.00	0.00	97.07	127958.3.6
	0.04	0.00	0.00	0.12	26.76	0.00	0.05	6.10	37.50	0.00	24.06	0.03	0.00	0.00	94.66	127958.4.4
Rutile																
	0.00	0.00	0.00	0.00	0.08	0.00	0.00	0.59	0.00	0.00	0.07	96.45	0.00	0.00	97.19	128000.4.1
	0.00	0.01	0.03	0.00	0.09	0.00	0.00	0.59	0.00	0.00	0.05	96.29	0.03	0.00	97.08	128000.5.3
	0.00	0.00	0.00	0.00	0.08	0.00	0.07	0.30	0.00	0.01	0.03	97.76	0.04	0.00	98.29	128000.6.3
Titanite																
	0.02	0.00	0.01	0.06	0.87	0.01	0.00	0.33	29.53	0.01	28.95	38.16	0.00	0.00	97.95	127971A.1.4
	0.03	0.04	0.00	0.05	0.86	0.00	0.05	0.66	29.13	0.02	28.58	38.51	0.00	0.00	97.91	127971A.1.8
	0.07	0.07	0.00	0.05	1.08	0.04	0.00	0.83	29.59	0.15	28.72	38.18	0.02	0.00	98.77	127971A.4.9
	0.00	0.00	0.06	0.03	1.45	0.04	0.00	0.46	29.20	0.03	28.81	36.79	0.01	0.00	96.86	127971A.5.1
	7.34	0.04	0.30	0.15	13.77	2.23	0.09	22.66	40.35	1.32	11.21	0.50	0.01	0.00	99.89	127951.2.3
	0.00	0.02	0.01	0.04	0.78	0.03	0.27	0.35	30.10	0.00	27.95	38.67	0.00	0.00	98.20	128000.4.2
	0.07	0.03	0.01	0.04	0.97	0.01	0.06	0.50	30.14	0.01	28.62	37.81	0.01	0.00	98.25	128000.4.3
Al-rich amphibole																
	13.72	0.04	0.06	0.12	10.92	2.86	0.06	9.64	41.65	1.13	11.40	4.59	0.24	-	96.39	127988.1.1
	4.07	0.00	1.72	0.24	15.63	2.14	0.00	25.83	37.75	1.78	10.26	0.10	0.00	-	99.13	127987.3.1
	4.88	0.00	2.05	0.23	14.47	2.06	0.07	25.34	37.96	1.78	10.57	0.13	0.00	-	99.07	127987.3.2
	4.85	0.00	2.22	0.20	14.26	2.27	0.02	25.44	38.10	1.72	10.30	0.15	0.00	-	99.02	127987.8.1
	4.58	0.00	2.58	0.17	14.29	2.15	0.00	26.14	37.86	1.88	10.57	0.11	0.00	-	99.75	127987.8.2
	7.11	0.02	0.19	0.16	14.37	2.05	0.03	20.69	39.25	1.15	10.85	1.00	0.01	0.11	96.94	127958.1.4
	15.06	0.00	0.05	0.06	10.30	3.29	0.05	8.46	39.51	0.97	11.75	4.00	0.63	0.02	94.14	19.2UM.8.2
	15.06	0.00	0.05	0.06	10.30	3.29	0.05	8.46	39.51	0.97	11.75	4.00	0.63	0.02	94.14	19.2UM.8.2
	11.33	0.02	0.17	0.23	6.93	1.67	0.00	19.25	46.70	0.46	10.84	0.92	0.04	0.00	98.51	127951.8.1

F: Detection limits for LA-ICP-MS and EPMA

LA-ICP-MS mineral major and trace element analyses

Element	Detection limit (ppm)
Li	0.1796
Mg	3.2140
Al	0.4688
Si	24.386
P	3.7560
Ca	33.438
Sc	0.0415
Ti	1.2050
V	0.0194
Cr	0.2956
Mn	0.1140
Fe	3.7080
Co	0.0153
Ni	0.5658
Zn	0.3964
Ga	0.0183
Rb	0.0205
Sr	0.0116
Y	0.0036
Zr	0.0540
Nb	0.0015
Ba	0.0185
La	0.0010
Ce	0.0011
Pr	0.0010
Nd	0.0044
Sm	0.0046
Eu151	0.0020
Eu153	0.0022
Gd	0.0062
Tb	0.0011
Dy	0.0044
Ho	0.0011
Er	0.0036
Tm	0.0008
Yb	0.0036
Lu	0.0007
Hf	0.0030
Ta	0.0017
W	0.0060
Pb	0.0049
Th	0.0005
U	0.0004

LA-ICP-MS whole-rock trace element analyses

Element	Detection limit (ppm)
Be	1
Y	0.2
Zr	1.1
Nb	0.07
Ba	0.9
La	0.1
Ce	0.07
Pr	0.03
Nd	0.21
Sm	0.13
Eu	0.03
Gd	0.3
Tb	0.04
Dy	0.16
Ho	0.04
Er	0.09
Tm	0.04
Yb	0.2
Lu	0.04
Hf	0.13
Ta	0.04
W	0.2
Bi	0.5
Th	0.03
U	0.01
Cs	0.4

EPMA mineral chemistry analyses

Oxide/ element	Nr. and name of standard	Chemical formula	Detection limit (ppm)	Conc. of oxide or element in standard
MgO	34. Olivine	$(Mg,Fe)_2SiO_4$	200	50,43 % MgO
F	4. Apatite	$Ca_5(PO_4)_3F$	300	3,77 % F
Cl	45. Tugtupite	$Na_4BeAlSi_4O_{12}Cl$	200	7,58 % Cl
MnO	46. Willemite	$(Zn,Mn)_2SiO_4$	200	4,82 % MnO
Al2O3	35. Plagioclase An65	$(Ca,Na)Al(Al,Si)Si_2O_8$	200	28,53 % Al_2O_3
Na2O	1. Albite	$NaAlSi_3O_8$	200	11,59 % Na_2O
P2O5	4. Apatite	$Ca_5(PO_4)_3F$	700	18,42 % P
FeO	34. Olivine	$(Mg,Fe)_2SiO_4$	200	7,51 % FeO
SiO2	34. Olivine	$(Mg,Fe)_2SiO_4$	300	41,58 % SiO_2
K2O	41. Sanidine	$KaAlSi_3O_8$	200	12,11 % K2O
CaO	29. Kaersutite	$Ca_2Na(Mg,Fe)_4TiSi_6Al_2O_{22}(OH)_2$	400	11,56 % CaO
TiO2	40. Rutile	TiO_2	400	59,94 % Ti
Cr2O3	37. Pyrope Garnet	$Mg_3Al_2Si_3O_{12}$	200	0,58 % Cr_2O_3

G: Whole-rock chemistry from ALS

Method	WEI-21	ME-ICP61	ME-ICP61	ME-ICP61	ME-ICP61	ME-ICP61	ME-ICP61	ME-ICP61	ME-ICP61	ME-ICP61	ME-ICP61	ME-ICP61	ME-ICP61	ME-ICP61	ME-ICP61	ME-ICP61
Analyte	Recvd Wt.	Ag	Al	As	Ba	Be	Bi	Ca	Cd	Co	Cr	Cu	Fe	Ga	K
Units	kg	ppm	%	ppm	ppm	ppm	ppm	%	ppm	ppm	ppm	ppm	%	ppm	%
LOR	0.02	0.5	0.01	5	10	0.5	2	0.01	0.5	1	1	1	0.01	10	0.01
Sample Description																
BKS127952	0.03	<0.5	9.43	<5	1190	2.2	10	3.59	<0.5	24	28	22	7.58	30	1.67
BKS132409	0.03	<0.5	8.86	<5	970	4.4	2	0.83	<0.5	28	53	37	4.77	20	2.95
BKS132410	0.04	<0.5	8.46	<5	690	3.1	3	0.61	<0.5	17	55	16	4.32	20	2.53
BKS132411	0.04	<0.5	8.93	6	590	3.7	<2	0.86	<0.5	18	50	13	5.06	20	2.65
BKS132413	0.03	<0.5	8.31	<5	540	3.5	4	1.27	<0.5	35	70	23	5.63	20	2.17
BKS132414	0.04	<0.5	9.80	<5	750	4.2	2	1.07	<0.5	21	63	17	6.19	30	2.86
BKS132415	0.03	<0.5	6.08	<5	160	0.8	21	6.01	0.6	62	202	39	9.89	20	0.50
BKS132416	0.03	<0.5	6.49	<5	140	0.6	8	5.67	<0.5	60	273	63	9.18	20	0.07
BKS132417	0.04	<0.5	6.26	9	280	0.8	10	5.85	<0.5	65	248	36	9.77	20	0.27
BKS132418	0.03	<0.5	6.91	<5	140	0.7	9	6.39	<0.5	49	116	41	9.17	20	0.29
BKS132420	0.03	<0.5	7.40	<5	200	0.9	14	6.16	0.5	48	43	38	10.75	20	0.42
BKS132421	0.03	<0.5	7.07	<5	110	1.2	14	6.28	0.5	43	180	39	8.79	20	0.80
BKS132423	0.04	<0.5	6.32	<5	190	0.8	9	6.09	<0.5	58	218	37	9.33	20	0.55
BKS132424	0.03	<0.5	7.24	<5	150	0.5	4	6.07	<0.5	61	177	52	9.62	20	0.43

Method	ME-ICP61	ME-ICP61	ME-ICP61	ME-ICP61	ME-ICP61	ME-ICP61	ME-ICP61	ME-ICP61	ME-ICP61	ME-ICP61	ME-ICP61	ME-ICP61	ME-ICP61	ME-ICP61	ME-ICP61	ME-ICP61
Analyte	La	Mg	Mn	Mo	Na	Ni	P	Pb	S	Sb	Sc	Sr	Th	Ti	Tl
Units	ppm	%	ppm	ppm	%	ppm	ppm	ppm	%	ppm	ppm	ppm	ppm	%	ppm
LOR	10	0.01	5	1	0.01	1	10	2	0.01	5	1	1	20	0.01	10
Sample Description															
BKS127952	40	1.61	1110	3	3.06	15	2390	12	0.07	<5	16	760	<20	1.11	10
BKS132409	90	0.85	631	2	1.40	32	560	22	0.21	<5	14	161	20	0.54	10
BKS132410	30	1.22	598	<1	1.53	25	670	16	0.01	<5	14	130	20	0.62	10
BKS132411	40	0.96	839	2	1.70	26	810	26	0.02	<5	15	189	20	0.50	10
BKS132413	50	1.69	514	2	1.60	119	620	15	0.07	<5	18	231	20	0.56	10
BKS132414	70	1.25	792	3	1.80	25	820	21	0.01	<5	18	182	30	0.37	<10
BKS132415	10	5.73	1360	3	1.72	249	1500	<2	0.12	<5	23	481	<20	1.74	20
BKS132416	<10	4.61	1350	2	0.70	171	640	9	0.18	5	25	287	<20	1.13	10
BKS132417	10	6.43	1300	3	0.79	297	1440	5	0.08	<5	22	443	<20	1.34	20
BKS132418	10	3.68	1250	1	1.92	115	1170	7	0.12	5	23	374	<20	1.45	10
BKS132420	10	3.20	1430	2	1.97	53	1450	4	0.03	<5	26	414	<20	1.62	20
BKS132421	10	3.47	1250	2	2.02	72	1470	11	0.05	<5	24	427	<20	1.66	10
BKS132423	10	5.31	1300	2	1.82	219	1430	<2	0.08	7	24	436	<20	1.50	10
BKS132424	10	5.36	1350	1	1.75	196	990	<2	0.08	<5	22	344	<20	1.02	10

Sample Description	Method	ME- ICP61	ME- ICP61	ME- ICP61	ME- ICP61	ME- MS81	ME- MS81	ME- MS81	ME- MS81	ME- MS81	ME- MS81	ME- MS81	ME- MS81	ME- MS81	ME- MS81	ME- MS81
	Analyte	U	V	W	Zn	Ba	Ce	Cr	Cs	Dy	Er	Eu	Ga	Gd	Hf	Ho
	Units	ppm	ppm	ppm	ppm	ppm	ppm	ppm	ppm	ppm	ppm	ppm	ppm	ppm	ppm	ppm
	LOR	10	1	10	2	0.5	0.5	10	0.01	0.05	0.03	0.03	0.1	0.05	0.2	0.01
BKS127952		<10	93	10	182	1250	85.1	40	0.87	7.55	3.37	4.19	31.1	10.05	17.3	1.45
BKS132409		<10	90	30	97	916	194.5	60	0.86	11.20	6.34	2.86	24.6	13.55	7.5	2.36
BKS132410		<10	82	20	61	796	115.0	80	1.22	6.26	3.55	1.39	28.4	5.87	12.6	1.28
BKS132411		<10	75	20	108	613	98.2	60	4.23	7.53	4.31	1.60	26.3	8.67	8.3	1.64
BKS132413		<10	110	40	76	575	129.0	90	3.32	10.25	5.42	2.37	30.2	12.10	6.9	2.13
BKS132414		<10	90	30	120	775	156.0	90	3.74	11.20	6.65	2.43	31.5	12.60	7.5	2.44
BKS132415		<10	213	30	137	162.5	32.7	310	0.52	6.01	2.59	2.45	20.8	7.21	3.8	1.06
BKS132416		<10	207	70	139	135.5	15.8	390	4.04	6.23	3.16	1.62	22.1	5.67	2.7	1.32
BKS132417		<10	198	30	132	278	33.4	370	1.11	5.31	2.47	2.11	21.8	6.61	3.6	1.01
BKS132418		<10	204	20	132	140.5	26.1	170	0.11	5.94	2.74	2.09	23.1	6.90	3.7	1.13
BKS132420		<10	224	20	151	191.5	35.8	60	0.13	6.07	3.02	2.26	25.2	7.50	4.6	1.22
BKS132421		<10	220	20	131	107.0	37.8	260	0.16	6.63	2.77	2.38	22.7	7.46	4.2	1.12
BKS132423		<10	210	20	130	186.0	32.4	340	0.17	5.41	2.68	2.28	22.9	7.48	3.5	1.14
BKS132424		<10	189	<10	118	148.5	21.0	250	0.68	4.02	2.06	1.42	19.9	4.52	2.0	0.79

Sample Description	Method	ME- MS81	ME- MS81	ME- MS81	ME- MS81	ME- MS81	ME- MS81	ME- MS81	ME- MS81	ME- MS81	ME- MS81	ME- MS81	ME- MS81	ME- MS81	ME- MS81	ME- MS81
	Analyte	La	Lu	Nb	Nd	Pr	Rb	Sm	Sn	Sr	Ta	Tb	Th	Tm	U	V
	Units	ppm	ppm	ppm	ppm	ppm	ppm	ppm	ppm	ppm	ppm	ppm	ppm	ppm	ppm	ppm
	LOR	0.5	0.01	0.2	0.1	0.03	0.2	0.03	1	0.1	0.1	0.01	0.05	0.01	0.05	5
BKS127952		40.6	0.39	48.9	51.8	11.45	37.0	11.45	2	740	2.1	1.36	1.57	0.48	0.75	105
BKS132409		99.7	0.95	21.2	87.3	23.0	95.0	15.60	3	148.5	1.3	1.92	16.55	0.96	3.99	88
BKS132410		40.1	0.63	24.9	40.5	10.40	102.0	7.90	5	142.5	1.7	0.92	21.4	0.56	2.89	95
BKS132411		41.4	0.67	18.2	44.2	11.00	141.0	8.68	4	189.0	1.3	1.30	17.50	0.74	3.02	84
BKS132413		65.6	0.81	21.7	63.3	16.30	109.5	13.15	3	246	1.4	1.75	22.0	0.84	3.94	123
BKS132414		78.8	0.92	23.5	74.1	18.90	134.5	12.95	3	182.0	1.7	1.77	24.3	0.94	3.33	105
BKS132415		14.1	0.26	21.2	24.8	4.79	13.1	6.62	4	441	1.1	1.01	1.30	0.31	0.41	229
BKS132416		6.7	0.35	5.2	12.4	2.39	7.2	4.26	3	271	0.4	1.03	1.89	0.42	0.78	224
BKS132417		15.0	0.24	21.1	23.2	4.71	24.6	6.23	2	425	1.2	0.96	1.47	0.28	0.53	216
BKS132418		11.4	0.34	14.9	18.8	3.76	3.8	5.52	2	356	0.8	0.98	0.86	0.37	0.25	226
BKS132420		15.9	0.38	22.8	24.5	4.80	11.3	6.53	2	383	1.3	1.00	1.36	0.42	0.44	243
BKS132421		16.5	0.36	19.1	25.7	5.23	10.8	6.86	4	384	1.1	1.09	2.13	0.38	0.56	231
BKS132423		14.3	0.25	20.7	24.0	4.59	13.2	6.31	2	428	1.1	1.00	1.57	0.36	0.44	233
BKS132424		9.3	0.20	13.7	15.4	3.05	13.1	4.26	1	317	0.7	0.67	1.15	0.24	0.41	195

Sample Description	Method Analyte Units LOR	ME- ICP06 SrO % 0.01	ME- ICP06 BaO % 0.01	OA- GRA05 LOI % 0.01	TOT- ICP06 Total % 0.01
BKS127952		0.08	0.13	0.43	100.61
BKS132409		<0.01	0.11	2.49	101.08
BKS132410		<0.01	0.08	2.58	100.76
BKS132411		0.01	0.07	1.35	101.69
BKS132413		<0.01	0.06	2.69	100.19
BKS132414		0.01	0.08	0.95	100.19
BKS132415		0.04	0.02	-0.10	100.34
BKS132416		0.02	0.02	-0.05	101.35
BKS132417		0.04	0.03	0.22	101.05
BKS132418		0.03	0.02	0.40	101.57
BKS132420		0.04	0.02	-0.36	100.65
BKS132421		0.04	0.01	0.37	100.02
BKS132423		0.04	0.02	-0.20	101.14
BKS132424		0.03	0.02	0.54	100.11

Sample Description	Method Analyte Units LOR	ME- MS81 W ppm 1	ME- MS81 Y ppm 0.5	ME- MS81 Yb ppm 0.03	ME- MS81 Zr ppm 2	ME- ICP06 SiO2 % 0.01	ME- ICP06 Al2O3 % 0.01	ME- ICP06 Fe2O3 % 0.01	ME- ICP06 CaO % 0.01	ME- ICP06 MgO % 0.01	ME- ICP06 Na2O % 0.01	ME- ICP06 K2O % 0.01	ME- ICP06 Cr2O3 % 0.01	ME- ICP06 TiO2 % 0.01	ME- ICP06 MnO % 0.01	ME- ICP06 P2O5 % 0.01
BKS127952		13	37.8	3.18	807	53.1	18.00	11.40	5.47	2.94	4.17	2.11	0.01	2.03	0.16	0.58
BKS132409		25	57.9	6.20	284	63.1	18.05	7.17	1.24	1.62	2.28	3.82	0.01	0.96	0.09	0.14
BKS132410		27	31.8	4.12	478	64.1	17.60	6.47	0.88	2.25	2.10	3.35	0.01	1.10	0.08	0.16
BKS132411		21	37.1	5.07	294	64.2	18.30	7.69	1.31	1.82	2.32	3.39	0.01	0.90	0.11	0.21
BKS132413		46	54.8	5.72	261	60.4	17.05	8.37	1.95	3.12	2.52	2.81	0.01	0.98	0.07	0.16
BKS132414		31	56.6	6.25	273	58.4	20.1	9.15	1.60	2.35	2.66	3.47	0.01	1.12	0.11	0.18
BKS132415		36	25.7	2.04	158	48.2	12.15	14.60	9.07	9.82	2.29	0.61	0.04	3.08	0.18	0.34
BKS132416		78	30.1	2.62	96	54.8	13.20	13.40	8.55	8.00	0.95	0.08	0.05	2.02	0.18	0.13
BKS132417		34	23.8	1.99	145	49.1	12.75	14.35	8.98	11.15	1.08	0.33	0.05	2.45	0.18	0.34
BKS132418		18	27.5	2.20	142	50.6	14.20	13.95	9.77	6.53	2.60	0.35	0.02	2.66	0.17	0.27
BKS132420		14	29.4	2.78	181	48.8	14.75	15.85	9.41	5.60	2.61	0.50	0.01	2.91	0.19	0.32
BKS132421		15	28.4	2.40	161	50.1	14.15	12.90	9.31	5.99	2.67	0.99	0.03	2.96	0.17	0.33
BKS132423		19	26.6	1.92	149	48.9	12.75	14.15	9.53	9.53	2.46	0.70	0.04	2.70	0.18	0.34
BKS132424		6	20.0	1.70	97	48.0	14.50	14.05	8.92	9.06	2.28	0.52	0.03	1.77	0.17	0.22

H: Detection limits from ALS

ME-ICP06 (ICP-AES) – Major element analysis

ELEMENT	SYMBOL	UNITS	LOWER LIMIT	UPPER LIMIT
Aluminum	Al_2O_3	%	0.01	100
Barium	BaO	%	0.01	100
Calcium	CaO	%	0.01	100
Chromium	Cr_2O_3	%	0.01	100
Iron	Fe_2O_3	%	0.01	100
Magnesium	MgO	%	0.01	100
Manganese	MnO	%	0.01	100
Phosphorus	P_2O_5	%	0.01	100
Potassium	K_2O	%	0.01	100
Silicon	SiO	%	0.01	100
Sodium	Na_2O	%	0.01	100
Strontium	SrO	%	0.01	100
Titanium	TiO_2	%	0.01	100

ME-ICP61 (ICP-AES) – Trace element analysis

ELEMENT	SYMBOL	UNITS	LOWER LIMIT	UPPER LIMIT
Molybdenum	Mo	ppm	1	10,000
Sodium	Na	%	0.01	10
Nickel	Ni	ppm	1	10,000
Phosphorus	P	ppm	10	10,000
Lead	Pb	ppm	2	10,000
Sulphur	S	%	0.01	10
Antimony	Sb	ppm	5	10,000
Scandium	Sc	ppm	1	10,000
Strontium	Sr	ppm	1	10,000
Thorium	Th	ppm	20	10,000
Titanium	Ti	%	0.01	10
Thallium	Tl	ppm	10	10,000
Uranium	U	ppm	10	10,000
Vanadium	V	ppm	1	10,000
Tungsten	W	ppm	10	10,000
Zinc	Zn	ppm	2	10,000

ME-MS81 (ICP-MS) – Trace element analysis

ELEMENT	SYMBOL	UNITS	LOWER LIMIT	UPPER LIMIT
Niobium	Nb	ppm	0.2	10000
Neodymium	Nd	ppm	0.1	10000
Nickel*	Ni	ppm	5	10000
Lead*	Pb	ppm	5	10000
Praseodymium	Pr	ppm	0.03	1000
Rubidium	Rb	ppm	0.2	10000
Samarium	Sm	ppm	0.03	1000
Tin	Sn	ppm	1	10000
Strontium	Sr	ppm	0.1	10000
Tantalum	Ta	ppm	0.1	10000
Terbium	Tb	ppm	0.01	1000
Thorium	Th	ppm	0.05	1000
Thallium	Tl	ppm	0.5	1000
Thulium	Tm	ppm	0.01	1000
Uranium	U	ppm	0.05	1000
Vanadium	V	ppm	5	10000
Tungsten	W	ppm	1	10000
Yttrium	Y	ppm	0.5	10000
Ytterbium	Yb	ppm	0.03	1000
Zinc*	Zn	ppm	5	10000
Zirconium	Zr	ppm	2	10000

ELEMENT	SYMBOL	UNITS	LOWER LIMIT	UPPER LIMIT
Silver*	Ag	ppm	1	1000
Barium	Ba	ppm	0.5	10000
Cerium	Ce	ppm	0.5	10000
Cobalt*	Co	ppm	0.5	10000
Chromium	Cr	ppm	10	10000
Cesium	Cs	ppm	0.01	10000
Copper*	Cu	ppm	5	10000
Dysprosium	Dy	ppm	0.05	1000
Erbium	Er	ppm	0.03	1000
Europium	Eu	ppm	0.03	1000
Gallium	Ga	ppm	0.1	1000
Gadolinium	Gd	ppm	0.05	1000
Hafnium	Hf	ppm	0.2	10000
Holmium	Ho	ppm	0.01	1000
Lanthanum	La	ppm	0.5	10000
Lutetium	Lu	ppm	0.01	1000
Molybdenum*	Mo	ppm	2	10000

I: Analyses of samarium (Sm) and neodynium (Nd) isotopes

Sample	MO-28771	P6.3	P5.2	UM-46	P9.4	UM-1D	UM-61	P5.1	UM-1A	MO-28770
Rock type	Host rock	Gabbro	Gabbro	Gabbro	Gabbro	Gabbro	Gabbro	Mafic dyke	Mafic dyke	Mafic dyke
UTM E33	485826	485990	485193	488127	487909	481390	482451	485155	481390	485696
UTM N33	7338733	7338443	7338574	7336112	7339147	7337541	7336086	7338781	7337541	7338864
Sm (ppm)	6.79	8.94	4.92	2.33	4.05	5.35	5.93	4.79	4.09	7.46
Nd (ppm)	31.6	40.5	21.8	8.17	13.7	19.3	22.6	17.3	13.0	26.7
$^{147}Sm/^{144}Nd$	0.1297	0.1335	0.1362	0.1722	0.1788	0.1672	0.1585	0.1674	0.1898	0.1687
$^{143}Nd/^{144}Nd$	0.511967	0.512275	0.512327	0.512775	0.512821	0.512805	0.512781	0.512673	0.512785	0.512764
2 s.e.	4	2	3	3	2	2	3	2	3	3
ε_{Nd} (0)	-13.1	-7.1	-6.1	2.6	3.5	3.2	2.8	0.6	2.8	2.4
Age (Ma)	565	565	565	565	565	565	565	565	565	565
ε_{Nd} (565 Ma)	-8.2	-2.5	-1.7	4.4	4.8	5.4	5.6	2.8	3.3	4.5
TDM (Ga)	1.96	1.46	1.41	1.00	0.99	0.81	0.75	1.22	1.64	0.96

J: Chemistry for samples analysed for Sm-Nd

Sample	MO-28771	P6.3	P5.2	UM-46	P9.4	UM-1D	UM-61	P5.1	UM-1A	MO-28770
SiO2	61.9	55.1	58.4	45.4	48.3	49.5	49.2	57	49.4	48.4
Al2O3	16.65	16.2	16.9	10.3	12.55	15.3	14.65	12.85	13.85	13.2
Fe2O3	7.8	11.45	7.9	16.7	14.65	10.85	11.9	10.6	13.2	15
FeO	7.02	10.30	7.11	15.03	13.18	9.76	10.71	9.54	11.88	13.50
CaO	1.03	6.56	5.19	7.08	9.96	11	10.1	7.3	9.25	8.39
MgO	2.88	3.9	4.02	18.9	10.6	7.07	7.81	5.66	8.76	9.25
Na2O	1.04	2.78	3.53	1.51	2.07	2.99	3.17	2.68	3.61	0.91
K2O	4.5	1.92	1.49	0.26	0.3	0.45	0.7	0.81	0.51	0.43
Cr2O3	0.01	0.02	0.02	0.03	0.06	0.03	0.06	0.03	0.05	0.05
TiO2	0.84	2.16	1.49	1.09	2.78	2.02	2.2	1.96	1.92	3.05
MnO	0.09	0.15	0.09	0.21	0.2	0.14	0.16	0.14	0.18	0.21
P2O5	0.18	0.3	0.19	0.12	0.21	0.25	0.3	0.21	0.23	0.46
SrO	0.02	0.02	0.03	<0.01	0.03	0.04	0.04	0.02	0.02	0.05
BaO	0.09	0.04	0.02	0.01	0.01	0.02	0.02	0.01	0.02	0.01
LOI	1.5	0.18	0.36	-0.59	-0.1	0.92	0.06	0.41	0.35	0.6
Total	98.5	100.78	99.63	101.02	101.62	100.58	100.37	99.68	101.35	100
Ag	<1	<0.5	<0.5	<0.5	<0.5	<0.5	<0.5	<0.5	<0.5	<1
Ba	757	431	184	79.3	118	164	185	112	173.5	98.7
Ce	95	79.9	38.4	11.6	18.4	25.4	32.3	27.4	17.2	37
Co	18.4	28	25	99	60	40	44	37	47	49.4
Cr	70	90	130	210	380	160	380	160	320	290
Cs	5.08	4.15	3.22	0.24	0.15	1.31	0.49	1.36	0.52	0.9
Cu	7	23	29	52	43	51	39	15	55	25
Dy	8.56	7.94	4.37	2.46	4.1	4.53	4.91	4.62	4.19	6.13
Er	5.81	4.31	2.83	1.16	2.17	2.19	2.43	2.32	1.98	2.93
Eu	1.06	2.71	2.09	0.81	1.42	1.79	1.85	1.92	1.48	2.09
Ga	26.9	25.2	20.5	12.6	17.3	18.5	21	18.9	20.2	20.8
Gd	6.91	8.21	4.24	2.35	4.6	5.4	6.06	4.86	4.82	7.39
Hf	6.3	5.6	6.6	1.1	2	3.8	3	2.9	2.7	4.7
Ho	1.89	1.51	0.89	0.5	0.76	0.85	0.9	0.9	0.78	1.12
La	29.2	39.4	20.2	5.3	8.6	11.8	14.3	13.3	7.3	16.1
Lu	0.78	0.65	0.48	0.16	0.21	0.23	0.25	0.31	0.22	0.32
Mo	<2	1	<1	<1	<1	<1	<1	1	1	2
Nb	20.6	27.4	14.9	7.6	15.6	22.1	23	17.3	14.7	30.1
Nd	30.4	40.8	19.4	7.8	13.3	18.4	22.6	18	13	25.3
Ni	31	26	84	604	269	111	116	91	160	187
Pb	14	12	14	4	3	2	2	12	2	<5
Pr	7.9	9.99	4.83	1.62	2.83	3.76	4.85	3.64	2.56	5.36
Rb	169.5	83.7	76.9	7.5	5.8	13.6	16.4	27.5	8.7	24.3
Sm	6.45	9.88	4.35	1.96	3.77	4.54	5.12	5.33	3.78	6.72
Sn	3	4	2	2	1	1	2	3	1	2
Sr	134.5	287	302	172.5	364	459	457	306	355	374
Ta	1.5	1.9	1	0.9	1.2	1.7	1.5	1.2	1.2	1.9
Tb	1.2	1.31	0.69	0.45	0.68	0.76	0.94	0.75	0.79	1.15
Th	20.1	8.89	5.61	0.66	0.77	1.08	1.44	2.14	1.05	1.94
Tl	<0.5	<10	<10	<10	<10	<10	<10	<10	<10	<0.5
Tm	0.81	0.59	0.43	0.17	0.26	0.28	0.29	0.34	0.25	0.4
U	2.09	1.92	1.77	0.18	0.22	0.36	0.42	0.99	0.49	0.74
V	83	222	113	144	196	162	199	190	213	215
W	1	1	<1	<1	<1	<1	<1	1	<1	1
Y	49	40.7	24.5	12.5	18.6	20.8	22.7	22.7	19.5	28
Yb	5.37	3.98	3.03	1.13	1.43	1.63	1.63	2.02	1.48	2.27
Zn	106	122	93	134	128	92	114	109	136	167
Zr	213	224	256	52	80	152	119	110	90	186

K: Compilation of partition coefficients

Stage 1			
Element	Olivine	Orthopyroxene	Clinopyroxene
Sr	0.00019	0.004	0.058
Ba	0	0	0
Y	0.009	0.101	0.46
Ti	0.0045	0.18	0.33
Zr	0.0047	0.016	0.084
Nb	0.01	0.0013	0.003
Th	0	0	0
Ni	12.2	6.66	4.13
Co	5.15	2.76	1.39
V	0.019	0.43	0.87
Cr	1.32	3.7	5.3
Sc	0.186	1.38	2.75
La	0.008	0.001	0.04
Ce	0.0076	0.004	0.079
Pr	0.00685	0.007	0.125
Nd	0.0061	0.01	0.177
Sm	0.0049	0.02	0.294
Eu	0.0052	0.035	0.337
Gd	0.0053	0.048	0.41
Tb	0.0051	0.061	0.443
Dy	0.0049	0.074	0.476
Ho	0.00535	0.105	0.455
Er	0.0058	0.161	0.479
Yb	0.0468	0.232	0.455
Lu	0.009	0.219	0.441
Min. prop	40	30	30
Norman, etal 2005		Tholeiitic Basalt	
Fujimaki etal, 1984		Tholeiitic Basalt	
Bougault & Hekinian, 1974		Basalt, low-K tholeiites	
Ewart etal, 1973		Basalt Andesite	
Villemant etal, 1981		Alkali basalt	
McKenzie & O'nions, 1991		Basalt	
Nikogosian & Sobolev, 1997		Basalt	
Green etal, 2000		Tholeiitic Basalt	

Stage 2				
Element	Opx	Cpx	Plg	(Garnet)
Sr	0.0012	0.07	1.71	
Ba	0	0	0.56	
Y	0.101	0.70	0.011	
Ti	0.27	0.481	0.029	
Zr	0.016	0.11	0.0051	
Nb	0	0.0081	1.3	
Th	0	0.03	0.01	
Ni	7.3	4	1.5	
Co	4.5	2.4	0.07	
V	0.6	1.14	**0.016**	
Cr	3.7	5.3	0.01	
Sc	1.9	4.11	0.015	
La	0.001	0.1047	0.035	0.37
Ce	0.004	0.1254	0.028	0.51
Pr	0.007	0.206	0.02	0.59
Nd	0.01	0.2866	0.022	0.68
Sm	0.02	0.4774	0.028	0.76
Eu	0.035	0.5618	0.16	0.214
Gd	0.048	0.5954	0.009	5.3
Tb	0.061	0.6086	0.0101	8.9
Dy	0.074	0.6218	0.0112	13.65
Ho	0.105	0.6287	0.0114	18.4
Er	0.161	0.6356	0.0116	22.65
Yb	0.232	0.601	0.0155	26.9
Lu	0.219	0.5602	0.012	24.6
Min. prop.	21	21	58	(5)

	Norman, 2005	Thol. Basalt
	Fujimaki, 1984	Thol. Basalt
	Ewart etal, 1973	Basalt Andesite
	Green, 2000	Tholeiitic basalt
	Zajac&Halter, 2007	Basaltic andesite
	Ewart & Griffin, 1994	Dacite **Andesite-basalt**
	Bacon & Druitt, 1988	Andesite
	Irving & Frey, 1978	Rhyolite-dacite
	Dostal, 1983	Basalt-Andesite
	Hauri, 1994	Basalt
	Villemant etal, 1981	Alkali basalt

Stage 3

	Cpx	Plg	Biotite	Ilmenite	K-feldspar	Quartz	Hornblende	(Garnet)
Sr	0.101	2.422	0.2	0.17	*1.48*	0.041	**0.495**	
Ba	0.001	0.186	4.04	0	*1.7*	0	**0.387**	
Y	0.949	0.012	0.6	1.6	*0.017*	0	1.47	
Ti	0.412	0.043	0	150	0	0.038	3.06	
Zr	0.097	0.55	0.13	1.98	0.01	**0**	0.35	
Nb	0.008	0.008	7.5	50.9	*0.15*	0	2.5	
Th	0.03	0.01	0.09	7.5	0.025	0.009	0.5	
Ni	4	1.5	4.25	**3.8**	0	0	6.8	
Co	2.4	0.12	6.32	2.2	0	0	**1.77**	
V	1.532	0.016	0	80	0	0	1.49	
Cr	9.7	0.5	1.52	3	0	0	**1.59**	
Sc	3.306	0.015	2.81	5.9	0.03	0.012	**4.2**	
La	0.082	0.088	0.318	7.1	0.026	0.015	**0.435**	**0.076**
Ce	0.18	0.077	0.377	7.8	0.017	0.014	**0.545**	0.3695
Pr	0.28	0.065	0.381	7.7	0.013	0.015	0.85	0.663
Nd	0.38	0.054	0.386	7.6	0.009	0.016	1.155	0.9565
Sm	0.61	0.033	0.39	6.9	0.0024	0.014	**1.46**	**1.25**
Eu	0.626	0.397	0.328	2.5	1.6	0.056	**1.49**	**1.52**
Gd	0.907	0.037	0.442		0	0.0365	**1.72**	**5.2**
Tb	0.9165	0.025	0.393	6.5	0.012	0.017	**1.96**	**7.1**
Dy	0.926	0.013	0.462	4.9	0.0095	0.014	1.825	15.45
Ho	1.009	0.017	0.532	4.6	0.007	0	1.69	**23.8**
Er	0.991	0.0135	0.601	4.4	0.0045	0	1.555	38.4
Yb	0.973	0.01	0.67	4.1	0.002	0	1.42	**53**
Lu	0.955	0.0065	0.743	3.6	0.003	0	1.31	**57**
Min. prop.	15	30	6	0.5	20	14.5	10	4

Pearce & Norry, 1979	Intermediate		
Ewart & Griffin, 1994	Dacite	**Andesite-basalt**	*Low silica rhyolite*
Severs etal, 2009	Dacite		
Ewart etal, 1973	Basalt andesite		
Nash & Crecraft, 1985	Rhyolite		
Matsui, 1977	Dacite	**Andesite**	
Irving & Frey, 1978	Rhyolite-daci	**Andesite**	
Sisson & Bacon, 1992	Rhyolite		
Paster etal, 1974	Tholeiitic basalt		
Dostal, 1983	Basalt-Andesite		
Luhr et al, 1984	Trachyandesite		
Mysen 1978	Basalt		
Sisson , 1994	Basalt-Andesite		
Villemant, 1988	Trachyte		
Stix & Gordon, 1990	High-silica rhyolite		
Hauri, 1994	Basalt		
Stimac & Mickmott 1994	Rhyolite		

L: Overview of minerals observed in thin section

Rock	Sample nr.	Green. ign hbl	Act	Amp	Cpx	Opx	Ol	Zrn	Cal	Pl	Kfs	Sericite	Ap	Qz	Ms	Bt	Ep	Czo	Ttn	Rt	Opaque	Chl	Grt	Scp	Srp
Monzodiorite	127952			x				x		x		x	x	x	x	x				x	x		x		x
Porphyritic diorite	127953A			x						x		x	x			x	x		x	x	x				
Monzodiorite	127958			x			x	x	x	x		x	x			x		x			x		x		
Monzodiorite	127960			x						x		x	x			x	x		x		x	x			
Monzodiorite	127961			x		x		x	x	x		x		x		x	x	x	x	x	x	x			
Monzonite	127968	x								x	x														
Monzonite	127977						x	x	x	x		x	x	x	x	x	x	x		x	x			x	
Monzonite	127987	x	x	x	x		x		x	x		x	x		x	x				x	x		x		
Monzodiorite	132404A	x	x	x	x	x	x		x	x	x	x	x	x	x	x		x	x	x	x				
Monzodiorite	132404B	x		x	x	x			x	x	x	x	x		x					x					
Granofels	127997								x						x				x	x			x		
Felsic rock	127964 a		x	x			x		x			x	x	x	x					x	x			x	x
Felsic rock	127964 b		x	x					x			x	x	x	x					x	x				x
Felsic rock	127966								x	x	x	x	x	x	x	x		x		x					
Felsic rock	127967	x				x		x	x	x	x	x	x	x						x				x	
Felsic rock	127971A							x	x	x	x		x		x	x	x	x		x					
Felsic rock	127971B						x	x		x	x		x	x	x	x	x	x	x	x				x	
Felsic rock	127973	x			x		x	x	x	x	x				x		x	x							
Felsic rock	127974						x			x			x			x		x		x					
Felsic+mafic material	127975 a		x			x	x	x	x	x	x	x	x		x	x				x					
Felsic rock	127975 b			x	x	x	x	x	x	x	x	x	x		x	x					x				
Felsic rock	127976							x	x	x	x	x	x	x	x										
Felsic rock	127990					x	x		x	x	x	x	x			x					x				
Contact granodiorite	132410								x	x			x	x	x					x	x	x			
Contact granodiorite	132411								x	x		x	x	x	x	x					x		x		
Contact granodiorite	132414								x	x		x	x	x	x				x	x			x		
Metased. host rock	132409							x		x			x	x	x	x			(x)	x	x	x	x		

Rock	Sample nr.	Act	Amp	Cpx	Opx	Ol	Zrn	Cal	Pl	Kfs	Sericite	Ap	Qz	Ms	Bt	Ep	Czo	Ttn	Rt	Opaque	Chl	Grt	Scp
Ol-gabbro	127955		x		x	x		x	x			x			x					x			
Ol-gabbro	127991			x	x	x		x	x						x					x			
Ol-gabbro	127983			x	x	x			x			x			x					x			
Ol-gabbro	127988			x	x	x			x						x					x			
Ol-gabbro	127998			x	x	x		x	x						x					x			
Gabbro	127951		x	x	x	(x)	x	x	x		x	x	x		x					x		x	
Gabbro	127963	x	x	x	x				x		x	x			x	x				x			
Gabbro	127965		x						x		x				x		x		x	x	x		x
Gabbro	127972		x					x	x						x		x			x			
Gabbro	127980A		x					x	x						x	x		x	x	x			
Gabbro	127980B		x						x						x	x		x	x	x			
Gabbro	127984		x					x	x		x		x		x	x	x		x	x		x	x
Gabbro	127985		x						x		x						x		x	x			x
Gabbro	127992		x					x	x					x			x		x	x			x
Gabbro	127996A	x	x	x	x				x			x			x					x			
Gabbro	127996B	x	x	x	x			x	x		x	x			x					x			
Gabbro (foliated)	127999A		x						x						x			x		x			
Gabbro (foliated)	127999B		x						x						x			x		x		x	
Gabbro	128000		x					x	x		x	x			x		x	x	x	x			x
Gabbro	132402A		x						x		x	x	x		x		x	x	x	x			
Gabbro	132402B	x	x		x			x	x		x	x			x					x	x		
Gabbro	132403		x						x				x		x	x	x	x		x			
Mafic enclave	127953 b		x						x		x				x			x		x			
Mafic enclave	127954		x						x		x				x			x		x			
Aphyric mafic dyke	127956		x					x	x		x				x			x	x	x			
Mafic porp. Mat	127957		x					x	x		x	x			x			x		x			
Aphyric mafic dyke	127962	x	x						x		x							x		x			
Mafic (porphyric) dyke	127969		x		x			x	x						x					x			
Mafic porphyric rock	127970		x						x				x		x			x	x	x			
Mafic dyke	127979		x		x			x	x			x			x					x			
Mafic fine grd dyke	127993		x	x	x		x	x	x			x			x					x			
Mafic fine grd dyke	127994		x	x	x				x						x					x			
Aphyric mafic dyke	127959		x					x	x						x			x	x	x			
Aphyric mafic dyke	127978		x				x		x						x				x	x			
Aphyric mafic dyke	127981		x						x						x	x		x		x			
Aphyric mafic dyke	127982		x						x						x	x		x		x			
Mafic (porphyric) dyke	127986		x		x				x			x			x					x			
Aphyric mafic dyke	127989		x		x				x			x						x		x			
Ultramafic dyke	127995		x			x									x					x			
Mafic (porphyric) dyke	132401		x		x			x	x						x					x			
Mafic enclave	132420		x						x		x	x			x					x			

M: Modelled trace element compositions

	F	Sr	Ba	Y	Zr	Nb	Th	Ni	Co	V	Cr	Sc
Stage 1	1	651.00	182.00	20.20	142.00	30.90	2.07	235.00	49.40	259.00	464.00	20.10
	0.98	664.03	185.71	20.54	144.80	31.53	2.11	203.53	47.15	262.17	443.58	19.97
	0.95	684.58	191.58	21.08	149.23	32.52	2.18	163.13	43.89	267.13	413.89	19.78
	0.92	706.47	197.83	21.64	153.94	33.57	2.25	129.82	40.76	272.34	385.33	19.58
	0.9	721.86	202.22	22.04	157.25	34.31	2.30	111.02	38.75	275.97	366.92	19.45
	0.87	746.26	209.20	22.67	162.50	35.49	2.38	87.22	35.84	281.67	340.23	19.24
	0.85	763.48	214.12	23.11	166.20	36.32	2.44	73.92	33.97	285.64	323.05	19.10
	0.85	763.48	214.12	23.11	166.20	36.32	2.44	73.92	33.97	285.64	323.05	19.10
	0.85	763.48	214.12	23.11	166.20	36.32	2.44	73.92	33.97	285.64	323.05	19.10
	0.85	763.48	214.12	23.11	166.20	36.32	2.44	73.92	33.97	285.64	323.05	19.10
Stage 2	1	763.48	214.12	23.11	166.20	36.32	2.44	73.92	33.97	285.64	323.05	19.10
	0.95	763.25	221.66	24.11	174.69	36.78	2.56	65.88	33.12	294.95	308.54	18.84
	0.95	763.25	221.66	24.11	174.69	36.78	2.56	65.88	33.12	294.95	308.54	18.84
	0.85	762.77	238.95	26.43	194.62	37.79	2.86	51.34	31.37	316.19	279.28	18.28
	0.85	762.77	238.95	26.43	194.62	37.79	2.86	51.34	31.37	316.19	279.28	18.28
	0.75	762.23	260.02	29.31	219.79	38.97	3.24	38.77	29.50	341.94	249.66	17.67
	0.75	762.23	260.02	29.31	219.79	38.97	3.24	38.77	29.50	341.94	249.66	17.67
	0.75	762.23	260.02	29.31	219.79	38.97	3.24	38.77	29.50	341.94	249.66	17.67
	0.7	761.93	272.42	31.03	235.03	39.63	3.46	33.21	28.52	357.01	234.69	17.34
	0.65	761.60	286.40	32.98	252.58	40.35	3.73	28.13	27.51	373.94	219.62	17.00
Stage 3	1	761.60	286.40	32.98	252.58	40.35	3.73	28.13	27.51	373.94	219.62	17.00
	0.95	755.78	289.70	34.08	262.65	40.50	3.89	26.55	27.36	370.44	209.49	16.81
	0.9	749.68	293.22	35.28	273.71	40.65	4.08	24.99	27.21	366.77	199.32	16.62
	0.85	743.30	296.98	36.60	285.90	40.81	4.28	23.43	27.06	362.94	189.10	16.42
	0.8	736.58	301.03	38.04	299.43	40.98	4.51	21.89	26.89	358.92	178.84	16.21
	0.75	729.50	305.40	39.64	314.54	41.16	4.76	20.36	26.71	354.69	168.52	15.99
	0.7	722.00	310.14	41.43	331.53	41.36	5.05	18.84	26.53	350.22	158.15	15.76
	0.65	714.04	315.32	43.44	350.80	41.57	5.38	17.34	26.33	345.48	147.72	15.51
	0.6	705.53	321.00	45.72	372.88	41.80	5.76	15.85	26.11	340.44	137.23	15.25
	0.55	696.40	327.30	48.34	398.46	42.05	6.21	14.37	25.88	335.04	126.66	14.97
	0.5	686.53	334.34	51.38	428.50	42.32	6.74	12.91	25.63	329.22	116.02	14.67
	0.45	675.79	342.30	54.96	464.35	42.63	7.37	11.47	25.36	322.91	105.30	14.35